UNIVERSITAT POLITÈCNICA DE CATALUNYA
BARCELONATECH

Modelling of Liberation in Ta- and W-Rich Minerals

A thesis submitted for the degree of Doctor of Philosophy at

Universitat Politecnica de Catalunya in October 2019

Department d'Enginyeria Minera, Industrial I TIC

Sarbast Ahmad Hamid

Name of the Supervisor: Prof. Pura Alfonso Abella
Prof. Josep Oliva Moncunill

Abstract

With the general trend across all commodities towards the treatment of lower grade and medium grade ores, it is becoming increasingly important to develop the proper design for comprehensive mineralogical characterization and a complete procedure based on image analysis and grade distribution is proposed for the measurement of the liberation in the particles to reach the mineral liberation modeling.

The tendency for the complexity of the mineral group in the ore to increase requires the use of more complicates tools in order to characterize the ore in the context of the implications of the mineralogy on its process response. Some of the key mineralogical attributes that are used to inform process selection and infer process response include: which identification of valuable minerals; the type and relative proportions of the minerals present (modal mineralogy); and the grain size, association and liberation characteristics of the valuable minerals.

Ta and W ores are typically complex in terms of their mineralogical characterization. There are a wide range of minerals that contain Ta and W in different proportions which can make it difficult to identify them. Additional challenges include the relatively low concentrations of Ta (ppm) within an ore, the large number of Ta and W-bearing minerals that can occur in a deposit and the potential for Ta and W to occur in wide range of different minerals. Therefore, understanding the mineralogical attributes of the ore, particularly the valuable minerals within the ore, is critical in developing an effective concentration processing strategy.

Automated SEM-based systems are a commonly used tool to quantify these attributes for an ore, but the low-grade and medium grade together with the large number of minerals that are potential hosts for Ta and W means that often, complementary analytical tools must be used in order to properly account for the valuable element.

This thesis aims to develop an appropriate methodology to characterize complex low-grade Ta and medium grade W ores for the purpose of developing the most appropriate physical separation strategy. As result of this investigation a methodology is proposed for the mineralogical characterization and it consists of three different levels of characterization using different analytical techniques. Level 1, the simplest (which included chemical analysis, XRD, optical microscopy, SEM, and EMPA), was applied to Penouta and Mittersill ores and successfully characterized the mineralogy. Level 2, which included mineral characterization of the processed ores, and were XRD, SEM, and EMPA were needed for ores. The ores required the added sophistication of Level 3. In addition to the techniques of Level 1 and Level 2, Level 3 included the use of chemical analysis and automated SEM to estimate the mineralogical attributes of the ores. The insights from the mineralogical characterization were then used to inform the physical separation testing that was undertaken, for example, selective or bulk concentration.

The ore characterization for Penouta deposit identified the presence of at least eight

tantalum-bearing minerals including coarse grained quartz. Mineralogical analysis of preconcentration test samples indicated that that columbite-group minerals (CGM) are the most abundant Nb-Ta rich phases in the Penouta leucogranite. These results, together with the mineralogical characterization, indicated that selective gravity separation would be an appropriate processing route for this ore. The fine-grained Ta minerals required a P80 of about 100 µm. The final flow sheet produced a rougher concentrate that contained 103 ppm of Ta, at a recovery of 52%.

In the Mittersill ore, the majority of the scheelite (>99%) was contained in hornblende, which itself represented approximately 33% of the ore. A bulk separation strategy using shaking table and the introduction of grinding to generate a P80 of 150 µm, was necessary to recover scheelite minerals to achieve a rougher concentrate of 2260 ppm W at a recovery of 87%.

The mineralogical characterization of Mittersill, during which an association was found between scheelite and quartz, accounting for more than 17% of quartz in this ore with most of the remainder occurring as fine-grained quartz helped to guide the mineralogical characterization.

This work describes a method for determining the downstream milling energy requirements for the mill products based on a Bond mill test performance. The grade distribution of particles at a given size fraction was calculated using a predictive liberation model. The concentration behavior of these particles in size fractions was evaluated using batch concentrate tests. The recovery of particles in size/grade classes, image analysis using mineral liberation analysis (MLA), and function calculations were implemented for the modeling of the liberation. By describing the size, grade, and recovery data of particles in size/grade classes, a technique for the measurement of distribution functions was developed that relates beta distribution, a model for the function based on the incomplete beta function, and a solution to produce liberation modeling. It was shown that the predicted results agreed well with the observed results. With a procedure for measuring the liberation, it was possible to carry out the first experimental measurement of the beta distribution. The model was implemented in MATLAB, a simulation model, with King's solution to the beta distribution function model that includes the liberation distribution.

The outcomes of this research include:

- A systematic method that enables the development of gravity separation strategies to achieve >50% tantalum and >80% scheelite recovery in laboratory rougher separation. Analyses of concentrate products were performed on unsized, size-by-size and size-by-liberation bases, opening a broad understanding of the behavior of complex low-grade tantalum and medium grade tungsten ores.
- A framework for assessing the 'liberation model' of tantalum and tungsten ores based on the mineralogical characteristics of the ores and the gravity separation performance.
- The liberation/concentrate model has wide potential applications for metallurgy and plant

design, where the liberation modeling is to be determined with the distribution density solution to the predictive mineral liberation function equation, which includes the liberation of ores samples and their liberation characteristics.

In summary this work provides a clear demonstration of how powerful a detailed mineralogical study at the onset of a project can be to guide the modeling the liberation test work for improved recoveries.

Publications during candidature

Peer-reviewed journal paper

Alfonso, P., Hamid, S.A., García-Vallès, M., Llorens, T., Moro, F. L., Tomasa, O., Calvo D., Guasch E., Anticoi H., Oliva J., & Parcerisa, D. (2018). Textural and mineral-chemistry constraints on columbite-group minerals in the Penouta deposit: evidence from magmatic and fluid-related processes. Mineralogical magazine, 82(S1), S199-S222. https://doi.org/10.1180/minmag.2017.081.107.

Hamid, S.A., Alfonso, P., Anticoi, H., Guasch, E., Oliva, J., Dosbaba, M., Garcia-Valles M., & Chugunova, M. (2018). Quantitative mineralogical comparison between HPGR and ball mill products of a Sn-Ta ore. Minerals, 8(4), 151. https://doi.org/10.3390/min8040151.

Hamid, S.A., Alfonso, P., Oliva, J., Anticoi, H., Guasch, E., Hoffmann Sampaio, C., Garcia-Valles M., & Escobet, T. (2019). Modeling the Liberation of Comminuted Scheelite Using Mineralogical Properties. Minerals, 9(9), 536. https://doi.org/10.3390/min9090536.

Conference paper

Guasch, E., Anticoi, E., Hamid, S.A., Oliva J., and Alfonso P., New approach to ball mill modelling as a piston flow process, 10th International Comminution Symposium (Comminution '16), April 11-14, 2016, Cape Town, South Africa.

Anticoi, H., Guasch, E., Hamid, S.A., Juan de Felipe, J., Oliva, J., and Alfonso, P. (2016). High pressure grinding rolls modelling with population balance models applied to tantalum ore." Comminution'16: 11-14 April 2016, Cape Town, South Africa. 2016. http://hdl.handle.net/2117/113134.

Anticoi, H., Ahmad Hamid, S., Guasch, E., Alfonso, P., Oliva, J., Garcia- Valles, M., (2016). Low Grade Tantalum Ores: Mineral Liberation Analysis Modelling, XXVIII International Mineral Processing Congress, September 11-15, Québec, Canada.

Anticoi, H., Guasch, E., Hamid, S.A., Oliva, J.and Alfonso, P., Escobet, T., Sanmiquel, L., Bascompta, M. (2016). Breakage Mechanism Modelling for High Pressure Roll Crusher with Population Balance Models Applied to Tantalum and Tungsten Ores, XXVIII International Mineral Processing Congress, September 11-15, Québec, Canada.

Hamid, S., Guasch, E., Anticoi, H., Alfonso, P., Oliva, J., Escobet, T. (2017). An overview of the modelling liberation of scheelite and the determination of the parameters function equation, 17th International Process Mineralogy, March 20-22, 2017, Cape Town, South Africa.

Hamid, S., Alfonso, P., Anticoi, H., Guasch, E., Oliva, J., Escobet, T. (2017). An approach to mineral processing by liberation modelling of Tantalum ore, 17th International Process Mineralogy, March 20-22, 2017, Cape Town, South Africa.

Hamid, S., Alfonso, P., Guasch, E., Anticoi, H., Oliva, J., Escobet, T. (2017). Liberation modelling based on comminution of tungsten ore using mineral liberation analysis, COM 2017, Conference of Metallurgists, August 27-30, 2017, Vancouver, BC, Canada.

Contributions by others to the thesis

The work in this thesis was discussed with my supervisors, Dr. Maria Pura Alfonso and Dr. Josep Oliva who also assisted in editing the thesis.

Dr. Pura Alfonso provided methodology during the development of this research work.

Dr. Josep Oliva for project administration and funding acquisition in this research work.

Dr. Pura Alfonso and Maite Garcia-Vallès performed the formal analysis and XRD and oxide characterization described in Chapter 4, in this thesis.

Hernan Anticoi and Eduard Guasch assisted in the perform of the crushing and milling of the material during the test work.

Dr. Teresa Escobet provided technical support by suggesting the use of MATLAB code for calculating the beta distribution function and liberation modeling of elements associated with Ta-W.

Tasmania University performed the MLA measurements described in Chapters 4 and 5. Pura Alfonso performed the optical microscopy described in Chapters 4 and 5. ALS providing the chemical assays described in Chapter 3, 4, 5 and 6. Marek Dosbaba performed the TIMA-X measurement described in Chapter 3, 4, 5 and 6.

Acknowledgements

This thesis would not be possible without the guidance, support, encouragement and generous contribution of my supervisors throughout my studies, and for these reasons I would like to express my appreciation to Dr. Maria Pura Alfonso and Dr. Josep Oliva.

Special thanks are for Pura, my principal supervisor, for all the time that she spent with me in revisions and fruitful technical discussions. Thanks, also to Josep who persuaded me to enroll in the PhD with enthusiasm and conviction. Also, they showed me that a person must be methodical to have successful in any objective that we have in life. I'll keep both of you in my heart my dear friends.

Hernan and Eduard have guided and were present in any moment that I need their technical support in the laboratories. I am grateful for the guidance received in some of the stages of my PhD from Dr. Marc Bascompte and special thanks for Maite Garcia-Valles for her help in analysing of the materials in different stage of the work.

I would like to acknowledge the department of Mining Engineering and Natural Resources from the Polytechnic University of Catalonia and all the staff of the university, professors Lluis Sanmiquel, David Parcerisa, Carlos Hoffman Sampaio, JJ de Felipe, Teresa Escobet and Toni Escobet. Thanks to Anna, Didac, David, and Marina for the memorable time that we spent together in the laboratories.

This thesis was performed under the frame of the European HORIZON2020 funding programme, number; 642201, and the project name: Increasing yield on Tungsten and Tantalum ore production by means of advanced and flexible control on crushing, milling and separation process, which was the acronym OptimOre. I would like to thank to all the OptimeOre project team for the support and contributions towards my study; prof. Rob Fitzpatrick and Yousef Ghorbani, from the University of Exeter, prof. Holger Lieberwirth, from the TU Bergakademie Freiberg, prof. Juan María Menéndez from the Universidad de Oviedo, prof. Martin Rudolph and Nathalie Kupka from the Helmholtz-Zentrum Dresden-Rossendorf.

I would also like to thank to the mining companies involved in this thesis. Strategic minerals Spain, owner of the Penouta mine, Javier Loez Moro, Teresa Liorenz, and its general director, Francisco Polonio. To the Wolfram Bergbau und Hütten AG, owners of the tungsten mine in Mittersill, Austria and Marek Dosbaba from Czech Republic to perform the TIMA-X.

I want to extend my thanks to my beloved wife Nishtiman for your love, support and absolute confidence in me during my life.

And, finally I want to thank God for guiding my life and for bring me to this special journey, for providing me permanent encouragement and support in every decision I take in life.

With Love, Sarbast.

Keywords

Process mineralogy, tantalum low-grade complex ores, tungsten ore, key mineralogical attributes, physical separation recovery, particle size, mineral liberation, beta distribution function, cumulative distribution, modeling the liberation.

Table of Contents

List of Figures

List of Tables

List of Abbreviations used in this thesis

%	: Percentage
2D	: 2 Dimension
3D	: 3 Dimension
Ab	: Albite
BM	: Ball mill
BSE	: Back-scattered electron
α^M	: Parameters that characterize the distribution
β^M	: Parameters that characterize the distribution
B (α, β)	: Beta function
C	: Concentrate
CGM	: Columbite group minerals
Char.	: Characterization
clf	: Columbite-(Fe)
clm	: Columbite-(Mn)
CT	: Computed tomography
∂	: Standard deviation
EDS	: Energy dispersive X-ray spectroscopy
EMPA	: Electron microprobe analysis
FK	: K-feldspar
Fl	: Fluorite
FT	: Ferrotantalite
$\bar{g}$	: Average grade
g^M	: Average grade without L1
g/t	: gram per tone
GXMAP	: Ford analysis or grain - based X-ray mapping

Hnb	: Hornblende
HPGR	: High pressure grinding roll
ICP-MS	: Inductively coupled plasma mass spectroscopy
Kln	: Kaolinite
kWh/t	: Kilo Wat hours per tone
L_0	: Mass fraction of the population that consists of liberated gangue particles
L_1	: Mass fraction of the population that consists of liberated mineral
MC	: Manganocolumbite
MLA	: Mineral liberation analyzer
MT	: Manganotantalite
Ms	: Muscovite
μm	: micron
n	: number of particles
P	: Penouta
P80	: 80% passing size
Pen	: Penouta
P(g)	: Cumulative mass
ρ(g)	: Density
ppm	: part per million
PSD	: Particle size distribution
PW	: Penouta waste
$(\sigma^2)^M$	: Variance of the interior distribution
Qtz	: Quartz
QEMSCAN	: Quantitative evaluation of minerals by scanning electron microscopy
rpm	: Revolutions per minute

tmn	: Tailings
TIMA-X	: TESCAN Integrated Mineral Analyzer
Tmn	: tantalite (Mn)
Tp	: Tapiolite
Sch	: Scheelite
SEM	: Scanning electron microscope
SXRD	: Synchrotron X-ray Diffraction
XBSE	: Extended back - scattered electron liberation analysis
XRD	: X-ray Diffraction
XRF	: X-ray Fluorescence
Wt.%	: Weight percentage

Chapter I

Introduction

Chapter I
Introduction

1.1. Context

One of the current trends in the mining industry is the need to move towards processing more complex and low-grade ores (Mudd, 2010). This presents new challenges and provides an opportunity to conduct research to improve the understanding of how mineralogy can affect the separation of among minerals. Particularly the importance of liberation of valuable minerals, the potential activation of gangue minerals and the presence of minerals that generate slimes that may coat the surface of the valuable mineral.

In nature ore minerals exist physically and chemically combined with the gangue, or minerals of non-commercial value. Removal of the unwanted gangue to concentrate ores in an economically viable manner is the basis of mineral processing operations. The greatest challenge to a mineral processor is to produce high grade concentrates with the maximum recovery from the ore body. To quantify recovery a reasonable idea of the initial concentration of mineral in a lode is required (Gupta, 2006).

An intimate knowledge of the mineralogical assembly of the ore is essential if efficient processing is to be carried out. This requires to know not only the nature of the ore and gangue minerals but also of their texture and mineral assemblage is required (Harris, 1990; Wills, 2006; Goodall et al., 2015; Sykora et al., 2018; Alfonso et al., 2019)).The processing of minerals should always be considered in the context of the mineralogy of the ore in order to predict grinding and concentration requirements, feasible concentrate grades and potential difficulties of separation (Hausen, 1991; Guerney et al., 2003; Baum et al., 2004). Microscopic analysis of concentrate and tailings products can also yield much valuable information regarding the efficiency of the liberation and concentration processes (Wills, 2006).

In mineral processing, the name "liberation" is used as synonymous to the study of mineral particle composition. In the same way, "liberation spectrum" is used in a broad manner to refer to the distribution of grades in a particle population (Schneider, 1995). This distribution can be multidimensional since there is no upper limit for the number of phases present in a mineral particle population. The simplest system, and probably the most common, is the binary ore, where one phase is regarded as gangue and the other as ore.

The importance of liberation to mineral processing operations has been recognized since

the late 1930's (Gaudin, 1939) and liberation has become an active field in mineral processing since the mid-1980's because of the high improvements in the analytical instrumentation, maturity of mineral processing simulation, and the increase in computing power.

Among the raw materials of high critical interest are the tantalum and tungsten ores, both included in the European Union list of critical raw materials (European Union, 2017); Figure 1.1)

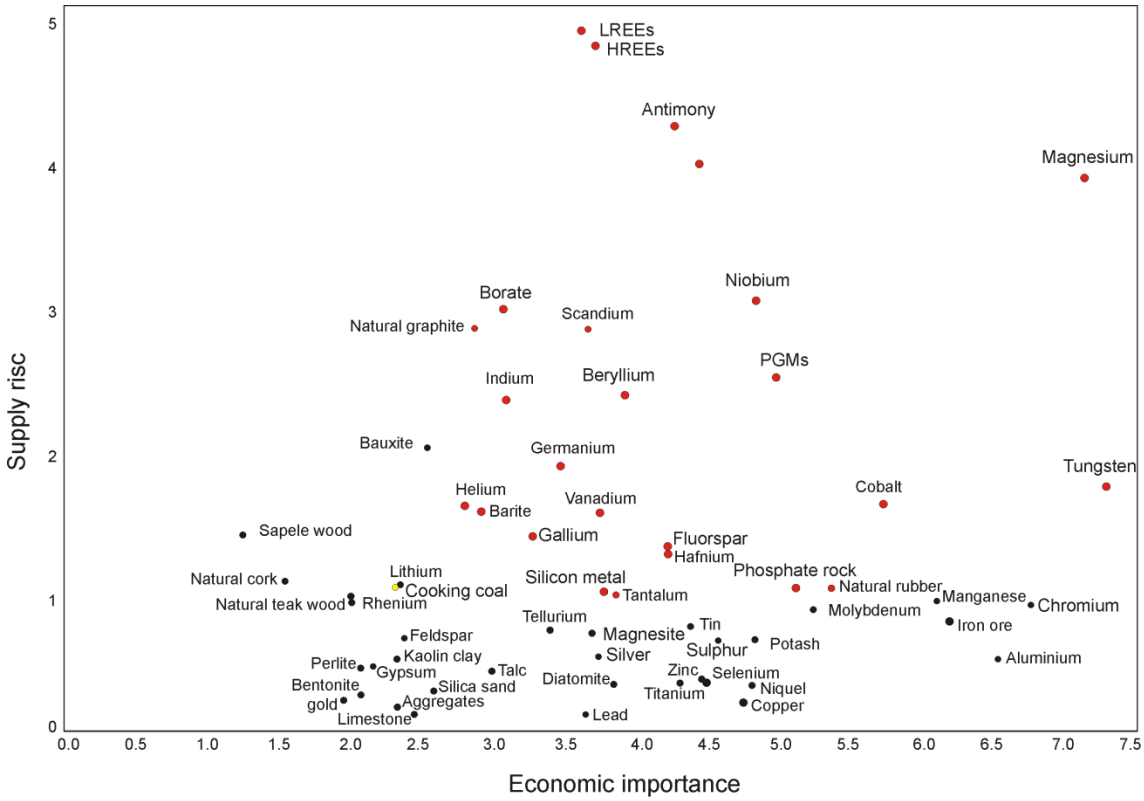

Figure 1.1. Raw materials classified according to the economic importance and supply risk in the EU (European Comission 2017). In red those considered as critical in the 2017 list.

Tantalum has a great relevance nowadays for its use in modern technologies., It is difficult to substitute using other metals and is considered a critical metal (Mackay and Simandl, 2014; Chakhmouradian et al., 2015). Europe needs to have greater self-sufficiency in the exploitation of strategic metals; for this reason, the exploitation of low-grade deposits should be considered. This is the case with the tantalum ore deposits in Europe.

Tantalum deposits are mainly pegmatites and rare metal granites (Černý et al., 2005). In general, low-grade tantalum ore deposits in rare metal granites are relatively abundant in the western and central parts of Europe. However, in order to make the exploitation of these deposits economically viable, their processing needs to be optimized. To this end, it is crucial to know the mineralogical and textural characteristics of the ores in order to be able to carry out their liberation in the most efficient way.

Tungsten is considered a critical raw material because its economic importance and local production (European Commission 2017). Tungsten has a wide range of application in industry

such as high temperature technology, chemical industry, lighting, X-ray technology, superalloyds (Mohammadnejad et al., 2018). Some properties made possible these applications, as its low vapor pressure, high melting point, good electrical and thermal conductivities, high density, high-elastic modulus, high wear resistance and good X-ray performance (Rieck 1967; Ilhan et al, 2013). More than 83 % of the world tungsten production comes from China and only 3.1% from Europe (USGS 2019). These made tungsten a critical metal for the European Union (European Commission, 2017) and it is also considered as critical by other entities as the US Department of defense and the government of the Russian Federation (Chakhmouradian et al., 2015). However, Europe has aa high potential for tungsten with abundant deposits (Table 1.1).

Table 1.1. Main tungsten mines and prospects in Europe.

Deposit	country	Metal	Type	Ore	References
Mittersill	Austria	W	Stratabound	Sch	Thalhammer et al. (1989)
Panasqueira	Portugal	W	Greisen	Wf	Kelly and Rye (1979)
Hemerdon	United Kingdom	W	Greisen	Fb	Shepperd and Miller (1988)
Los Santos	Spain	W	Skarn	Sch	Tornos et al. (2008)
Barruecopardo	Spain	W	Greisen	Sch, Wf	Antona et al. (1994)
La Parrilla	Spain	W	veins	Sch	Mangas and arribas (1988)
San Finx	Spain	W-Sn	Greisen	Wf, Cst, Sch	Gonzalo Corral, Gracia Plaza (1985)
Santa Comba	Spain	W-Sn	Greisen	Wf, Cst	Cuenin and Gagny (1983)
Morille	Spain	W	Stratabound	Sch	Arribas (1979)
Borralha	Portugal	W (Cu,Ag)	veins	Wf, Sch	Norohna (1984)
Covas	Portugal		Skarn	Sch, Wf, Fb	Coelho et al. (1988)
Salau	France	W-Cu-Au	Skarn	Sch	Fonteilles et al. (1989)
Montbelleux	France	W-Sn	Veins	Wf	Chauris et al. (1989)
Puy –les-Vignes	France	W	Veins	Wf	Harleux et al. (2015)
Enguialès	France		Veins	Wf, sch	Lerouge et al. (2000)
Fumade	France	W	Skarn	Sch	Safa et al. (1987)
Krásno	Czech republic	Mo-W	Greisen	Wf	Beran and Sejkora, (2006)
Cínovec	Czech republic	Sn-W-Li-Ta	Greisen	Wf	Breiter et al. (2017)
Carrock	United Kingdom	W	Greisen	Wf, Sch	Ball et al. (1985)
Myszków	Poland	Sn-W	Skarn	Sch,Wf	Podemski (2001)
Yxsjoberg	Sweden	W	Stratabound	Sch, Mo	Romer and Öhlander 1994)

Tungsten con be exploited in different types of deposits, the most important are vein and stockwork, greisen, skarns, and stratabound. Usually, grisen-type and vein-stockwork deposits coexist in the same area. The main tungsten ores are scheelite ($CaWO_4$) and wolframite, which is member of a solid solution constituted by hubnerite ($MnWO_4$) and ferberite ($FeWO_4$). Approximately two-thirds of the world tungsten reserves consist of scheelite deposits (Lassner and Schubert, 1999; Hu., 2012; Shepeta, 2012).

Most liberation models, including the first quantitative model proposed by (Gaudin, 1939), are based on the analysis of the mineral texture of an ore. In these models, the mineralogical texture of an ore is simplified and characterized in such a way so that the liberation distribution of the particles can be predicted as a function of size. For example, regularly arranged cubes are used to model ore texture and fracture patterns in Gaudin's model. Although this model was simple, the idea of superimposing fracture patterns on an ore texture seeded much of the work that followed.

Recovery of minerals using ore dressing and concentration operations is based on methods that separate particles on the basis of their physical or chemical properties. Individual minerals can be completely separated only if each particle contains only one mineral. Two minerals in the same particle can never be separated using physical separation methods alone. Separating minerals at the particulate level is referred to as liberation since the individual minerals are liberated from each other in a physical way. In practice, however, the comminution processes that are used to reduce mineralogical raw materials to the particulate state are, for the most part, unselective, and, apart from a few unusual cases, the particles that are formed consist of mixtures of the mineral components that are present in the original ore.

During comminution, however, there is a natural tendency toward liberation, and particles that are smaller than the mineral grains that occur in the ore can appear as a single mineral. It happens when the particle is formed entirely within a mineral grain. Obviously, this will occur more frequently as the particle size gets smaller, and it is impossible when the particle is substantially larger than the mineral grains in the ore. Methods that can be used to model these distributions are presented in this report. These methods must necessarily be quite complex because the geometrical structure of any mineralogical material is not uniform and cannot be described by the familiar conventional, regular geometrical entities such as spheres and cubes. Mineralogical textures have indeterminate geometries that are, to a greater or lesser extent, random in size, shape, orientation, and position. Likewise, the particles that are generated by comminution operations are irregular in shape and size. Thus, the particle population is made up of individuals that have irregular shapes and sizes and which are composed of material that itself has an irregular and complex texture of mineral phases. In spite of this lack of regularity, the distributions of particles with respect to composition do show some regular features, particularly with respect to the variation of the distribution with particle size.

A liberation study is also useful to improve the performance in other mineral processing operations. The product particles of the comminution stage will be subjected to classification according to one or more of its properties. In order to study the behavior of particles in the classification process, it is important to know the liberation distribution of the particles.

King (1975) developed a predictive liberation model based on distribution grade of valuable mineral and gangue when describes a population of particles that have a distribution of mineral content which produced during grinding process. He proposed that the fraction of the population which is fully liberated mineral, and fraction consist of gangue particles produced by random breakage.

King (1979) proposed a theory which was completely free of empirical constants or other parameters. The theory predicts that the fractional liberation of mineral at mesh size D is given by:

$$L(D) = 1 - \frac{1}{\mu}\int_0^{D_u}\{1 - N(l|D)\}\{2 - F(l)\}dl \qquad (1\text{-}1)$$

where $F(l)$the distribution of linear intercept lengths for the mineral and μ is the mean linear intercept length for the mineral. $N(l|D)$ is the linear intercept distribution function for particles of mesh size D and Du is the largest intercept length across any particle of mesh size D.

Schaap (1979) was extended this model including the compound particles and liberated particles produced during random breakage.

A liberation model based on the texture of the parent rock has been described by Barbery, (1991); Barbery and Leroux, (1988). According to Barbery (1991) the grade distribution of valuable mineral and gangue based on ore texture and particle structure has been estimated.

Several models have been developed to describe the liberation properties of mineral particles include liberation characteristics in predicting downstream separation process by using texture and grade distribution of low-grade ores (Schaap, 1979; Subasinghe, 2008).

Barbery (1991) and King (2012) to describe the shape of the valuable and gangue minerals, developed beta distribution function with parameters α and β. This is only an approximation to the distribution measurements and has shown that it is generally applicable for low- and high-grade ores. It has also been assumed that the model may be extended to composite ores as valuable mineral and gangue. This distribution function was developed (King, 2012) for the description of the populations of particles that have variable mineral content. This distribution function is based on the beta distribution that is widely used in mathematical statistics could be estimated from:

$$P(\mathrm{g}) = (1 - L_0 - L_1)\frac{g^{\alpha-1}(1-g)^{\beta-1}}{B(\alpha,\beta)} \qquad 0 < g < 1 \qquad (1\text{-}2)$$

where g is the average grade of the particle produced from random grinding made on a plane section of the parent rock, α and β are the distribution parameter and B (α, β) is distribution function.

Zhang (2012) measured the linear intercept grade distribution of valuable mineral and gangue and found that the particle breakage may have occurred during the grinding process provided a better fit to simulated data in different size classes (e.g. 300 μm and 800 μm). A comparison mainly of liberated and gangue minerals using a binary ore has been done and developed a liberation model to predictive the liberation by Zhang and Subasinghe (2016) and the grade distribution of comminuted particles were determined from linear measurements.

1.2. Objectives

The research objectives have been divided into the overall objective and specific objectives; both are described in the following paragraphs.

1.2.1. Overall objective

The overall objective of the present research was to develop an appropriate methodology to characterize the liberation properties of complex low-grade tantalum and tungsten ores for the purpose of developing the most appropriate separation process.

The aim is to produce the maximum degree of mineral concentration and improve the performance in mineral processing operations. In fact, using liberation modelling, we'll predict the distribution of valuable minerals in particles and determine the optimal particle size for a comminution unit.

1.2.2. Specific objectives

The principal purpose of liberation in a mineral processing plant is to break the ore to a size sufficiently small to release or liberate the ore. Therefore, valuable minerals to be recovered by concentration process, such as gravity or magnetic concentration. The study is reaching these goals:

1) To determine the process mineralogy of the feed minerals: characterization of the mineral's phases and mineralogical texture.
2) The measurement and calculation of the liberation.
3) To asses of the quantitative predication of liberation in the separation process.
4) Modelling of liberation in comminution by simulation.
5) The distribution of liberated types in the process.
6) To find the liberation size in the process.
7) To connect the libation results with the mechanical processing.
8) To improve method of concentration in mineral processing.

This work is focused on using a combination of mineralogical characterization and comminution test-work to recover Ta and W from two different ore types; from a complex low-grade tantalum deposit in Spain and the tungsten ore which scheelite associated with calc-silicate minerals in Austria. This work has resulted in the development of a systematic approach for identifying unknown Ta and W-bearing minerals.

This study determines the mineral liberation modelling of tantalum and scheelite ores, using quantitative mineralogy and simulation to complete the characterization. The liberation modelling has been obtained using back calculation method in MATLAB with the distribution density solution to the predication mineral liberation. Knowledge of the key mineralogical attributes of each ore (including Ta and W behavior, liberation and grain size) are shown to be critical in the development of the processing strategies used to treat each ore.

1.3 Statement of Originality Contribution to Knowledge

This research has made the following contributions to current knowledge:

1) A methodology for mineralogical characterization of the Ta and W ores.

2) Identification of a new association between minerals that is described in the published literature.

3) A systematic method that enables the development of physical separation strategies to achieve >90% Ta and W recovery in a laboratory rougher process.

4) A framework for assessing the tantalum and tungsten based on the mineralogical characteristics of the ores.

1.4 Scope of the thesis

Mineralogical characterization provides the attributes of a given ore sample and this key information is then used to select the most appropriate physical separation processes to recover the minerals containing the valuable elements present in the ores. There are a range of beneficiation processes that can be used for recovering commodities from the ores, namely crushing. comminution, separation and concentration processes, shown schematically in Figure 1.2. The red dashed box in Figure 1.2 shows which processes are included in this thesis, i.e. the beneficiation process under investigation is liberation. The investigation of other potential beneficiation routes is outside the scope of this work.

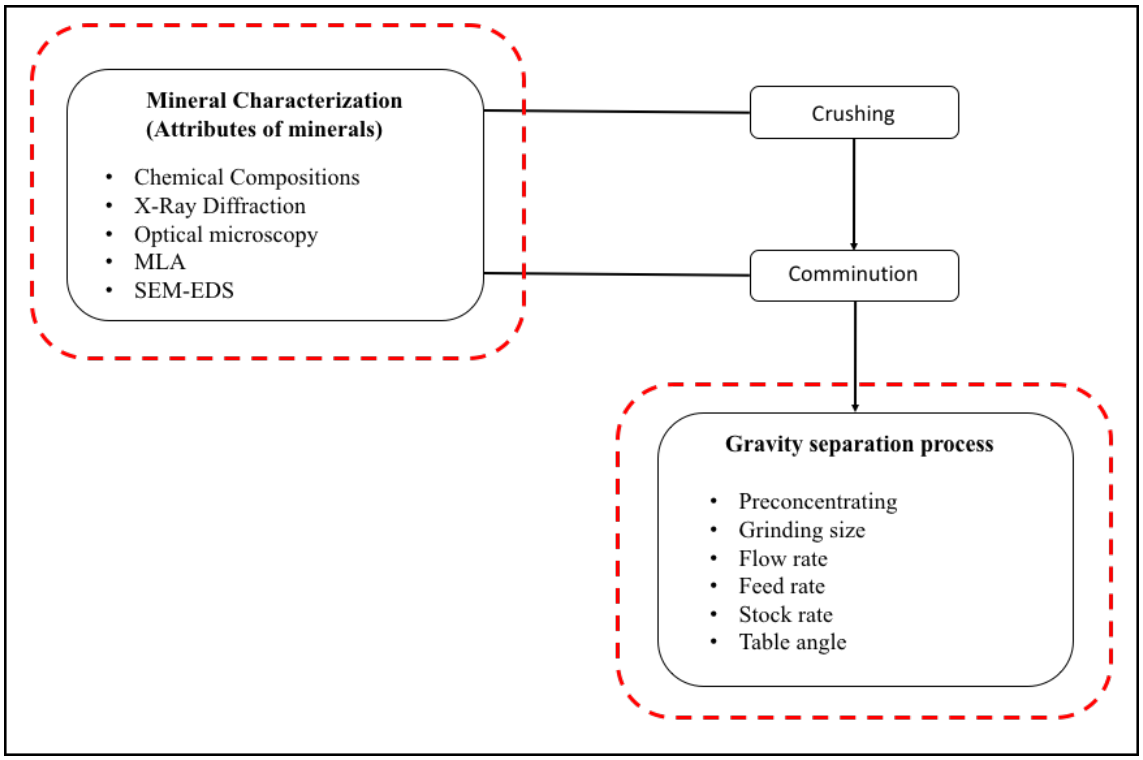

Figure 1.2. Scope of the thesis.

A detailed description of the scope of the thesis is provided in Figure 1.3, which shows

the inputs, mineralogical characterization and outputs of the research scope. The inputs are the two case studies that relate to the two different ore types. For each case study, Level 1 mineralogical characterization was undertaken. If this level of analysis was sufficient to identify the key mineralogical attributes for tantalum and tungsten minerals and gangue minerals, then development of a concentration strategy could follow. For cases where the key mineralogical attributes of the ore were unable to be identified, mineralogical characterization progressed to Level 2 and then Level 3, both incorporating increasingly advanced analytical techniques. In terms of the mineralogical characterization, modal mineralogy will play an important role, not only by providing the deportment of Ta and W but also to determine the gangue mineralogy. This information will help to develop proper strategies in order to depress the gangue minerals that might dilute the concentrates.

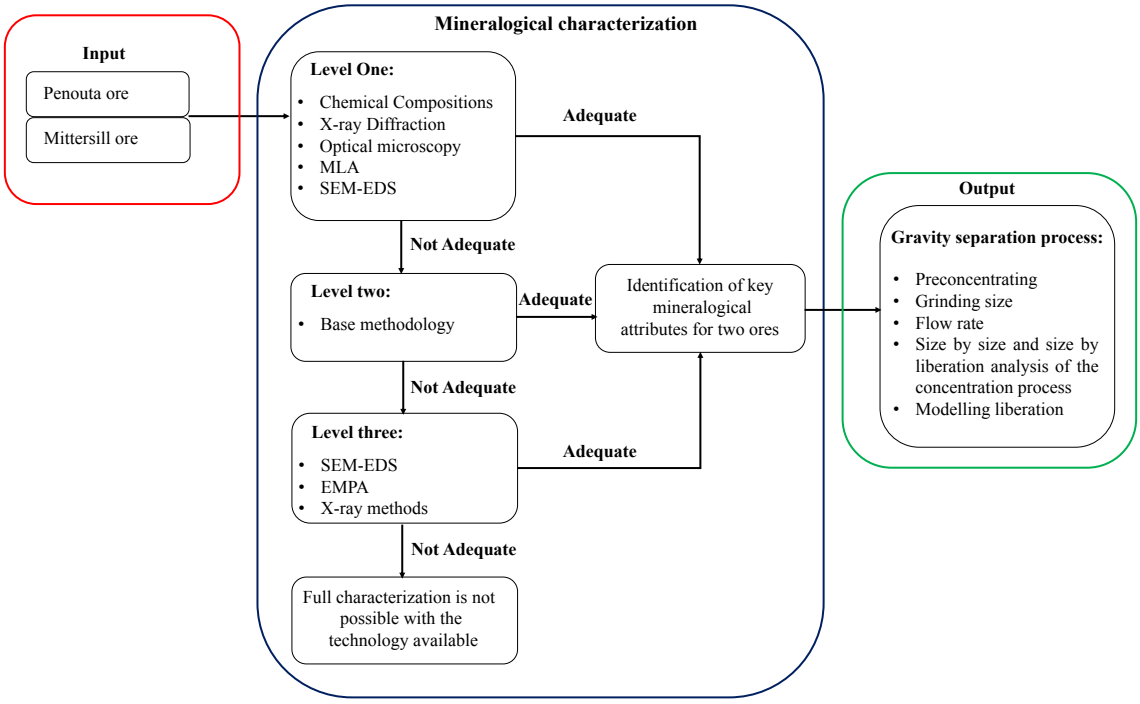

Figure 1.3. Mineral characterization and beneficiation process to be applied.

1.5 Thesis outline

The following is an outline of the chapters contained in this thesis.

Chapter I presents an overview of this research work and describes the objectives and research path developed for this work.

Chapter II provides a review of the literature related to the mineralogy of tantalum, the techniques available for mineralogical characterization A description of the strategies used for concentrating tantalum using gravity separation is discussed, and finally, two examples describing

how process mineralogy is applied in the context of tantalum are provided.

Chapter III provides details of the experimental methodology used in this research, and provides detailed descriptions of the ores studied. The different levels of the mineralogical characterization methods used, as well as the concentration characterization protocols are also described. In addition, an approach for identifying Ta and W minerals that was developed as part of this research is described.

Chapter IV describes the results of the mineralogical characterization of the low-grade tantalum and medium grade tungsten ores, where key mineralogical attributes were able to be defined using the Level 1, 2, and 3 methodology. This allowed the development of a selective physical separation strategy that enabled a concentrate of 103 ppm Ta with 52% recovery and 2260 ppm W with 87% recovery to be achieved in laboratory concentration tests. A procedure based on liberation distribution and using beta distribution function to describe the liberation modeling have been developed.

Chapter V discusses the key findings from this work and the implications in the context of how understanding of the complexity of the ore characteristics will provide insights into the physical separation strategy. The concept of liberation modeling as it applies to the tantalum and tungsten ores studies in this work is also discussed and a framework for describing how liberation a tantalum or tungsten ore is likely to be is predictive using simulation and liberation modeling.

Chapter VI describes how the objectives and outlined in Chapter I were achieved and tested respectively, and identifies potential areas for future work related to complex low-grade tantalum and medium-grade tungsten ores i.e., mineralogical characteristics that results in different stages of processing flow sheet and predictive liberation that possibly changed the flow sheet design adding more unit process in the treatments.

Chapter II

Literature Review

Chapter II
Literature Review

This chapter examines the literature relating to the mineralogy and processing of tantalum and tungsten ores. It begins with the different Ta-W deposits and tantalum and tungsten minerals that can be found worldwide, then reviews the techniques currently used to identify and characterize tantalum and tungsten minerals. The literature that describes the liberation processing routes for tantalum and tungsten minerals is also discussed, with particular emphasis on the different strategies used to concentrate tantalum and tungsten minerals. The chapter concludes with literature examples of process mineralogy in the context of tantalum and tungsten, leading to the identification of gaps in the literature that will be addressed in this thesis.

2.1 Introduction

Tantalum is a transition metal with atomic number 73 and atomic weight 181. The element is usually found together with niobium with an atomic number 41 and atomic weight 93 (Table 2.1). Tantalum is a grey blue, ductile metal with a high melting point and high resistance to chemical attack at temperatures below 150 °C. It is, however, dissolvable in hydrofluoric acid or in acidic solutions containing fluoride ion, sulphur trioxide and potassium hydroxide.

Niobium is a lustrous, gray, ductile metal with a high melting point, relatively low density, and superconductor properties. Tantalum is a dark blue-gray, dense, ductile, very hard, and easily fabricated metal. It is highly conductive to heat and electricity and is renowned for its resistance to corrosion by acids. It is these special properties, especially hardness, conductivity, and resistance to corrosion, that determine the primary uses of niobium and tantalum today. Niobium has similar physical and chemical properties to tantalum, which makes them sometimes difficult to distinguish (USGS, 2017).

Tantalum and niobium have unique mechanical, electrical and chemical properties, which make them indispensable in many industrial applications. In addition to the properties listed above, they also have nearly zero electric resistance at low temperatures, high corrosion resistance, shape memory properties and high capacitance.

Niobium (Nb) and tantalum (Ta) are transition metals that are very similar in their physical and chemical properties (Table 2.1). They are almost always found together in nature. Both are named after tragic figures from Greek mythology—Niobium is named after Niobe, and tantalum is named after Niobe's father, Tantalus. Niobium was first discovered in 1801 by English

chemist Charles Hatchett, who named it columbium after Columbia, the poetic name for North America. Columbium was used interchangeably with niobium until 1949 when niobium was officially accepted as the designated name by the International Union of Pure and Applied Chemistry. Tantalum was first discovered by Swedish scientist Anders Ekeberg in 1802, but because it was difficult to separate from niobium, tantalum was confused with niobium until 1864, when it was confirmed to be a separate element. Relatively pure tantalum metal was not produced until 1903 (USGS, 2014).

Table 2.1. Selected properties of niobium and tantalum. (Source: Winter (2014). Å, angstrom; °C, degree Celsius; g/cm^3, gram per cubic centimeter; nΩ-m, nano ohm-meter) (Source: USGS, 2017).

Property	Niobium (Nb)	Tantalum (Ta)
Atomic number	41	73
Atomic weight	92.90638	180.94788
Atomic radius (Å)	1.46	1.46
Density (g/cm^3)	8.57	16.69
Melting point (°C)	2,477	3,017
Boiling point (°C)	4,744	5,458
Hardness (Mohs scale)	6.0	6.5
Electrical resistivity (nΩ-m)	152 at 0 °C	131 at 20 °C
Crystal structure	Body-centeredcubic	Body-centeredcubic

Tungsten is a metal of superlatives. The melting point of 3410 °C is the highest of all metals. The density of tungsten is 19.25 g/cm³, which is almost as high as the density of gold. Tungsten has the lowest vapor pressure and the lowest expansion coefficient of all metals. The total consumption of tungsten metal is 40.000 t/year. Best known is the usage of tungsten wire in various lamps. Wires for filaments of household lamps have a diameter of 17 to 45 µm. 3 kg of sintered tungsten will yield 365.000 m of a 24 µm filament corresponding to 500.000 coils for a 40 – W lamp. 60 – 70 % of the tungsten metal is further processed to tungsten monocarbide, which is the main constituent of hard metals. The latter materials are used in a wide range of applications in the industry. Well known are drill bits which are inserted in tools, used in the mining-, oil- and gas industry and in mechanical engineering (Wolfram, 2015).

Tungsten is a hard, very dense, steel-grey to greyish-white metal. It has the highest melting point of all non-alloyed metals and the second highest of all elements behind carbon. Of all pure metals, tungsten has the lowest coefficient of expansion and the highest tensile strength at temperatures over 1650 °C (Christie and Brathwaite, 1996). Tungsten is also known for its high density, which is similar to gold, and its high thermal and electrical conductivities. It has excellent corrosion resistance, does not react with air or water at room temperature (although fresh surfaces will oxidize) and is largely unaffected by most acids. Key properties are summarized in Table 2.2 (BGS, 2014).

Table 1.2. Selected properties of tungsten (Source: BGS, 2014).

Property	Value	Units
Symbol	W	
Atomic number	74	
Atomic weight	183.84	
Density at 25 °C	19254	kg/m^3
Melting point	3422	°C
Boiling point	5555	°C
Hardness (Mohs scale)	7.5	
Specific heat capacity at 25 °C	0.13	J/(g °C)
Electrical conductivity	18.2×10^6	S/m
Coefficient of linear thermal expansion	4.5×10^{-6}	/°C
Tensile strength at 20 °C	1000	MPa
Tensile strength at 1650 °C	approx 100	MPa
Thermal conductivity	174	W/(m °C)

2.2 Tantalum Production

Global tantalum mine production peaked in 2004 at just greater than 1,400 metric tons of elemental tantalum and mostly declined since 2006 to 770 metric tons in 2011. The decrease in tantalum production reflects the drop-in tantalum prices that accompanied the global economic downturn and the increased volume of tantalum coming out of areas of armed conflict in Congo (Kinshasa). Since 2012 the global tantalum production has been shown another increase, where in 2017 greater than 1800 metric tons of elemental tantalum (Figure 2.1). Australia and Brazil have been the leading national producers of tantalum mineral concentrates, although since 2009, production from Australia has decreased, and production from Mozambique and some other countries has increased (Papp, 2013a). Australia shows another increase of production since 2015 from 20 metric tons to 90 metric tons in 2018. The leading companies producing tantalum mineral concentrates in 2011 were Companhia Industrial Fluminense Mineração S.A. (Volta Grande Mine) and Mineração Taboca S/A (Pitinga Mine) in Brazil and Noventa Ltd. (Marropino Mine) in Mozambique. The leading tantalum producer in other years was Global Advanced Metals from its Greenbushes and Wodgina Mines in Western Australia. Other countries, including Burundi, Canada (Tanco Mine), China (Yichun Mine), Congo (Kinshasa), Ethiopia (Kenticha Mine), Nigeria, Russia (Lovozero Mine), Rwanda, and Uganda also produced tantalum mineral concentrates in 2011 (USGS, 2017).

About one-half of all tantalum production consists of tantalite ore, and the remainder comes from tin slag, from such other minerals as strüverite and columbite-tantalite, and from recycling and synthetic concentrates. Tin slag is produced primarily in Southeast Asia, Australia, and Brazil. Tantalum is mined from both open pit and underground operations. Heavy minerals that contain tantalum are separated from the bulk ore by gravity methods and flotation. The

concentrate is then subject to electrical (electrostatic and [or] electromagnetic) separation and other methods used to separate tantalum minerals from other heavy minerals. Because most mining of tantalum recovers minerals that also contain niobium, a chemical processing step involving the addition of potassium fluoride is necessary to separate niobium from tantalum, resulting in compounds of Nb_2O_5, Ta_2O_5, potassium niobium fluoride ($K_2Nb_2F_5$), and potassium tantalum fluoride ($K_2Ta_2F_5$). The tantalum compounds are then smelted to make tantalum metal products (Roskill Information Services Ltd., 2012). The global supply of tantalum historically has been 70 percent from concentrates, 10 percent from tin slag, and 20 percent from recycling and synthetic concentrates (Schwela, 2010).

Conventional mining accounted for 51 percent of the world's tantalum supply in 2011, artisanal mining accounted for 29 percent, and tin slags and synthetic concentrates accounted for 10 percent (Roskill Information Services Ltd., 2012).

Tantalum has a unique set of properties that make it useful in a number of diverse applications. The ability of the metal to store and release electrical energy makes it ideally suited for use in certain types of capacitors that are widely used in modern electronics. Approximately 60 percent of global tantalum consumption is in the electronics industry (Bleiwas, 2015). The ductility and corrosion resistance of the metal lends itself to application in the chemical processing industry, and its high melting point and high strength retention at elevated temperatures make it an important component of super alloys used in aircraft engines (Global Advanced Metals Pty Ltd, 2010).

Although developed countries dominated tantalum mine production in the early 2012s, production today is dominated by countries in the Great Lakes Region of Africa (Figure 2.1 and 2.2). There is concern that the sales of minerals, including columbite-tantalite or "coltan" a mineral from which tantalum is derived, have helped finance rebel groups accused of violating human rights as part of the continuing armed conflict in the Democratic Republic of the Congo (DRC) and neighboring countries.

These accusations have prompted the passage of legislation in the United States to curb the procurement of these mineral commodities, referred to as "conflict minerals," from the DRC. Specifically, section 1502 of the 2010 Dodd-Frank Wall Street Reform and Consumer Protection Act (Public Law 111–203, 124 Stat. 2213–2218) requires companies that source tantalum, tin, tungsten, and gold (3TG) to perform due diligence on their supply chains to determine if the materials they use originate from the DRC or adjoining countries (defined as sharing a border with the DRC) (U.S. Securities and Exchange Commission, 2012; Chasan, 2015; U.S. Department of State, 2015).

The DRC, Rwanda, and surrounding countries are not globally significant sources of tin, tungsten, or gold, accounting for only about 2 percent of the mined world supply for each of these elements. The region has, however, evolved to become the world's largest producer of mined

tantalum.

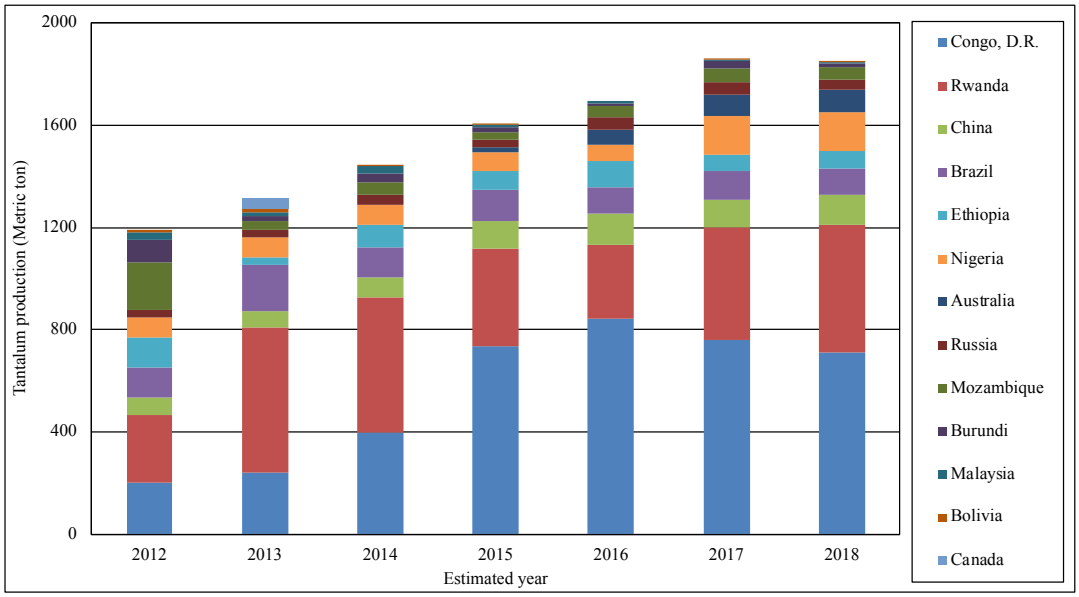

Figure 2.1: Bar charts showing percentage of average annual world production of tantalum, for the period 2012–18, by country (Source: World Mining Data 2019). Canada had reported tantalum production only in 2014.

A further complication of the production of tantalum stems from the opacity of the tantalum market. Unlike most base and precious metals, tantalum concentrates are not publicly traded through commodities exchanges but are bought and sold through networks of dealers and on contract between producers and consumers, some of whom may not provide accurate statistical data concerning the amounts, origins, and destination of the concentrates (Browning, 2015;). Some price data can be found in trade journals or in other publications; however, there are no recognized official set exchange prices for either concentrate or tantalum metal. Because price is determined by negotiation between buyer and seller (Browning, 2015), published prices for concentrate are probably not representative of global prices paid for concentrate. The development of a mine-to-market supply-chain analysis is complicated and difficult because many of the industry participants that produce, trade, and consume tantalum do not publish statistical information, contracts are long term between miners and buyers, and much of the industry is vertically integrated.

As a result of these and other considerations, tantalum is considered by many to be a “critical” commodity (National Research Council, 2007; Erdmann and Graedel, 2011; Meinert, 2014; Australia Geoscience, 2015). This fact sheet identifies and addresses the major geographic shifts in the sources of mine production of tantalum which have occurred over the past 18 years, some of the factors that drove these shifts, and some of the related consequences.

The estimated annual mine production of tantalum contained in tantalum and tin concentrates for 2012 –2016 is shown in Figure 2.2 for 11 countries. The USGS–NMIC analysis

does not address the amount of tantalum ultimately recovered from these concentrates, which may be considerably less because of the losses experienced during processing to produce marketable products.

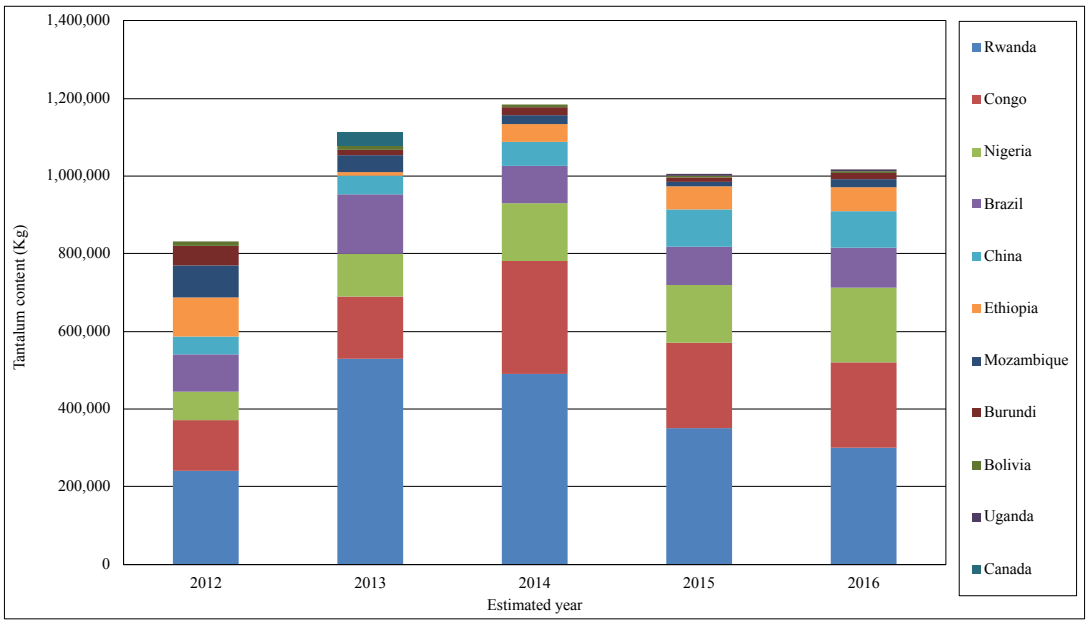

Figure 2.2. Mine production of tantalum contained in concentrates, by country of origin, for 2012 - 2016 (Source: USGS, 2016).

Data limitations prevent estimating the amounts of potentially recoverable tantalum contained in tantalum and tin concentrates that are produced annually in a number of countries. Most of this production is a byproduct of the mining and smelting of cassiterite. Tantalum contained in slags from past smelting activities in Australia, Portugal, and several Asian countries also is excluded from the estimates because of data limitations. The level of information required to develop estimates of undocumented tantalum production that originated in conflict and some nonconflicted areas in Africa, South America, and some other locations was not available (USGS, 2017).

The data indicate that the total amount of tantalum contained in tantalum and tin concentrates in the countries studied averaged about 94,000 kilogram per year (Kg/yr) (expressed as tantalum contained in concentrate) for the period 2012 to 2016. Tantalum derived from mining, is a component of total supply, which also includes secondary production (recycling), and contributions from releases of inventories.

In 2012, a total of approximately 76,500 kilograms (Kg) of tantalum in concentrate was produced among the countries studied. Canada was by far the dominant global producer of mined tantalum in concentrates with a 3 percent share of global production. Other leading producers in that year were Rwanda (47 percent), the DRC (14 percent), and Brazil (13 percent).

The estimated annual production of tantalum contained in tantalum and tin concentrates

in the DRC and Rwanda was relatively modest for the period 2000 through 2006, averaging 101 t and 73 t, respectively. Combined, the contribution of the two countries to tantalum-in-concentrate production among the countries studied averaged less than 15 percent during the 7-year period. In 2007, however, reported production in the DRC increased to 320 t of tantalum in concentrate, nearly three times the average of the previous years, and mine production in Rwanda increased to 170 t of tantalum in concentrate (Figure 2.3).

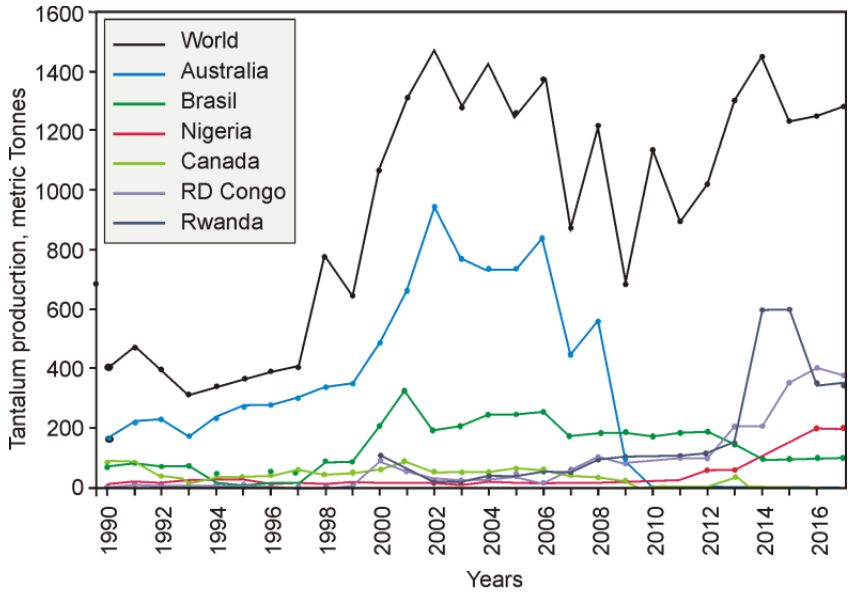

Figure 2.3 Main producers of tantalum as principal product of mining. (Data from USGS 2017 and Mackay and Simandl 2014).

The increase in production in the DRC and Rwanda and the decline in production in Australia were already underway prior to the global economic downturn in 2008–2009 and the drop-in tantalum prices. This was a time of reduced demand for electronics and a drop in the price of tantalum. The actions on the part of the Australian mining companies were reportedly taken in response to a combination of the comparatively high costs associated with hard rock mining, the bankruptcy of the owner/operators of the Greenbushes and Wodgina Mines, and an increasing amount of lower-priced tantalum concentrates entering the supply chain from central Africa (Schwela, 2007; Taylor, 2011).

Australian and Brazilian mines, the dominant producers from 2000 through 2008, were considered low risk for supply disruptions. Although these countries had modern mining operations and transparent commerce characteristics, the Australian hard rock mines had relatively high operating costs. In contrast, concentrates supplied from Africa were mostly sourced from small, labor intensive, and relatively unsophisticated artisanal mines, producing at lower costs. Brazil was able to maintain a position as one of the world's major producers because most of the countries concentrate was derived from relatively low-cost unconsolidated placer

deposits. African production increased, and the price for tantalum dropped because of decreased global demand during the global recession. Australian operations decreased or suspended production (Schwela, 2010) and, by 2007, the country had lost a significant share of global supply to the DRC and Rwanda (Figure 2.3).

In 2009, the geographic distribution of world tantalum mine production shifted dramatically from Australia and Brazil, with a combined global share of 18 percent, to the DRC and Rwanda, with a combined share of 51 percent (28 percent and 23 percent, respectively). Although still retaining a major share of global production, the DRC had begun to decline in production from the high of 410 t achieved in 2008 (Figure 2.3).

In 2013, Rwanda became the world's leading producer of tantalum contained in tantalum and tin concentrates with an estimated 600 t, which is nearly 50 percent of the total estimated production from the countries studied. This was a major increase from the estimated 310 t of tantalum in concentrate produced in Rwanda in 2012 when it represented about 28 percent of the production among the countries studied. In December 2013, the Rwandan Government disclosed that they had "dramatically" increased their tantalum concentrate exports and had become the world's largest exporter, mostly to China, which has been a major importer of concentrates from Rwanda (Bleischwitz et. al., 2012; Browning, 2015). This noteworthy increase in production may be attributed to the Government privatization of its mining operations and opening new concessions to investors and artisanal cooperatives (Yager, 2014).

Reports indicate that the implementation of the Dodd-Frank Act resulted in an increase in tantalum concentrate production in parts of the DRC that were determined to be conflict free (Bafilemba et. al., 2014). In 2013 and 2014, the estimates of annual mine production in the DRC decreased to about 200 t of tantalum in concentrate but continued to represent about 17 percent of estimated mine production among the countries studied (Figures 2.3 and 2.4). There have been claims over the years by nongovernmental organizations, United Nations observers, and others that at least some portion of Rwanda's reported production for the period analyzed originated from concentrates smuggled across the border from conflict areas in North Kivu and South Kivu in the DRC and was exported through Rwanda's domestic tagging system as a nonconflict source (Bleischwitz et. al., 2012; Polinares, 2013; Bafilemba et. al., 2014).

In 2012, the total production of nearly 1,200 t of mined tantalum in concentrate from 13 countries studied was substantially lower than what was estimated just prior to the global recession in 2008 when nearly 1,800 t was produced. Possible reasons for the reduction include (1) global tantalum consumption had still not recovered to the previous levels of a more robust economy; (2) improvement in the efficient use of the metal or increased substitution; (3) drawdown of producer inventories; (4) increased usage of secondary (recycled) material; and (5) unaccounted tantalum production entering the supply chain, some of which may originate from conflict-affected sources (USGS, 2017). The USGS–NMIC has no statistical information with

regard to the undocumented amounts and origins of conflict minerals in the global supply chain.

2.3 Tungsten Production

World tungsten resources have been estimated at seven million tones (contained tungsten metal) including deposits that have so far not been proven to be economically workable (Hinde, 2008). It is believed that 30 per cent of the resources are wolframite (76.5 per cent tungsten trioxide) and 70 per cent are scheelite (80.5 per cent tungsten trioxide) ores (Hinde, 2008). Werner et al., (1998) noted that the ten largest known deposits at that time were located in Kazakhstan, Canada, China and Russia. However, since then new deposits have been discovered, for example O'Callaghan's in Australia, and previously identified occurrences have been found to contain more tungsten than previously thought, for example Hemerdon in the United Kingdom. It is clear that China, Kazakhstan and Russia have considerable resources but detailed Information is difficult to obtain. Resources in Canada are known to exceed one million tons of contained tungsten, whereas resources in Australia are believed to be nearly 0.5 million tons of contained tungsten.

The USGS (Shedd, 2012a) estimated in January 2012 that reserves stood at 3.1 million tones (contained tungsten metal) with more than 60 per cent of these located in China (Figure 2.4). The National Bureau of Statistics of China reported that their reserves of tungsten in 2010 were approximately 1.75 million tons of contained metal (NBSC, 2012) and it is believed this is concentrated in the provinces of Hunan and Jiangxi (Pitfield et al., 2010). These two provinces also receive the highest proportion of China's production quota (Shedd, 2012b). Deposits of tungsten are known to exist in many other Chinese provinces but it is not known whether they are categorized formally as resources or reserves. In Russia, reserves of tungsten are believed to be mainly located in the North Caucases area and the Far East region. Canadian reserves are dominated by the huge deposit at Mactung and the nearby operating mine at Cantung, which are located in the Yukon and North West Territories, respectively.

In 2013, total world production was nearly 86,000 tones of tungsten. This was a nine percent increase compared to 2012, shown in Figure 2.4. Tungsten is currently produced in approximately 23 countries. China has been the world's leading tungsten producer for many years. In 1989 it accounted for 58 per cent of the world total but this rose to reach a peak of 82 per cent in 2016.

In recent years this proportion has increased slightly but it was still about 82 per cent in 2017 (Figure 2.5). China's output was produced mainly in Jiangxi and Hunan provinces, accounting for 44 per cent and 24 per cent of the total respectively (Research in China, 2011). Its major operating mines are at Shizhuyuan in Hunan Province and Yangchulin, Xingluokeng and Xianglushan in Jiangxi Province. There are further mines, in these and other provinces, and new

mines are believed to have opened but accurate information is difficult to obtain. Vietnam, also has been shown an increase in production from 1100 tones in 2012 to 5141 tones in 2017. Russia's output is believed to come from Tyrnyauz in the North Caucases and the Vostok-2 area of the Far East region, but Russian mines were reported to be struggling in the economic crisis (Levine, 2011). Historically, Bolivia has had numerous small-scale mining operations extracting tungsten and this is thought to still be the case (Anderson, 2011). However, output from Bolivia has decreased significantly in recent years from approximately 1461 tones of contained tungsten in 2015 to 1015 tones in 2017 (Reichl, 2019). Austria's output comes from the Mittersill mine, operated by Wolfram Bergbau and Hütten AG, while Canada's is from the Cantung mine in the Yukon Territory, which is operated by North American Tungsten Corp. Other countries producing tungsten in 2017 included: Portugal (mainly from the Panasqueira mine), Rwanda, Spain, Uzbekistan, Brazil, Thailand, Burma (Myanmar), North Korea, Burundi, Kyrgyzstan, Democratic Republic of Congo, Uganda, Australia (mainly from the Kara mine on Tasmania) and Mongolia (Reichl, 2019).

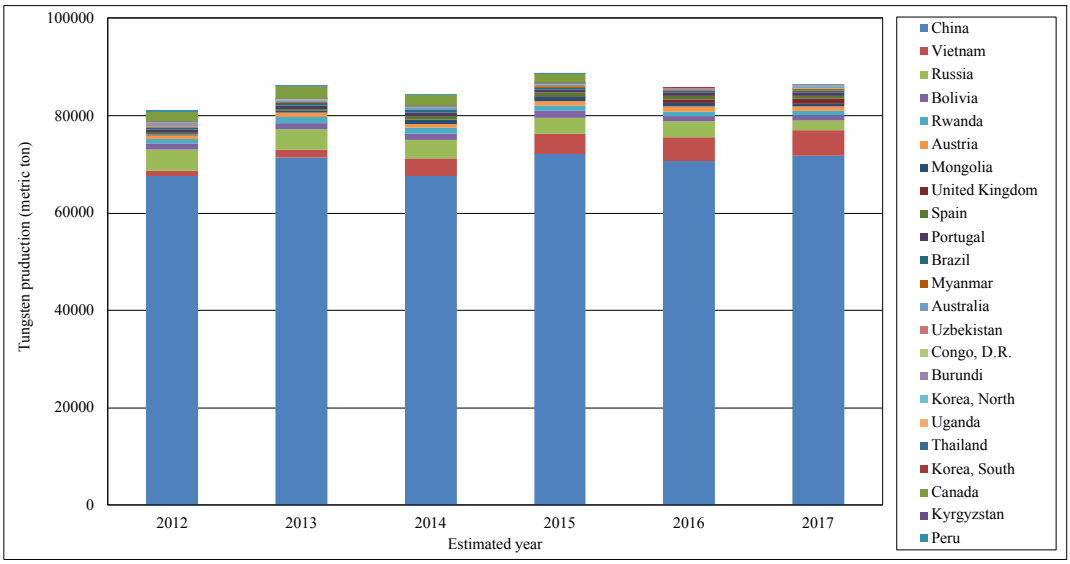

Figure 2.4. Mine production of tungsten, 2012–2017. (Data from British Geological Survey, World Mineral Statistics database, 2018).

The concentration of production in China is a relatively recent occurrence, as illustrated by Figure 2.5. Prior to the 1990s, China's share of the total world production was less than 35 per cent. Between 1980 and 1990, although the total world production remained approximately the same, China's share of that total more than doubled from 29 per cent to 62 per cent. Total world production had dropped significantly by 2000 and in tonnage terms China's output fell too, but other countries' production levels reduced by proportionally greater extents. The result was that China's share of the world total increased to 77 per cent despite the decrease in output. Between 2000 and 2010 total world production recovered, and in 2010 was higher than 1990, but the

majority of this increase has been in China. It is likely that this pattern of supply is related to tungsten prices and market availability. In the late 1970s and the 1980s there was a significant increase in the availability of tungsten concentrates and intermediate products from China at cheaper prices than the rest of the world. This led to oversupply and a significant fall in tungsten prices, with the result that many mines could not sustain economic production and world output decreased. The cost of production was probably lower in China than other countries and consequently output there fell less. As demand and prices recovered, Chinese producers were able to react more quickly and therefore China's output has grown much more rapidly than that in the rest of the world. The sub sequent imposition of production and export quotas in China has pushed prices up further and encouraged both the exploration for new deposits and the development of new mines outside of China (BGS, 2014).

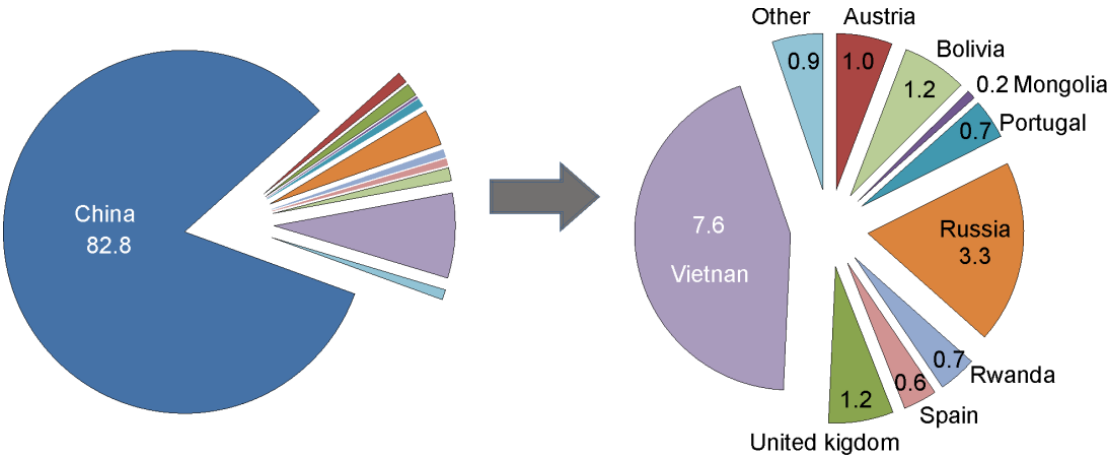

Figure 2.5. Main producers of tungsten as principal product of mining during 2017. (Data from British Geological Survey, World Mineral Statistics database, 2018).

2.4 Tantalum ores

2.4.1 Geochemistry

Niobium and tantalum generally show strongly coherent geochemical behavior because they are identical in charge (5+ under most geologically relevant oxidation conditions) and nearly identical in effective ionic radius (Table 2.3). As a result, they are closely associated and found together in most rocks and minerals in which they occur. Both elements are lithophile, in that they show a strong affinity for oxygen, and they are high-field-strength elements (HFSEs), meaning that their ions are relatively small and have intense electrostatic fields. Their HFSE characteristics significantly reduce their potential to substitute for more common elements in most rock-forming minerals and make them essentially immobile under most natural conditions (Wood, 2005); as a result, their concentrations in the surface environment are generally low. The average abundance of niobium and tantalum in bulk continental crust is 8.0 parts per million (ppm) niobium and 0.7

ppm tantalum (Rudnick and Gao, 2003). In surface waters, concentrations are generally in the low parts per trillion.

Niobium and tantalum are depleted in continental crust relative to other highly incompatible elements (elements that do not readily substitute for more common elements in major rock-forming minerals), such as cesium, rubidium, thorium, and uranium, and the light REEs, including cerium and lanthanum. As a result, continental crustal rocks are typically characterized by high lanthanum to niobium (La:Nb) ratios— the average crustal ratio is about 2.5 (Rudnick and Gao, 2003).

Table 2.3. Selected Tantalum and Niobium Minerals.

Mineral name	**Mineral group**	**Formula**	**Nb_2O_5 (%)**	**Ta_2O_5 (%)**
Columbite	CGM	$(Fe,Mn)(Nb,Ta)_2O_6$	78.72	n.a.
Tantalite	CGM	$(Mn,Fe)(Ta,Nb)_2O_6$	n.a.	86.17
Pyrochlore	Pyrochlore supergroup	$(Na,Ca)_2Nb_2O_6(O,OH,F)$	75.12	n.a.
Microlite	Pyrochlore supergroup	$(Na,Ca)_2Ta_2O_6(O,OH,F)$	n.a.	83.53
Betafite	Pyrochlore supergroup	$(Fe,Mn)(Ti,Nb,Ta)_2O_6$		
Tapiolite	Tapiolite	$(Fe,Mn)(Ta,Nb)_2O_6$	1.33	83.96
Ixiolite	Ixiolite	$(Ta,Nb,Sn,Mn,Fe)_4O_8$	8.30	68.96
Wodginite	Wodginite	$(Ta,Nb,Sn,Mn,Fe)O_2$	8.37	69.58
Euxenite	Euxenite	$(Y,Ca,Ce,U,Th)(Nb,Ti,Ta)_2O_6$	47.43	22.53
Struverite	Rutile goup	$(Ti,Ta,Fe)O_2$	11.32	37.65
Iimenorutile	Rutile group	$Fe_x\ (Nb,Ta)_{2x}\ 4Ti_{1-x}\ O_2$	27	N.A.

The depletion of niobium and tantalum in continental crust is attributed to the formation of crustal rocks at convergent margins above subduction zones where titanium-rich minerals that host niobium and tantalum may remain as residual phases in the source region during generation of the magmas (Kelemen et. al., 2003).

Although niobium and tantalum generally show coherent geochemical behavior, some chemical processes are able to separate them, which results in preferential enrichment or depletion of one or the other. These processes are still poorly understood, although crystal fractionation during magma evolution is the most commonly invoked mechanism. Niobium and tantalum show limited substitution for tin, tungsten, and zirconium in some rock-forming minerals, but particularly for titanium in such minerals as ilmenite ($FeTiO_3$), rutile (TiO_2), and titanite (sphene) ($CaTiSiO_5$). As niobium and tantalum become more highly enriched in residual igneous melts, a variety of chiefly oxide and hydroxide niobium and tantalum minerals may form, depending on melt composition, temperature, pressure, and fluid composition. In addition, some evidence suggests that later alteration by hydrothermal (hot) fluids—in particular, concentrated fluoride solutions (Wood, 2005) - may pla a role in mobilizing and enriching niobium and tantalum.

Tantalum is a fairly widely distributed element but relatively rare, with an average crustal abundance of 1.7 mg/kg (0.000017%); niobium crustal abundance is 20 mg/kg. Tantalum and niobium are hosted in a variety of minerals, some of which are listed in Table 2.3. Niobium and tantalum do not occur naturally as pure metals, but they are essential components in a variety of oxide and hydroxide minerals, as well as in a few rare silicates and one borate (Parker and Fleischer, 1968). The economically important mineral species are all oxides (Table 2.3); pyrochlore is the principal ore mineral for niobium, and tantalite is the principal ore mineral for tantalum. Until the discovery of pyrochlore-rich deposits in the 1950s, niobium was produced as a byproduct of mining columbite-tantalite- bearing pegmatites for tantalum.

2.4.2 Mineralogy

Tantalum and niobium are almost exclusively found in complex oxide and hydroxide minerals. Silicates of these elements exist but they are relatively rare, one such example is the eudialyte mineral ($Na_4(Ca,Ce)_2(Fe{+}{+},Mn,Y)ZrSi_8O_{22}(OH,Cl)_2$) (Moreno, 2011). Tantalum and niobium also substitute ions in common oxide groups, such as the titanium minerals, rutile and ilmenite. The oxides comprise the majority of the economically important minerals. The most common tantalum and niobium minerals occur in a solid solution named columbite group minerals (CGM) ($(Fe,Mn)(Nb,Ta)_2O_6$. When the predominate the Ta atoms in the structural formula, it is called tantalite and when the Nb atoms predominates it is columbite. The name "coltan" is a popular terminology, non-scientific, used to refer to CGM. The CGM is a nearly compete solid solution. Columbite and tantalite have very similar properties because they have the same structure and similar chemistries, but tantalite has a much higher specific gravity (8.0+) than does columbite. Tantalite also has a dimorphic relation (same chemistry but different crystal structure) to the mineral tapiolite. Columbite-tantalite minerals are found as accessory phases in rare-metal granites and pegmatites (Černý, 1991a, b).

The pyrochlore-supergroup minerals crystallize in the isometric crystal system and exhibit a unit cell characterized by a ~10.4 Å and Z = 8 (Rouse et al. 1998). They conform to the general formula: $A_{2-m}B_2X_{6-w}Y_{1-n}$ (Atencio et. al., 2010).

In this formula, A typically is a large [8]-coordinated cation with a radius of ~1.0 Å or a vacancy (□), but can also be H_2O (includes ions with or without lone-pair electrons on sites 16*d* or 96*g* in *Fd*3*m*). The *A* site therefore may host Na, Ca, Ag, Mn, Sr, Ba, Fe^{2+}, Pb^{2+}, Sn^{2+}, Sb^{3+}, Bi^{3+}, Y, Ce (and other REE), Sc, U, Th, □, or H_2O. The main constituents are shown in *B* is a [6]-coordinated cation (site 16*c*), typically of high field-strength. This site thus may contain Ta, Nb, Ti, Sb^{5+}, W, but also V^{5+}, Sn^{4+}, Zr, Hf, Fe^{3+}, Mg, Al and Si. *X* typically is O, but can include subordinate OH and F (site 48f).

Y typically is an anion, but can also be a vacancy, H_2O, or a very large (>> 1.0 Å)

monovalent cation (site 8*b*). Examples are OH–, F, O, □, H_2O, K, Cs, Rb. Displacements to 96*g,* 32*e* and 192*i* positions were also located.

The symbols *m, w,* and *n* represent parameters that indicate incomplete occupancy of the *A*, *X* and *Y* sites, respectively. Vacancies have not been found to occur at the *B* site (Borodin & Nazarenko 1957, van Wambeke 1970). Compositions with a substantial concentration of vacancies at the A site have been described as "defect pyrochlores". However, it is undesirable to give this term official status in this context, since it is non-specific, and likely to be used to describe other deviations from the ideal structure and stoichiometry. Lumpkin & Ewing (1992, 1995), Ercit & Robinson (1994), Brugger *et al.* (1997), and Nasraoui & Waerenborgh (2001) noted vacancies at the X site in some extreme cases of secondary alteration. According to Lumpkin & Ewing (1995), the following ranges are encountered: $m = 0$ to 1.7, $w = 0$ to 0.7, and $n = 0$ to 1. Actually, *m* can range up to 2 (Ercit *et al.* 1994, Brugger *et al.* 1997).

Atencio in 2010 presented the new scheme of nomenclature based on two prefixes and a root name allows one to use the root names without prefixes, or with only one prefix [*e.g.*, "plumboelsmoreite"] to specify at least a group for minerals that have not been fully analyzed. The first prefix will refer to the dominant anion (or cation) of the dominant valence [or H_2O or □] at the Y site. The second prefix will refer to the dominant cation of the dominant valence [or H_2O or □] at the A site. Given the Classical Greek derivation of "oxy-", "hydro-" and "hydroxy-", he suggested "keno-" to represent "vacancy", from the Greek k*evos*, meaning "empty".

He also, proposed that the occupancy of the A position in pyrochlore-supergroup minerals by cations is in some cases very low (<50%). Where the zero-charge group exceeds any valence group of the A site, the second prefix "keno" is proposed for species in which □ exceeds H_2O, and the second prefix "hydro" is proposed for species in which H_2O exceeds □.

The Hogarth (1977) rules of nomenclature that reflect the chemical composition at the A position have been modified to conform to the dominant-valence rule. Consequently, where neutral species are not the largest valence-based group at the A position, a second prefix is now to be applied for the dominant cation of the dominant valence. Nomenclature based on the dominant element in a dominant-valence group is simple and reproducible. This is not true for the alternative scheme of one end member is equal to one name, which is another reason for rejecting that model. In multidimensional coupled solutions, particularly where there are several different valence-groups at more than one site, it is not easy to define a rigorous, reproducible way of extracting a unique dominant end-member (Atencio et. al. 2010).

Pyrochlore-supergroup minerals show a variable Y-site composition. In the past, variations in Y-site occupancy were not reflected in species nomenclature, in part owing to a lack of knowledge of the structural chemistry of pyrochlore, but also owing to difficulties with the determination of some Y species. As the dominant constituent at the Y position can now commonly be established via EPMA and structure analysis, it is reasonable to indicate the

composition of this site in the nomenclature. Rouse et al. (1998) demonstrated the presence of structural (OH) groups by infrared spectroscopy. The dominant-valence rule is also valid for anionic sites (Hatert & Burke 2008).

where root is the name of the group, determined by the dominant species of the dominant valence group at the B site, y indicates the dominant species of the dominant-valence group at the Y site, and a indicates the dominant species of the dominant-valence group at the A site (Atencio et al. 2010).

2.4.3 Ore deposits

Tantalum and niobium deposits are usually associated with igneous rocks (e.g. pegmatites, granites, syenites and carbonatites). Pegmatites and granites enriched with lithium minerals, caesium, as well as tantalum and niobium, are the main sources of tantalum in the world and usually contain lower levels of niobium.

Other oxide minerals, such as loparite, ixiolite, tapiolite, and the perovskite group (Table 2.3) are fewer common sources of niobium and tantalum (USGS, 2017). Klaus also explained that microlite is the tantalum-rich end member of the pyrochlore mineral group and is generally found in pegmatites in association with columbite-tantalite. The titanium-bearing mineral strüverite has been a low-grade source of tantalum recovered from tin-mining waste in Southeast Asia. Niobium- and tantalum- bearing silicate minerals are relatively rare and found mostly in alkaline igneous rocks.

Tantalum and niobium minerals are found in a variety of igneous rocks around the world but only rarely in concentrations great enough to be of economic interest. Primary niobium and tantalum mineral deposits are found in three main types of igneous intrusive rocks (Table 2.4; Küster, 2009):

1. Carbonatites and associated alkaline rocks (Nb dominant),
2. Alkaline to peralkaline granites and syenites (Nb dominant), and
3. Rare-metal granites and pegmatites of the lithium- cesium-tantalum (LCT) family (Ta dominant) (Černý and Ercit, 2005).

In addition, some secondary concentrations have been formed by weathering of primary deposits (laterites) and by sedimentary processes (placers). The secondary deposits are of particular interest because they can be less expensive to mine and can have higher grades than primary hard-rock deposits. Because secondary deposits typically occur in close proximity to their primary sources, they are not described separately below.

Deposits of niobium and tantalum are found around the world (Table 2.4), but major production is currently restricted to only a few countries. Grade and tonnage figures for these deposits are shown in Figure 2.6. Generally, grades for niobium are higher (from about 0.1 to 3.0

percent niobium pentoxide [Nb_2O_5]) than those of tantalum (generally <0.1 percent tantalum pentoxide [Ta_2O_5]). Carbonatites generally have the highest grades and tonnages of niobium, although they overlap with those of alkaline granite and syenite-hosted deposits. In addition, some alkaline granite- and syenite-hosted deposits have higher tonnages at similar grades of tantalum than do rare-metal granite and pegmatite- hosted deposits (Figure 2.6). The ratios of niobium to tantalum in the alkaline granite and syenite deposits are much higher (>10 to 20) because of the predominance of niobium-rich minerals, such as pyrochlore and columbite.

Table 2.4. Major types of niobium and tantalum deposits, with key characteristics and examples. (Modified from British Geological Survey (2011). Grades and tonnages are highly variable among deposits, and the grades and tonnages given in this table are generalizations only. LCT, lithium-cesium-tantalum; Mt, million metric tons; Nb, niobium; Nb_2O_5, niobium pentoxide; Ta, tantalum; Ta_2O_5, tantalum pentoxide).

Deposit type	Brief description	Typical grades and tonnage	Major examples
Carbonatite-hosted primary deposits	Nb >Ta: Niobium deposits commonlyconsisting of members of the perovskite and pyrochlore mineral groups found within carbonatite intrusions in alkaline igneous provinces	Deposits show a wide range in both grade and tonnage. Morro dos Seis Lagos is the largest reported deposit; it contains about 2,900 Mt at a grade of 2.85 percent Nb_2O_5. More typicalis the deposit at Niobec, whichcontains about 46 Mt at a gradeof 0.53 percent Nb_2O_5	Niobec and Oka, Canada; Araxá, Catalão I and II,and Morro dos Seis Lagos, Brazil
Alkaline granite and syenite	Nb >Ta: Deposits containing niobium and lesser amounts of tantalum; the deposits are related to silicic alkaline granite and syenite igneous intrusions	Generally, <1,000 Mt at grades of 0.1 to 1 percent Nb_2O_5 and < 0.05 percent Ta_2O_5	Motzfeldt and Ilímaussaq, Greenland; Lovozero, Russia; Thor Lake and Strange Lake, Canada
Rare-metal granite	Ta > Nb: Deposits containing tantalum and lesser amounts of niobium; the deposits are generally found in the uppermost parts of peraluminous and (commonly) hydrothermally altered late-stage granitic plutons	Generally, <100 Mt at grades of < 0.05 Ta_2O_5	Yichun, China; Abu Dabbab and Nuweibi, Egypt
LCT-type pegmatite	Ta > Nb: Deposits containing tantalum and lesser amounts of niobium; the deposits are LCT-enriched-type pegmatites	Generally, <100 Mt at grades of < 0.05 Ta_2O_5	Greenbushes and Wodgina, Australia; Tanco, Canada; Volta Grande, Brazil; Kenticha, Ethiopia
Secondary(regolith) deposits	Niobium and (or) tantalum ore minerals concentrated in zones of intense weathering above carbonatite and granite or pegmatite intrusions, or in sedimentary placer deposits derived from such intrusions	Lateritic deposits generally have <1,000 Mt at grades of up to 3 percent Nb_2O_5. Placer deposits, such as the deposit at Tomtor, can have very high grades ofup to 12 percent Nb_2O_5	Araxá and Catalão, Brazil; Tomtor, Russia; Greenbushes, Australia

Carbonatites and associated alkaline rocks

Carbonatites are typically enriched in barium, fluorine, niobium, phosphorus, REEs, strontium, thorium, uranium, and zirconium. Not all carbonatites show similar enrichments in all elements, however; those related to carbohydrothermal fluids (hot fluids rich in carbon dioxide

and water±fluorine) typically have enriched REEs and strontium, but not niobium, whereas carbonatites associated with alkaline igneous rocks are typically enriched in niobium, phosphorus, and titanium, but not REEs (Mitchell, 2005). The most common niobium- bearing minerals in carbonatites include members of the pyrochlore and perovskite mineral groups, as well as niobium- rich silicates, such as titanite. The diversity of mineral types in carbonate-hosted deposits, their diverse compositions, and textural evidence for replacement and resorption of mineral phases suggest that the niobium-bearing minerals represent transported and (or) mixed mineral assemblages and are not in situ products of crystallization (Mitchell, 2005). Along with serving as the major source of niobium, carbonatites can also host deposits of barite, copper, fluorite, magnetite, phosphate, REEs, titanium, and vermiculite (Mariano, 1989).

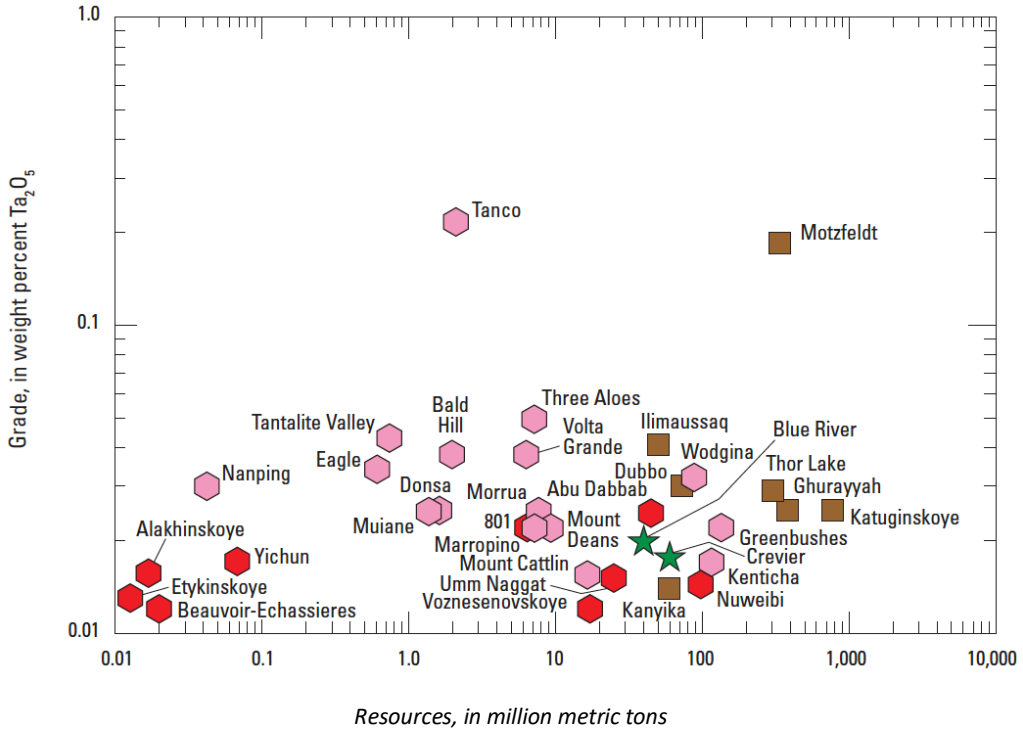

Figure 2.6. Log-log plots of deposit grades and tonnages of tantalum by deposit type. The data include different levels of probability, including measured, indicated, and inferred resources and (or) proven and probable reserves. Data and sources are given in Table 2.4. P, primary deposit; R, residual deposit, Nb_2O_5, niobium pentoxide; Ta_2O_5, tantalum pentoxide (USGS, 2017).

Brazil is the world's leading supplier of niobium (about 90 percent); its major deposits occur in Late Cretaceous carbonatite complexes. These complexes were emplaced along deep-seated faults located along the southwestern border of the ancient (Archean) São Francisco craton (Cordeiro et. al., 2011). The Araxá deposit is the largest operating deposit; it has more than 460 million metric tons of weathered ore with a mean grade of 2.48 percent Nb_2O_5 (Cordeiro et.al., 2011). The Barreiro carbonatite complex that hosts the Araxá deposit is approximately circular in shape with a diameter of about 4.5 kilometers (km); it is composed of carbonatite, glimmerite (altered ultramafic rock composed almost entirely of biotite or phlogopite), and phoscorite (a rock

composed of magnetite, apatite, and one of the silicate minerals clinopyroxene, olivine, or phylogopite) (Nasraoui and Waerenborgh, 2001). The complex is surrounded by a 2.5km wide aureole of metasomatized (fluid-altered), alkali-enriched quartzite and mica schist country rocks. Phoscorite, which forms thick masses in dolomitic carbonatite in the central part of the complex, shows the highest concentrations of pyro- chlore, the main niobium-bearing ore mineral, either as indi- vidual grains or in veins associated with magnetite. Intensive tropical weathering over the central part of the carbonatite complex has produced a lateritic cover up to 230 meters (m) thick that is enriched in pyrochlore and comprises the residual ore at Araxá (Nasraoui and Waerenborgh, 2001). The lateritic residual ore is exploited by open pit mining.

At Catalão, Brazil, niobium deposits are associated with two alkaline-carbonatite complexes, Catalão I and Catalão II (Cordeiro et. al., 2011). The Catalão I complex consists of a vertical pipe-like, zoned intrusion about 6 km in diameter at the surface. Two pipe-like orebodies, the Mine II and the East Area, have been defined (Cordeiro et. al., 2011). The Mine II orebody is hosted mainly by dolomitic carbonatite, and the East Area orebody is hosted by glimmerite. Both orebodies have been confirmed by drilling to extend to at least 800 m depth. The main niobium-bearing mineral in both deposits is pyrochlore, which in the East Area deposit is concentrated in late-stage dikes composed of nelsonite (magnetite-apatite-phlogopite rock). As at Araxá, current mining at Catalão II is in the weathered lateritic zone above the center of the complex.

The leading producer of niobium outside of Brazil is the Niobec Mine in Quebec, Canada. This mine is the only operating underground niobium mine in the world. The Niobec Mine is hosted by the Saint-Honoré carbonatite complex dated at 650 mega-annum (Ma) (Belzile, 2009), which is covered by Paleozoic limestone and glacial deposits. The ellipsoidal Saint-Honoré carbonatite complex is zoned with an outer ring of feldspathic (feldspar-bearing) and feldspathoidal (minerals that resemble feldspar but have a different structure and much lower silica content) alkaline rocks and an inner zone consisting of a series of carbonatite lenses. Like the Brazilian deposits, pyrochlore is the main niobium-bearing mineral, but it is very fine-grained (0.2 to 0.8 millimeters) and rarely visible. Although dissemi- nated throughout the carbonatite, pyrochlore is especially concentrated in steeply dipping (>70 degrees) mineralized lenses that are rich in, in order of abundance, magnetite, apatite, and biotite (Belzile, 2009). Some lenses extend to a vertical depth of at least 730 m and have average grades of between 0.44 and 0.51 percent Nb_2O_5. Other carbonatite complexes in Canada, including the nearby Crevier syenite- carbonatite complex, the Oka carbonatite complex to the south, and the Blue River complex in British Columbia, are currently being evaluated for their niobium resources.

Other carbonatite complexes around the world are known to host niobium mineralization, but none are currently in production. Two complexes are claimed to contain particularly large resources. The Tomtor complex in northern Siberia, Russia, is claimed to contain more niobium than the Araxá complex in Brazil along with significant REE resources (Kravchenko and

Pokrovsky, 1995); grade and tonnage figures for the deposit are not publicly available. Although the central carbonatite in the Tomtor complex is reported to be mineralized, the higher-grade niobium (>12 percent niobium) and REE-rich ore is in weathered carbonatite and in a buried placer deposit interpreted to have formed in an ancient lake overlying the complex (Kravchenko and Pokrovsky, 1995).

The Morro dos Seis Lagos carbonatite in northwestern Brazil is poorly known but is reported to contain the world's largest single niobium deposit; its resources are said to be 2,900 million metric tons grading 2.85 percent Nb_2O_5 (Pollard, 1995).

Woolley and Kjarsgaard (2008) report 23 carbonatites in the United States. Of these, the Elk Creek carbonatite, which is located in the subsurface of Nebraska, is currently being evaluated. The inferred resources at the deposit are reported to be 102.6 million metric tons grading 0.638 percent Nb_2O_5 (Daigle, 2012).

Alkaline to Peralkaline Granites and Syenites

The term "alkaline" encompasses a large variety of igneous rocks containing certain sodium- or potassium-rich minerals, such as feldspathoids and (or) alkali-rich pyroxenes and amphiboles and generally little or no quartz (Sørensen, 1974). Peralkaline rocks are a subset of alkaline rocks and are characterized by having a molecular amount of Na_2O+K_2O that exceeds Al_2O_3 (termed the agpaitic index >1). Alkaline rocks can range from ultramafic to felsic and from silica- undersaturated (feldspathoid-bearing) to silica-oversaturated (quartz-bearing). They are most commonly found in intraplate settings, such as continental rift zones (for example, the East African rift zone) and oceanic islands (for example, the Azores, Hawaii, and Réunion), but they can also be found in some orogenic belts where they were emplaced after major tectonic deformation. An important feature of alkaline rocks, but particularly peralkaline rocks, is unusual and locally extreme enrichment in alkalis; HFSEs, including zirconium, niobium, titanium, uranium, yttrium, and REEs; and halogens, such as fluorine and chlorine (Salvi and Williams-Jones, 2005). As a result, alkaline igneous rocks can contain mineral deposits with high contents of HFSEs, including niobium, but they less commonly have high contents of tantalum.

Alkaline magmas are the product of low degrees of partial melting in a deep, chemically undepleted mantle (Niu and O'Hara, 2003). As a result, alkaline magmas are enriched over many other magma types in incompatible elements, including the HFSEs. These incompatible elements become further enriched as the alkaline magmas cool and crystallize, becoming concentrated in the most evolved, volatile-rich granitic and syenites (same general composition as granite but with potassium feldspar dominant and little or no quartz [<5 percent]) melts and eventually forming disseminated ore minerals in the crystallized rocks. In addition, because the HFSEs form relatively dense minerals, they can accumulate into layers through crystal settling and be transported and mixed by currents or new injections of magma (Mitchell, 2005). Many alkaline

igneous complexes also show extensive evidence of hydrothermal alteration, commonly with the most altered rocks also having the highest HFSE and REE contents.

Although the role of fluids in the transport of HFSEs and REEs is still a matter of debate, growing evidence suggests that these elements are mobile in fluids that are enriched in fluorine, chlorine, and (or) carbon dioxide (CO_2) (Salvi and Williams- Jones, 2005). Typical ore minerals in mineralized peralkaline granites are usually niobium-rich pyrochlore and columbite.

Alkaline intrusive complexes are not currently major sources of niobium and tantalum production, although exploration is ongoing in some areas (for example, Strange Lake in Canada and Ghurayyah in Saudi Arabia). Examples of alkaline igneous complexes include the Pitinga complex in Brazil, the Strange Lake and Thor Lake complexes in Canada, the Ilímaussaq and Motzfeldt complexes in southern Greenland, the very large Lovozero complex in Russia, and the Pilanesberg complex in South Africa. Alkaline intrusive complexes have been identified in the United States, including Bokan Mountain in Alaska and Magnet Cove in Arkansas, but they are not known to contain significant niobium and tantalum resources of current economic interest.

The Devonian Lovozero alkaline complex on the Kola Peninsula of Russia and the adjacent Khibina complex together make up the largest peralkaline igneous intru- sions in the world, covering an area of about 2,000 square kilometers (km^2). The Khibina complex is host to one of the largest phosphate resources in the world (2.7 billion metric tons averaging 17.5 percent phosphorus pentoxide [P_2O_5]), whereas the Lovozero complex hosts zirconium, niobium, REEs, yttrium, strontium, barium, and phosphorus, which occur as eudialyte (a zirconium-bearing silicate mineral), loparite, and apatite (Salvi and Williams-Jones, 2005). The Lovozero complex, which is exposed over an area of 650 km^2, occurs as a trough-shaped intrusion composed of three main intrusive phases (Figure 2.7) (Kogarko et. al., 2010). The oldest phase (phase 1), which accounts for about 5 percent of the total volume, consists of nepheline syenites with varied mineralogy, but it contains no loparite or eudialyte. The next phase, (phase II), which accounts for about 77 percent of the total volume, consists of layered nepheline syenites with varied mineralogy and locally accessory loparite or eudialyte. Loparite is concentrated up to 25 percent, by volume, in some layers (Kogarko et. al., 2002). Loparite concentrate has been produced intermittently during the past 50 years; about 30,000 metric tons grading 8 percent Nb_2O_5 and 0.7 percent Ta_2O_5 has reportedly been produced annually (Semenov, 1997). The third intrusive phase (phase III), which is also known as the eudialyte complex, accounts for about 18 percent of the total volume and consists of nepheline syenites that, particularly in the upper part of the complex, can contain seams and lenses of almost monomineralic eudialyte (50 to 85 percent) (Kogarko et. al., 2010).

The Mesoproterozoic Ilímaussaq alkaline complex in southwestern Greenland is one of the most studied alkaline complexes in the world (Sørensen, 2001). It is 1 of 10 alkaline intrusions in the Gardar igneous province, which is a failed continental rift that was active between 1,350

and 1,140 Ma (Upton et. al., 2003). The Ilímaussaq alkaline complex is the type locality for the rock-type peralkaline nepheline syenite and also 27 minerals. It contains large concentrations of a number of rare elements, including beryllium, lithium, niobium, REEs, uranium and thorium, yttrium, and zirconium, contained in about 220 different minerals, of which 9 are unique to this complex (Sørensen, 2001). The complex covers 136 km^2 and has an exposed vertical thickness of 1,700 m; its total depth is not known. The main rare-metal deposits with potentially exploitable niobium, REEs, yttrium, and zirconium are present in 29 separate eudialyte-rich layers interpreted to have formed by crystal settling (Sørensen, 2001). Cumulatively, these rocks are estimated to contain a resource of about 54 million metric tons grading 1.1 percent zirconium dioxide (ZrO_2), 0.09 percent yttrium xide (Y_2O_3), 0.56 percent rare-earth oxides, and 0.11 percent Nb_2O_5 (Steenfelt, 1991). The Motzfeldt intrusion, which is another of the alkaline intrusions in the Gardar igneous province, has zones of hydrothermally altered syenite containing niobium-tantalum-REE-bearing pyrochlore mineralization (Steenfelt, 1991), which is the focus of ongoing exploration.

Rare-Metal Granites and Lithium-Cesium- Tantalum–Type Pegmatites

All economically important tantalum mineralization is related to rare-metal granites (also called rare-element granites) and lithium-cesium-tantalum (LCT)-type pegmatites. The rare-metal granites are generally peraluminous (have molecular Al_2O_3>[$CaO+Na_2O+K_2O$]), muscovite- and albite- rich granites that display high degrees of chemical fractionation, and represent the last stages of felsic magma evolution in upwardly differentiated granitic intrusions (Linnen and Cuney, 2005). The parental magmas are formed by partial melting of preexisting crustal rocks, particularly aluminous sediments, and are generally emplaced at shallow levels of the crust (in the upper few kilometers) during the late stages of or after major tectonic deformation and regional metamorphism in orogenic belts. They may show pervasive hydrothermal alteration and host disseminated tantalum and niobium mineralization, as well as tin and tungsten, in complex vein systems (stock works) that developed from circulation of late-stage hydrothermal fluids. Typical mineralization consists of microlite, columbite-tantalite, tantalum-rich cassiterite (tin oxide), and lepidolite (lithium-rich mica).

LCT-type pegmatites are generally small (meters rather than kilometers in length and width) granitic intrusions characterized by extremely coarse but variable grain-size and enrichments in lithium, rubidium, cesium, beryllium, tantalum, and niobium (Ta>Nb) (Černý and Ercit, 2005).

They are the products of highly fractionated and volatile-rich granitic magmas generally derived from rare-metal granites. They commonly occur in aureoles surrounding the roof of their parental granite intrusion, and the mineralized and most fractionated pegmatites are found the farthest away (Figure 2.8). Most LCT-type pegmatites are concentrically but irregularly zoned

(Figure 2.9), and typically have a thin border zone, a wall zone, an intermediate zone, an albite zone, and a core zone (Cameron et. al., 1949; Fetherston, 2004). Tantalum mineralization is mostly concentrated in the intermediate and albite zones and generally consists of columbite-tantalite, ixiolite, microlite, and (or) wodginite. Additional minerali- zation may be present, including beryllium (as beryl, a beryllium aluminum silicate), cesium (as pollucite, a cesium zeolite), lithium (as spodumene, a lithium pyroxene; petalite, a lithium aluminum silicate; and lepidolite), tin (as cassiterite, a tin oxide), and a number of gemstones. LCT-type pegmatites are also mined for albite, muscovite, potassium feldspar, and ultrapure quartz. Like their parental rare-metal granites, LCT-type pegmatites are widely distributed globally, and range in age from Archean to Mesozoic, but they are found to be concentrated particularly during times of conti-nental collision and supercontinent assembly (Bradley and McCauley, 2013). By far the largest LCT-pegmatite-hosted mineral deposits are of Archean age, however (for example, the Greenbushes and Wodgina deposits in Australia and the Tanco deposit in Canada).

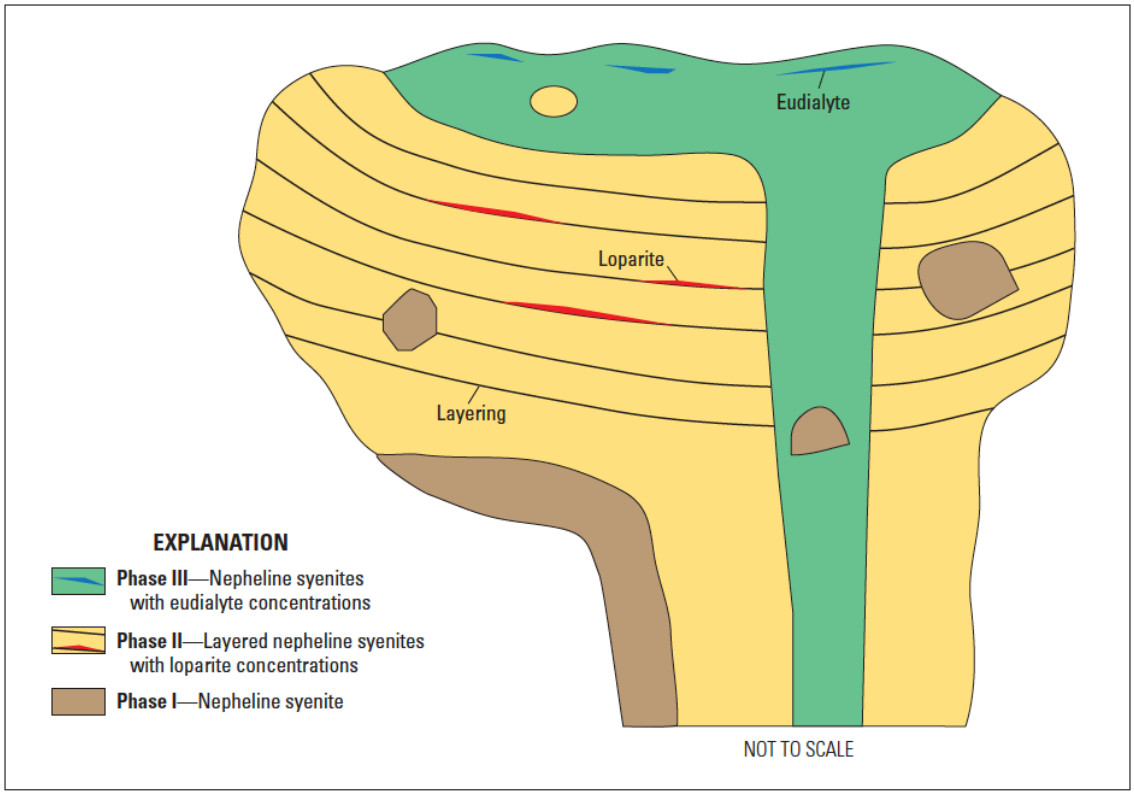

Figure 2.7. Schematic cross-section of the Lovozero alkaline intrusion, Kola Peninsula, Russia, showing the relation among the three intrusive phases and the niobium mineralization contained in eudialyte and loparite. (After Kogarko and others (2002)).

In recent years, pegmatites in the State of Western Australia, Australia, have been major world suppliers of tantalum, particularly the Greenbushes and the Wodgina Mines. The giant (>3 km long) Greenbushes pegmatite is located 250 km south of Perth and has been mined for tin and tantalum since 1888, and more recently also for kaolin and lithium (Partington et. al., 1995).

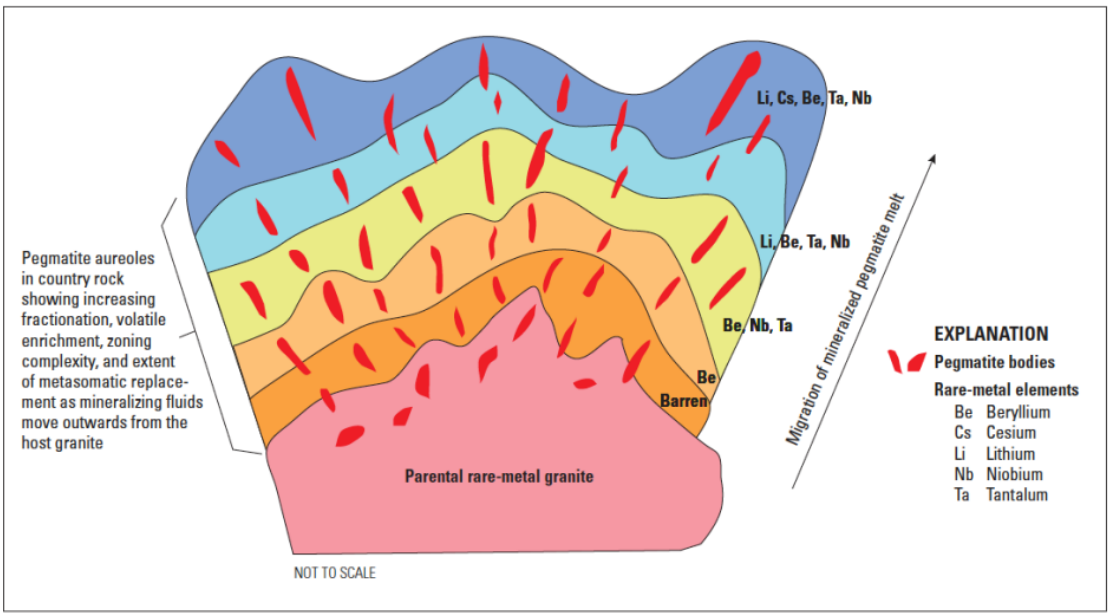

Figure 2.8. Schematic representation of regional lithium-cesium-tantalum (LCT) rare-metal-bearing pegmatite zoning above a parental granite. (After Černý (1991b)).

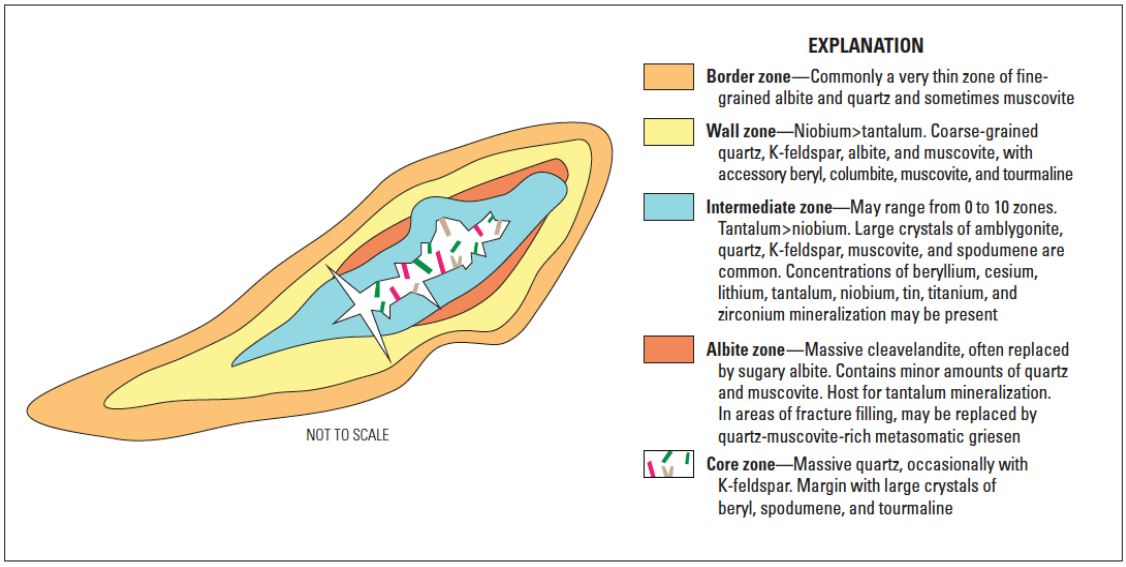

Figure 2.9. Schematic cross-section of a concentrically zoned lithium-cesium-tantalum (LCT) rare-metal-bearing pegmatite. (After Černý (1991a) and Fetherston (2004)).

It contains the world's largest identified pegmatite-hosted tantalum resource and mining operation. The pegmatite is late Archean in age and appears to have been intruded along a crustal fault zone synchronously with deformation. Unlike many other pegmatite districts, there is no evidence for a nearby parental granite pluton for the Greenbushes pegmatite. Four major compositional zones have been identified; however, the most compositionally evolved zones (that is, the most lithium-rich) occur at the top and bottom of the pegmatite rather than at the center. Early formed tantalum minerals are mainly wodginite and ixiolite; later tantalum minerals (tantalite and tapiolite) occur within fractures, whereas microlite is related to later hydrothermal mineralization (Partington et. al., 1995). The main ore zones generally occur within the more

tourmaline-rich portions of albite-rich zones in the pegmatite. Most ore produced at Greenbushes since 1888 has been by open pit mining of weathered pegmatite and alluvial sources; recently, however, underground mining of hard-rock ore has also begun.

The Wodgina pegmatite district is one of more than 27 pegmatite districts located in the northern part of Western Australia, Australia; it includes the Wodgina main lode and Mount Cassiterite tantalum-mineralized pegmatites (Sweetapple and Collins, 2002). The Wodgina main lode pegmatite is a north-south-trending, easterly dipping (20 to 50 degrees) dike with a total length of about 1 km and a thickness ranging from 5 to 40 m; most mining has been in the northern, thicker end. Originally discovered in 1902, the Wodgina pegmatite has intermittently produced beryl, tantalum, and tin during the past 100 years. The main tantalum mineral is manganese-rich tantalite, which, together with some manganese-rich columbite and wodginite, is found mainly in marginal cleavelandite (a platy form of albite) (Sweetapple and Collins, 2002). In the Mount Cassiterite pegmatite, which lies just south of Wodgina, wodginite is the main tantalum mineral (Sweetapple and Collins, 2002). Tantalum from both pegmatites is recovered by open pit mining. Additional tantalum-bearing pegmatites occur in Western Australia, including the producing Mount Cattlin pegmatite, as well as the Bald Hill and the Mount Deans deposits, which are under development (Fetherston, 2004).

A number of pegmatite fields are present in Africa. Pegmatites in Ethiopia (Kenticha) and Mozambique (Marropino) were significant tantalum producers in the 2000–13 time period (Bleiwas et. al., 2015); others were undergoing exploration or development for tantalum and associated resources (for example, the Morrua and the Mutala pegmatites in Mozambique). Mining of columbite-tantalite (also called coltan) from weathered pegmatites and from secondary placer deposits derived from pegmatites in central Africa, particularly in Burundi, the Democratic Republic of the Congo (Congo [Kinshasa]), Nigeria, Rwanda, and Uganda, has been conducted mainly by artisanal family mining groups and prospectors. The Main Kenticha pegmatite in Ethiopia is a Cambrian-age intrusion exposed across a length of more than 2 km (Küster, 2009). The pegmatite displays asymmetric internal textural and mineral zonation with manganese-rich tantalite as well as ixiolite concentrated in the upper intermediate and core zones. The deposit also contains valuable lithium resources, although these are not currently mined. Tantalum production has been from deeply weathered regolith over the pegmatite; however, exploration drilling of the hard-rock pegmatite is being conducted to evaluate the size of the primary mineralization (Küster, 2009). To the south of Kenticha, the Alto Ligonha pegmatite province in Mozambique contains numerous mineralized pegmatites, which have been mined intermittently since 1926. Tantalum concentrate was produced from ore from the Marropino Mine, concessions were held for the Morrua and Mutala deposits, and exploration was ongoing in adjacent areas. In Egypt, rare-metal granites were the focus of ongoing exploration and development activities, including the Abu Dabbab and Nuweibi granites (Küster, 2009). These deposits consist of fine-

grained columbite-tantalite minerals disseminated throughout the granite intrusions. In addition, these intrusions host tin mineralization and ceramic-grade feldspar (Bleiwas et. al., 2015).

In China, the Yichun tantalum-niobium-lithium deposit is the leading tantalum producer, accounting for more than one-half of China's tantalum output (Fetherston, 2004).

The deposit is in a small, sheet-like rare-metal granite that represents the most fractionated and youngest phase of the Jurassic Yanshan granite intrusion (Yin et. al., 1995). The main tantalum minerals in this deposit are columbite-tantalite and tantalum-rich cassiterite along with minor microlite. The 801 Mine, which is located in the eastern part of the Inner Mongolia Autonomous Region about 640 km northeast of Beijing, is reported to have large resources of niobium, REEs, tantalum, and zirconium (Fetherston, 2004). Additionally, pegmatites in the Altai region of northwestern China and in the Nanping region of southeastern China have also produced columbite-tantalite.

In South America, the Volta Grande pegmatite mine located near the city of Nazareno in the State of Minas Gerais, Brazil, is a significant supplier of lithium, niobium, and tantalum. The main deposit is in a large, about 1-km-long, subhorizontal, zoned albite-spodumene pegmatite body of Paleoproterozoic age (Lagache and Quéméneur, 1997). Cassiterite, microlite, and tantalite are the main tantalum-niobium-bearing minerals. A distinctive feature of pegmatites in the Volta Grande district is that they are exceptionally enriched in lithium and rubidium (Lagache and Quéméneur, 1997).

The only pegmatite mine in North America producing tantalum in the 2000–13 time period was the Tanco deposit at Bernic Lake in southeastern Manitoba, Canada (Bleiwas et. al., 2015). Operated briefly as a tin mine beginning in 1929, tantalum production began only in 1969. Full-scale mining to produce lithium from spodumene (the underground mine's major product), along with cesium, rubidium, and tantalum, began in 1984. Tanco is part of the rare-metal-bearing Bernic Lake pegmatite group, which intrudes metamorphosed Archean volcanic rocks. The Tanco pegmatite occurs as a shallowly dipping sheet that is up to about 100 m thick and can be traced for about 1,600 m along strike. The pegmatite consists of nine zones, each of which has a different mineralogy, texture, and location, as well as a halo of altered mafic host rock. The deposit has a very complex mineralogy—more than 80 minerals are present, including 14 tantalum-bearing minerals (Černý, 2005). Wodginite is the principal ore mineral, and it occurs mainly in a zone lying below the quartz core (Grice et. al., 1972). Numerous other tantalum-bearing pegmatites have been identified in Ontario and Manitoba (Selway et. al., 2005); several were undergoing evaluation of their tantalum and associated resources. In the United States, niobium-tantalum minerals, chiefly columbite, were recovered intermittently from a number of pegmatites in the past (Barton, 1962). The Harding pegmatite in New Mexico, which is a complexly zoned lithium- and beryllium-bearing pegmatite, was an important source of tantalum briefly during World War II and supplied about 3 metric tons of microlite concentrate (Parker and Adams, 1973). There has

been no reported tantalum mine production in the United States since 1959.

2.4.4. Uses, Applications, and Consumption

The electronics industry accounts for about one-half of tantalum consumption, mainly as powder and wire (Schwela, 2010). Electronic capacitors are the leading end use of tantalum owing to tantalum's particular ability to store and release energy. Because of this ability, components can be exceptionally small and are favored in space-sensitive, high-end applications, such as telecommunications (for cell phones), data storage (for hard drives), and implantable medical devices (for hearing aids and pacemakers). To date, no effective substitute has been found for tantalum in electronic devices without loss in performance.

Tantalum's low mechanical strength and high biocom- patibility allows it to be used as a coating on stronger substrates, such as stainless steel, for such medical applications as stents to support blood vessels, plates, bone replacements, and suture clips and wire. In addition, tantalum is used to impart strength and high temperature resistance to cracking in the manufacture of superalloys for use in aerospace applications and energy generation. Its resistance to corrosion makes tantalum useful in the chemical industry, generally as a lining to pipes, tanks, and vessels. World consumption of tantalum, by material produced, is shown in Figure 2.10, (TIC, 2019).

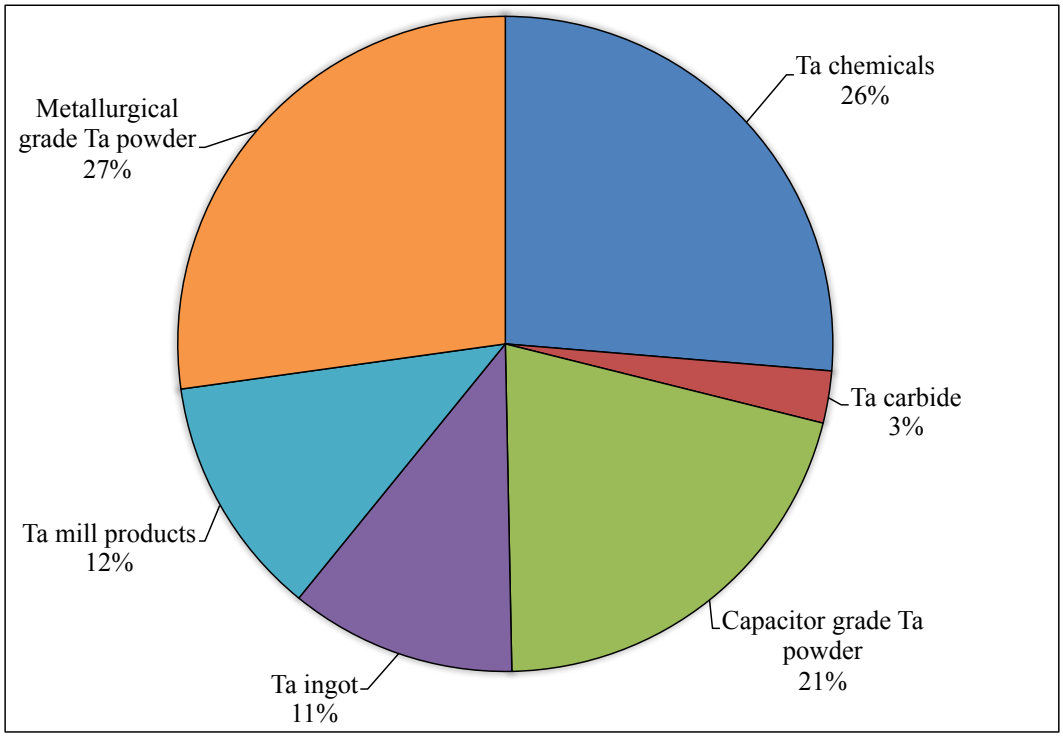

Figure 2.10. Pie charts showing percentage of reported world consumption of tantalum in 2017, by material produced (Data source: TIC, 2019). Ta, tantalum.

Tantalum oxide is used to increase the refractive index of lens glass, whereas the hardness

of tantalum carbide makes it ideal for cutting tools. The leading uses are metallurgical-grade powder (27%), tantalum chemicals (26%), followed by capacitor-grade tantalum powder (21%), and other uses (26%); and tantalum mill products (12%), tantalum ingot (11%); and tantalum carbide (3%). In 2017, world consumption of tantalum (measured as elemental tantalum) was 2,371 metric tons, which was an increase of 15% from consumption in 2009.

2.5 Tungsten mineralogy, types and deposits

2.5.1 Mineralogy

Tungsten does not occur in nature as a free metal, but only in the form of chemical compounds with other elements. Although several tungsten-bearing minerals are known, most are rare or very rare. Only scheelite and the wolframite group are abundant enough to be considered ores (Table 2.5). Scheelite, a calcium tungstate ($CaWO_4$), is typically white to yellowish in color, and has blue-white fluorescence in ultraviolet light; a property which is especially utilized in exploration and mining.

Table 2.5. Properties of the most common tungsten minerals (Source: BGS, 2017).

		Wolframite Group		
	Scheelite	Ferberite	Worframite	Hubnerite
Chemical formula	$CaWO_4$	$FeWO_4$	$(Fe,Mn)WO_4$	$MnWO_4$
Tungsten trioxide content (WO_3%)	80.6	76.3	76.5	76.6
Specific gravity ($g/cm^{3)}$	5.4-6.1	7.5	7.1-7.5	7.2-7.3
Color	Pale yellow to orange, green to dark brown, dark blue to black, white and colorless	Black	Dark gray to black	Red-brown to black
Lustre	Vitreous or resinous	Submetallic to metallic	Submetallic to metallic	Submetallic to adamantine
Hardness (Mush scale)	4.5-5.0	5.0	5.0-5.5	5.0
Crystal Structure	Tetragonal	Monoclinic	Monoclinic	Monoclinic

The color of the fluorescent light is influenced by the molybdate content and changes from blue to cream and then to pale yellow and orange with increasing molybdenum content (Lassner and Schubert, 1999). Wolframite is a general term for iron–manganese tungstate and is a solid-solution series between two end members: ferberite ($FeWO_4$, with less than 20 percent manganese) and hübnerite ($MnWO_4$, with less than 20 percent iron). In practice, the name wolframite is often used for the intermediate mineral between these two end members. The wolframite group exhibit typically tabular morphology, and are usually black, dark grey or reddish-brown in color (Lassner and Schubert, 1999). Secondary tungsten minerals, such as hydrotungstite ($H_2WO_4 \cdot H_2O$) or cerotungstite ($CeW_2O_6(OH)_3$), can be produced by alteration processes or weathering and may cause problems during processing leading to reduced recovery

of tungsten (Schmidt, 2012).

2.5.2 Deposit types

Tungsten deposits usually occur within, or near to, orogenic belts resulting from subduction related plate tectonics. All major deposit types are associated with granitic intrusions or with medium- to high-grade metamorphic rocks. The locations of selected major tungsten mines and deposits are shown in Figure 2.11. Werner et al. (1998) classified major tungsten deposits into seven types: vein/stock work, skarn, disseminated, porphyry, strata bound, placer, and brine/evaporite. Four additional types of relatively minor economic interest were also identified as: pegmatite, breccia, pipe, and hot-spring deposits. In reality the categorization of individual localities can be complicated by multiple stages of formation creating deposits that could be ascribed to more than one of these types. Table 2.6 contains a summary of typical sizes and grades for the major producing deposit types.

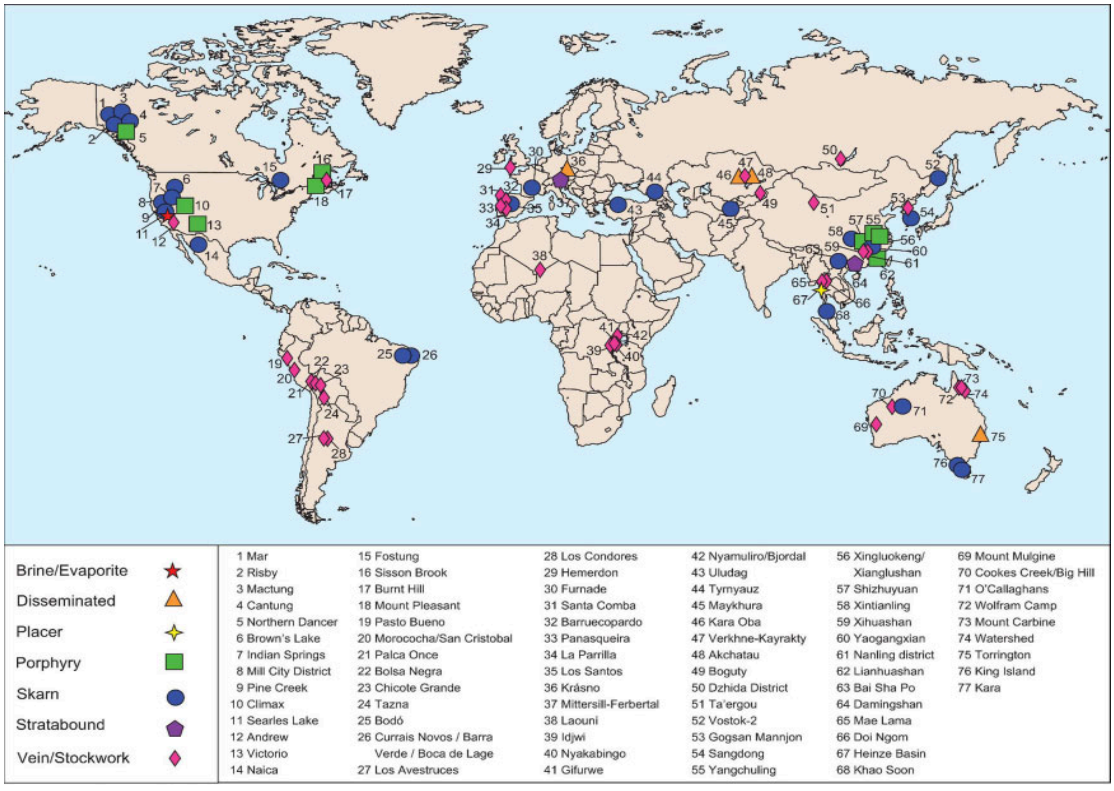

Figure 2.11. The location of selected major tungsten mines and deposits. Note: In China there are many other deposits noted in the literature and it is not possible at this scale to include them all.

Vein and stockwork deposits

Vein and stockwork deposits are genetically related to the development of fractures that occur in or near granitic intrusions during emplacement and crystallization. These fissures are frequently filled with quartz and can be up to several meters in width.

Table 2.6. Typical size and grade of major producing tungsten deposit types (Source: BGS, 2017).

Deposit type	Deposit size range (metric tons)	Typical range (WO_3%)	Examples
Vein/Stockwork	$<10^5$ to 10^8	0.1 to 0.8	Panasqueira (Portugal), Hemerdon (UK)
Skarn	$<10^4$ to 10^7	0.1 to 1.5	Mactung and Cantung (Canada)
Disseminated	$<10^7$ to 10^8	0.1 to 0.5	Akchatau (Kazakhstan)
Prophyry	$<10^7$ to 10^8	0.08 to 0.4	Xingluokeng and Yangchulin (China)
Stratabound	$<10^6$ to 10^7	0.2 to 1.0	Mittersill-Ferbertal (Austria)

Large vein deposits may contain several individual veins, while stockworks comprise swarms of parallel, or near parallel, veins with interconnecting veinlets (Werner et al., 1998). The veining is commonly bordered by greisen (a form of endoskarn alteration) and is often spatially associated with disseminated greisen and porphyry-style tungsten mineralisation. The mineralogy of vein deposits ranges from the simple, consisting almost entirely of quartz and wolframite, to the complex, as at Pasto Bueno in Peru (Landis and Rye, 1974) or Panasqueira in Portugal (Kelly and Rye, 1979) where more than 50 vein-forming minerals have been identified. The wolframite series is the main tungsten-bearing mineral but scheelite also occurs in some deposits of this type. Tin, copper, molybdenum, bismuth and gold may also be present in economic quantities. In addition, uranium, thorium, rare earth elements and phosphate minerals may also occur (Elliott et al., 1995).

In general, vein and stockwork deposits tend to be low grade. However, even with grades as low as 0.1 per cent tungsten trioxide they can still be exploited economically by bulk mining methods, as demonstrated at Mount Carbine mine in Australia (De Roo, 1988), which operated successfully at this low grade between 1973 and 1986. Other notable examples of vein/ stockwork deposits are found at Verkhne-Kayrakty, Kazakhstan (Rubinstein and Barsky, 2002); Xihuashan in the Nanling tungsten–tin province, China (Elliott, 1992; Guiliani et al., 1988; Wang et al., 2011); Bolsa Negra and Chicote Grande, Bolivia (Cox and Bagby, 1986) and Hemerdon, United Kingdom (Mining Magazine, 1979; Keats, 1981). The tungsten mineralization at Hemerdon in Devon, is hosted in sheeted greisen's-bordered vein systems and stockworks in the apex of a steeply dipping, dyke-like, granite body (known as Hemerdon Ball) on the south-west side of the early Permian-age Dartmoor pluton. Mineralisation extends to depths of at least 400 meters below surface. The Ta'ergou tungsten deposit, located in the western part of the Qilian orogen in Gansu Province, north-western China, consists of scheelite skarn bodies and wolframite–quartz veins. The deposit is genetically related to the Caledonian Teniutan granodiorite emplaced within Proterozoic rocks bordering the Archaean North Chine Plat form. The tungsten veining overprints the calcic skarns (Zhang et al., 2003). The tungsten vein system in the Nanling Range, South China, has been described using a so-called "five-floor building" model (Gu, 1982; Liu and Ma, 1993; Li et al., 2011). Within this model there are broadly five vertical zones: a thread or stringer zone at the top, over a veinlet zone, thin vein or mixed zone, large vein zone and finally a thin-

out or extinction zone (Figure 2.12). Large veins can also be sparsely developed in the underlying granite where typically they are weakly mineralized. The large-vein zone and the thin-vein or mixed-vein zones are the most economically valuable.

	Morphological zones	Zones thickness (metres)	Average vein width (metres)	Density (veins per metre)		Mineral association
I	Stringer or thread zone	100–200	0.001–0.01	0.05–5	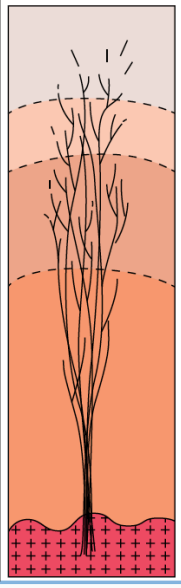	muscovite, cassiterite, wolframite, tourmaline
II	Veinlet zone	50–150	0.02–0.1	5–20		cassiterite, wolframite, chalcopyrite, bismuthine, beryl, muscovite, pyrite
III	Thin vein or mixed zone	150–250	0.05–0.5	1–8		wolframite, cassiterite, scheelite, chalcopyrite, pyrite, molybdenite, bismuthine, beryl, galena, sphalerite
IV	Large vein zone	200–450	0.2–2	0.03–2		wolframite, chalcopyrite, molybdenite, potash, feldspar, pyrite, galena
V	Extinction or thin-out zone	>50	0.05–2	0.05–0.1		wolframite, molybdenite, chalcopyrite, pyrite, potash, feldspar

Figure 2.12. Schematic model of 'five-floor building' vein-type tungsten deposit. (Data sourced from: Gu, 1982; Huang and Xiao, 1986.).

Skarn deposits

Skarns are coarse-grained rocks dominated by calc-silicate minerals that have formed by metasomatic processes in sequences containing carbonate- bearing rocks such as limestone (Einaudi et al., 1981). Most are found adjacent to plutons and are often associated with hornfels, skarnoid, marble and other similar rocks in the thermal aureoles. They can also occur along faults, major shear zones, in shallow geothermal systems and in metamorphic rocks at lower crustal depths (Meinert et al., 2005). Less common types of skarns form in contact with sulfidic or carbonaceous rocks such as banded iron formations or black shales. Calcic skarns are characterized by calcium- and iron-rich silicates (andradite, hedenbergite, wollastonite); magnesian skarns by calcium- and magnesium-rich silicates (forsterite, diopside, serpentine); and aluminous skarns by aluminium- and magnesium-rich calc-silicates (grossularite, vesuvianite, epidote). Dolomitic rocks tend to inhibit the development of tungsten bearing skarns; consequently, magnesian tungsten-bearing skarns are uncommon (Ray, 1995).

Newberry and Einaudi (1981) distinguished two types of skarn on the basis of host-rock composition and relative depth: reduced skarns such as the Cantung and Mactung deposits in the North West Territories, Canada, and oxidized skarns, such as King Island, Tasmania, Australia

(Kwak and Tan, 1981; Kwak, 1987). In general, oxidized tungsten bearing skarns are smaller than reduced tungsten bearing skarns. The highest grades in both systems are associated with hydrous minerals and retrograde alteration (Meinert et al., 2005). Scheelite is the principal tungsten mineral and this may occur as disseminated grains or fracture fillings. Copper, molybdenum, tin, zinc and bismuth may also be present and can be economically recoverable. Economically exploitable skarn deposits usually contain between 0.1 per cent and 1.5 per cent tungsten trioxide (Werner et al., 1998). Mactung in the Yukon Territory, Canada, is the one of the largest tungsten-bearing skarn deposits, with a NI43-101 compliant resource estimate including 33 million tones @ 0.88% WO_3 in the indicated category and a further 11.9 million tones @ 0.78% WO_3 in the inferred resource category (Narciso et al., 2009). The deposits occur in the thermal aureole of a late Cretaceous felsic intrusion, which was emplaced into a dominantly pelitic, Lower Paleozoic sequence along the eastern margin of the Selwyn basin. The mineralisation is stratabound and confined to four individual beds (Dick and Hodgson, 1982). Other tungsten-bearing skarn deposits include Los Santos in Spain (Tornos et al., 2007), Tyrnyauz and Vostock-2 in Russia (Soloviev and Krivoschchekov, 2011) and Xintianling and Yaogangxian in China (Zhao et al., 1990; Chang, 2005). The Xintianling scheelite deposit, located on the north-east side of the Qitianling batholith in Hunan Province, is one of the largest amongst several tungsten-bearing skarn deposits in China. It is spatially associated with two-stage granite emplacement into Carboniferous dolomitic limestones over a 10 Ma interval in the mid–late Jurassic. Skarn ore formation is related to the older stage granite. It is a typical example of the Jurassic tungsten–tin ore-forming event in the Nanling Range of south China (Zhang et al., 2011).

Disseminated or greisen deposits

In disseminated or greisen deposits wolframite or scheelite are disseminated in highly altered (greisenised) granite or granitic pegmatite. Greisen comprises mainly quartz and mica and is formed by post-magmatic metasomatic replacement of the primary granite minerals. Disseminated deposits are distinguished from the greisen- bordered veins and stockworks by the pervasive nature of the alteration and the absence of fluid pathways. In reality, these deposit types commonly coexist. Disseminated greisen deposits usually occur near to the upper parts of intrusions that are emplaced at depths of between 0.5 and 5 km, where fluids can boil but are prevented from escaping to the surface. Tungsten is usually present as wolframite although some deposits also contain scheelite. Tin, molybdenum, bismuth and other base metals may also be present, along with quartz, topaz, white mica, tourmaline and fluorite. Tungsten grades are generally low but exploitation can be economic as a by-product of tin extraction. Examples of disseminated deposits include the Akchatau and Kara Oba deposits in central Kazakhstan (Zaraisky and Dubinina, 2001), the Torrington district of New South Wales, Australia and the

Hub stock at Krásno in the Czech Republic (Jarchovsky, 2006).

Porphyry deposits

Porphyry deposits are extensive, low-grade deposits formed following the separation of metal-rich fluids from a crystallizing wet magma. Tungsten tends to be concentrated in stockwork zones and fractures either in or near to the upper parts of granitic intrusions emplaced at shallow depths. Mineralized breccia zones may also be present. Tungsten occurs either as wolframite or scheelite, and sometimes both are present. Molybdenum, bismuth and tin often occur and may represent an opportunity for co-production. Tungsten-bearing porphyry deposits tend to be large in size but may not be economic due to their low grade. Nevertheless, important examples include Northern Dancer (formerly known as Logtung), Sisson Brook and Mount Pleasant in Canada (Brand, 2008; Snow and Coker, 1986; Kooiman et al., 1986) and the Xingluokeng, Shizhuyan, Lianhuashan and Yangchulin deposits in China (Liu, 1980; Zhaolin and Zhongfang, 1996; Werner et al., 1998). The Northern Dancer porphyry of the Western Cordillera, which straddles the boundary between Yukon Territory and British Columbia Province, comprises multiple, mid-Cretaceous felsic intrusions hosting four vein systems with different tungsten/molybdenum ratios (Noble et al., 1984). Mineralization is centred on a felsic porphyry dyke complex and includes stockworks, sheeted vein systems, disseminations and skarns but mostly comprises typical porphyry-style crackle breccias showing many similarities with porphyry molybdenum deposits. Resources, which are NI43-101 compliant, are estimated to include 30.8 million tonnes @ 0.114% WO_3 in the measured category, 192.6 million tonnes @ 0.1% WO_3 in the indicated category and a further 201.2 million tonnes @ 0.089% WO_3 in the inferred resource category (Molavi et al., 2011). The Xingluokeng tungsten–molybdenum deposit of the Fujian province is hosted in a late Jurassic Yanshanian granite porphyry stock in the Wuyishan metalloorganic belt. The central zone underwent strong silicic and potassic alteration and is enriched in rare earth elements (Zhang et al., 2008). The Shizhuyuan deposit in the Dongpo orefield of Hunan Province is a world-class polymetallic tungsten deposit. The mineralization is diverse in character and has a complex origin related to multiple phases of granite intrusion (Lu et al., 2003). It comprises dominantly W–Mo–Bi–Sn–F calcic skarn-greisen zones developed around the late Jurassic Qianlishan granite complex of the Yanshanian granitoid province. The highest tungsten grades occur in vein/stockwork W–Sn–Mo–Bi–Be mineralization associated with a later granite phase which is superimposed on the early stage massive skarn-greisen zone. On this basis some researchers have described this deposit as porphyry in style (Li et al., 2004).

Breccia deposits

Breccia deposits are composed of angular, broken fragments of rock located within,

above or marginal to the apex of an intrusion. They are formed either by magmatic/hydrothermal hydraulic fracturing or by explosive interactions between water and magma. Many vein/stockwork and porphyry deposits have breccia zones associated with them. However, some tungsten-bearing breccia bodies appear to have formed independently of other deposit types (Werner et al., 1998). An example is the Washington copper–molybdenum–tungsten breccia pipe in Sonora, Mexico (Simmons and Sawkins, 1983).

Stratabound deposits

Tungsten mineralization in strata bound deposits is confined to a single stratigraphic unit, although they may not be strictly conformable to bedding, i.e. mineralization may cross bedding planes. Stratabound deposits occur in volcano-sedimentary sequences and are considered to be syngenetic in origin. They can be distinguished from skarn deposits which are largely controlled by the composition of the host rock lithology and are assumed to be epigenetic. Strata bound tungsten mineralization occurs within iron–magnesite and dolomitic marbles in the Eastern Alps (Neinavale et al., 1989). Many strata bound tungsten occurrences appear to have been affected by later mobilization and reconcentration and therefore their syngenetic origin is questionable (Werner et al., 1998). Examples of this type of tungsten deposit include the Mittersill-Ferbertal deposits in the Salzburg province of Austria and Damingshan in China (Ma, 1982). The Cambrian-age Mittersill- Ferbertal orefield comprises several lenses of scheelite-rich quartzite, an underlying vein-stockwork zone, an eruption breccia and quartz-rich aureole to a granitoid intrusion. Further scheelite enrichments occur along shear zones. Geochronological and geochemical data on the Ferbertal deposit indicate a genetic link with mantle dominated granitic melts (Eichhorn et al., 1999). Subsequent metamorphic events and granitic intrusions have remobilised the scheelite (Höll and Eichhorn, 2000). The Cambrian-Ordovician Damingshan tungsten deposit in the Danchi metalloorganic belt in Guangxi Province includes Late Cretaceous vein and stockwork wolframite mineralization as well as the massive stratiform types (Li et al., 2008).

Pegmatite deposits

Pegmatites are coarse-grained igneous rocks, generally of granitic composition, formed by the late stage crystallization of magma and containing many incompatible elements such as lithium, beryllium, niobium, tantalum, tin and uranium. Tungsten is not a common constituent of pegmatites and tungsten-bearing pegmatite deposits are therefore rare. Grades for tungsten tend to be low but it can be extracted as a by-product. For example, tungsten occurs in the pegmatite which is worked primarily for tantalum at the Wodgina mine in Western Australia, and it is also found in the Okbang deposit in South Korea (Chung, 1975).

Pipe deposits

Pipe deposits can be cylindrical or irregular, elongated or bulbous masses or quartz that occur at the margins of granitic intrusions. Mineralization, most frequently wolframite, is often erratically distributed in high-grade shoots or pockets containing up to 20 percent wolframite, but deposits tend to be small. Examples include the Wolfram Camp deposit in Queensland, Australia (Plimer, 1975).

Hot-spring deposits

These deposits are probably derived from bedrock tungsten-bearing deposits and are formed by circulating hot ground water. Deposits of calcareous tuffs or travertine are formed by precipitation as this hot ground water cools and tungsten mineralization has been found in selected locations. Examples, where these deposits have been worked in the past, include Golconda in Nevada, USA (Kerr, 1940; Marsh and Erickson, 1975) and Uncia in Bolivia (Werner et al., 1998).

Placer deposits

Placer deposits are concentrations of heavy and chemically resistant minerals that occur in sediments. Wolframite and scheelite, although heavy, will eventually decompose during weathering and therefore, tend not to be preserved long enough to form widespread placer deposits. However, they do occur, in both alluvial and coastal sediments, albeit they are usually small in size. Typically, they are located very close to the bedrock deposit from which they were originally derived (Werner et al., 1998). A few tungsten bearing placer deposits have been worked on an industrial scale, for example in the Heinze Basin in Burma (Myanmar) (Goosens, 1978) and in the Dzhida district of eastern Siberia.

Brine and evaporite deposits

Tungsten-bearing brines and evaporite deposits occur in recent lakes and/or palaeolake settings in arid regions of Asia and North America. The tungsten is thought to have been leached from bedrock deposits by hot fluids. The most significant example of this type of deposit is the Searles Lake deposit in California, USA (Guerenko and Schmincke, 2002; Altringer, 1985). Stratabound scheelite at Halls Creek in Western Australia is of evaporitic origin analogous to continental-sabkha playa basins of the Mojave desert (Todd, 1989).

2.6 Mineralogical characterization

2.6.1 Quantitative mineralogy

A wide range of micro analytical techniques exists that can be used to examine an ore. During the 1980s, Gasparrini (1984A) noted that optical microscopy and electron microprobe (EMPA) were the techniques used for studying silver carriers in an ore, being that the optical properties were the most important features for the identification of silver deportment at that time. Currently, advanced microscopic techniques provide detailed quantitative information of the minerals present in the ores, directly analyze the structure and composition of the ore, and quantify the key mineralogical attributes (such as modal mineralogy, deportment of the elements, and textures, among other relevant attributes).

Factors that affect the identification of minerals are mainly the grain size of the minerals (Gasparrini, 1993; Zhou, 2010), textures present in the ore and the detection limits of each microscopic technique used in the mineralogical characterisation (Knights and Patterson, 1988; Basto et al., 1995). In the following paragraphs the techniques used in the present study are described. It is also necessary to comment that there are other micro analytical techniques, which are outside the scope of this work, for example, Sensitive High-Resolution Ion microprobe analysis (SHRIMP), Proton induced microprobe (μ-PIXE), among others.

- **SEM-based automated mineralogical systems**

Automated mineralogical systems are used widely in process mineralogy and mineral characterization. They can measure key mineralogical attributes in a few hours, such as modal mineralogy, grain size, association and liberation of minerals (Jones and Gravilovic, 1970; Gottlieb et al., 2000; Petruk, 2000; Gu, 2003; Lastra, 2007). SEM-EDS are equipped with commercial software that controls the SEM-EDS, making it automatic. There are two well-known software products used worldwide – Quantitative Evaluation of Minerals by Scanning Electron Microscopy (QEMSCAN) and Mineral Liberation Analyser (MLA).

- **Electron microprobe analysis (EMPA)**

Electron microprobe analysis (EMPA) is the most mature of the micro beam analysis techniques, providing quantitative analyses for small areas of polished samples (Reed, 2005). The information given by the use of these techniques is shown in Table 2.7.

Table 2.7. Information gained by analytical techniques (from Lamberg, 2011).

Analytical technique	Level of information
Chemical Assays	Elements
MLA/QEMSCAN	Minerals
XRD	Minerals
Mineral conversion	Minerals
EMPA	Elements, minerals
ICP-MS	Elements, minerals
MLA analysis	Elements, minerals, particles
Synchrotron – based methods	Elements, minerals

Generally, this method is considered the most useful for the analysis of major and minor elements within a sample, with an accepted minimum detection limit (MDL) for trace elements by wavelength dispersion in the order of 100 ppm (Newbury et al., 1986; Goodall and Scales, 2007; Zhou, 2010). This method is used primarily to quantify the chemical composition of minerals.

2.6.2 Key mineralogical attributes

Butcher (2010) and Evans (2010) noted that, in an ore more than one texture may be present with varying deportment of valuable elements. Figure 2.13 illustrates an example of different micro- textures where copper may occur in ores given by Butcher (2010), i.e. copper can be present as chalcopyrite inter-grown with pyrite, discrete native copper, chalcocite rimming pyrite, or others as shown in the figure.

1. **Modal mineralogy:** the relative proportions of minerals present in an ore. Mc Arthur (1996) described the traditional method to measure this as point counting using optical microscopy methods. Currently, the newer methods, such as QEMSCAN, MLA and Quantitative X-Ray Diffraction (QXRD), allow the measurement of modal mineralogy "using a quantitative and unbiased approach" (Bonnici, 2012). QEMSCAN/MLA in some modes uses the point counting approach, in others a different basis is used.
2. **Elemental deportment:** indicates the minerals in which the valuable element is present and what proportion of the total elemental concentration is accounted for by those minerals.

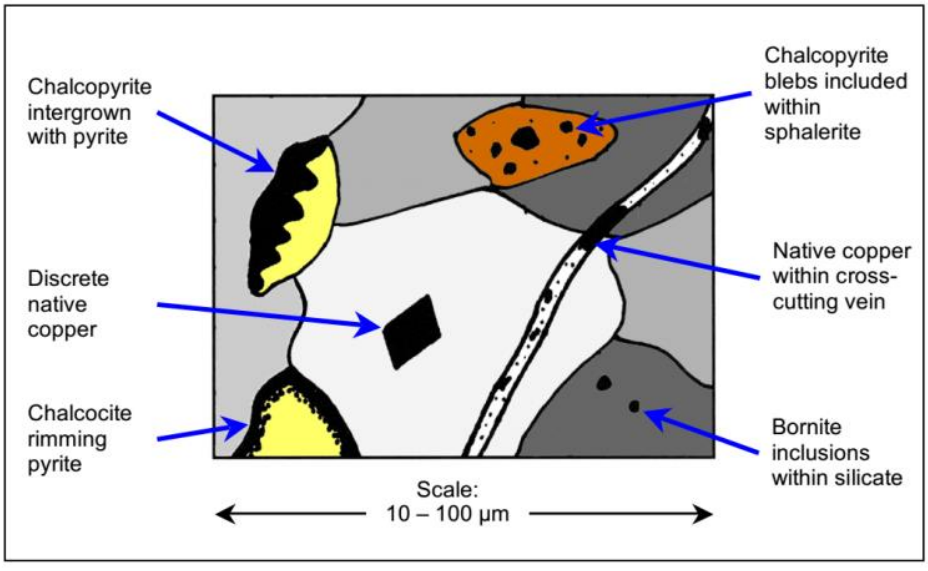

Figure 2.13. Various copper minerals and the textures that may be present in an ore (from Butcher 2010 and modified by Evans, 2010).

3. **Textures of ores:** According to Bojcevski (2004), texture is closely related to mineral liberation of the ores. There are three different scales that describe texture: macro (ores are

at scale of Km-m), meso (ores are at scale of m-cm) and micro (ores are observed at the scale of micrometres-examples of these micro-textural characteristics include mineral grain size and mineral association). For metallurgists, micro-textures are the most relevant of the textures for consideration of processing properties.

Texture also considers grain size and mineral association because together they largely describe the texture of ores.

- ***Grain size:*** As stated by Craig (2001), "(i)t is important to note that size of grains is vital in interpreting growth histories of ores and in predicting the degree of liberation and potential recovery of minerals during processing".
- ***Mineral association:*** describes how the boundary of a mineral is shared with other minerals. These associations have a direct impact on the potential liberation of the target minerals, and therefore on flotation and recovery (Petruk, 2000; Bojcevski, 2004; Goodall and Scales, 2007; Becker *et al.*, 2008).

Butcher (2010) discussed the basic textures that have some influence in flotation – these are equigranular and inequigranular. Also, complex textures have influence on the processing to liberate the valuable minerals, for example: "rims, disseminated inclusions (or exsolutions), or as interstitial phases – as this will control breakage mechanisms during blasting, crushing and grinding (intragranular versus intergranular), and will make it either relatively easy, or difficult (or impossible) to liberate and float effectively" (Butcher, 2010). Figure 2.14 shows the basic and complex textures that affect the processing of the ores.

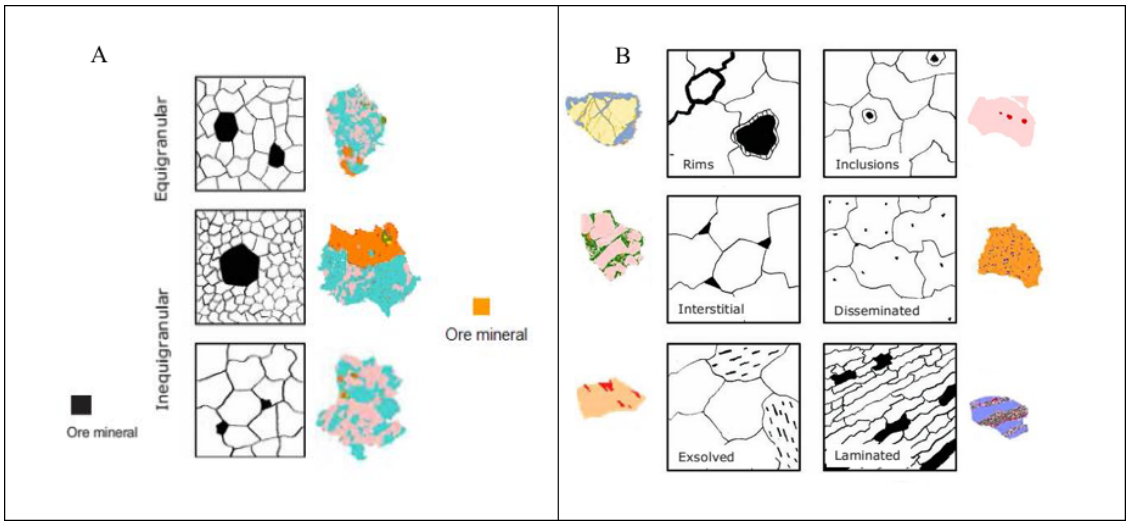

Figure 2.14. A) basic textures; B) complex textures present in an ore that influence processing (after Butcher, 2010).

4. **Degree of liberation:** The degree of particle liberation is a function of the grade and distribution of particles that contain the valuable mineral. Butcher (2010) commented on the

modern techniques used to quantify this. He stated that "the degree of mineral liberation can be quantified using a variety of optical and SEM-based image analysis techniques". Figure 2.15 illustrates an ore that starts as unbroken ore and undergoes crushing and grinding to obtain some degree of liberation.

Additionally, there is a relationship between the degree of liberation and grain size. The size of grain is crucial on predicting the degree of liberation and therefore the potential recovery of metals during treatment (Craig, 2001). Thus, it is necessary to know the degree of mineral liberation of the feed for complex sulphide ores to design the flow sheet, monitor plant performance and optimise circuits (Johnson and Munro, 2002). They also commented about the ranges of liberation and the effect on the separation process (Table 2.8) based on their experience with the data and the sulphide flotation process. These numbers will not necessarily be the same for all ores.

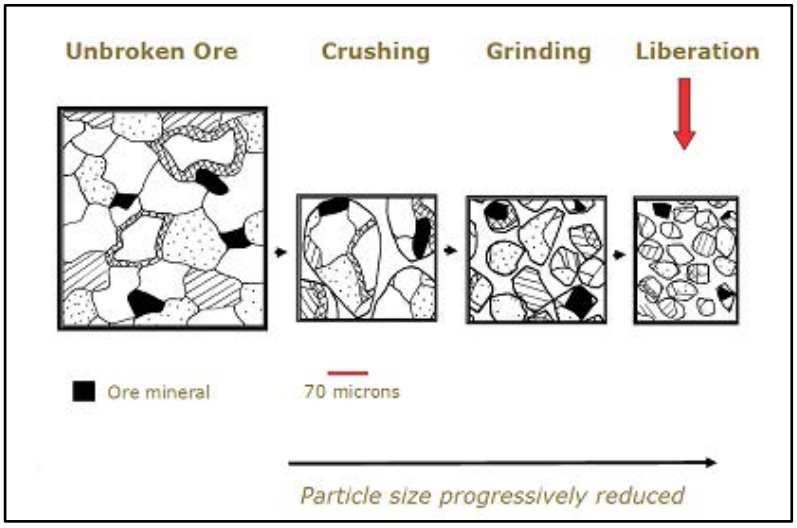

Figure 2.15. From unbroken ore – to obtain liberation of valuable minerals in an ore (from Butcher, 2010).

Table 2.8. Degree of liberation for minerals of interest (from Johnson and Munro, 2002).

Liberation value for mineral of interest*	Expected or theoretical possible separation process
< 70%	Poor separation results
70% to 80%	Sound of separation results
> 80%	Good separation results

*uncorrected 2D value

The degree of liberation is typically examined by mounting particles into resin and sectioning them to obtain 2D (areal) information (Butcher, 2010). By analysing these particles using optical microscopy or automated SEM, it is possible to classify them into the following groups: liberated particles, binary composites, ternary composites or quaternary composites. This is illustrated in Figure 2.16 where A, B, C and D represent different minerals.

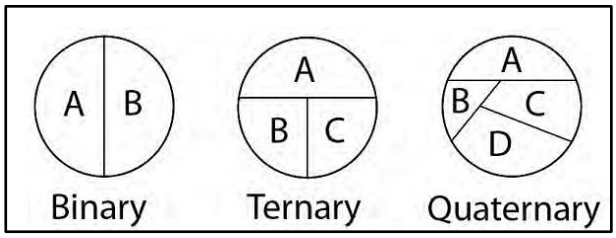

Figure 2.16. Particle compositions for binary, ternary and quaternary composites (from Jones, 1987).

2.6.3 Mineralogical characterization for tantalum

Tantalum mineralogy has been studied by many researchers including Bale (1989), Zihu et al. (2012), Martin et al. (2014), Ghorbani et al. (2017) and Allain (2019). These researchers have developed well-defined approaches for the mineralogical characterization of tantalum. According to the previous studies, the most common techniques used for tantalum characterization are listed in Table 2.6. For bulk mineral analysis, they are X ray fluorescence (XRF) for major elements. Minor elements were measured using ICP-MS from acid digestion of fused glass beads, Petrographic and mineralogical characterisations were carried out by X-ray powder diffraction (XRD), optical microscopy and scanning electron microscopy (SEM–EDS) and EMPA was used to obtain the chemistry of minerals. Mineral liberation analysis (MLA) and TIMA-X were performed to obtain textural and compositional information of a large number of particles.

A well described methodology to follow for tantalum characterization is provided by Ghorbani et al. (2017). It starts with sampling, then performing a chemical characterisation, followed by mineralogical characterisation to identify the key mineralogical attributes for tantalum processing.

Ghorbani (2017) described the Penouta mine as a tantalum deposit in Spain. The mineralogical study was carried out. Quantitative mineralogical analysis was conducted on the samples using a QEMSCAN® 4300 which is based on a Zeiss EVO 50 series SEM and consists of four light elements Bruker SDD (Silicon Drift Droplet) Energy Dispersive X-ray Spectrometers (EDS) and an electron backscatter detector (Rollinson, 2011). Both the Field scan and PMA measurement modes were used on the samples depending on the sample particle sizes. iMeasure v. 4.2 was used for data acquisition, and iDiscover v. 4.2 and 4.3 were used for the data processing. Bulk geochemical analysis was carried out using a Bruker S4 Pioneer WDS X-ray Fluorescence (XRF) instrument. Portable X-ray Fluorescence analysis (PXRF) was carried out using an Olympus DP-6000C PXRF to provide more in-depth analysis on sized fractions of gravity test products. Detailed spatially resolved chemical analysis of minerals was carried out by Electron Probe Microanalysis (EPMA) using a JEOL JXA-8200 Electron Microprobe.

Hamid (2018) the mineral characteristics of the Penouta ore grinding products were

analyzed using a Tescan Integrated Mineralogical Analyzer (TIMA-X) and X-ray powder diffraction (XRD). Mineralogy was determined by optical microscopy, X-ray powder diffraction (XRD), scanning electron microscopy with energy-dispersive spectral analysis (SEM–EDS) in the back-scattered electron mode (BSE), and EMPA. Electron microprobe analyses were obtained in a JEOL JXA-8230 electron microprobe.

2.6.4 Mineralogical characterization for scheelite

The mineralogy of scheelite is not more complex than that of tantalum, as discussed. Although several authors have studied the mineralogy of scheelite, a systematic approach for the characterization of scheelite has not been well defined. Combinations of different techniques need to be applied for each new scheelite ore, making it impractical to have a strictly defined procedure for scheelite. A practical framework to systematically characterize scheelite ores is required.

Many authors have described methods for identifying scheelite in different contexts; however, a consistent framework for characterisation has not been applied. A number of microscopic techniques that could be used to determine the average level of scheelite using microprobe techniques, and ICP-MS. As well, by using point counting and QEMSCAN or MLA, the average weight percentages of the minerals present in the ore could be quantified.

Nevertheless, there have been some mineralogical studies performed for different scheelite mines around the world that apply a mineralogical characterization method for sheelite. Some of these are discussed in the following paragraphs.

Martins (1996) investigated the low-grade concentrate was supplied by Minas de Tarouca. Chemical analysis, by atomic absorption spectroscopy and gravimetric methods, mineralogical composition, by X-ray powder diffraction pattern, and sieve analysis have been done.

X-ray diffractometer (D8-ADVANCE Bruker-AKS) was run in the reflection mode with Cu Kα radiation (λ = 1.5406, tube potential of 40 mV, and tube current of 40 mA), and a goniometer speed of 4 (°)/min. The shape characterization of milled particles was imaged by the JSM-6490LV SEM instrument have been studied by Hu (2012).

To determine impurities in minerals samples, chemical analyses were performed (Filippova et al., 2014). Pure minerals were used in micro-flotation. The pure minerals sources were as follows: calcite from France, apatite from Madagascar, fluorite from France and scheelite from China.

Filippov (2018) was analyzed scheelite through inductively coupled plasma mass spectrometer (ICP-MS) and inductively coupled plasm atomic emission spectroscopy (ICP-AES). He also both the floated and the non-floated products were dried in an oven at 80 °C, weighted and ground in a laboratory disc mill to obtain a −10 μm powder. The powder was analyzed by

Energy Dispersive X-ray fluorescence spectroscopy (ED-XRF) using a Thermo Scientific Niton™ Xl3t portable XRF analyzer.

These examples demonstrate that the approach used to characterise scheelite varies widely and there is an opportunity to develop a standard systematic approach to characterise scheelite in ore deposits.

2.7 Gravity concentration to recover tantalum and scheelite

This research will focus on the gravity concentration process, which is used on a laboratory scale to selectively separate valuable minerals from non-valuable minerals. Gravity concentration is the separation of minerals based upon the difference in density (Wills et al., 2006). Many machines have been designed and built to effect separation of minerals by gravity (Burt, 1985). Design and optimization of gravity circuits is discussed by Wells (1991) and innovations in gravity separation are reviewed by Honaker et al. (2014). The Vanner, a vibrating continuous belt, was developed in the 1860s and bumping tables followed before the modern differential shaking table was developed by Wilfley in 1896 (Gupta et al., 2016).

2.7.1 Description of gravity concentration

Concentration occurs within a two-phase, solid-liquid system containing finely ground particles, and water. A schematic of the operation of a shaking table system is shown below in Figure 2.17. When a film of water flows over a flat, inclined surface, the water closest to the surface is retarded by the friction of the water absorbed on the surface and the velocity increases toward the water surface. If mineral particles are introduced into the film, small particles will not move as rapidly as large particles, since they will be submerged in the slower-moving portion of the film (Figure 2.18). Particles of high specific gravity will move more slowly than lighter particles, and so a lateral displacement of the material will be produced (Wills & Finch, 2015).

The shaking table consists of a slightly inclined deck, on to which feed, at about 25% solids by weight, is introduced at the feed box and is distributed across the table by the combination of table motion and flow of water (wash water). Wash water is distributed along the length of the feed side, and the table is vibrated longitudinally, using a slow forward stroke and a rapid return, which causes the mineral particles to “crawl” along the deck parallel to the direction of motion. The minerals are thus subjected to two forces, that due to the table motion and that, at right angles to it, due to the flowing film of water. The net effect is that the particles move diagonally across the deck from the feed end and, since the effect of the flowing film depends on the size and density of the particles, they will fan out on the table, the smaller, denser particles riding highest toward the concentrate launder at the far end, while the larger lighter particles are washed into the tailings launder, which runs along the length of the table. An adjustable splitter

at the concentrate end is often used to separate this product into two fractions a high-grade concentrate (heavy product) and a middling's fraction. Separation can be influenced by the length of stroke, which can be altered by means of a hand-wheel on the vibrator, or head motion, and by the reciprocating speed (Wills & Finch, 2015).

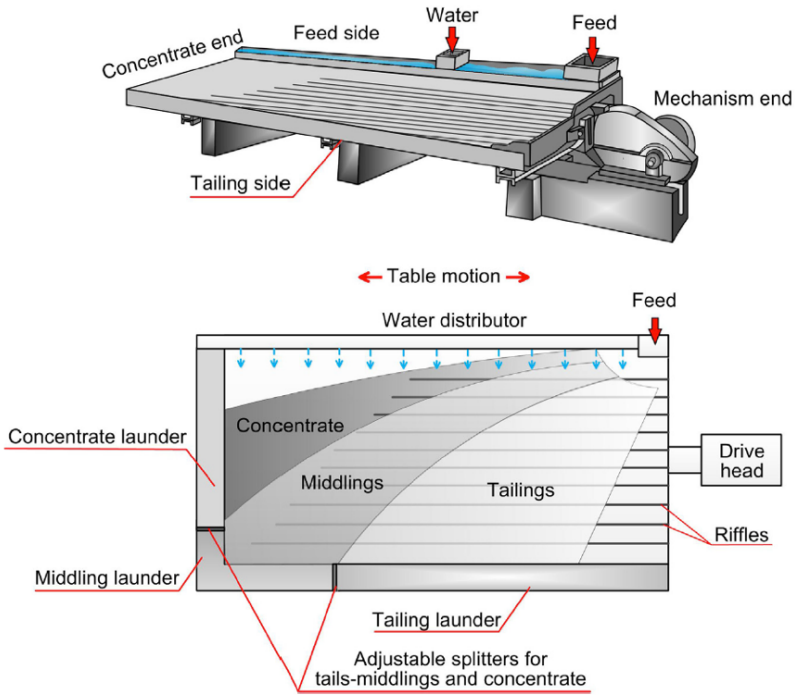

Figure 2.17. Operation of shaking table (Wills & Finch, 2015).

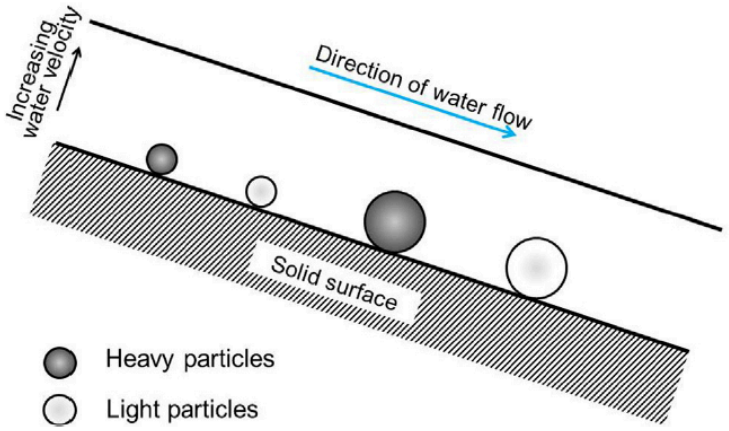

Figure 2.18. Action in a flowing film (Wills & Finch, 2015).

Tables slope from the feed to the tailings (light product) discharge side and the correct angle of incline is obtained by means of a handwheel. In most cases the line of separation is clearly visible on the table, so this adjustment is easily made. The table is slightly elevated along the line of motion from the feed end to the concentrate end. The moderate slope, which the high-density particles climb more readily than the low-density minerals, greatly improves the separation, allowing much sharper cuts to be made between concentrate, middling's, and tailings.

The correct amount of end elevation varies with feed size and is greatest for the coarsest and highest specific gravity feeds. The end elevation should never be less than the taper of the riffles, otherwise there is a tendency for water to flow out toward the riffle tips rather than across the riffles. Normal end elevations in ore tabling range from a maximum of 90 mm for a very heavy, coarse sand, to as little as 6 mm for an extremely fine feed (Wills & Finch, 2015).

◊ **Particle size in gravity concentration**

Particle size is an important factor governing over the shaking table, especially important are the effect of the coarser and finer particle sizes on the recovery of the valuable minerals. The variation of concentration recovery with particle size follows the general pattern of inverted "u" shape shown in Figure 2.19., where the recovery for fine particles is low, increases with particle size (intermediate region) reaching a maximum and then decreasing for coarser particles. Predictions from laboratory tests can be improved if the mineral recovery from the batch tests is expressed as a function of particle size (Wills and Napier-Munn, 2006).

The determination of an optimum grind size for particles in a given ore depends not only on their grain size (Finch et al., 1979). In the case of real complex ores, an initial examination should be made to determine the degree of liberation in terms of particle size so that an estimate of the required fineness of grind can be made (Wills and Napier-Munn, 2006). The potential for liberation of the minerals contained in the ore and the texture of ore samples can be characterized by using automated image analysis techniques, such as the MLA.

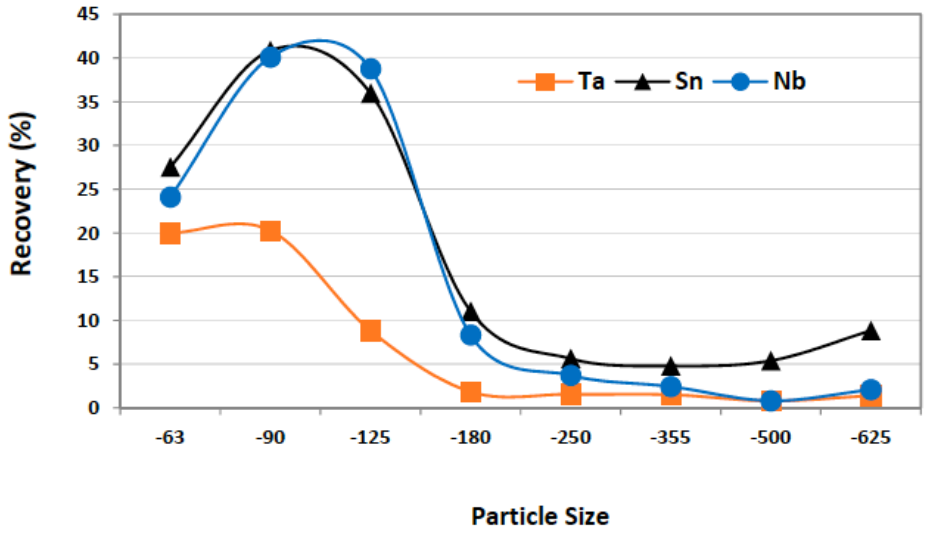

Figure 2.19. Average recovery by particle size during separation by a Knelson concentrator. Recoveries calculated from PXRF results (Ghorbani, 2017).

2.8 Mineral liberation modelling and prediction of the ores

A major portion of the scientific work on liberation has focused on the prediction of the natural mineral liberation; considerably less attention has been given to the problem of predicting the liberation spectrum produced when concentration processes occur simultaneously to that of size reduction (Schneider et al., 1991). Such concentration processes are very common in mineral processing operations, the definitive example being milling in closed circuit with a shaking table. This is not surprising, since liberation is a very complex process and the prediction of the natural liberation spectrum is a formidable task, requiring complex mathematical formulation.

The first attempt to develop a procedure for predicting the natural liberation spectrum was made by Gaudin in 1939. Gaudin's approach was essentially geometrical, based on the superposition of very simple regular fracture and texture patterns.

Wiegel and Li 1967 randomized Gaudin's model, recognizing that the textural structure of real mineralogical materials is better described by probabilistic models. The latest expansion of Gaudin's model is due to Meloy et al. 1987, who proposed solutions to the superimposition of a randomized fracture pattern that produces spherical particles in shape and four distinct, regular texture patterns.

The first, known as the integral geometry approach, is due to Barbery, 1991, and the second, known as the stereological approach, is due to King, 1979.

The integral geometry approach is the ultimate application of superimposition of complex, more realistic, texture patterns with fracture patterns, both controlled by random polyhedral processes, in three dimensions. However, it is rather complicated to model the liberation process directly in three-dimensional space, which makes King's approach considerably more attractive (Schneider, 1995). This consists of modelling texture and fracture in one dimensional space with great advantage in simplicity.

However, no realistic transformation function was available until 1985, when Lin et al., 1986 first measured it from computer generated PARGEN particles. Following that work, Lin, 1987 generated the first solutions to the stereological transformation equation, and the first attempts to measure the liberation spectra of real mineralogical particles were made. Finally, Schneider et al., 1991 presented a procedure for inverting the stereological equation which generated a mildly constrained volumetric grade distribution, which was used for the first time in conjunction with King's Random Fracture Model to predict the natural liberation spectra produced by the breakage of a copper and an iron ore.

The only known method for predicting the liberation spectra produced by the breakage of mineralogical particles is the one based on population balance modelling (Schneider, 1995).

Also, a model for the quadrivariate breakage function based on PARGEN simulations is proposed, and incorporated into MODSIM, the Modular Ore Dressing Simulator (Schneider, 1995).

A method was proposed by Ueda, 2016 for estimating the number of particle sections that

should be analyzed in order to achieve a degree of apparent liberation in 2D and a degree of liberation in 3D for a desired arbitrary reliability.

Attempts have been made in the past to explicitly include liberation characteristics in predicting downstream separation process performance for disseminated low grade ores (Schaap, 1979; Subasinghe, 2008) with limited success (Zhang, 2012).

Welsby et al. (2010) determined the floatability of each size/grade class of a Pb/Zn ore by back-calculation and considered it to be constant for a given the flotation environment.

A predictive liberation model without any ore texture and particle structure assumption has been developed and the details have been given elsewhere (Zhang, 2012; Zhang and Subasinghe, 2013).

Using the measured distributions and the distribution equations, the extent and the linear grade distribution of the composite and liberated particles have been calculated. The calculated values are compared with the measured distributions in Figure 2.20 for two size fractions (Zhang and Subasinghe, 2016).

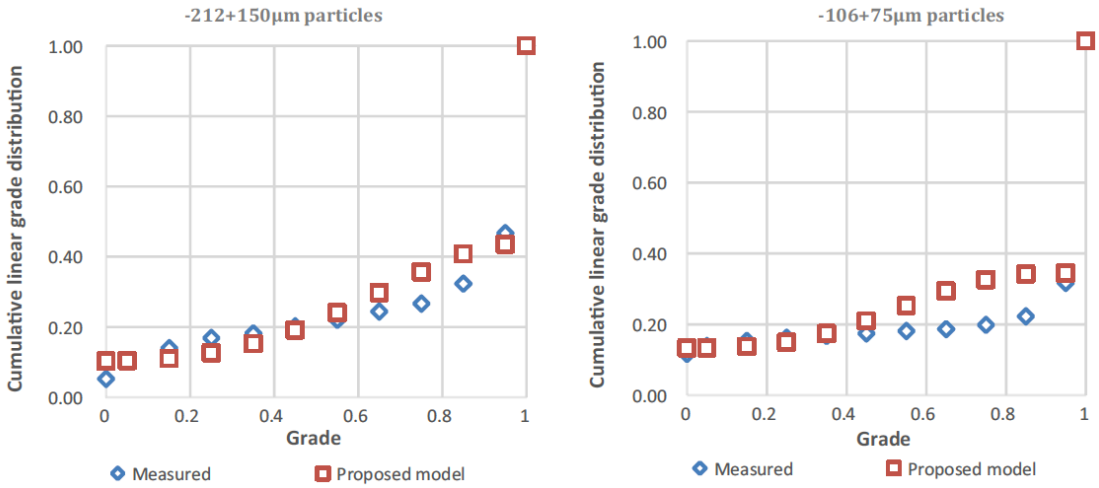

Figure 2.20. Comparison of cumulative linear grade distributions of particles at from measurements and model predictions (Zhang and Subasinghe, 2016).

2.9 Applying mineralogy to increase recovery of valuable metals from ores

Process mineralogy is a science that combines mineralogy and mineral processing, with the capabilities of identifying bulk mineralogy, degree of liberation and the presence of problematic minerals in an ore to develop or improve the processing flow sheet for that ore (Hagni, 1982; Henley, 1983; Hagni, 1986; Baum et al., 2004). There are a number of researchers who have applied process mineralogy to tantalum and scheelite (Bose 2008; Ayeni et al., 2012; Allain, 2019). Allain (2019) studied an ore body that had tantalum and niobium naturally occur in cassiterite deposits and are concentrated in the slag during the smelting process.

The concentration of tantalum and niobium oxides in a solid residue have been studied. Starting from a slag containing about 15% $(Ta,Nb)_2O_5$, sequential alkaline and acid leaching stages resulted in the production of a 63% (Ta+Nb) oxides concentrate, which is comparable to commercial grade of mineral concentrates. SEM-EDS was performed on the tailings to investigate which form of tantalum present in the ore was lost.

In 2017, Li carried out the surface properties and flotation behavior of scheelite particles having a size of −74 + 38 μm produced by ball and rod mills were studied through single mineral flotation experiment, scanning electron microscopy (SEM) observation, wettability measurement, and X-ray diffraction (XRD) test. The SEM analysis further confirmed that mineral grains obtained from the rod mill possess larger elongation and flatness values, which are essentially required for their attachment with air bubbles. The flotation results showed that the rod mill particles have a higher flotation recovery and are much easier to achieve a mono layer adsorption of collector compare to the ball mill ones

Therefore, before any metallurgical characterization is attempted, the following key mineralogical factors need to be studied:

◊ Modal mineralogy

◊ Tantalum and scheelite carriers or valuable mineral deportment

◊ Mineral locking/ liberation

◊ Grain size

◊ Mineral association

2.10 Key findings

As a consequence of tantalum and scheelite having a lower price in the metal market for many years, it has not been a target for recovery in many mine sites around the world. However, with recent increases in its price, those previously uneconomical sources of tantalum and scheelite have become more attractive to process. Within this category, it can be seen that old tailings and low-grade ores are now considered new resources of this noble element and offer an important opportunity for opening research, and applying or developing new techniques to recover tantalum and scheelite, which necessitates the development of a systematic approach to characterize tantalum and scheelite.

Tantalum mineralogy is more complex than scheelite mineralogy, due to the variety of CGM minerals that may be present in a tantalum ore. A wide range of grain sizes are also found, and the quantification of tantalum deportment is difficult to achieve. There are a number of explanations for the difficulties in identifying the deportment of tantalum: i) tantalum has different mobility in different environments, which includes the different operational conditions to which the ore is exposed during mineral processing operations; ii) the large number of CGM

minerals present in an ore, which could affect the accuracy of identifying its mineralogy; and iii) the texture of some CGM minerals present. Therefore, it becomes more important to perform the mineralogical characterization, in order to develop a clear understanding of which mineral processing routes should be tested for both situations.

In terms of mineral processing, there are different strategies that can be applied to recover tantalum and scheelite, and these strategies play an important role in developing the flow sheet design for recovering tantalum and scheelite. Due to the large number of CGM minerals present within an ore that can react differentially to different mineral processes, comprehensive characterization of the nature of CGM minerals within an ore is needed before a suitable processing route can be selected.

The following gaps were identified in the literature review:

a) The development of a standardized approach to determine tantalum and scheelite deportment in low-grade tantalum and intermediate scheelite ores;
b) A systematic approach to establish appropriate gravity separation strategies, based on tantalum and scheelite deportment, to achieve adequate recovery of tantalum and scheelite through shaking table stages;
c) Presentation of a framework that clearly describes what makes tantalum and scheelite ores simulation and modelling based on the results obtained through this work;
d) Investigation of the concentrate of tantalum and scheelite ores on size-by-size and size-by-liberation basis, which is not reported in the literature.

As a result of the identification of these points, the aim of this thesis is to develop an appropriate methodology to characterize complex low-grade tantalum and intermediate scheelite ores for the purpose of developing the most appropriate gravity separation strategy.

Chapter III

Materials and Methodologies

Chapter III
Materials and Methodologies

This chapter describes the overall framework used in this research to study two different ore types all from the different deposit. Descriptions of the ores used and of the general test-work procedures are presented, followed by descriptions of the conditions pertaining to the equipment, and the methodologies used for the mineralogical, chemical and physical separation product characterization.

3.1. Ore samples

3.1.1 Penouta ore

The tantalum ore used for this study came from the Penouta ore deposit where is located in the Penouta village, municipality of Viana do Bolo, Ourense, Galicia, northeast of Spain. It is a Sn-Ta greisen-type ore deposit. The Sn-Ta mineralization occurs Ta as disseminations in a leucogranite stock intruded in Precambrian-Lower Cambian gneisses and mica-schists of the Viana do Bolo series. The Penouta mine is composed of leucogranite hosted in metamorphic rocks, mainly constituted by gneisses and mica-schists corresponding to the Viana do Bolo series that was exploited up to de 1980s. Samples from the open pit and the tailings were used in the experiments.

An exhaustive sampling was obtained from leucogranite located in ancient open pit and from the tailings of the previous exploitation. There are more than 60 tailings from the leucogranite processing; two of them will be reprocessed for the Sn and Ta recovering:

Balsa Grande (B1) tailing. It is composed of 6 Mt residue of the leucogranite processing. Tantalum-rich minerals have not been processed; then, this tailing has similar tantalum content as leucogranite. The Strategic Minerals enterprise indicate that here the T_2O_5 content is of 60 ppm.

Balsa Pequeña (B2) tailing. It is composed of 300.000t of residue of the leucogranite processing that was reprocessed for Sn.

These ore were processed in the laboratory of mines of the Universitat Politècnica de Catalunya, in Manresa, Spain. For the mineralogical characterization, physical separation was the process investigated to treat the ore due to the fact that Penouta Was constructing a separation plant to process the ore.

- **Geology of Penouta deposit**

The Penouta deposit is located in the Central Iberian Zone of the Iberian Variscan Massif, near the contact with the Asturoccidental–Leonese Zone (Figure 3.1), according to the classification of Julivert et al. (1972). In the Central Iberian Zone the Variscan orogeny generated most of the extant structures, the internal deformation and the metamorphism. During the first Variscan deformation phase (D1), a low-grade slaty cleavage (S1) and recumbent folds were developed in the northern domain of the CIZ. The second Variscan deformation event yielded thrusting toward the external zones, crustal anatexis and a pervasive subhorizontal tectonic foliation (S2) linked to extension in the internal domains. The Variscan D3 phase led to upright folds, open to tight folds and occasionally a crenulation cleavage (S3) associated with subvertical shear zones with a dextral wrench component (Iglesias and Choukroune, 1980).

The Penouta deposit is located in the hinge of a D1 Variscan antiform (Figure 3.1) that is obliterated by the D3 Ollo de Sapo anticlinorium. This megastructure follows a NW–SE direction (Figure 3.1) and forms a continuous outcrop that extends ~300 km, from the island of Coelheira (Lugo) to the point where it disappears under the Tertiary materials of the Duero Basin (Arribas and Mangas, 1991; Arias et al., 2002) (Figure 3.1). The metamorphic rocks of the area consist of a lower part which crops out in the core of a gneiss dome around the Viana do Bolo village, the so-called Viana do Bolo Series (Ferragne, 1972); this is overlain by the Ollo de Sapo Formation. The Viana do Bolo Series constitutes the oldest material in the area and is a metamorphic complex consisting of quartzites, followed by mica-schists with garnet and Ca-silicate rocks which crop out NE of Penouta, and orthogneisses deformed during the Variscan orogeny, which crop out in the Covelo and Ramilo localities, near Penouta (Díez Montes, 2006) (Figure 3.1). The lower part of the series is considered to be Lower Cambrian (Arias et al., 2002) but the age of the upper part is not well known and a range of ages from Middle Cambrian to the lowermost Ordovician has been reported (Díez et al., 2010). These materials are overlain by the Ollo de Sapo Formation, which is a volcanogenic sequence consisting of fine- to coarse-grained massive gneisses with ocellar texture. With regard to igneous rocks in the area, synkinematic granites (Bembibre granite) are scarce and crop out close to Viana do Bolo village, whereas late to post-kinematic granodiorites (Veiga Granodiorite) and granites (Pradorramisquedo granite) are more important volumetrically (Figure 3.1).

The Penouta deposit is a greisenized cupola with four units: albite leucogranite, aplite-pegmatite dykes, greisen and quartz veins hosted in the metamorphic country rock (Llorens González et al., 2017). The Penouta stock is a leucogranitic body that intruded the Viana do Bolo Series and Ollo de Sapo Formation. Study of the outcrops has revealed that the granite intruded following planar anisotropies developed in the country rock corresponding to the regional D2 Variscan fabric. There are no ages available for the Penouta granite and only a relative dating can

be inferred from structural and contact relationships. The lack of foliation and significant internal deformation in this body are features typical of the late- to post-Variscan, similar to the Veiga and Pradorramisquedo plutons (Figure 3.1), which have been inferred to be related to a strikeslip shear zone (Vegas et al., 2001), this stage being similar in age (~308 Ma, Gutiérrez-Alonso et al., 2015) to other Sn-bearing granites dated recently in the CIZ (e.g. Logrosán Sn-(W) ore deposit, 308 ± 1 Ma, Chicharro et al., 2015). The Penouta albite granite is similar in composition to other albite granites in the Iberian Massif, most of them located in the innermost part of the Iberian Variscan Belt, namely, in the Central Iberian Zone. Most of these albite leucogranites were affected by an intense albitization, kaolinitization and greisenization (Mangas and Arribas, 1991; Clauer et al., 2015), probably related to fluid saturation in the apical zone of the leucogranite (López Moro et al., 2017).

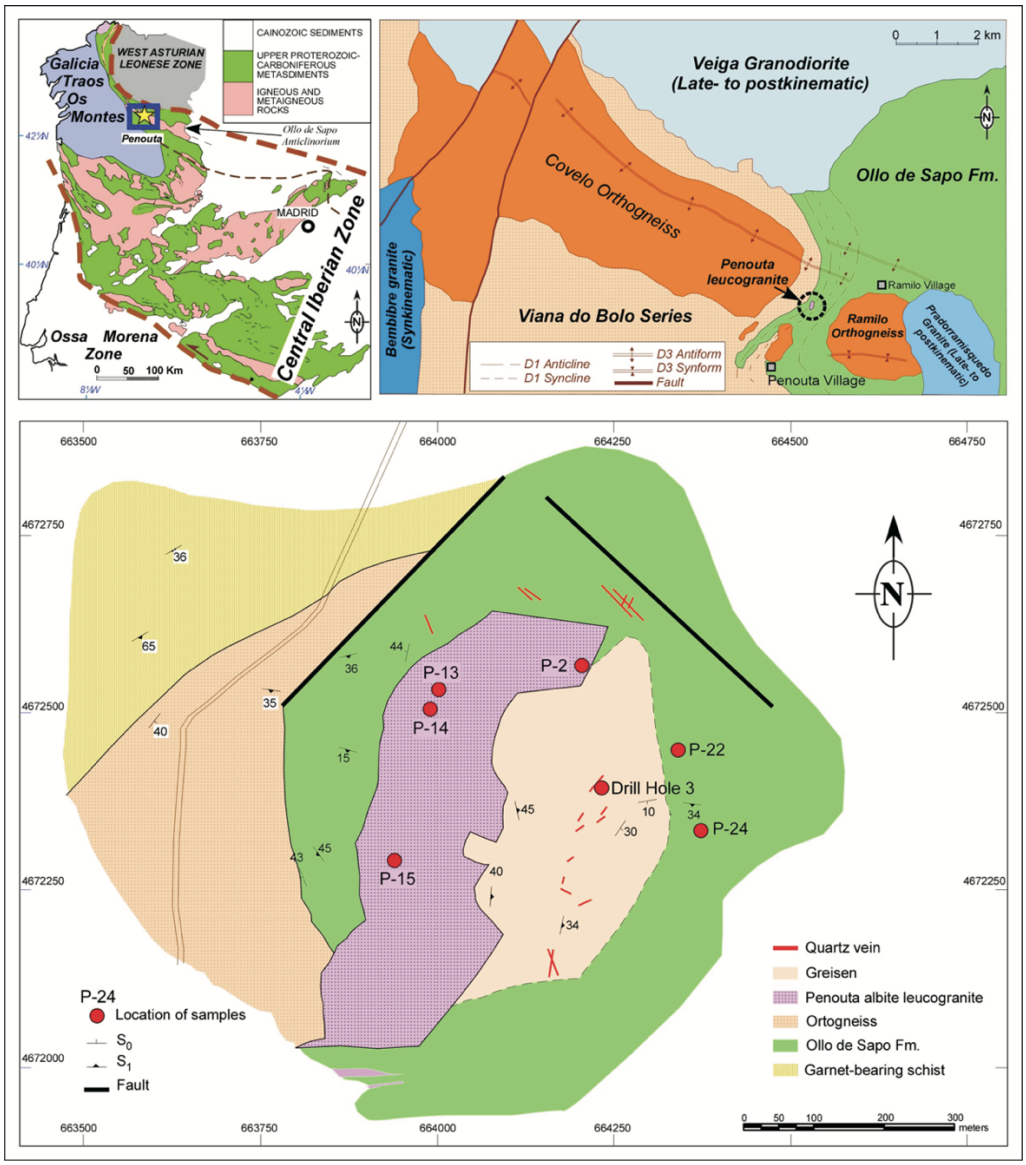

Figure 3.1. Detailed geological map of the Penouta deposit showing the locations of the samples. Upper left: location of Penouta in the Iberian Variscan Massif; upper right: geological sketch of the Ollo de Sapo Anticlinorium in its western region (Alfonso et al., 2018, modified from López Moro et al., 2017).

3.1.2 Mittersill ore

The tungsten material used for this study was a scheelite ore from the crushing step in the processing plant of Mittersill mine, Austria and provided by the exploitation enterprise. The sheelite ore is e associated with calc-silicate minerals. Scheelite is exploited from veins hosted in an amphibolite rock mainly composed of quartz, plagioclase of albite, hornblende, actinolite, K-feldspar, and biotite, muscovite and epidote as minor minerals.

- **Geology of Mittersill deposit**

The Mittersill tungsten depòsit, located in the Salzburg province, in the Hohe Tauern range of the central Eastern Alps, Austria, is a stratabound mineralization, where ore is hosted in a Cambro-Ordovician metavolcanic arc sequence with minor Variscan granitoids in the central Tauern Window (Raith and Stein, 2006).

The deposit is hosted in amphibolites and felsic gneisses of the volcano-sedimentary Habachs series. This series is part of the lower schist cover of the Tauern window. Above a basal amphibolite member, which belong to the Stubach Group, followed by a sequence of metaclastic rocks and an up to 4500 m thick magmatic unit, grading into the phyllite-dominated Habachphyllit unit.

The deposit consists of two parts, the Eastfield open pit and the Westfeld underground mine (Figure 3.2). The hornblendite units consist of hornblendites coarse-grained amphibolites, and intercalations of rhyolitic to dacitic gneisses. The metavolcano-sedimentary units contain associated fine-grained amphibolites and gneisses. The entire sequence has undergone multiple metamorphism and deformation, up to 530°C and 5-6 Kbars (Thalhammer et al., 1989).

The amphibolites are fine-grained banded and foliated rocks composed of variable amounts of major amphiboles, plagioclase, biotite, garnet and epidote group minerals and minor chlorite, muscovite, carbonate, quartz and opaque minerals. Hornblende prasinites and hornblende schists also belong to this group of amphibolites (Raith and Schmidth, 2010).

The tungsten and its associated sulfide-sulfosalt mineralization occurs within the entire metavolcanic sequence but the only zone of economic importance occurs in the hornblendite, located in the bottom of the magmatic unit, where WO_3 attains up to 1 % (Thalhammer et al., 1989).

In the deposit four generations of scheelite are distinguished (Raith and Schmidt 2010): Scheelite 1, or fine grain, up to 0.4 mm,it has white, with yellowish-white fluorescence, and usually with growth zoning. This generation occurs in the laminated scheelite ore in the western zone and in the underlying stockwork of the eastern zone.

Scheelite 2 is fine to coarse grained, up to 1 cm, gray with greasy brightness, yellow

fluorescence if it contains between 0.1-1.7 wt% Mo substitution. There is much in the western part and less in the eastern part. Often it presents a fragile deformation with cracks that contain solutions of molybdenum and tungsten.

Scheelite 3 usually it is forms re-crystallisation rims and overgrowths around as well as fracture fillings within Scheelite 1 and 2. It has from gray to white color with blue fluorescence that reflects its low content in Mo. Commonly it is associated with fine grain molybdenite.

Scheelite 4 is rare and forms isolated porphyryblasts: pale white with blue fluorescence that reflects its extremely low concentration of Mo. It is given in Alpine metamorphic quartz veins or as "weeds" in older scheelite generations.

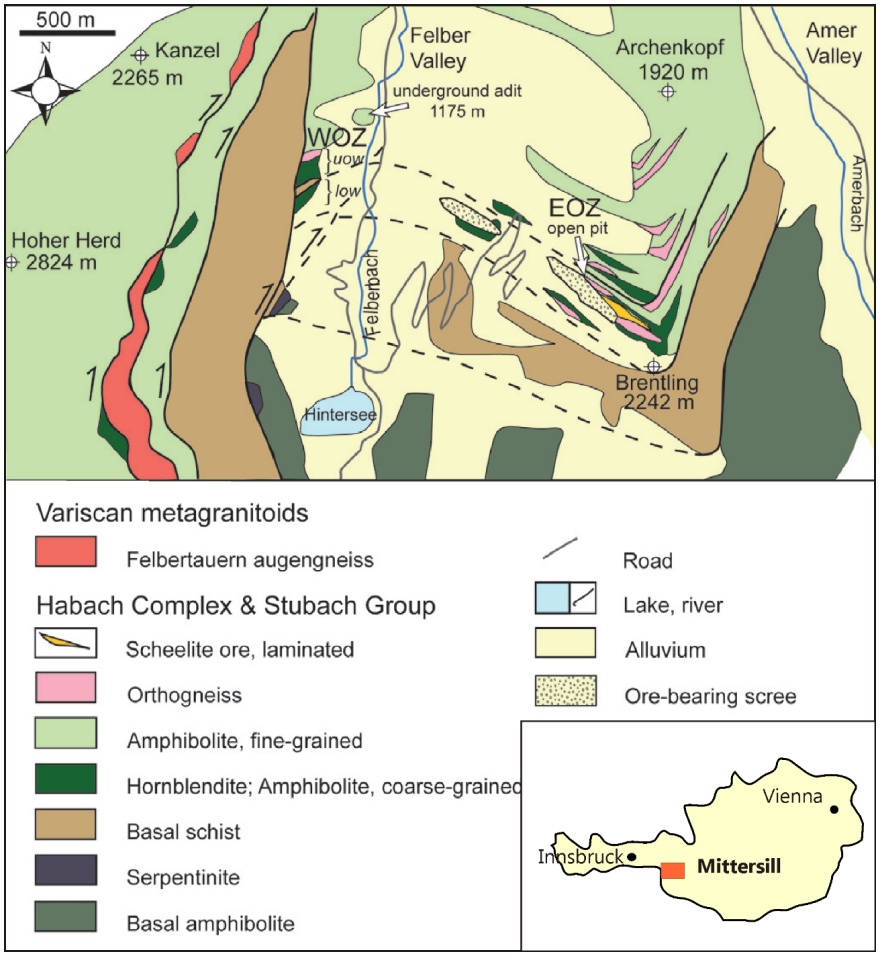

Figure 3.2. Geological map of the Mittersill deposit area (Höll and Eichhorn, 2000; Raith and Schmidt, 2010).

3.2. Approach procedure

The framework used to study the ore is shown in Figure 3.3, which illustrates the steps used for the sample preparation, and for the detailed mineralogical characterization of the samples received (ore characterization), mill product, shaking table product for each of the samples. The approach comprised the following steps:

- Sample preparation which included:
  - ✓ Crushing the ore types to 100% passing – 20 mm.
  - ✓ Sample homogenization.
  - ✓ Milling the sample – 600 µm.
  - ✓ Splitting the sample into charges of 7.5 kg of ore in sealed plastic bags to be stored until further processing.
- Detailed mineralogical characterization of the ore which can be divided into three sections: ore characterization, mill product characterization, pre-concentration properties and concentration properties was applied to the ore using a laboratory scale model shaking table separation (Wilfley - Holman), with a feed rate of 75 kg/h and a stoke rate of 280 RPM.
- Each product of the shaking table test (concentrates and tailings) was submitted for chemical analysis to evaluate the mineralogical performance (i.e. recovery and grade) of the ore.
- Mineralogical characterization using MLA and TIMA-X was performed on a size-by-size for the shaking table products resulting from the conditions which produced the best performance from each ore. This was carried out to investigate the influence of the degree of liberation of valuable minerals and how they are locked with other minerals in the ore.

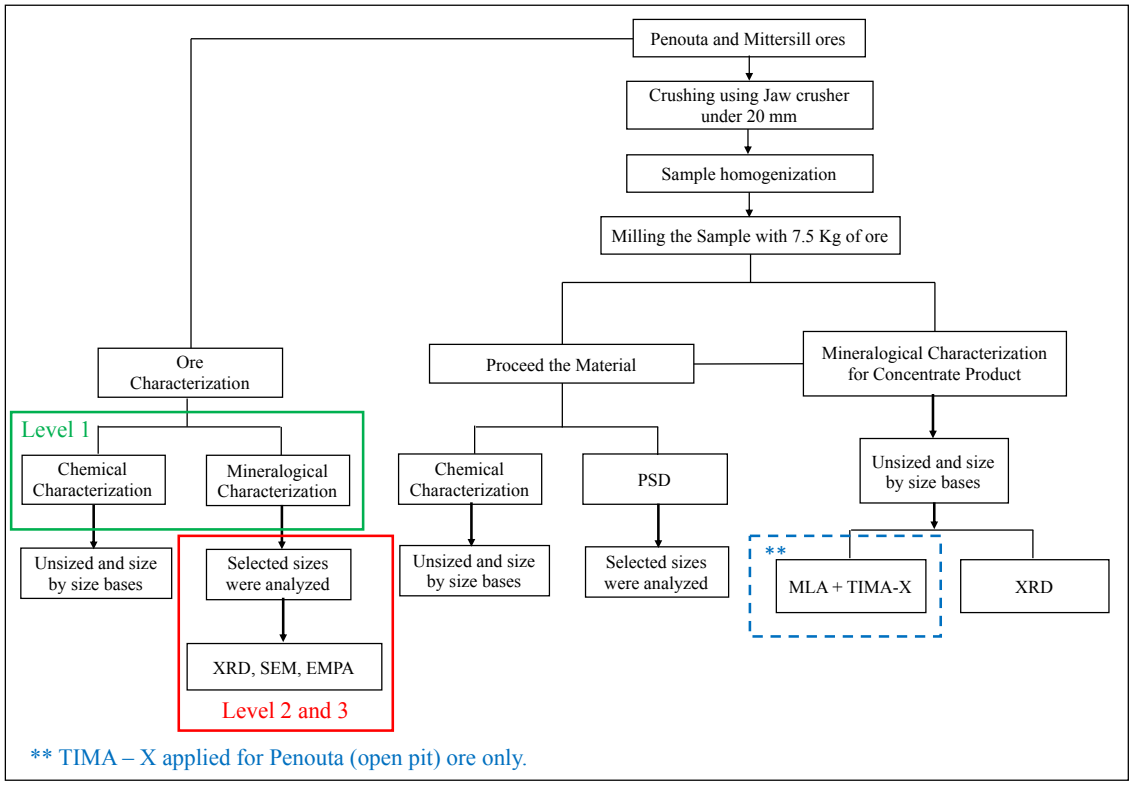

Figure 3.3. Approach procedures for all case studies (Penouta and Mittersill ores).

For practical measurement of liberation, a particle is considered liberated when more than 80% of its surface is liberated. Another concept that it is important to mentioning is the degree of liberation that is stated by mass or volume present as liberated divided by the mass or volume of the phase present in the population.

3.3 Sample preparation

Two types of samples were characterized:

a. Original sample obtained from the open pit or tailings of Penouta and material from the processing plant of Mittersill ore.
b. Samples processed by gravity concentration in order to facilitate the study of the liberation characteristics.

a. Original samples

The original sample from Penouta mining sites were obtained and the Mittersill material used in this study was scheelite consisting of the crushed ore of a processing plant of the Mittersill tungsten mine. It was obtained several samples to know the possible mineralogical variations in the deposit. The next step was doing the chemical and mineralogical characterization of these materials (determination of the grain size, whole rock chemical and mineralogical composition and distribution of tantalum and tungsten in the different minerals where it can be present. Grain size distribution were determined via sieving and laser. Mineralogy were established by x-ray powder diffraction, optical microscopy, scanning electron microscopy and electron microprobe.

b. processing of samples

The ores were crushing 100% passing – 20 mm by jaw crusher. Stage crushing minimizes the production of fines ahead of grinding. The samples, after the primary crushing by jaw crusher, using Jones riffle splitter and quartering method, fifty kilograms (50 kg) of the samples pour into a conical heap, flatten and divide into four identical parts using a metal cutter. Two opposite corners take as sample for further crushing by either HPGR, rod mill and ball mill; the other two corners of sample were put into charges of ores in sealed plastic bags to be stored until further processing. Ball mill tests were carried out in a mill with an internal diameter of 305 mm and 305 mm long, with conditions shown in Guasch et al. (2018).

HPGR test was conducted using a unit of 25 cm diameter rolls and 15 cm width that was fully equipped to control and record the hydraulic and nitrogen pressures and throughputs operating at a pressure of 40 bar. The portion chosen as the sample was further coned and quartered and this continued until a sample of the Penouta and Mittersill obtain for sieve, chemical

analyses, XRD and MLA.

For Penouta material (open pit), all samples undersize of 600 μm and thereafter feed into a conducted laboratory scale model shaking table separation (Wilfley - Holman), with a feed rate of 75 kg/hr and a Stoke rate of 280 RPM. The equipment starts and the sample process for about 60 minutes. The valve of water is open at a rate of 6 L/min. The sample top size (+600 μm) from HPGR was fed to the ball mill and comminuted for 10 min. in the same way as the first ball milling. Then all samples under 600 μm was feed through the hopper at a rate of 130 g/min of the table and the sample will gradual spread on the table. The screened samples under 600 μm were physically separated into two fractions (- 250 μm and - 600 + 250 μm) in order to obtain concentrate samples. The flow of water and the shaking transfer the feed material through the table. The high-density material in the feed separate from the feed at the top of the table and collect in the left side of the table. For maximum recovery, the tilt and angle of the table adjust according to the sample size. Figure 3.4 shows the schematic diagram of sample preparation, C1, C3, and C5 are - 250 µm and C2, C4, and C6 are - 600 + 250 µm (Hamid et al., 2018).

A composite sample from a pit test of a tailings called "Balsa Grande" was obtained. This tailing is a 6 Mt residue of leucogranite previously processed for Sn. Due the low Ta concentration in this tailing, a concentration was necessary in order to obtain a high number of particles to be studied and a about 15 kg of representative sample were obtained. First the sample was grinded, up to less than 1 mm. Then it was sieved and thereafter fed into a laboratory scale model shaking table separation (Wilfley - Holman), with a feed rate of 75 kg/h and a Stoke rate of 280 rpm. The screened sample under 212 µm were used through the separation in shaking table. First the sample between 212 µm and 106 µm and then the sample under 106 µm was treated in the shaking table (Figure 3.5).

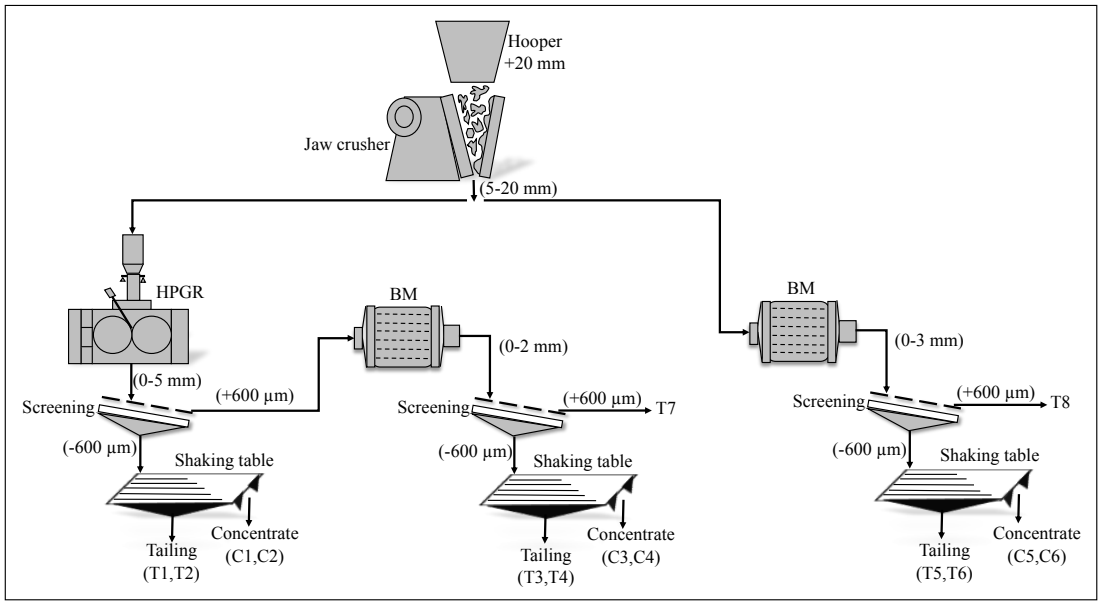

Figure 3.4. Schematic diagram of the Penouta open pit sample preparation. C, concentrate sample, T, tailing.

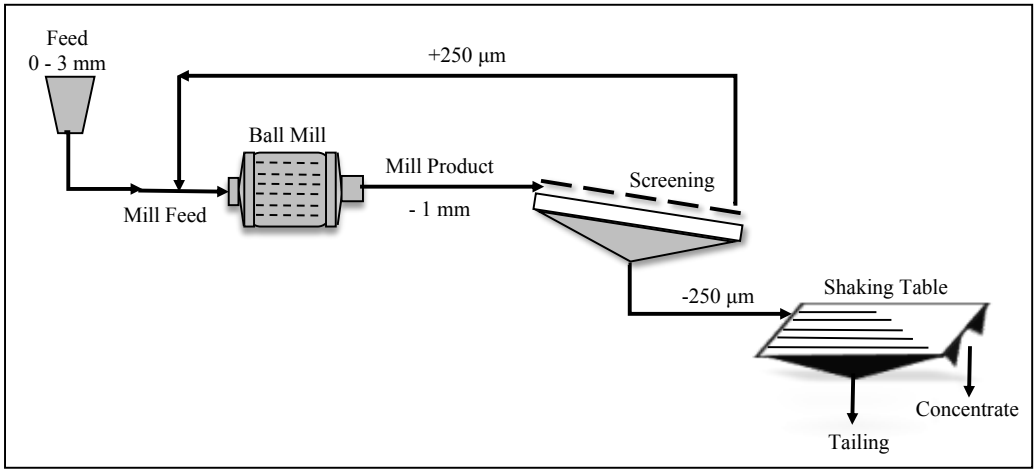

Figure 3.5. Schematic Diagram of Penouta tailings sample preparation.

In case of the Mittersill sample, the feed material, with size of 20 mm, was crushed in a jaw crusher to obtain a -1 mm size fraction for all the material. To complement the laboratory data, sample was filled into a grinding batch rod mill at 46 RPM and it should be noted that the laboratory test work, carried out under repeatable, controlled conditions forms the back-bone of this study. Most scheelite occurs in the fine fraction (Anticoi et al. 2018), then the ore was grinded up to a size lower than 250 µm. Then, scheelite was physically concentrated in a shaking table (Figure 3.6). To reach the liberation size, the sample and steel rods were loaded to the rod mill and dry grinding test was run and material was sieved at 250 µm and the non-passing fraction was ground into the rod mill, for different time intervals (4, 6 and 8 min). For each stage, milled material +250 µm size fraction were combined with the rest of the mill discharge as feed for the next grinding interval. The passing fractions (−250 µm) were all used in the shaking table feed (Hamid et al., 2019).

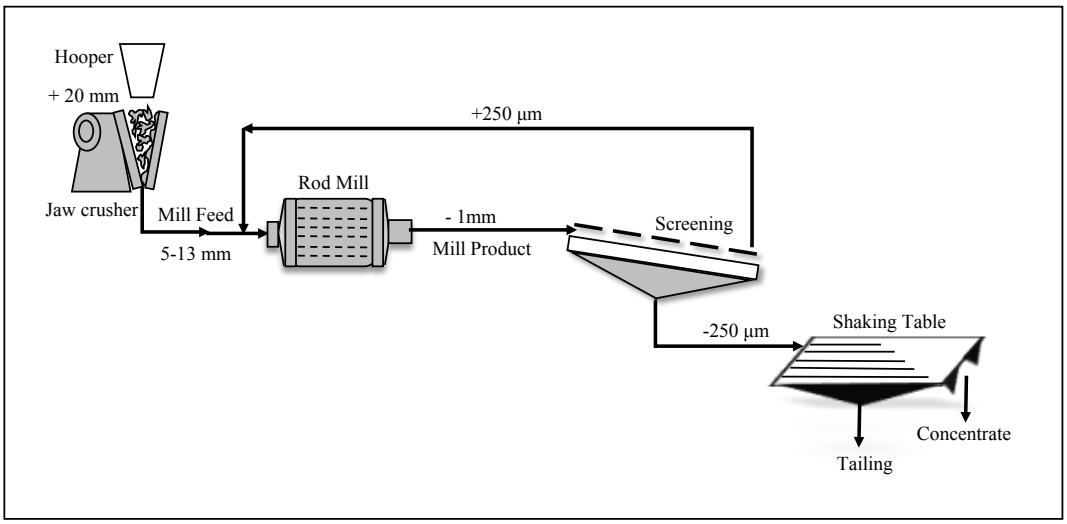

Figure 3.6. Schematic diagram of Mittersill preparation in the laboratory.

The sample preparation for ore characterization is described as follow:

- ✓ Three sub-sample (256 grs each sub-sample) of a 7.5 kg sample was sieved into 13 size intervals for each ore type, namely +2 mm, -2+1mm, -1mm+750 μm, -750+600 μm, -600+425 μm, -425+300 μm, -300+212 μm, -212+150 μm, -150+106 μm, -106+75 μm, -75+53 μm, -53+38 μm and -38 μm.
- ✓ A remaining unsized portion (256 grs) of the split sample was kept for further analysis.
- ✓ From size intervals, selected size fractions were submitted for a range of different analyses as described in the previous section.

3.4 Analytical methods

In this section, the experimental conditions of the analytical techniques used for ore, mill product and shaking table products characterization are described. In this section the term ore head made referenced to feed samples and mill product is the sample prior to feed to shaking table.

3.4.1 Chemical analysis

The chemical analysis was performed on unsized samples (feed samples, mill products and shaking table products) and on size-by-size samples (mill product and the shaking table products for each ore tested under optimum conditions). Table 3.1 shows the sizes fractions submitted to chemical analysis for each ore.

Table 3.1 Samples submitted to chemical analysis as unsized and size-by-size bases.

Ore	Unsized	Size by Size
Penouta open pit	Whole rock/ Shaking table product	Mill product, Concentrates and tailings: +600, - 600 + 250, - 250 µm
Penouta tailings	Whole rock/ Shaking table product	Mill product, Concentrates and tailings: +600, - 600 + 250, - 250 µm
Mittersill	Whole rock/ Shaking table product	Mill product, Concentrates and tailings: +1000, - 1000 + 250, - 250 µm

Inductively-coupled mass spectroscopy (ICP-MS) was used to measuring for minor elements from acid digestion of fused glass beads. Fusion was obtained using lithium or sodium borate.

The whole rock of Penouta sample and the Sn, Ta, Nb, U, and Th of all the grinding products were analyzed by X-ray fluorescence (XRF) using glass beads, followed by acid

digestion and Inductively Coupled Plasma Mass Spectrometry (ICP-MS) at ALS laboratories and Activation Laboratories (ACTLABS) Ontario, Canada.

Chemical composition of the original and processed Mittersill sample was obtained at the ALS laboratories where W was measured using ICP-MS from acid digestion of fused glass beads.

3.4.2 Mineralogical characterization

The objective was to identify the key mineralogical properties (modal mineralogy, particle size distribution, morphology and texture of particles and degree of liberation) necessary for developing an adequate concentration process for each ore. This characterization consisted of two stages, one called ore characterization and the second called comminuted products characterization, both characterizations were applied to the samples of the ores under study.

Petrographic characterization of the Penouta open pit leucogranite was obtained from 15 thin sections observed with the petrographic microscope coupled with transmitted and reflected light.

Mineralogical characterizations of the bulk sample were completed by powder X-ray diffraction (XRD), optical microscopy and scanning electron microscopy (SEM).

3.4.2 .1 X-ray diffraction (XRD)

The XRD spectra were measured from powdered samples in a Bragg-Brentano PANAnalytical X'Pert Diffractometer (graphite monochromator, automatic gap, Kα-radiation of Cu at $\lambda = 1.54061$ Å, powered at 45 kV–40 mA, scanning range 4 – 100° with a 0.017°2θ step scan and a 50 s measuring time. Identification and Rietveld semi-quantitative evaluation of phases were done using the PANanalytical X'Pert HighScore software.

These analyses were performed for Penouta and Mittersill samples in the Centres Cientifics i Tecnològics de la Universitat de Barcelona.

3.4.2.2 Scanning electron microscopy

A Scanning electron microscope (SEM) with Energy-dispersive spectral (EDS) for chemical microanalysis was used to mineralogical, textural and mineral chemistry characterization. SEM was used in the back-scattered electron mode (BSE).

A Hitachi TM-100 was used in the department d'Enginyeria Minera, Industrial I TIC from the UPC.

3.4.3 Electron microprobe analysis (EMPA)

EMPA was performed to obtain the chemistry of minerals by a JEOL JXA-8230 EMPA equipment located at the Centres Cientifics i Tecnològics de la Universitat de Barcelona. Analyes were carried out on Nb-Ta-rich minerals at 20 kV, an electron beam current of 20 nA, and a beam diameter of 2 μm. Each element was counted for 5 s, except Ti, Sc and Pb, which were counted for 10 s and F for 15 s. with the following elements measured by EMPA, Standards used were: Nb (NbLα), Ta (TaLα), Fe_2O_3 (FeKα), rhodonite (MnKα), rutile (TiKα), ThO_2 (ThMα), UO_2 (UMβ), Sn (SnLα),W(WLα), Sc (ScKα), albite (NaKα), apatite (FKα), and wollastonite (CaKα). The detection limits are 0.17 wt % U; 0.1% wt. Th andW; 0.06 wt % Ta, Sn and Nb; and <0.03 wt % for other elements.

The structural formulae were calculated on the basis of 24 oxygens and 12 cations per unit cell (apfu) for CGM. The number of cations was fixed by a method of charge balance by conversion of part of Fe^{2+} to Fe^{3+} as proposed by Ercit et al. (1992a). The structural formula of tapiolite and cassiterite were calculated on the basis of 6 and 4 oxygens, respectively. The structural formula of microlite was calculated on the basis of a fully occupied B site (Nb+Ta+W+Ti=2 apfu) and OH- was calculated by charge-balancing to the anion total of 7 (Černý et al., 2004). The wodginite formula was calculated according to the general formula ABC_2O_8 (Z =4); A = Mn^{2+}, Fe^{2+}, Li, □, B = Sn^{4+}, Ti, Fe^{3+}, Ta; C = Ta, Nb (Ercit et al. 1992a, b, c). When the C site had more than 2 apfu, the excess was corrected by extraction of Ta to B site. The Fe^{3+} was calculated up to B site (Ti+Sn^{4+}+Zr+Hf+Fe^{3+}) was fully occupied, with 1 apfu.

3.4.4. Automated quantitative mineralogy

3.4.4.1. Mineral Liberation Analyzer (MLA)

The samples that were analyzed by MLA was performed on a polished thick section of particles of ore and shaking table products at the University of Tasmania using a FEI MLA 650 ESEM to obtain textural and compositional information from a large number of particles. These polished blocks composed of mixing the particles with a two-part epoxy resin to make a block with a diameter of 30 mm. Figure 3.7 shows some blocks used for these analyses.

Figure 3.7. Polished thick sections used in this thesis.

The block sample is polished with an automatic polishing machine to provide a high-quality flat surface.

In this study, MLA modes were selected for analysis of ore. The ore characterization was measured with a GXMAP so that mapping of the high BSE phases could be undertaken to capture the complex textures observed in the ores. XBSE was used for the mill product tailings; and for the concentrate products, XBSE was used. The MLA was performed for Penouta open pit (Concentrate), Penouta tailings (bulk sample) and Mittersil (Concentrate and tailings).

Grain based x-ray mapping (GXMAP) combines the use of X-ray mapping and area X-ray analysis for phase identification. X-ray mapping analysis is used to resolve any overlaps in BSE. For this method, different grains of interest in the analysis can be selected through a BSE trigger (this targets grains within a set BSE threshold), as discussed by Fandrich et al. (2007); for these ores a high BSE trigger was selected so that bright phases in the particles underwent X-ray mapping.

Unsized Penouta tailing bulk sample were chosen to MLA analysis for this type of sample. These unsized fractions were made in order to preserve the texture in the ore and maximizing the number of particles to be measured.

In the case of the processed material, the material that was selected for the shaking table product characterization corresponds to the best concentration test obtained through the experimental design. The best test of each ore sample was made by triplicates to have the statistic of the samples and also the sufficient mass for performing the MLA and chemical analysis. The size fractions analyzed were: - 250 µm for Penouta tailing and Mittersill samples, - 250 µm and - 212 µm for Penouta open pit. XBSE mode looks for target minerals of interest, using a BSE threshold (i.e. using BSE gray-scale range), then using XBSE measurement for each particle that was identified. It is used for samples where the mineral of interest is present at low levels, typically between 0.01 to 1.0 %, being the typical application for Ta-Nb and W characterization, as well as valuable mineral liberation in tailings, and penalty elements in concentrates.

3.4.4.2 TESCAN Integrated Mineral Analyzer (TIMA-X)

Automated mineral liberation analysis was used to quantify the mineralogical characteristics of particles and grains. Samples from all the concentrates obtained from HPGR and BM were analyzed using a new generation of the Tescan Integrated Mineralogical Analyzer (TIMA-X). All samples were micro-riffled to produce a representative subsample to be mounted and polished for TIMA-X analysis. Samples were prepared with an addition of graphite flakes. Perpendicular cross-sections through the mounts were created once the epoxy was cured. The cross-sections were remounted in order to avoid the effect of heavy particle settling. It was carried out at the Tescan facilities in Brno, Czech Republic. Measurements were performed using an acceleration voltage of 25 kV and a current of 7.47 nA. Dot mapping analytical mode was used for the analysis. The image was segmented in two stages using this approach. The BSE imaging-

based segmentation with a resolution of 2 µm and preceded the actual collection of EDS spectra. The EDS analytical points (3000 counts) were placed in the middle of each segment smaller than the predefined distance of 10 µm. Segments larger than this value were covered with a regular mesh of analytical points 10 µm apart. Segment boundaries were adjusted based on the chemical information obtained by EDS in the next stage of segmentation (Hrtska et al., 2018).

The selected materials for the shaking table product characterization by TIMA-X were C1, C2, C3, C4, C5, and C6 of concentrates from the Penouta open pit.

3.5 Experimental methods

3.5.1 Ore characterization

The ore characterization was performed using mineralogy, chemical analysis; ICP-MS; X-ray diffraction; SEM-EDS; and MLA.

The objective of the mineralogical characterization was to identify the key mineralogical properties (modal mineralogy, particle size distribution, morphology and texture of particles and degree of liberation) necessary for developing an adequate concentration process for each ore. This characterization consisted of two stages, one called ore characterization and the second called comminuted products characterization, both characterizations were applied to the samples of the ores under study.

Level 1 was the minimum Level of characterization used to identify key mineralogical properties and was performed on each ore. When this Level of characterization was insufficient to identify Ta and W bearing, which is one of the key specific needed for the mineralogical characterization, additional measurements were required. These measurements were divided into Level 1 and 2. A comprehensive description of what comprised each of the Level is provided in the following sections.

The Level 1 is consisted of a combination of complementary techniques that are commonly used in ore characterization. This Level included: chemical analysis; XRD; SEM-EDS; and mineral liberation analysis. This protocol was used for the ore characterization in this work because each of these analytical techniques complemented the others. A summary of the techniques used is presented in Table 3.2. This step of characterization was found to be sufficient to describe the mineralogical properties for the Mittersill ore.

To complete the mineralogical characterization, level 2 was performed which included all of the analytical techniques described in previous Level and also incorporated the use of base methodology to analyze mineral grains. This Level was applied to both Penouta and Mittersill ores and was found to be sufficient to adequately characterize the mineralogical properties for the Penouta ore (open pit) and Penouta tailings.

The Level 3 in ore mineralogical characterization was included after Level 1, 2 and

incorporated a highly intensive search for Ta and W bearing minerals. This Level was used as the last resort for the ore characterization, due to the time consuming of this technique and has higher associated cost due to the equipment needed for it. This resulted in the development of a new protocol for identifying previously unknown vision for Ta and W minerals which could then be enable to reclassification of measured data and recalculation of the Ta and W behavior.

Table 3.2 presents the summary of the mineralogical characterization by steps used for the ores under study and the sizes that were analyzed.

Table 3.2. Summary of the mineralogical characterization by steps used for three samples.

Methodology	Technique	Size Evaluated
Level 1	Chemical Analysis	Unsized and size by size
	XRD	Unsized and size by size
	SEM-EDS	-600 µm
	MLA	-600 µm
Level 2	Same techniques used in Level 1 and ICP-MS, Base methodology	-250 µm
Level 3	Same techniques used in Level 2 and other methodology for identifying the unknown tantalum and tungsten minerals	-1000 + 250 µm

3.5.2 Mill product characterization

The purpose of the mill product (shaking feed) characterization was to quantify the level of liberation of the key minerals that were the recovery targets in the concentration process.

- ✓ 7.5 kg of each Penouta ore (open pit) and Penouta tailings was ground for 10 minutes in a laboratory ball mill and 7.5 kg of Mittersill ore was ground for 4, 6 and 8 minutes in a laboratory rod mill to develop the grinding calibration curve, with the aim of estimating the time required to achieve a P80 of 600 µm.
- ✓ To validate the calculated grinding time, a sample of the ore was ground for the estimated time and the product sized to confirm that the target had been reached.

The mill product for each ore was then sieved into two size fractions (-600+250 µm, -250 µm, were obtained by sieving). A sub-sample of each size fraction was analyzed by MLA and TIMA-X.

3.5.3 Characterization of concentration products

Concentrates and tailings were analyzed on a size-by-size basis using chemical analysis,

XRD and liberation data (MLA and TIMA-X). This was done to obtain the key mineralogical parameters (recovery, grade, and liberation) and to identify and understand the behavior of the valuable minerals in each stream obtained by the concentration process. Figure 3.8 illustrates the path used for this characterization.

The liberation data measured using MLA and TIMA-X on particle less than 600 µm basis. Overall stream liberation was calculated based on the distribution of the mineral across each size fraction and the liberation within those size fractions. As described in previous chapter, In the context of concentration, particles that contain more than 80% of the valuable mineral by weight are considered concentrated and for this reason the 'liberated' class includes all particles that contain greater than 80% by weight of the mineral of interest.

3.5.3.1 Quantifying Ta and W bearing

As described in the literature review, the identification and concentration of tantalum and tungsten carriers is complex. The inability to adequately describe tantalum and tungsten deportment for the ores, i.e. differences between the calculated analysis from XRD, MLA and TIMA-X measurement and the chemical analysis for tantalum and tungsten; was the main driver for performance the Level 2 and Level 3 characterization protocols. The objective of Level 2 characterization was to identify the presence of tantalum and tungsten in the sample, while the objective of Level 3 characterization was to identify the remaining hosts for tantalum and tungsten that were still not able to be accounted for, by Level 1 and 2.

In this study, MLA was able to identify Ta and W-bearing minerals in these ores which are present on the mineral reference library. The approach for identification of unknown Ta - W minerals from complex Penouta low-grade and Mittersill ores, was a combination of manual and auto SEM, EMPA, XRD and XRF analysis, which were used with the primary objective of identifying tantalum and tungsten - bearing minerals that had previously been classified as "unknown". The first step in the analysis was to perform elemental mapping using EMPA, to detect any associations between tantalum, tungsten and other key elements, such as Nb, Sn, epidote and others. The objective here was to find any relationship between tantalum, tungsten and other elements to assist in the identification of potential minerals hosts for the unaccounted for tantalum and tungsten. The second step in the analysis was to search for particles containing grains with high BSE intensity. Grains that contain Ta and W are brighter than the grains that contain gangue minerals, which usually have a low BSE value. These bright grains were identified qualitatively using EDS, which was applied in the center of the grain to search for the spectra that contained tantalum and tungsten.

For Penouta ore, CGM (Columbite Group Mineral) usually occur as grains of less than 250 µm with variable composition, consisting of tantalite and columbite distributed in the same

grain following different patterns. The most common textural pattern is presented as grains with a Nb-rich core and a Ta-rich rim.

The third step was to confirm statistically the presence of new tantalum and tungsten minerals, using an auto SEM-EDS.

Finally, using X-ray fluorescence (XRF) and X-ray diffraction (XRD) was used to investigate the presence of any other tantalum and tungsten minerals that had not been identified through the previous techniques mentioned.

The process is complete when the tantalum analysis modulation (MLA, TIMA-X, XRD and chemical analysis) is adequate, after including tantalum and tungsten in the modulation, were identified as part of Level 3 analysis.

3.5.4 Physical separation of the ores

For each ore, a different flow sheet configuration was used, based on the information obtained from the mineralogical characterization. In some cases, some of the strategies for concentrate tantalum and tungsten minerals that were discussed in the literature review were adopted; in all cases the flow sheet was optimized to achieve a Ta and W recovery over 80 % and mill product (shaking table feed) size target beginning with a (P80) of 600 µm. The screened samples under 600 µm was transferred from the laboratory batch ball and rod mill to the laboratory scale shaking table (Figure 3.8). At this point, selective or concentrate was undertaken, depending on the tantalum and tungsten bearing in the ore.

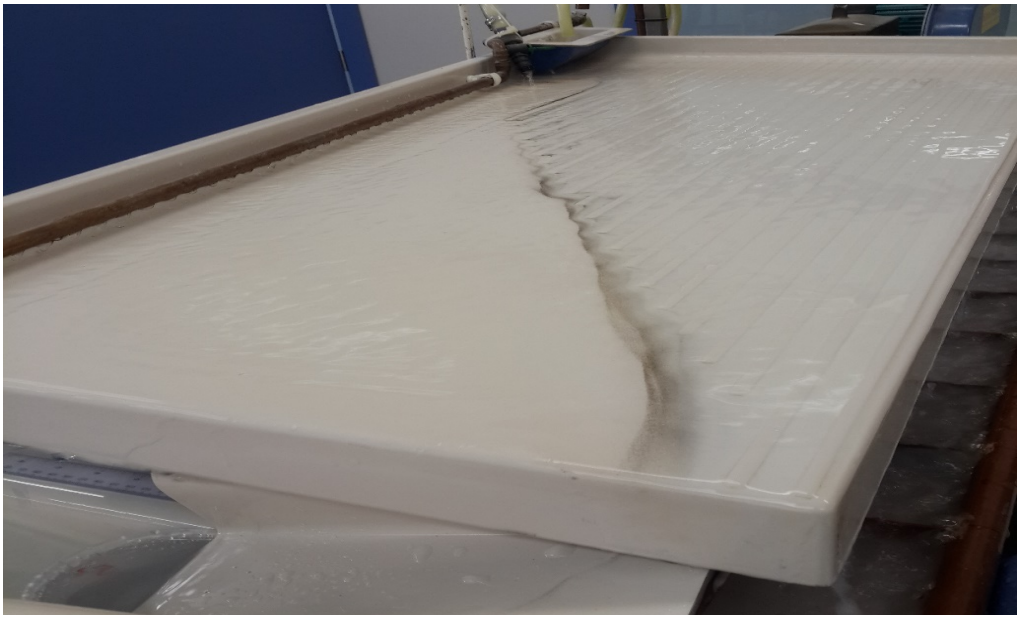

Figure 3.8. Wilfley – Holman shaking table used for the experiments with the Penouta materials.

3.5.4.1 General Batch concentration procedure

The general batch concentration procedure is described in the following lines:

- ✓ The ore was ground at the required P80 using the ball and rod mill at 130 g/min with the required grinding time. After the ore was ground, grinding rate were measured and recorded.
- ✓ The milled sample was then transferred to a shaking table (Wilfley – Holman), bottom-driven batch shaking table, and fresh water was used to wash the solid sample through the shaking table. The flow rate of liquid and sample were measured and recorded.
- ✓ The feed flow rate was adjusted to the required target for concentration using the hooper. When the feed flow rate was adjusted, with a feed rate of 75 kg/hr and a stoke rate of 280 RPM, the ores where obtained from the sieves were concentrated by shaking table.
- ✓ The required screened samples for the ores were introduced into the shaking table according to the feed flow rate required for each test, with a 5-minute interval between them to allow time for collecting the concentrate and tailing material.
- ✓ The total number of concentrates and tailings varied according to the ores, depending on the grade and the strategy used to concentrate the ores. Concentrates and tailings material were typically collected after each test with shaking table.
- ✓ Each concentrates product, and all concentrates and tailings were collected and dried.

3.5.4.2 Concentration strategies

a) Pre-concentration

Pre-concentration tests were performed to determine the characteristics of the valuable minerals, angle of the table and feed flow rate in the ores. The procedures described in this section were used in each test.

- ✓ 1 kg aliquots of the ore were ground in a laboratory ball and rod mill for about10 minutes.
- ✓ The screened sample was introduced to the shaking table and fresh water was introduced.
- ✓ The concentrates were collected after 2, 4, 6 and 8 minutes. Only the concentrate products of the ore through MLA and TIMA-X and the tailing products through XRD were analyzed due to the nature of the tantalum and tungsten grades.

b) Changing grind size

Finer P80s were tested for the ores; a P80 of 600 µm and 250 µm was examined. These extra analyses were made due to the results received from the mineralogical characterization, indicating that the grain sizes of some of the minerals of interest in the ore were finer and required finer grinding to obtain the necessary degree of liberation. Figures 3.9, 3.10 and 3.11 shows the

particle size distribution (PSD) for the Penouta ore (open pit), Penouta tailings and Mittersill ores. The P80 of different steps from milling products feed to the shaking table, for the ore was measured using dry sieving.

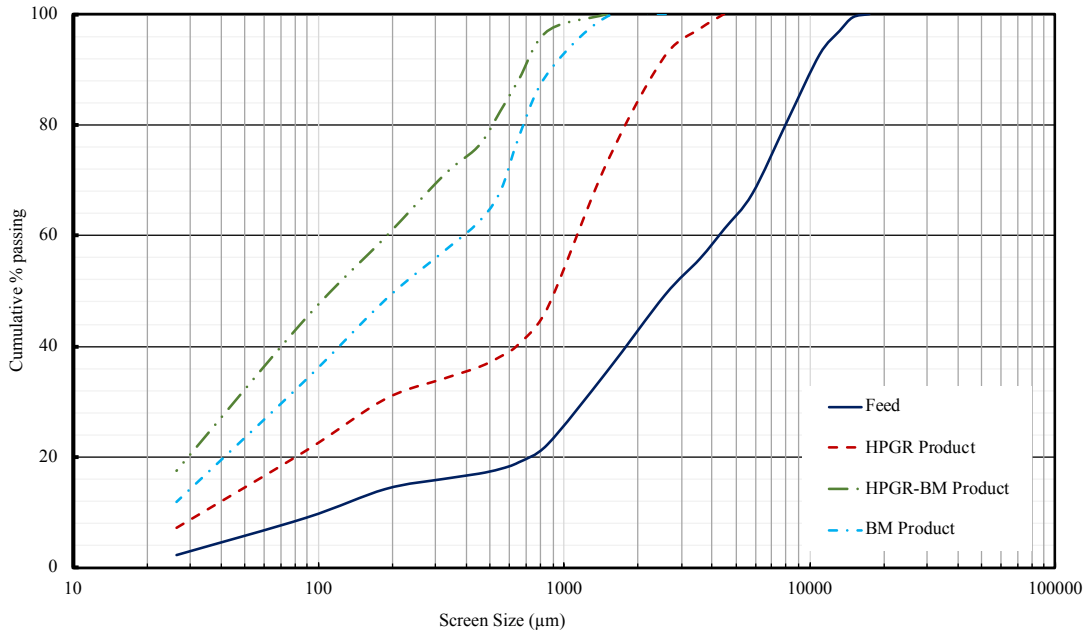

Figure 3.9. Particle size distribution for the Penouta ore (open pit) using dry sieving instrument with 95% confidence.

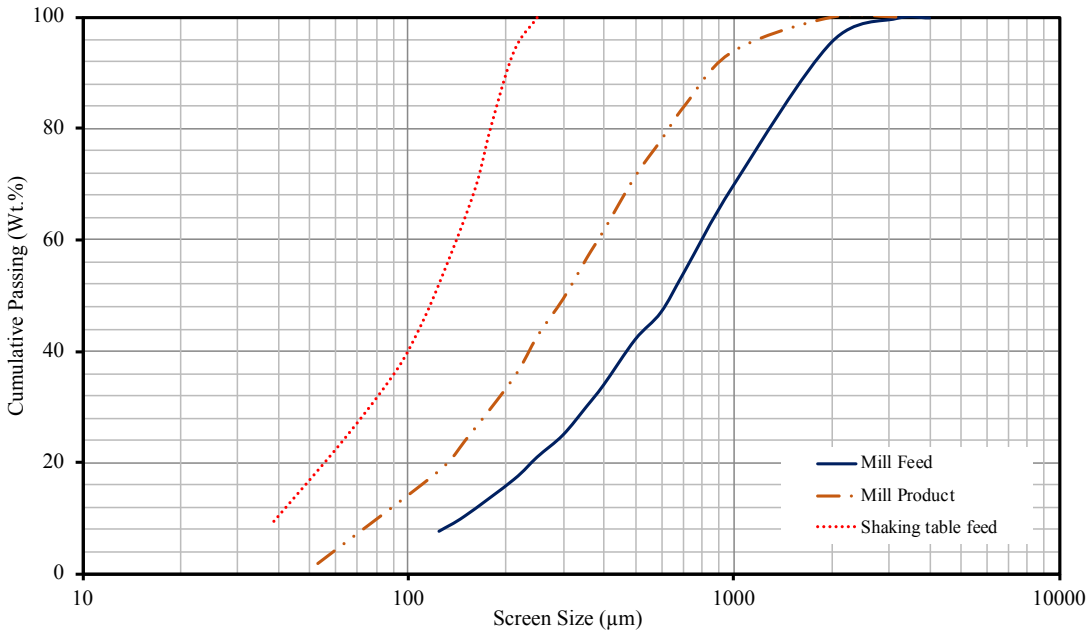

Figure 3.10. Particle size distribution for the Penouta tailings using dry sieving instrument with 95% confidence.

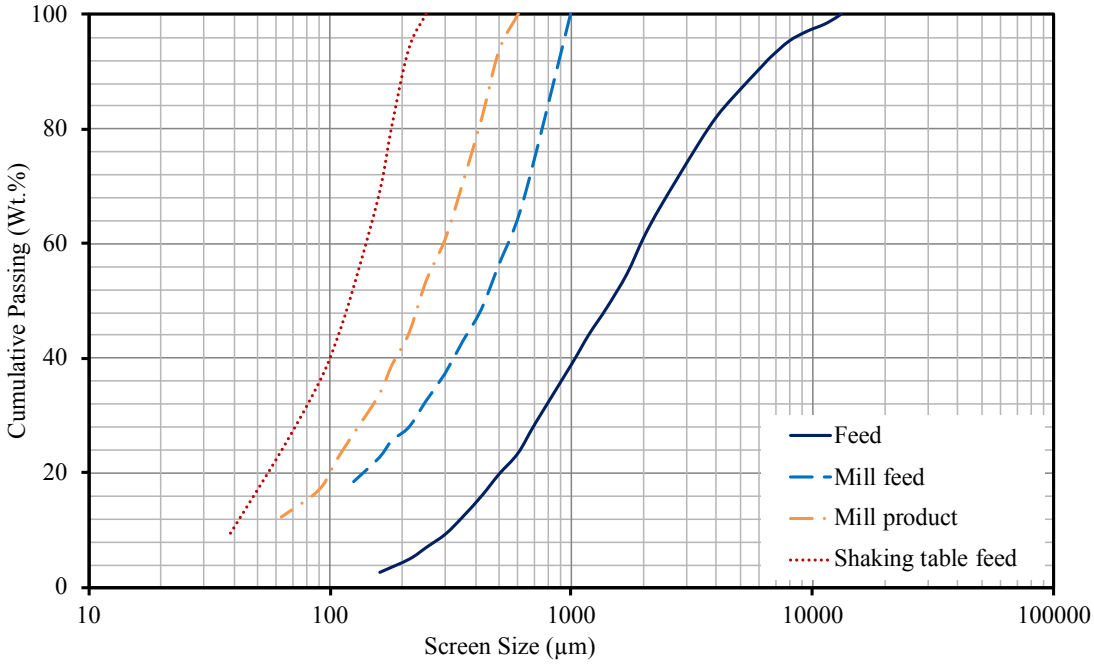

Figure 3.11. Particle size distribution for the Mittersill ore using dry sieving instrument with 95% confidence.

3.5.4.3 Experimental design

To improve the concentration results with the Penouta and Mittersill ores, a factorial design was proposed and used, aiming to improve understanding of the key concentration parameters that affect the concentration response of the ores. For this study, the 80 percent passing size of the shaking table feed and the collected sample (concentrate and tailings) were tested. The results are described in the Chapters 4 and 5 for Penouta ore. In the cases of the shaking table, the method of changing of the flow rate of liquid and sample, angle and tilt "one factor at a time" was used to find the best conditions for obtaining optimal recoveries and grades for the ores. This approach helped to find the best flow sheet configuration which contained the procedure for preparing the shaking table and using the feed flow rate and the proper angles to allow the concentrate of this ore. When the best flow sheet was achieved for the ores replicate tests were performed to obtain an estimate of the experimental error.

3.6 Concentration analysis

3.6.1 Batch shaking table test

There are a number of parameters that can be calculated and used to assess the outcomes of a batch shaking table test. These calculations are used to understand the concentration response of key minerals and to provide explanations as to their appearance in either the concentrate or

tailings streams. These calculations can be performed on an unsized or size-by-size basis, using mass balanced data (Ozcan, 2019).

In each test, the overall mineral (concentrate and tailings) and water recoveries were calculated as well as the rate constants for each test, and the entrainment value based on the following equations.

- The final recovery (R) is defined as the recovery of the valuable mineral in the concentrate out of the total mineral present in the feed (eq. 3-1)

$$R = \frac{C \times c \times 100}{F \times f} \qquad (3\text{-}1)$$

Where;

R: Final recovery [%],

C: Total amount of concentrate [g],

c: Valuable grade in concentrate [%],

F: Total amount of feed [g],

f: Valuable grade in feed [%].

- The water recovery (R_W) is calculated as (eq 3-2)

$$R_W = \frac{W_c}{W_f} \times 100 \qquad (3\text{-}2)$$

where;

R_W: Water recovery [%],

W_c: Water mass flow present in the concentrate [g],

W_f: Water mass flow present in the feed [g],

3.6.2 Size-by-size and Size-by-liberation analysis

Size-by-size and size-by-liberation analyses were performed for each of the concentrate products. Calculation of mineral recovery-by-size was performed using the equation (3-3)

$$R_{i,j} = \frac{C_{i,j}}{F_{i,j}} \qquad (3\text{-}3)$$

Where $C_{i,j}$ and $F_{i,j}$ are the flow of particle size "i" and mineral liberation class "j" in the concentrate and feed respectively.

The liberation classes used in this thesis work are based on particle composition and are divided into the following classes: liberated (containing more than 80% of the mineral of interest), binary composites (containing the mineral of interest and one other mineral) and ternary composites (containing the mineral of interest and at least two other minerals).

3.7 Errors from measurements and calculations

There are many sources of error when concentration experiments are carried out. Examples of these sources of errors are sampling, feed preparation, assaying, by operator, machine and others. It is important to understand the contribution of these errors to uncertainties in the experimental results which will impact on the interpretations made from the data.

3.7.1 Propagation of error analysis of recovery distribution

A propagation of error analysis was performed with respect to overall recovery values (Ozcan, 2019). The analysis is acquired from the recovery expression given by Equation 3.1.

The expression for the specific error of the flotation recovery can be estimated using Equation 3.4 (Riquelme, 2014).

$$Error_R = \frac{\partial_R}{\partial_C} * SD_C^2 + \frac{\partial_R}{\partial_c} * SD_c^2 + \frac{\partial_R}{\partial_{CF}} * SD_F^2 + \frac{\partial_R}{\partial_f} * SD_f^2 \qquad (3\text{-}4)$$

The standard deviation (SD) was assumed as 5%, and R is recovery. The partial derivatives can be directly computed as shown in eq. 3-5 to 3-8:

$$\frac{\partial_R}{\partial_C} = \frac{C}{Ff} \qquad (3\text{-}5)$$

$$\frac{\partial_R}{\partial_c} = \frac{c}{Ff} \qquad (3\text{-}6)$$

$$\frac{\partial_R}{\partial_{CF}} = \frac{F}{F^2 f} \qquad (3\text{-}7)$$

$$\frac{\partial_R}{\partial_f} = \frac{f}{Ff^2} \qquad (3\text{-}8)$$

3.7.2 Confidence limits

Confidence limits at 95% confidence were used for estimating the confidence in the mineralogical parameters. It was calculated as the Equation 3-9 (Riquelme, 2014):

$$confidence\ limits = \mu \pm \frac{\partial}{\sqrt{n}} * 1.96 \qquad (3\text{-}9)$$

Where;

μ: average

∂: standard deviation

n: number of observations or analysis

3.7.3 Stereological Correction

Stereological correction of the distribution of linear grades is a very important problem when dealing with both the measurement and prediction of mineral liberation. It is comparatively easy to measure the distribution of linear grades in a sample of mineralogical material in particulate form. In fact, it was measurements made by Jones (1977) that provided much of the impetus for research in mineral liberation that has been undertaken during the past 20 years.

By contrast, measurement of the distribution of volumetric particle composition directly by particle fractionation is usually difficult and often impossible. However, the measurement of liberation is not the only application for making the stereological correction. In 1979 King showed that it is possible to predict the linear grade distribution that will be obtained when a binary ore is comminuted, and the application of the stereological correction extends the prediction to the full distribution of particle volume grade (Schneider, 1995).

The stereological correction is required because a linear probe through multiphase particulate material will report a significantly larger fraction of liberated intercepts than there are liberated particles. The entire linear distribution is considerably more dispersed than the volumetric distribution of grades that generates the linear distribution.

The stereological correction procedure has been known, at least in principle, for particle populations of a single size (King, 1982).

Optimization of mineral processing operations requires knowledge of the spatial distribution of valuable minerals in the multiphase ore particles. Accurate mineral liberation analysis enables us to avoid overgrinding, which reduces the cost and energy required in the comminution process. In addition, accurate mineral liberation analysis also gives assessment of mineral processing products and helps to suggest action to improve the separation efficiency (Wang et. al., 2018).

In general, the liberation distribution, also known as volume grade distribution and liberation spectrum, is obtained by 2D examining resin mounted, sectioned, and polished particle sections. These two-dimensional (2D) observations are conducted using a traditional microscope (Wills, 2006) or scanning electron microscopy/energy dispersive X-ray spectroscopy (SEM/EDX) based automatic analyzer such as mineral liberation analyzer (Sandmann, 2015). This 2D approach inevitably result in stereological bias in the liberation distribution, because a liberated particle always appears like a liberated section, whereas a multi-phased particle may appear as liberated section (Gaudin, 1939).

Some approaches have been proposed to avoid this error and directly obtain three-dimensional (3D) liberation information by X-ray computed tomography (Videla et al., 2007) and serial particle sectioning (Schneider et al., 1991). These approaches have proven successful at a research stage but have not been applied because of inadequate analysis speed, cost, and accuracy

of mineral identification. Therefore, stereological correction, in which the 3D liberation distribution is estimated from 2D data obtainable by sectional analysis, has attracted extensive interest (Ueda et al., 2017).

Latti and Adair (2001) have investigated the significance of stereological bias in a multiphase, natural ore and ascertains whether computer generated theoretical particles accurately represent natural textures.

Herbst et. al. (1988) and King and Schneider (1998) proposed a correction method converting 11 or 12 classes of 2D liberation distribution into their 3D counterparts using a kernel function. This method requires a separation test with a high degree of accuracy to determine the kernel function. Given that the kernel function may be influenced by the particle's texture and being unrealistic to determine the kernel for each mineral sample, a systematic study on the influence of the particle texture on the kernel function is required (Ueda et al., 2017).

Chapter IV

Results

Chapter IV
Results

Chapter 4 describes the results of the mineralogical, concentration product characterization and mineral liberation modelling of Penouta ore (open pit) and Penouta tailings and Mittersill ores. The ore characterization identified the presence of Ta and W - bearing minerals including coarse grained of quartz in Penouta ore and hornblende and pyrite in Mittersill ore. Mineralogical analysis of preconcentration test samples indicated that columbite-group minerals (CGM) are the most abundant Nb-Ta rich phases in the Penouta leucogranite. Scheelite is the only W-bearing mineral from the Mittersill ore. Other phyllosilicate minerals as muscovite and chlorite occur in minor amounts. These results together with the mineralogical characterization indicated that selective physical separation would be an appropriate processing route for these ores. An experimental design was used to optimize some of the shaking table conditions. The concentration products were studied on an overall and size-by-size basis, with the final flowsheet producing a rougher concentrate that Penouta ore contained 103 ppm of Ta, at a recovery of 52 wt. %for columbite-group minerals (CGM) and in the Mittersill ore, W content is 2260 ppm at a recovery of 87 wt. %.

4.1 Penouta deposit

In the following section, the results of the ore and mill product characterizations are discussed, with emphasis on understanding the liberation of the valuable minerals that needed to be recovered through concentration and mineral liberation modelling of the ore. As explained in Chapter 3, mineralogical characterization was used for this ore.

4.1.1 Chemical composition of the Penouta deposit

The Penouta leucogranite from the open pit area shows a range from 81 to 140 ppm Ta and 50 to 64 ppm of Nb (Alfonso et al., 2018). The sample used in this study has between 103 ppm of Ta, 81 ppm of Nb, 383 ppm of Sn and 35 ppm of W. Radioactive elements are present in small amounts, 2.40 ppm of Th and 2.48 ppm of U (Table 4.1).

Table 4.1. Chemical composition of samples from the leucogranite of Penouta.

Oxides (Wt%)	Pen-13	Pen-14	Pen-15	Pen-Tot
SiO_2	69.10	70.38	73.38	74.90
Al_2O_3	17.67	17.95	15.70	15.30
FeO	0.46	0.48	0.54	0.67
MnO	0.03	0.03	0.05	0.05
CaO	0.10	0.11	0.13	0.15
MgO	0.03	0.03	0.02	0.04
K_2O	3.38	4.23	4.79	0.03
Na_2O	-	5.59	-	5.14
P_2O_5	0.03	0.02	0.03	0.03
Total	90.80	93.23	94.63	99.46
Traces (ppm)				
Nb	53.9	63.8	51.1	81
Ta	81.3	140	92.6	103
Sn	131	569	373	569
W	104	105	2.4	35
U	1.4	1.6	1.4	2.5
Th	2.8	3.3	2.2	2.4
Pb	6.8	7.8	6.4	-
Li	120	129	133	130
Rb	901	1070	1350	966
Cs	32.8	43.4	64.2	64
Ba	40	87	16	16
Be	150	125	158	-

4.1.2 Mineralogical characterization of the Penouta deposit

4.1.2.1. Petrography

Textural characteristics of tantalum ores from granitic rocks usually are important for the processing planning. The texture of the rock and the characteristic texture of the columbite-group minerals (columbite-tantalite) will define the behavior of this material during comminution.

The Penouta leucogranite is a homogeneous microgranular rock of creamy nearly white color in which a white mass and mm-sized grey quartz grains are differentiated. The rock is relatively soft and easily o crush with the hammer. Under the microscope the rock has an inequigranular snowball texture with large grains of quartz, about 1 mm in size, included in a matrix of other grains of less than 0.5 mm constituted by quartz, K-feldspar (microcline), albite and muscovite. Occasionally, K-feldspar and muscovite also occurs in relatively large crystals. Locally, kaolinite can be present in major amounts. Minor contents of garnet (spessartine), tourmaline, zircon, monazite, beryl, cassiterite, and Nb-Ta oxide minerals were also observed. Under the petrographic microscope Ta-rich minerals appear as crystals, usually smaller than 300 μm in liberated particles or associated mainly with quartz and muscovite (Figure 4.1).

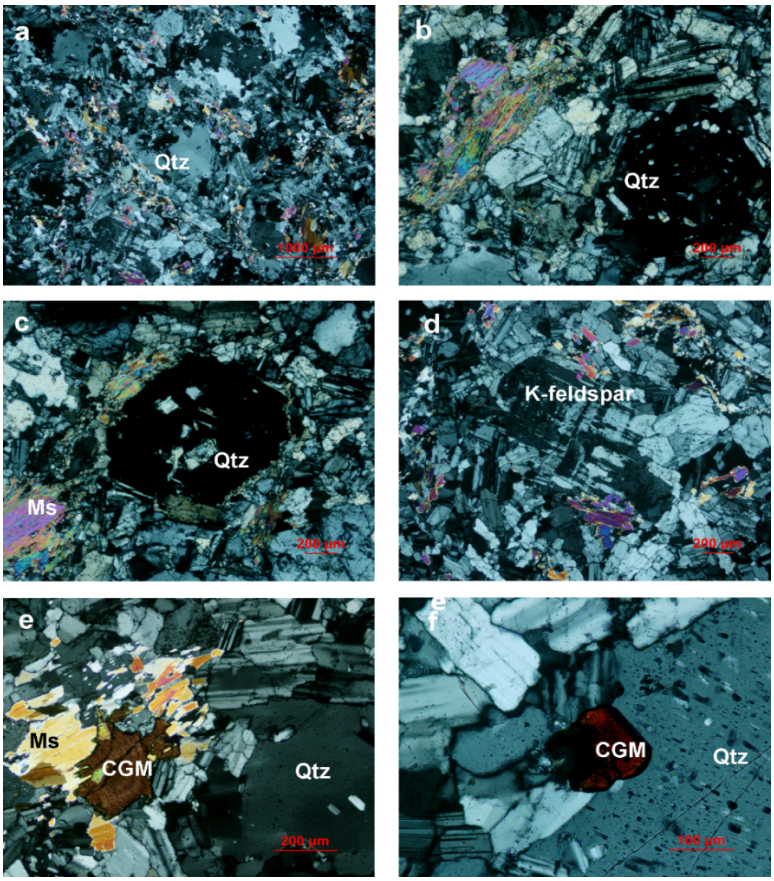

Figure 4.1. Petrographic images of the rare metal leucogranite from the Penouta deposit where columbite-group minerals (CGM) are associated with quartz (Qtz), muscovite (Ms) and albite. a) general view; b, c) snowball texture, d) megacrystal of k-feldspar within a quartz, albite and muscovite matrix; e) CGM associated with muscovite; f) CGM associated with quartz.

4.1.2.2 Tantalum-bearing oxide minerals

A detailed characterization of Nb-Ta oxide minerals from Penouta is presented in (López Moro et al., 2017; Llorens González et al., 2017; and Alfonso et al., 2018). Nb and Ta occur mainly in minerals of the CGM. This group is constituted by a solid solution of columbite and tantalite, with a general formula of $(Fe,Mn)(Nb,Ta)_2O_6$ and four end members: columbite-(Fe), $FeNb_2O_6$; columbite-(Mn), $MnNb_2O_6$; tantalite-(Fe), $FeTa_2O_6$ and tantalite-(Mn), $MnTa_2O_6$.

CGM occur as platy crystals usually lower than 200 μm, with an average size of 80μm. Crystals usually constitute isolated grains but are occasionally associated with quartz, muscovite, plagioclase, cassiterite, zircon and other Nb-Ta rich minerals as wodginite and microlite. These minerals usually exhibit a zoned texture with Nb-rich cores and Ta-rich rims (Figure 4.2).

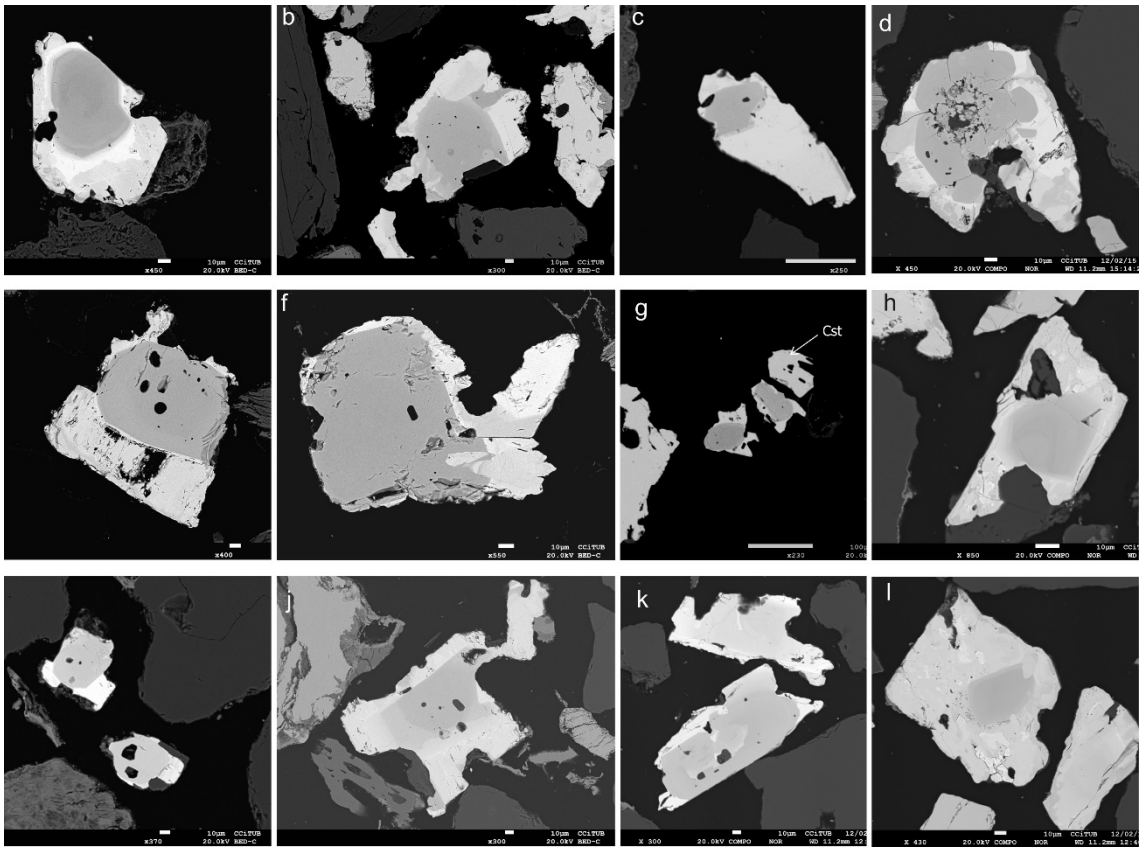

Figure 4.2. Columbite group minerals from the Penouta open pit leucogranite showing the most common texture, with, concentric zoning; (e-f), patchy zoning. Dark grey, columbite-(Mn); bright grey. tantalite-(Mn).

Occasionally this zonation is progressive, but in other cases there is a sharp boundary between them, so that the Ta rich phase could be considered as an overgrowth. Moreover, these rims are partially dissolved (Figure 4.3). Oscillatory zoning also occurs, with multiple bright Ta-rich, and dark Nb-rich bands. Reverse zoning, where the core is Ta-rich and rims are Nb-rich (Lathi, 1987) is quite abundant. This zoning is relatively common in Nb-Ta group minerals

(Belkasmi et al., 2000; Neiva et al., 2008; Abdalla et al., 2009; Anderson et al., 2013). Irregular patchy zoning is also present, as is usual in CGM from pegmatitic occurrences (Alfonso et al., 1995; Tindle and Breaks 2000; Uher et al., 2007). In other cases, these minerals exhibit convoluted zoning or are homogeneous. Zoning often shows a complex combination of different types, such as oscillatory and patchy. Patchy zonation is interpreted as evidence for replacement involving partial resorption of an early columbite and the generation of a more Ta-rich composition usually along the margins of crystals (Abdalla et al., 1998).

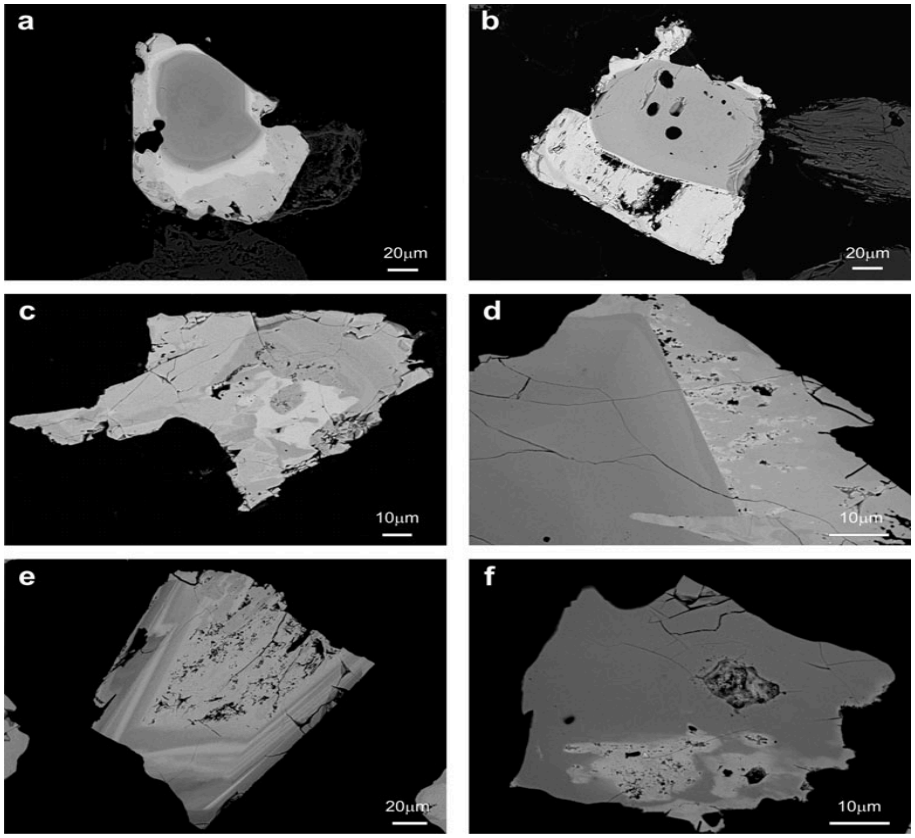

Figure 4.3. Back-scattered SEM images of CGM from the Penouta leucogranite: (a) typical zoned crystal with a Nb rich core (dark) and a Ta-rich rim (bright); (b) columbite crystal with an overgrowth of tantalite; (c) columbite-tantalite with patchy zoning (d) Columbite with a rim of tantalite; (e) reverse oscillatory zoning, with a dissolution texture in the innermost Ta-rich phase; (f) columbite with a Ta replacement.

Many of the CGM exhibit corrosion or dissolution with sponge-like textures that affect to columbite and especially to the tantalite rims. This corrosion destroys columbite that is replaced by tantalite. Similar dissolution textures are evidenced in other Nb-Ta minerals from pegmatites (eg. Wise and Brown, 2010; Dill et al., 2015).

Chemical composition of 490 points of CGM from approximately 130 crystals was determined (Table 4.2). Atomic compositions and ratios were calculated and plotted on the columbite quadrilateral, where most compositions are tantalite-(Mn) and columbite-(Mn) (Figure 4.4). The Mn/(Mn+Fe) ratio varies between 0.33 and 0.97 and the Ta/(Ta+Nb) ratio between 0.07

and 0.93. These values are typical of highly evolved magmatic systems. Two clusters can be observed, both at Mn/(Mn+Fe) = 0.8, one at Ta/(Ta+Nb) = 0.1-0.2 and the other at Ta/(Ta+Nb) = 0.5-0.8, that correspond to the cores and rims of the crystals, respectively. The TiO_2 content is lower than 0.5 wt.%, except in one grain, where TiO_2 ranges from 2.17 to 2.76 wt.%. This grain is also relatively Y-rich, varying from 1.09 to 1.30wt.% Y_2O_3.

Table 4.2. Representative chemical composition of CGM from the Penouta Open Pit. Clm= columbite-(Mn); tmn= tantalite (Mn); clf= columbite-(Fe).

Oxides, wt.%	P1 clm	P2 clm	P3 clf	P4 clm	P5 tnm	P6 tnm	P7 tnm	P8 tnm
WO_3	0.23	0.11	0.52	0.33	0.19	0.16	0.33	0.43
Ta_2O_5	19.13	20.47	30.22	47.29	55.80	57.69	63.55	69.87
Nb_2O_5	61.06	60.17	50.46	33.87	27.33	24.21	19.52	13.57
TiO_2	0.04	0.02	0.06	0.10	0.00	0.09	0.12	0.00
UO_2	0.00	0.02	0.00	0.31	0.04	0.24	0.00	0.11
ThO_2	0.00	0.00	0.00	0.22	0.00	0.00	0.08	0.00
Sc_2O_3	0.14	0.16	0.07	0.01	0.08	0.37	0.30	0.01
SnO_2	0.06	0.08	0.10	0.11	0.18	0.22	0.22	0.24
Fe_2O_3	0.52	0.34	0.14	1.12	0.29	1.28	0.71	0.34
FeO	2.86	3.07	9.80	7.74	1.63	2.14	7.55	3.38
MnO	16.35	16.16	8.68	8.53	14.48	12.98	7.65	11.36
Total	100.41	100.60	100.05	99.65	100.02	99.38	100.03	99.31
				Atomic contents				
W^{6+}	0.015	0.007	0.034	0.024	0.015	0.012	0.025	0.035
Ta^{5+}	1.259	1.352	2.099	3.580	4.374	4.603	5.195	5.972
Nb^{5+}	6.673	6.599	5.827	4.263	3.560	3.211	2.653	1.928
Ti^{2+}	0.007	0.003	0.011	0.022	0.000	0.021	0.028	0.000
U^{4+}	0.000	0.001	0.000	0.019	0.003	0.016	0.000	0.008
Th^{4+}	0.000	0.000	0.000	0.014	0.000	0.000	0.006	0.000
Sc^{3+}	0.012	0.016	0.022	0.028	0.046	0.055	0.058	0.065
Sn^{4+}	0.015	0.017	0.008	0.001	0.011	0.048	0.040	0.000
Fe^{3+}	0.095	0.062	0.027	0.235	0.063	0.285	0.149	0.080
Fe^{2+}	0.577	0.622	2.094	1.803	0.393	0.523	1.898	0.888
Mn^{2+}	3.347	3.321	1.878	2.011	3.535	3.226	1.948	3.024
CATSUM	12.000	12.000	12.000	12.000	12.000	12.000	12.000	12.000

Columbite group minerals are relatively poor in minor elements (Table 4.3). Microprobe analyses reveal variable contents of Sn and W, usually lower than 1 wt. %, although they can occasionally reach 2.71 and 2.54 wt.%, respectively. Ca, Y, U, and Th are negligible. ZrO_2 content is up to 0.28 wt.% and HfO_2 up to 0.16 wt.%. Sb and Bi are below the detection limits of the EMPA.

Table 4.3. Representative chemical composition of CGM and tapiolite from the Penouta leucogranite. MT, tantalite-(Mn); FT, Ferrotantalite; MC, columbite-(Mn); Tp, tapiolite.

Oxides (wt. %)	P31 MT	P42 FT	P91 MT	P94 MT	P112 MT	P117 MT	P119 MC	P120 MC	P143 Tp
WO_3	0.31	0.32	0.26	0.15	0.41	0.24	0.35	0.21	0.41
Ta_2O_5	67.82	66.47	64.64	52.20	55.08	65.41	44.92	19.28	76.42
Nb_2O_5	15.47	16.68	18.54	30.04	27.61	17.94	36.57	60.71	5.77
TiO_2	0.00	0.00	0.05	0.00	0.23	0.07	0.06	0.05	0.11
UO_2	0.02	0.35	0.10	0.09	0.00	0.29	0.30	0.08	0.16
ThO_2	0.00	0.00	0.00	0.03	0.00	0.00	0.00	0.00	0.00
Sc_2O_3	0.20	0.24	0.22	0.19	0.22	0.22	0.17	0.04	0.24
ZrO_2	0.07	0.28	0.07	0.04	0.04	0.09	0.02	0.00	0.07
HfO_2	0.04	0.16	0.03	0.05	0.00	0.00	0.00	0.00	0.04
SnO_2	0.76	0.27	0.02	0.07	0.04	0.16	0.20	0.08	1.18
Fe_2O_3	0.38	0.43	1.29	0.95	0.37	0.74	0.21	0.37	0.70
FeO	1.48	7.92	4.72	0.95	3.35	2.81	7.97	3.52	12.36
MnO	13.30	7.09	10.04	14.96	12.75	12.13	9.02	15.70	1.29
CaO	0.03	0.00	0.01	0.00	0.01	0.01	0.00	0.00	0.00
PbO	0.12	0.00	0.00	0.00	0.00	0.03	0.00	0.00	0.05
Total	99.99	100.22	100.00	99.73	100.11	100.14	99.78	100.04	98.80
				Atomic contents					
W^{6+}	0.025	0.026	0.020	0.011	0.031	0.019	0.025	0.013	0.009
Ta^{5+}	5.685	5.528	5.304	4.029	4.295	5.393	3.357	1.274	1.715
Nb^{5+}	2.156	2.306	2.529	3.855	3.579	2.459	4.544	6.668	0.215
Ti^{2+}	0.000	0.000	0.012	0.000	0.050	0.016	0.012	0.009	0.007
U^{4+}	0.001	0.024	0.007	0.006	0.000	0.020	0.018	0.004	0.003
Th^{4+}	0.000	0.000	0.000	0.002	0.000	0.000	0.000	0.000	0.000
Sc^{3+}	0.054	0.063	0.057	0.047	0.054	0.057	0.040	0.009	0.017
Zr^{4+}	0.010	0.042	0.010	0.006	0.006	0.013	0.003	0.000	0.003
Hf^{4+}	0.004	0.014	0.003	0.004	0.000	0.000	0.000	0.000	0.001
Sn^{4+}	0.104	0.037	0.003	0.009	0.005	0.021	0.024	0.008	0.043
Fe^{3+}	0.088	0.099	0.293	0.203	0.080	0.169	0.043	0.068	0.043
Fe^{2+}	0.382	2.025	1.191	0.231	0.803	0.713	1.833	0.715	0.853
Mn^{2+}	3.472	1.836	2.566	3.597	3.096	3.115	2.100	3.231	0.090
Ca^{2+}	0.009	0.000	0.004	0.000	0.001	0.002	0.001	0.000	0.000
Pb^{2+}	0.010	0.000	0.000	0.000	0.000	0.002	0.000	0.000	0.001
CATSUM	12.000	12.000	12.000	12.000	12.000	12.000	12.000	12.000	3.000
Ta/(Ta+Nb)	0.725	0.706	0.677	0.511	0.545	0.687	0.425	0.160	0.888
Mn/(Fe+Mn)	0.881	0.464	0.633	0.892	0.778	0.779	0.528	0.805	0.091

Ferrotapiolite

Tapiolite is rare; only one crystal of 10 μm was detected as an inclusion in cassiterite. Its chemical composition shows a Ta/(Ta+Nb) ratio of 0.89 and Mn/(Mn+Fe) ratio of 0.11.

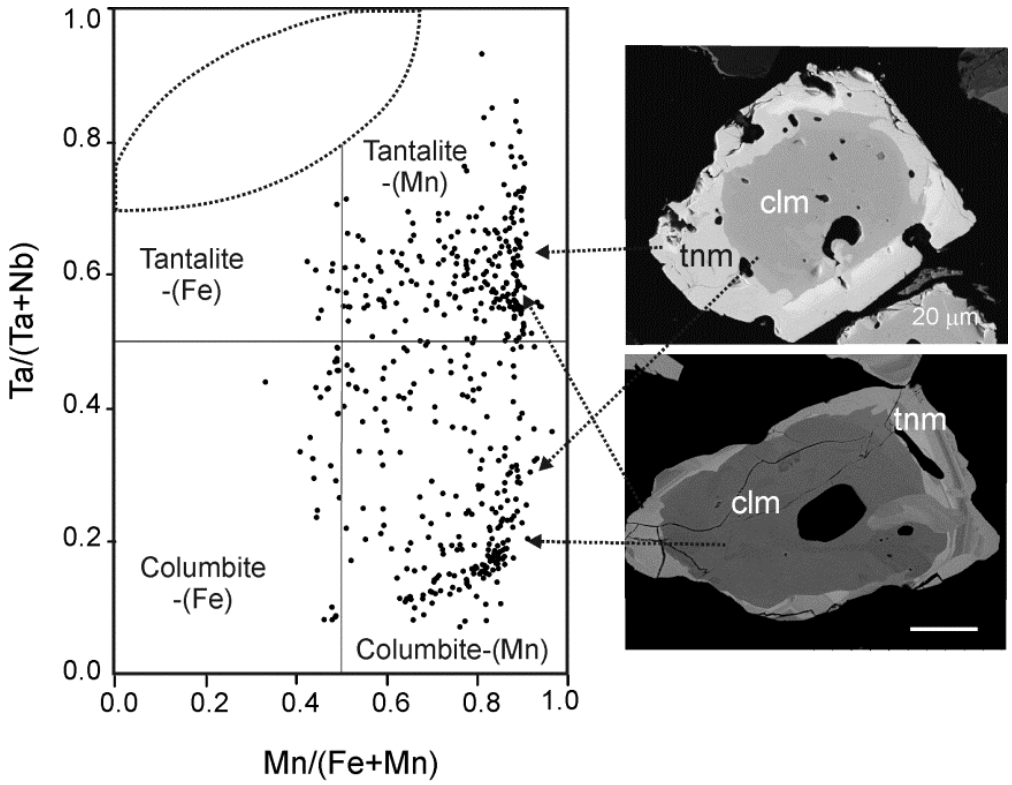

Figure 4.4. Chemical composition of CGM from the Penouta open pit in the columbite quadrilateral (Alfonso, 2018) and two illustrative SEM images. Clm, columbite-(Mn); tnm, tantalite-(Mn).

Microlite

Microlite, $(REE,U,Y,Ca,Na)_2(Ta,Nb)_2O_6(O,OH)$, usually is present in Penouta as crystals of few microns in size. Primary euhedral microlite crystals are rare; this mineral usually occurs as a late phase associated to CGM. In most cases microlite is enclosed to tantalite and cassiterite (Figure 4.5).

According to the MLA data only 12 wt.% of the microlite crystals are free, whereas 24 wt.% were in contact with tantalite and 14 wt.% with cassiterite. Representative compositions of microlite are given in Table 4.4. Microlite is always Ta-rich, Ta/(Ta + Nb) values varying between 0.91 and 0.99. Its composition ranges from 64.00 to 80.27 wt.% of Ta_2O_5 and 2.36 to 16.92 wt.% of Nb_2O_5, TiO_2 reaches 0.25 wt.% and SnO_2 varies between 0.38 and 3.44 wt.%. The occupation of the A site varies considerably; Ca is the most abundant cation, up to 11.89 wt.%, but U and Pb can also be important, with up to 6.01 and 8.46 wt.%, respectively. Plumbomicrolite occurs as a thin rim around microlite (Figure 4.5). Na_2O contents reaches 5.86 wt.%, whereas SnO reaches 3 wt.%. Fluorine is present in low amounts, up to 0.17 wt.%. Sb and Bi were not detected.

Wodginite

Wodginite, $Mn(Sn,Ta)(Ta,Nb)_2O_8$, occurs associated with cassiterite and tantalite (Figure 4.6, 4.7 and 4.8) as late replacements or inclusions. The differentiation between ixiolite and wodginite is based on the structure, but stoichiometric criteria can also be used (Wise et al., 1998).

As shown in Table 4.5, most analyses fit well with the formula of wodginite. The B and C sites are completed and only A site values are slightly lower than that of the ideal formula (Table 4.5). This can be due to the presence of lithium or vacancies (Ercit et al., 1992a).

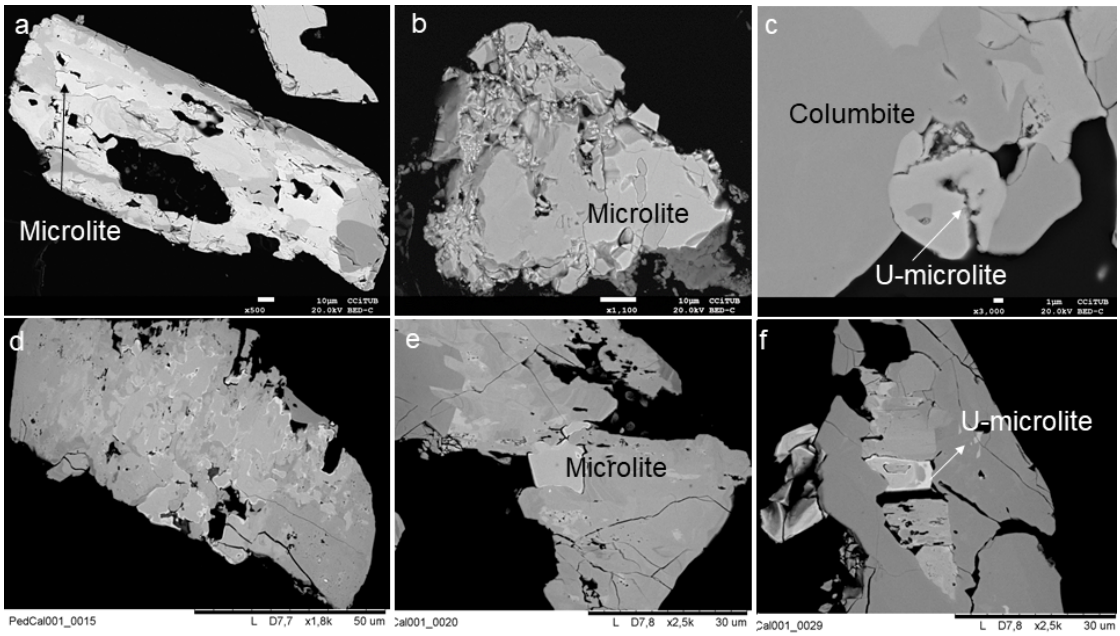

Figure 4.5. Back-scattered SEM images of Na-Ta oxides from the Penouta leucogranite: (a) columbite–tantalite crystal with microlite (Microl) enclosed (bright); (b) microlite crystal; c) uranmicrolite hosted in columbite; d,e) microlite replacement of columbite with bright rims composed of plumbomicrolite (Pb-Microl); f) uranmicrolite rimming microlite enclosed in a fracture of a CGM.

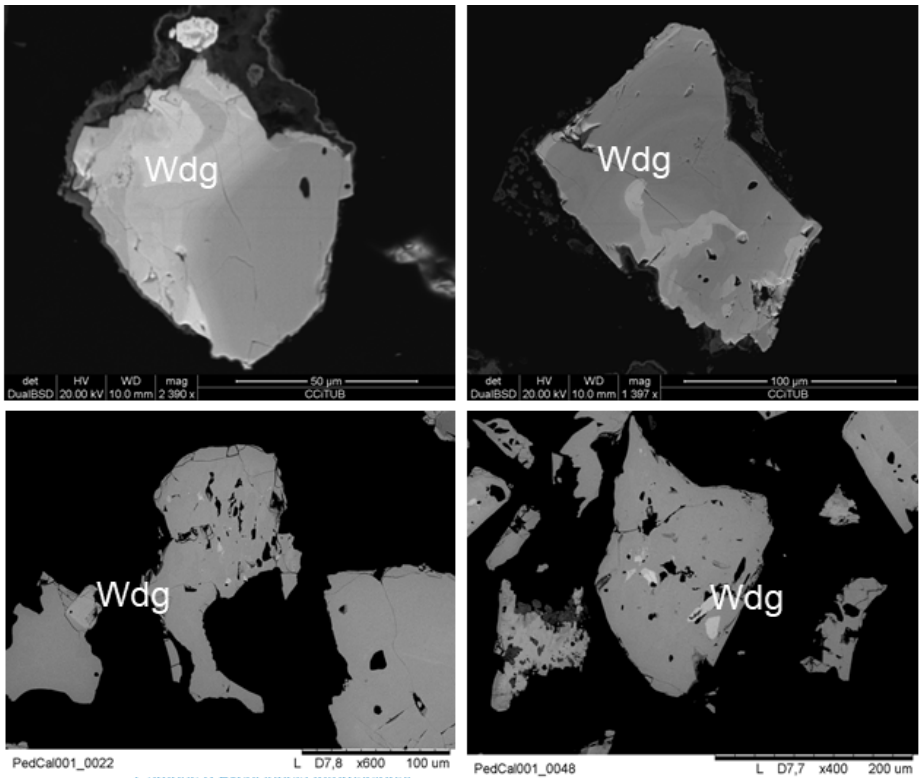

Figure 4.6. and Wodginite (Wdg) from the Penouta open pit leucogranite hosted in CGM.

Table 4.4. Representative chemical composition (wt. %) of microlite from the Penouta leucogranite.

Sample	P034	P037	P132	P057	P202	P2036	P2037	P2026
WO_3	0.33	0.22	0.43	0.40	0.25	0.25	0.17	0.35
Ta_2O_5	75.00	75.15	74.63	73.78	71.72	71.02	71.30	70.41
Nb_2O_5	3.10	2.92	2.95	3.36	5.20	5.50	5.34	4.94
TiO_2	0.06	0.07	0.08	0.10	0.25	0.14	0.17	0.12
UO_2	1.48	1.31	1.71	6.07	1.51	0.26	0.19	1.49
ThO_2	0.00	0.00	0.00	0.00	0.00	0.47	0.39	0.05
Sc_2O_3	-	-	-	-	-	0.13	0.15	0.25
ZrO_2	-	-	-	-	-	0.00	0.15	0.14
HfO_2	-	-	-	-	-	0.00	0.00	0.07
CaO	10.87	10.92	10.53	9.56	0.88	11.36	11.51	11.03
Y_2O_3	0.12	0.00	0.05	0.16	0.00	0.00	0.00	0.00
MnO	0.16	0.09	0.28	0.41	0.55	0.05	0.10	0.13
FeO	0.24	0.68	1.43	0.25	0.71	0.09	0.10	0.11
SnO	1.91	1.88	1.72	0.93	2.67	2.99	2.61	2.56
PbO	0.18	0.15	0.06	0.26	8.46	0.09	0.17	0.04
Na_2O	5.92	5.72	5.74	4.40	0.03	4.94	5.11	4.63
F	-	-	-	-	0.07	0.13	0.15	0.12
OH	0.78	0.78	0.60	1.01	4.76	0.85	0.08	0.85
O=F					-0.97	-0.94	-0.94	-0.95
Total	100.14	99.88	100.21	100.69	96.08	97.34	96.75	96.33
			Atomic contents					
Ca^{2+}	1.062	1.070	1.035	0.941	0.085	1.108	1.119	1.092
Y^{3+}	0.006	0.000	0.002	0.008	0.000	0.000	0.000	0.000
U^{4+}	0.030	0.027	0.035	0.124	0.030	0.005	0.004	0.031
Th^{4+}	0.000	0.000	0.000	0.000	0.000	0.010	0.008	0.001
Pb^{2+}	0.004	0.004	0.002	0.006	0.206	0.002	0.004	0.001
Sn^{2+}	0.070	0.068	0.063	0.038	0.108	0.122	0.106	0.105
Na^{+}	1.047	1.014	1.021	0.784	0.005	0.872	0.899	0.829
Fe^{2+}	0.018	0.052	0.110	0.019	0.054	0.007	0.008	0.009
Mn^{2+}	0.012	0.007	0.022	0.032	0.042	0.004	0.008	0.010
ΣA site	2.250	2.242	2.289	1.953	0.530	2.129	2.155	2.08
W	0.008	0.005	0.010	0.009	0.006	0.006	0.004	0.008
Nb	0.128	0.121	0.122	0.140	0.213	0.226	0.219	0.206
Ta	1.861	1.869	1.862	1.844	1.765	1.758	1.759	1.769
Ti	0.004	0.005	0.006	0.007	0.017	0.010	0.011	0.008
Zr	-	-	-	-	0.000	0.000	0.007	0.006
Hf	-	-	-	-	0.000	0.000	0.000	0.002
ΣB site	2.000	2.000	2.000	2.000	2.000	2.000	2.000	2.000
F^{-}	-	-	-	-	0.020	0.038	0.042	0.035
OH^{-}	0.477	0.476	0.367	0.620	2.875	0.517	0.503	0.524
Oxygens	6.523	6.524	6.633	6.380	4.105	6.445	6.455	6.441
Σanions	7.000	7.000	7.000	7.000	7.000	7.000	7.000	7.000
Ta/(Ta+Nb)	0.94	0.94	0.94	0.93	0.89	0.89	0.89	0.90

Table 4.5. Representative chemical composition (wt. %) of wodginite from the Penouta leucogranite.

	PW1	PW2	PW3	PW4	PW5	PW6
WO_3	0.49	0.36	0.39	0.35	0.17	0.21
Ta_2O_5	61.85	62.02	61.35	63.52	63.27	63.69
Nb_2O_5	7.51	7.05	7.40	6.20	7.23	6.10
TiO_2	0.11	0.09	0.21	0.08	0.05	0.08
UO_2	0.10	0.00	0.00	0.207	0.00	0.05
ThO_2	0.00	0.00	0.00	0.00	0.00	0.05
Sc_2O_3	0.21	0.08	0.14	0.14	0.08	0.11
ZrO_2	0.37	0.55	0.40	0.54	0.44	0.46
HfO_2	0.67	0.77	0.46	1.00	0.63	0.47
CaO	0.04	0.06	0.05	0.04	0.06	0.06
MnO	5.17	5.63	5.07	9.03	8.18	6.60
FeO	6.1	5.65	6.31	1.87	3.05	4.53
SnO_2	14.83	15.31	16.26	14.36	15	15.32
Fe_2O_3	1.53	1.40	1.17	1.77	1.57	1.44
PbO	0.13	0.03	0.00	0.00	0.20	0.15
Total	99.10	98.99	99.21	99.11	99.93	99.33
Atomic contents						
Mn^{2+}	1.828	1.996	1.785	3.239	2.878	2.349
Fe^{2+}	2.129	1.984	2.193	0.662	1.060	1.591
Ca^{2+}	0.018	0.016	0.020	0.018	0.026	0.029
U^{4+}	0.009	0.000	0.000	0.020	0.000	0.004
Th^{4+}	0.000	0.000	0.000	0.000	0.000	0.005
Pb^{2+}	0.014	0.003	0.000	0.000	0.022	0.017
ΣA site	3.998	3.999	3.999	3.938	3.986	3.995
Sn^{4+}	2.761	2.874	3.015	2.712	2.779	2.871
Ti^{4+}	0.035	0.029	0.064	0.026	0.016	0.024
Fe^{3+}	0.481	0.442	0.366	0.437	0.491	0.455
Ta^{5+}	0.491	0.422	0.368	0.541	0.523	0.457
Sc^{3+}	0.078	0.029	0.050	0.050	0.028	0.042
Hf^{4+}	0.080	0.092	0.055	0.121	0.074	0.057
Zr^{4+}	0.075	0.111	0.082	0.112	0.090	0.095
ΣB site	4.000	4.000	4.000	4.000	4.000	4.000
Ta^{5+}	6.530	6.758	6.568	6.774	6.623	6.820
Nb^{5+}	1.417	1.204	1.391	1.187	1.358	1.159
W^{6+}	0.053	0.039	0.043	0.038	0.019	0.023
ΣC site	8.000	8.001	8.002	7.999	7.999	8.002
CATSUM	15.998	16.001	16.001	15.937	15.986	15.997

According to the classification criteria of Ercit et al. (1992b), most of the analysed wodginite group minerals are wodginite, and only some compositions are ferrowodginite,. Ta_2O_5 ranges from 48.36 to 65.35 wt.%., SnO_2 from 14.63 to 19.37, MnO from 4.36 to 10.91.W is usually less than 1 wt.% but it can reach up to 4.19 wt. %. The W content is correlated with the total Fe (Figure 4.7). Hf and Zr are present in relatively high contents, up to 1.34 wt.% of HfO_2

and 1.29 wt.% of ZrO_2. The average Zr/Hf ratio is about 0.7. Such high contents have only been reported in Černý et al. (2007) for granitic pegmatites. In contrast with Černý et al. (2007) there is a slight correlation here between the Ta/(Ta+Nb) and Hf/(Hf+Zr) (Figure 4.8).

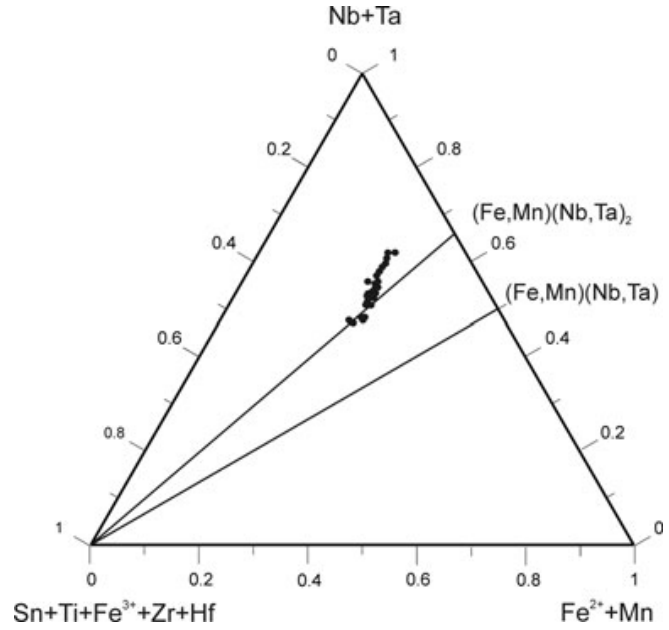

Figure 4.7. Compositions of wodginite-group minerals in the (Nb,Ta)–(Sn,Ti,Fe^{3+})–(Fe,Mn) diagram (atomic ratios).

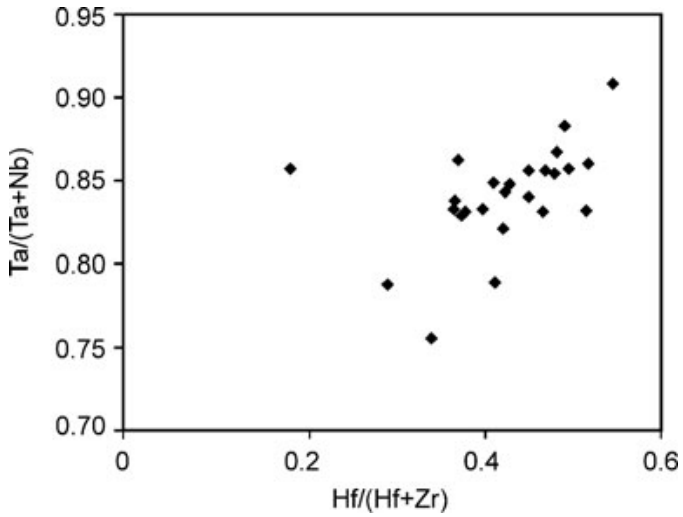

Figure 4.8. Correlation between the Ta/(Ta + Nb) and Hf/(Hf + Zr) in wodginite from Penouta ore.

Cassiterite

Cassiterite is the main oxide mineral in the Penouta leucogranite. It occurs as subhedral to euhedral crystals usually no longer than 200 μm. Under BSE cassiterite seems to be homogeneous in appearance. However, the chemical composition varies. Two generations can be recognized. The first generation consist in homogeneous crystals nearly pure in composition, whereas in the second-generation Ta can reach up to 8.51 wt.% Ta_2O_5, and Nb content is up to 1.94 wt.% Nb_2O_5. As usual in greisens and veins from granites Fe is dominant over Mn (Černý

and Ercit, 1989), reaching 1.45 wt.% and 0.20 wt.%, respectively. In granitic pegmatites the presence of Nb and Ta within cassiterite is attributed to the typical substitution scheme $(Fe, Mn)^{2+} + 2(Nb,Ta)^{5+} \leftrightarrow 3(Sn,Ti)^{4+}$, or tapiolite substitution (Černý et al., 1985, 1991), then the (Fe+Mn)/(Nb+Ta) ratio is in a 1:2 proportion (Černý et al., 2004). Most analyses from the Penouta cassiterite show the 1:2 ratio attributed to the tapiolite substitution (Figure 4.9a).

The cassiterite grains are often rich inclusions of Nb-Ta-rich minerals (Spilde and Shearer, 1992). Similarly, wodginite inclusions have been also found in other deposits (Masau et al., 2000; Černý et al., 2007; Rao et al., 2009). Masau et al (2000) described Hf-Zr-rich wodginite formed by exsolution from cassiterite, which was favoured by its high Zr and Hf contents. In the present study the Hf and Zr contents are relatively high in wodginite, suggesting a possible similar origin. However, inclusions of CGM in cassiterite constitute discrete grains probably trapped when cassiterite formed after CGM, as in other occurrences (Martins et al., 2011).

Cassiterite is the most abundant ore mineral in Penouta and occurs as homogeneous subhedral to anhedral grains. The chemical composition shows a high Ta content, up to 9 wt.% of Ta_2O_5.

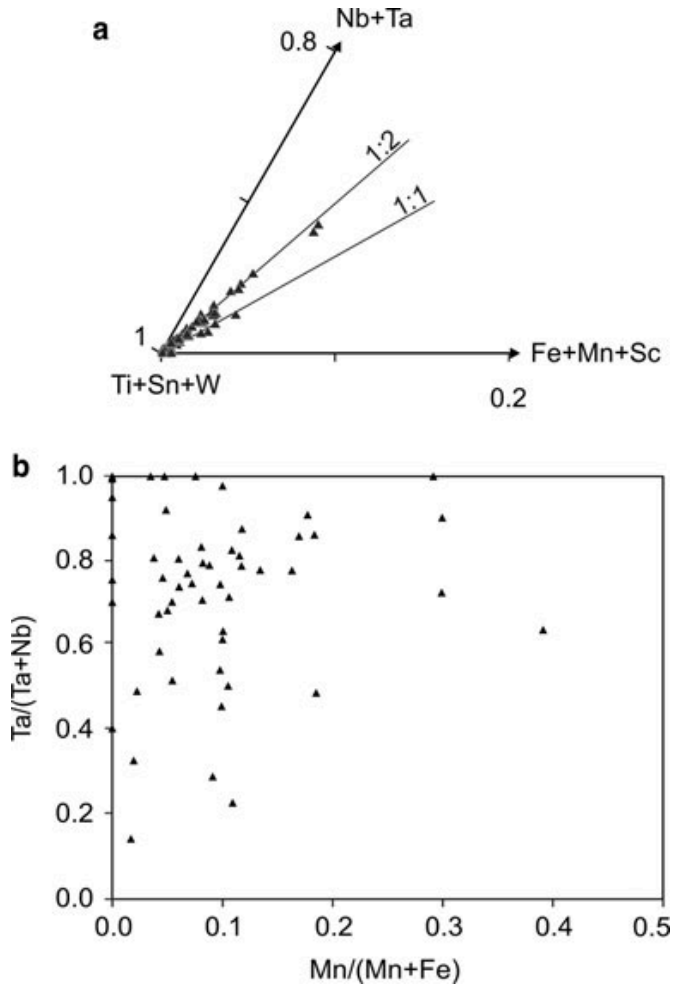

Figure 4.9. Cassiterite composition from the Penouta leuogranite: (a) plot in the (Ti + Sn +W)–(Fe + Mn + Sc)–(Nb + Ta) triangle; (b) in the columbite quadrilateral (atomic ratios).

4.1.3. Characterization of the processed tantalum ores

The development of a rougher concentration flow sheet for Penouta ore (open pit) was driven by the mineralogical characterization that is described in the previous section, which provided the mineralogical attributes needed for developing an appropriate flow sheet to recover tantalum from this complex Penouta low-grade tantalum ore. Also, it is important to mention that concentration tests were performed through two different flowsheets in this ore, being also a base to understand the behavior of this ore.

4.1.3.1 Size distribution characteristics of the sample

❖ **particle size distributions (PSD)**

The particle size distributions obtained after grinding using HPGR and a BM, or only a BM, are similar (Figure 4.10). After the HPGR grinding 40 wt.% of the material is smaller than 600 µm. From this, 31.8 wt.% is lower than 250 µm, and 8.8 wt.% is in the range 250–600 µm. Finally, only 11 wt % of the material is coarser than 600 µm. In the BM product, 22.8 wt % of processed material is higher than 600 µm, and about 61 wt % is lower than 250 µm. According to Reference (Kazerani Nejad and Sam, 2017), when the HPGR unit was in an open circuit together with a BM, it had no significant effect on the fineness of the final comminuted product. However, in the present investigation, the BM combined with a previous step of HPGR produces a finer end product than with the BM alone.

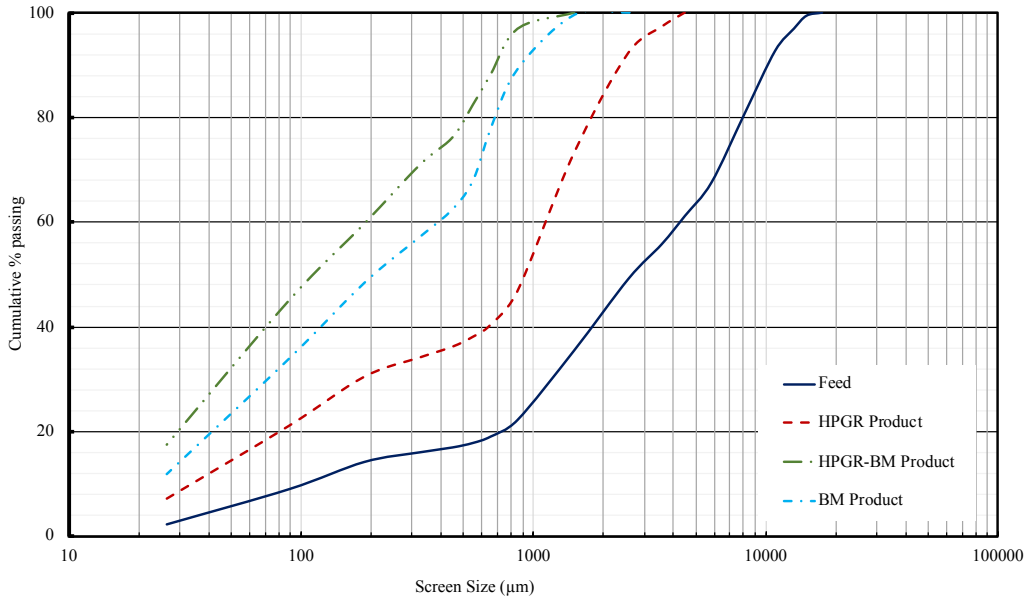

Figure 4.10. Particle size distribution curves for the feed and ground products.

❖ **Mineral grain size**

The mineral grain size information (Figure 4.11) illustrates that the Tantalum minerals show a finer grain size distribution when compared to the cassiterite and columbite minerals present in the ore. The tantalum mineral grains show a P80 of 99.53 µm, followed by columbite (P80 of 112.84 µm) and then by cassiterite (P80 of 153.16 µm), while microlite, which is the other tantalum carrier in this ore, has a P80 of 64.47 µm (Appendix C).

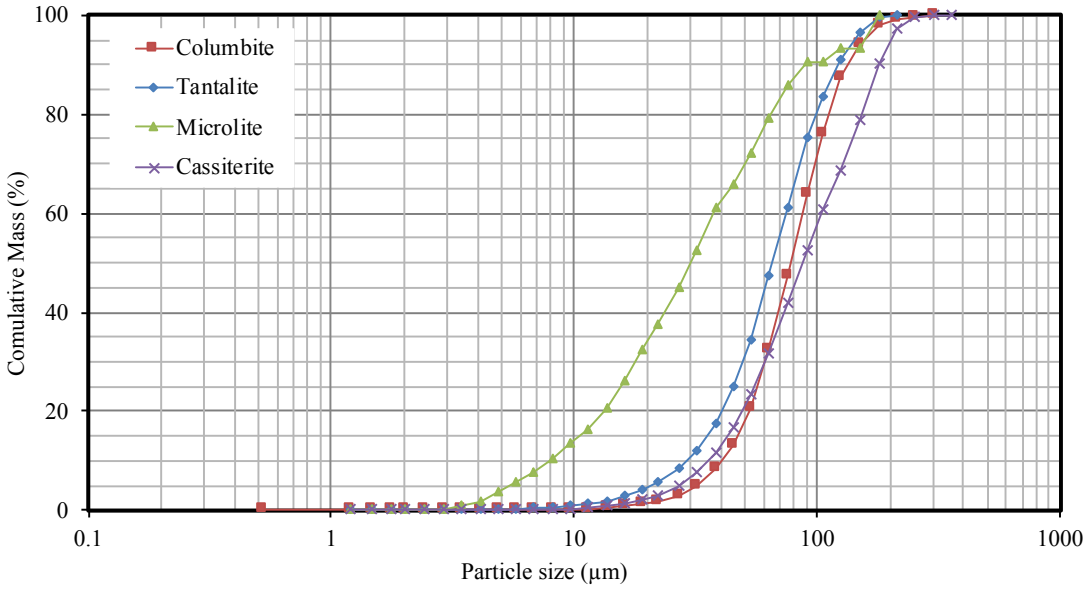

Figure 4.11. Mineral grain size distribution for Penouta ore (open pit).

4.1.3.2 Modal mineralogy

Preliminary estimation of modal mineralogy for this case study (preconcentration sample) was carried out for Penouta (open pit) determined by MLA (Figure 4.12). The figure shows that the concentrate mineralogy was represented predominantly by cassiterite (53.61 wt.%), followed by spessartine (5.13 wt.%). Lesser amounts of albite (5.13 wt.%) and Fe_oxide (2.40 wt.%) were found. Other silicate minerals determined by MLA are garnets of spessartite type (Appendix D).

The modal mineralogy of concentrates from open pit of Penouta was also determined by TIMA-X (Figure 4.13) and the composition of the resulting tailings was obtained by XRD. The combination of both techniques is useful to obtain a complete mineralogical characterization. XRD ensures representativeness in coarse-grained samples, thus it measures millions of particles, as a result of the grinding sample to less than 60 µm. However, this technique only can detect minerals in concentration over than 1 wt.% (Hill et. al., 1993). Thus, these techniques are complementary and often the combination of both is necessary to obtain satisfactory results.

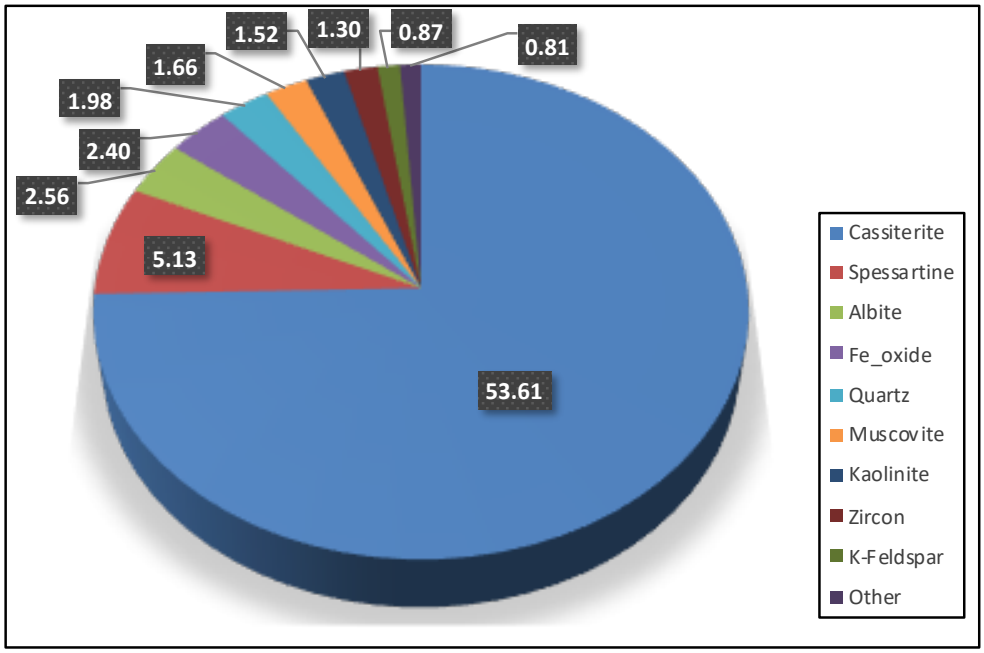

Figure 4.12. Modal mineralogy for grinding products for Penouta ore (open pit).

Albite is the most abundant mineral in all fractions of –250µm, whereas quartz is the dominant in concentrates from the coarser fractions of the final processes (C4 and C6) and the equivalent ratios in tailings (T4 and T6). K-feldspar is microcline, as indicated by the XRD data and by the presence of the grid twining. This mineral occurs in variable amounts being more abundant in concentrate products of coarser size, with 7-10 wt.% in products of size less than 250 µm and 15-50 wt.% in products between 250 and 600 µm.

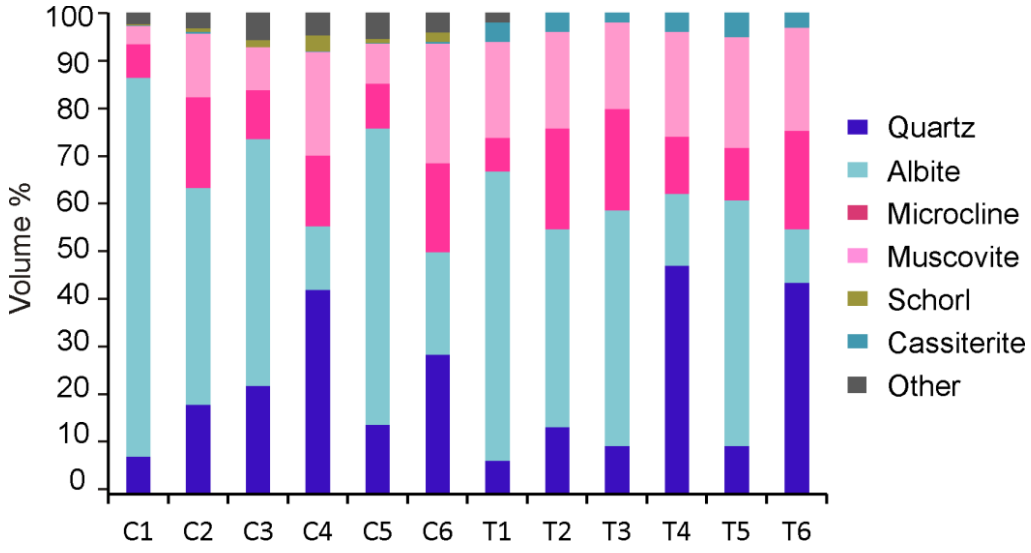

Figure 4.13. Modal mineralogy of the grinding products. C1 to C6 are the concentrates analyzed by TIMA and in tailings (T1-T6) determined by XRD.

Optical and XRD allowed determining that K-feldspar is microcline. This is homogeneously distributed except that in the fraction of –250µm obtained from the HPGR grinding, which has a lower content. Muscovite contents is considerably different in concentrates and tailings. The most significant difference between the mineralogical data obtained from TIMA-X and XRD is about muscovite. The sheet structure of this mineral makes the quantification difficult in the analysis of sections and also in XRD estimations. Muscovite is usually overestimated in XRD analyses due the preferential orientation of crystals (Moore, 1989). Other studies also found discrepancies in the content of micas between the results provided by both techniques (Rahfeld, 2018).

Minor minerals have been included in Figure 4.13 as other minerals. These are mainly beryl, phosphates, such as apatite, xenotime and monazite, and scheelite, pyrite, hematite and ilmenite. The composition of minerals in the tailings after the gravity concentration of Nb-Ta minerals is presented in Table 4.6. Albite is the most abundant mineral the tailing products finer than 250µm, whereas quartz is predominant in products of +600 µm (T7 and T8). In the size fraction of 250-600 µm, although the obtained quartz contents were higher in the tailings, they vary proportionally with those from the respective tailings.

Table 4.6. Semiquantitative mineral composition of the product tailings determined by XRD.

Mineral (Wt.%)	T1	T2	T3	T4	T5	T6	T7	T8
Quartz	7	14	10	48	10	43	62	37
Albite	60	41	51	15	51	11	15	30
Microcline	7	21	23	12	11	20	13	14
Muscovite	20	20	14	22	23	21	7	16
Kaolinite	4	4	2	4	5	3	1	1
Beryl	2		-	-	-	-	-	2

4.1.3.3 Morphology and texture of particles

The mineral composition maps of the Nb-Ta rich minerals (Figure 4.14) show their morphology and mineral association. Although columbite and tantalite usually occur in the same particle, tantalite occurs in particles smaller than those of columbite. This is also partly evident in the images due to a possible stereological error.

An essential parameter for mineral processing is the shape of the ground particles and this can be influenced by the methods used for comminution (Vizcarra, 2010). HPGR produced a higher surface than other comminution devices, such as jaw crushers (Han, 2012). In the ground Penouta ore using HPGR the particles exhibit higher angularity than that obtained from the BM and then, a larger specific surface (Figure 4.15).

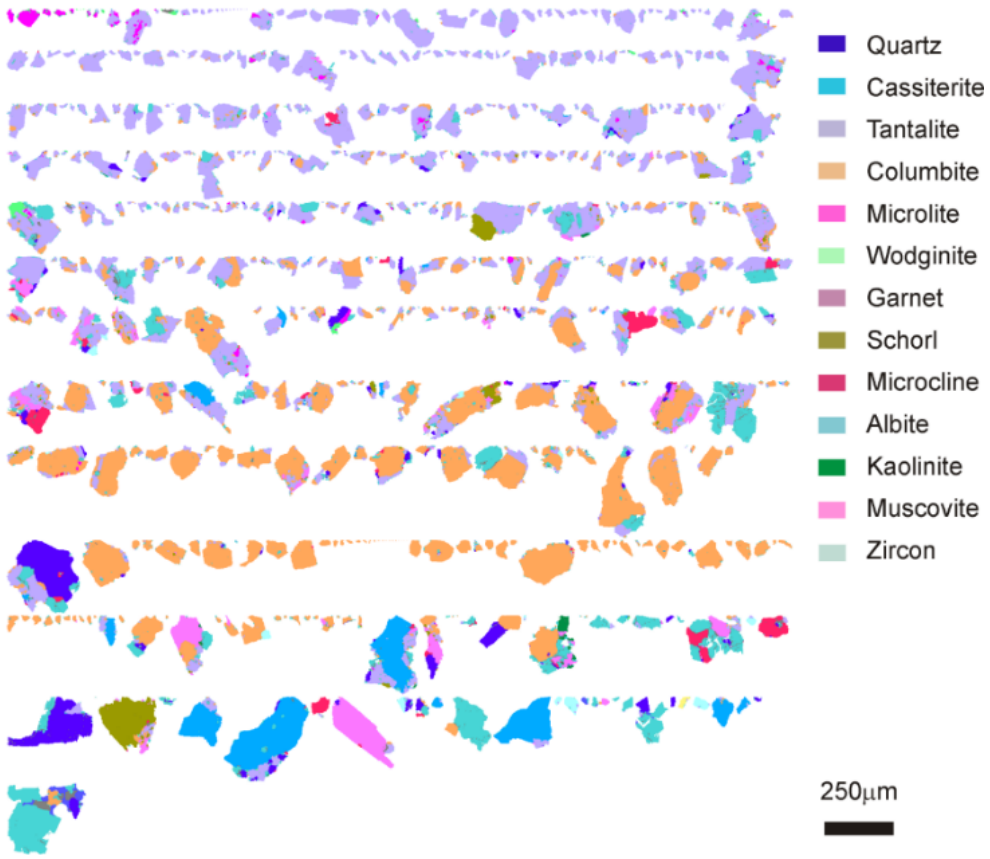

Figure 4.14. TIMA false color image of columbite-tantalite from concentrate of less than 250µm obtained from the ground material using the ball mill.

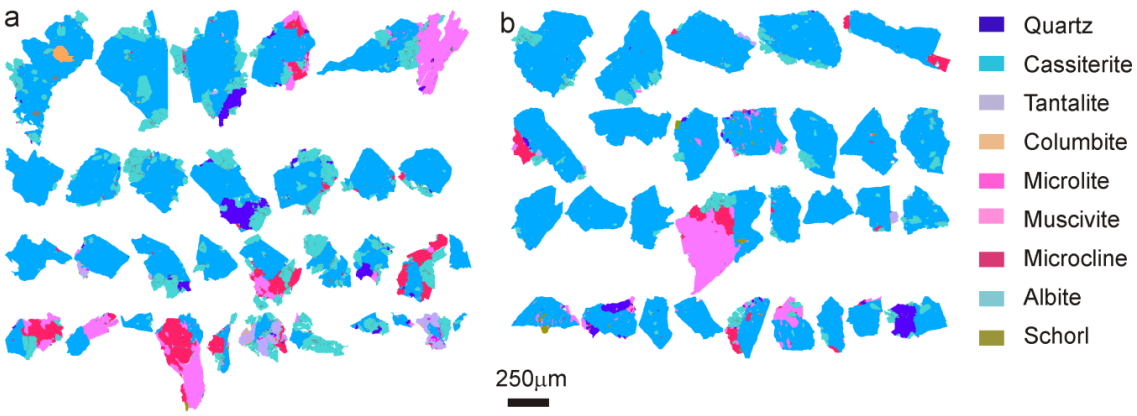

Figure 4.15. TIMA false color images for comparison of shape of the cassiterite-rich particles in the 250-600 size fraction obtained (a) with HPGR and (b) BM.

4.1.3.4 Mineral associations

The mineral associations indicated if there was tantalum that tended to be associated with problematic minerals (cassiterite or quartz minerals for the concentration process). The results in Figure 4.16 show that tantalum is associated mainly with Kaolinite (44.4%), followed by quartz and to a lesser extent with muscovite (16.5%) and others. Cassiterite has highest free surface

compared to other ore minerals (Figure 4.16) due to the higher grain size of this mineral.

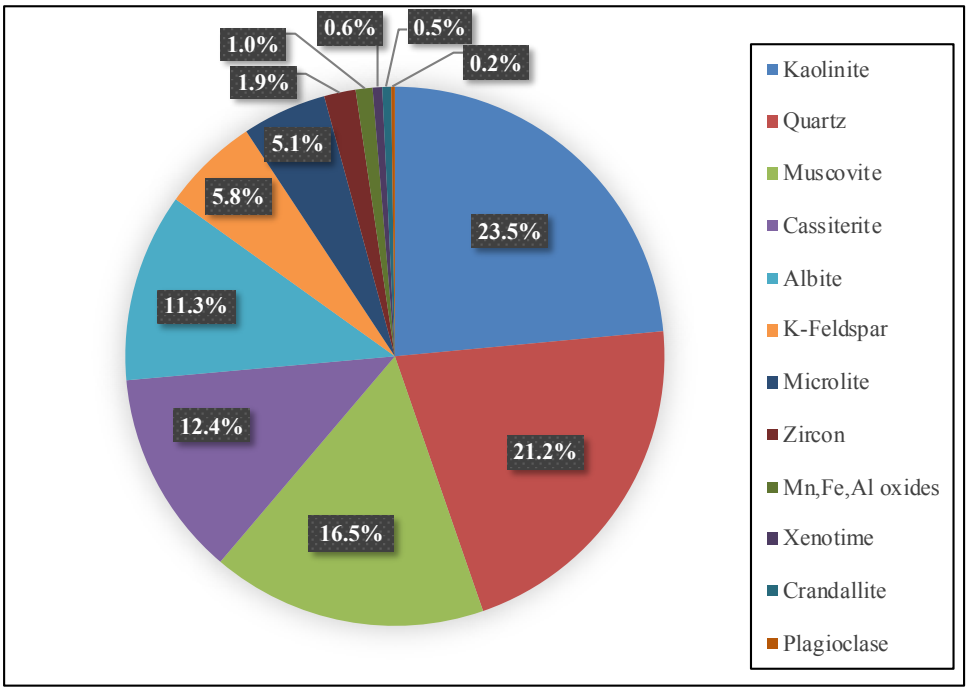

Figure 4.16. Mineral association in the Penouta tailings resulted of the processing of the Penouta open pit material in this study.

The most common mineral association with CGM are quartz, muscovite and kaolinite. Most mixed particles consist of columbite and tantalite together with cassiterite, quartz, muscovite and K-feldspar. Often tantalite is enclosed into cassiterite (Figure 4.17). Tantalite is 2.2 to 2.7 times more liberated than columbite, probably due to the lower grain size of this mineral. The columbite-tantalite liberated particles are between 66 and 78 %. Most of the non-liberated columbite-tantalite particles are binary, where this mineral is mainly associated with muscovite or quartz, and less frequently with feldspar. A significant amount of tantalite from the open pit can occur associated with kaolinite. These results are significant for the optimization of the comminution and recovering process (Appendix E).

The preconcentration assessment showed that none of the minerals present in the ore exhibited natural concentrated. The MLA analyzed a total of 68,218 grains, with 70,194 particles measured for the size fraction - 250 μm, were measured. The measurements on the size fractions were used to determine the key mineralogical attributes, such as modal mineralogy, elemental deportment, and texture, which were needed for the ore characterization.

Cassiterite is liberated in most of the particles (73-81 %). In other particles it is associated with muscovite (about 8%) or quartz (4.4%), Mn,Fe,Al oxides (4.2%) and K-feldspar (2.1%).

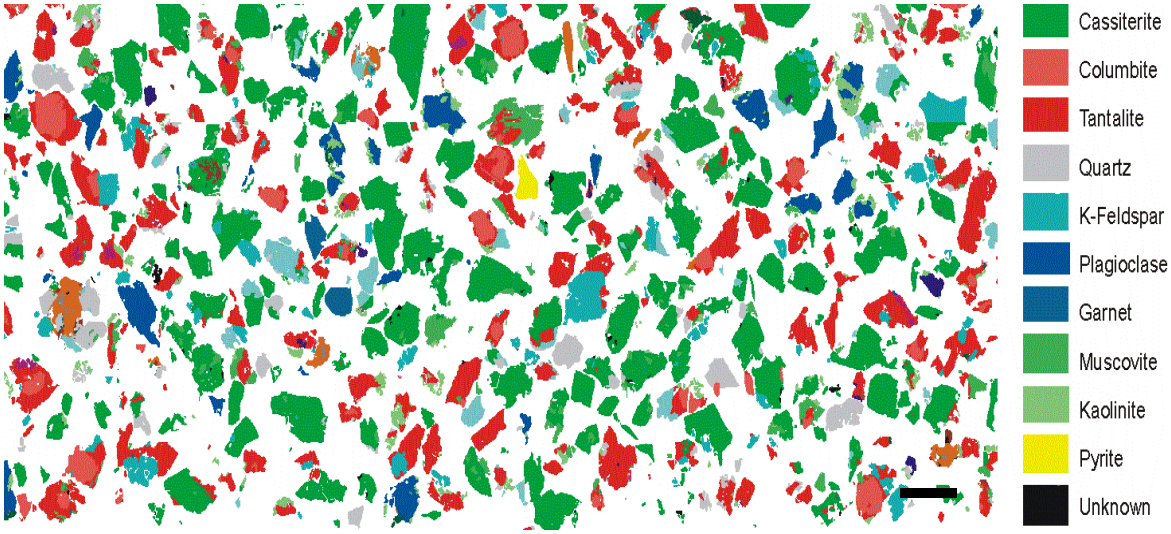

Figure 4.17. Representative pseudo-color particle maps showing mineral association of CGM from Penouta ore (open pit). Scale bar: 200 µm.

These CGM grains are mainly associated with albite, quartz, muscovite and cassiterite (Figure 4.18). The locking properties of ores from the Penouta open pit are highly dependent on the relationship between the mineral and particle sizes. The free surface indicates those minerals that are not surrounded by others. This is the highest in cassiterite compared to the other ore minerals (Table 4.7), due to the higher grain size of this mineral. In the CGM, as often they constitute crystals with a columbite core with a tantalite rim, tantalite presents more free surface than columbite. In the case of microlite and wodginite, these minerals are few microns in size and usually they are genetically associated with columbite and tantalite (Alfonso et. al., 2018), thus in most cases they are locked in these minerals and also in albite and cassiterite. CGM and cassiterite association occurs mainly in coarse particles, where usually tantalite is in contact or included in cassiterite.

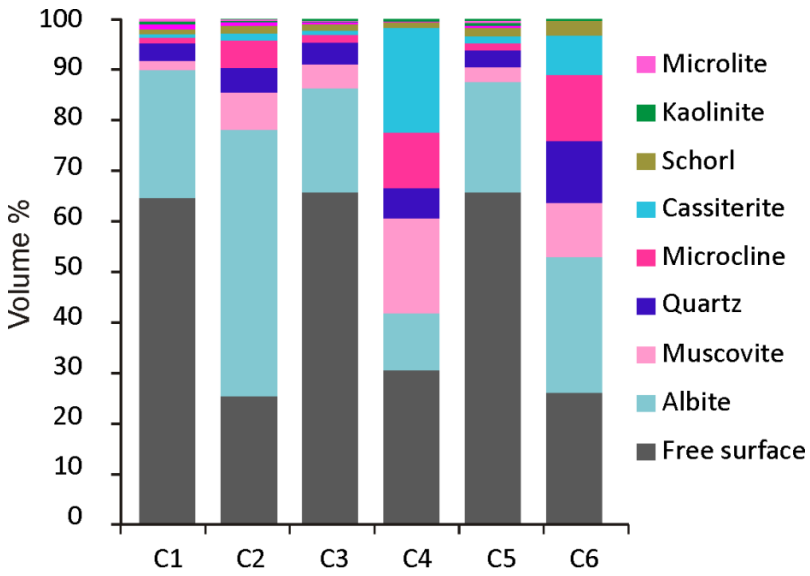

Figure 4.18. Mineral locking of CGM from the Penouta Open Pit.

Table 4.7. Free surface of ore minerals from the Penouta open pit.

Mineral (wt.%)	C1	C2	C3	C4	C5	C6
Cassiterite	84.06	48.55	87.97	71.05	82.38	67.66
Columbite	45.62	11.13	50.39	30.13	52.40	13.44
Tantalite	50.45	18.66	53.59	23.65	48.19	26.17
Microlite	8.38	1.96	26.29	0.39	26.59	0.00
Wodginite	5.72	1.07	11.66	0.18	14.20	0.43

Key findings of mineralogical characterization

According to the information obtained through the mineralogical characterization, the ore should be processed through physical separation, but considering that tantalum is present mainly as solid solution in CGM, a tantalum concentrate is needed to recover CGM. The degree of liberation at a P80 of 250 microns for the mineral of interest is adequate for obtaining a good concentrate response (based on the information presented in Table 4.7).

4.1.4 Metal distribution

The chemical composition of concentrates and tailings obtained in this study is shown in Table 4.8. Nb and Ta occur in significant amounts in all the particle size fractions obtained in the experiments. After the HPGR grinding the Ta content is similar in both fraction sizes (less and more than 250 μm), whereas in the BM always the smaller fraction is Ta-richer; Ta-rich minerals move to the concentrate, remaining in the tailing a minor amount. Similar behavior exists for Nb and Sn. However, in the size fraction of +250 μm higher contents are in the tailings, especially in the case of products obtained from the HPGR grinding, where 80 ppm remain in the tailings. Tailings of product with size +600 μm are poor in Nb and Ta, but still have high Sn contents, 336-528 ppm.

The mineral content of the ore minerals was determined by TIMA and a theoretical composition was also calculated from the chemical composition data of the different fractions (Table 4.8). As columbite and tantalite are the main Ta-Nb bearing phases, all Ta was assigned to tantalite and all Nb is in columbite. The TIMA results show that the most abundant ore mineral in the concentrates is cassiterite, followed by tantalite and columbite; determined from the chemical composition were calculated assuming that all Ta is in tantalite and all Nb is in columbite. The contents of microlite and wodginite have not been considered due to the low significance of their content.

The tantalite/columbite ratio in the calculated minerals is between 1.2 and 1.4 in the concentrates and significantly lower in the tailings especially in tailings of +600 μm, where it is from 0.5 to 0.9. This could be due to the fact that in the gravity concentration tantalite moves

more easily to the heavy fraction (density of tantalite-(Mn) is 8.1) than columbite (density of columbite-(Mn) is 5.28).

The tantalite contents determined by TIMA are higher, whereas the Nb contents are similar in both determinations (Figure 4.19). The tantalite /columbite ration is double, in the cases of the lower particle size. This could be due to the stereological error produced during the analysis of image sections (Spencer, 2000; Ueda, 2017).

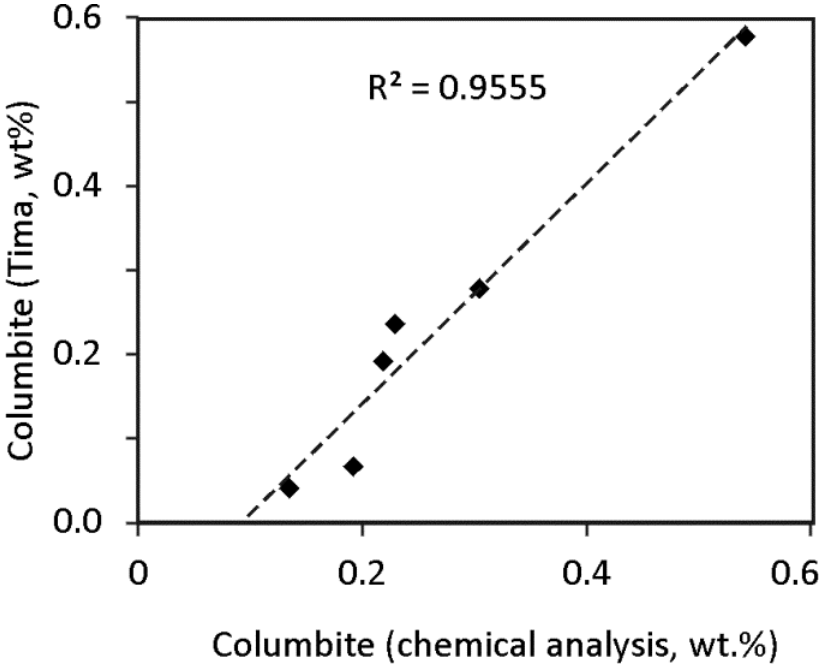

Figure 4.19. Comparison of the columbite content of the grinding products determined by TIMA and from the chemical composition.

Table 4.8. Chemical composition and mineralogy of the grinding products of the Penouta ore.

				Chemical composition (ppm)					Mineralogy (wt.%)					
									(Normative)		(TIMA-X)			
Grinding method	Size (µm)	Sample	Type	Sn	Nb	Ta	Cst	Tn	Cl	Tn/Col	Cst	Tant	Cl	Tn/Cl
HPGR	–250	PN-1	C1	3010	1080	1980	0.38	0.28	0.23	1.22	0.39	0.72	0.24	3.07
HPGR	+250	PN-3	C2	-	1030	1990	-	0.28	0.22	1.29	1.81	0.58	0.19	3.02
HPGR+BM	–250	PN-5	C3	-	1435	2720	-	0.39	0.30	1.26	1.30	0.63	0.28	2.26
HPGR+BM	+250	PN-7	C4	-	635	1355	-	0.19	0.13	1.42	3.76	0.06	0.04	1.43
BM	–250	PN-9	C5	-	2550	5000	-	0.71	0.54	1.31	1.99	1.13	0.58	1.96
BM	+250	PN-11	C6	-	905	1895	-	0.27	0.19	1.40	3.23	0.11	0.07	1.68
HPGR	–250	PN-2	T1	67	14	30	0.01	0.00	0.00	1.43				
HPGR	+250	PN-4	T2	224	58	80	0.03	0.01	0.01	0.92				
HPGR+BM	–250	PN-6	T3	88	17	30	0.01	0.00	0.00	1.18				
HPGR+BM	+250	PN-8	T4	131	45	40	0.02	0.01	0.01	0.59				
BM	–250	PN-10	T5	118	23	40	0.01	0.01	0.00	1.16				
BM	+250	PN-12	T6	132	49	50	0.02	0.01	0.01	0.68				
HPGR+BM	+600	PN-19	T7	528	42	30	0.07	0.00	0.01	0.48				
BM	+600	PN-20	T8	336	46	60	0.04	0.01	0.01	0.87				

4.1.5 Work index and energy consumption

The work index of the studied ore ranges from 6.30 to 38.00 kWh/t, according to the particle size of the feed. The increase in the work index indicates a change in the consumed energy of the ore during the grinding. As was seen before, most of the liberated Ta has a size smaller than 100 µm, and about 80% of the liberated Ta has a size smaller than 100 µm. This has a negative impact on the milling energy costs. From a size smaller than 100 µm, with the progress of Ta liberation production, the increase in the ore work index increases the energy consumption per ton of milled ore. This information helps determine the optimum operational conditions of mineral liberation in order to reduce energy consumption.

In order to evaluate the relationships between the work index and the degree of tantalum liberation in the processed material, the cumulative distribution of the liberated tantalum with the class mean size and the work index is shown in Figure 4.20. These relationships can be explained by the fact that almost all liberated tantalum mineral is in fine fractions, which causes the work index and energy consumption to increase.

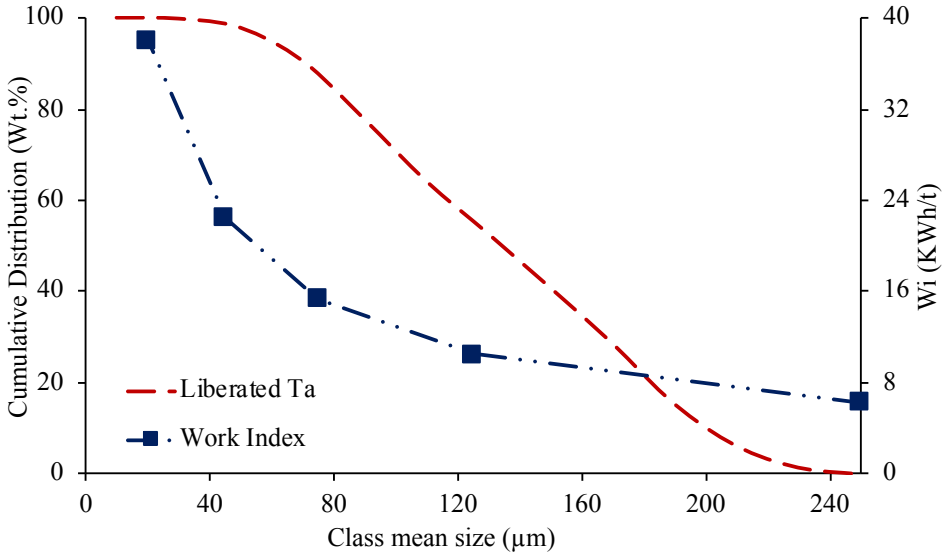

Figure 4.20. Dependence of work index on the cumulative distribution of scheelite content in the material.

4.1.6 Simulation and Predication of Mineral Liberation for Penouta ore (open pit)

4.1.6.1 Mineral liberation analysis (MLA)

The mineral liberation analysis (MLA) results from Penouta ore (open pit) also were represented in particle size and grade to intervals in front of mass fraction. In each interval there are some particles measured. Intervals without these particles class result is zero. It is necessary to consider that the analyzed samples are concentrates from the processes explained in the

previous point, and these are statistical processes. The Penouta concentrates represent 0,02% of the total initial sample. The total content of Ta in the original sample is low, 103 ppm, and then, it should be concentrated in order to analyze a high number of particles.

The Penouta mineral liberation distribution density (Figure 4.21) indicates that the CGM particles liberated are smaller than 250 microns and most of them have a grade of more than 70%. There is not clear at which size the total CGM liberation starts, but it is probably below 20 microns. This size is not a realistic industrial size, for this reason the plant concentrate will be limited (see Appendix A).

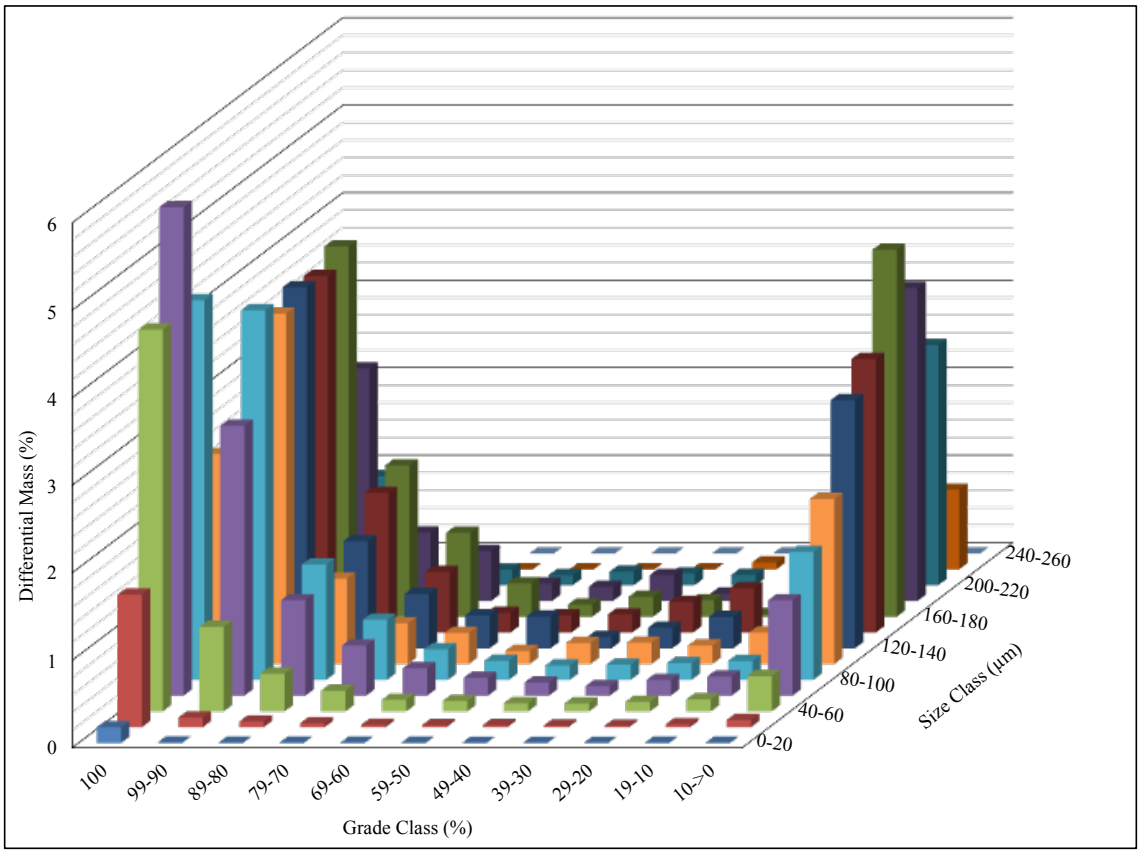

Figure 4.21. Predicted liberation as a function of particle size after comminution of Penouta ore (open pit).

4.1.6.2 Mineral liberation by TIMA-X

In the present study an ore is considered as liberated when represents >90 vol. % of the particle volume. The TIMA analyzer provided the liberation characteristics of ores from the different steps of the treatment. The degree of columbite-tantalite liberation depends on the particle size (Figure 4.22). The highest degrees of liberation are achieved in particles smaller than 250 µm that have been comminuted with the combination of HPGR and BM, especially in the case of cassiterite where in this case the 84 wt.% is liberated compared to 69.76 wt.% when only used BM (Table 4.9).

In the fraction of less than 250 µm about 65 wt.% of the columbite-tantalite minerals are liberated, whereas, only 25-30 wt.% is liberated in particles larger than 250 µm. This is caused by the grain size of CGM, which usually is lower than 200 µm.

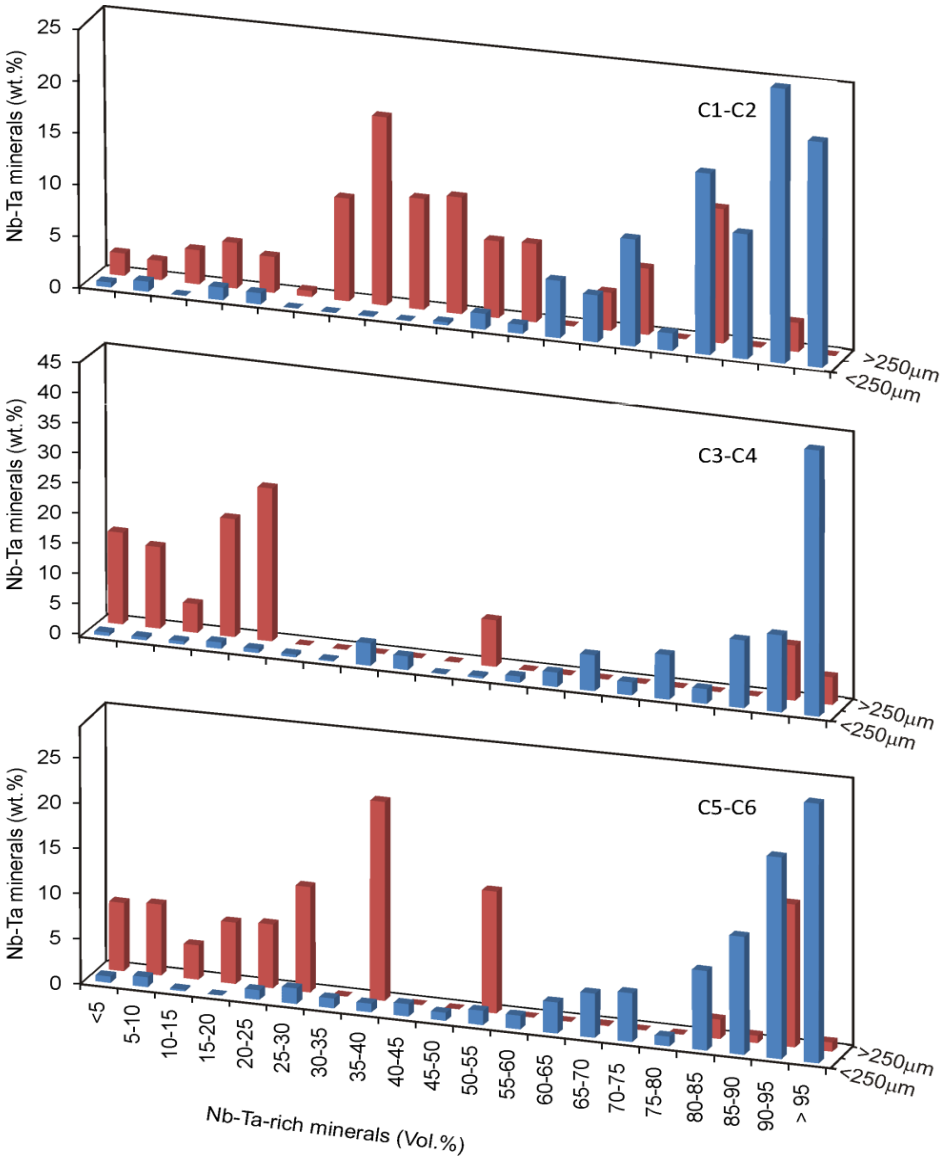

Figure 4.22. Distribution of the Nb-Ta rich minerals in the concentrate material from the Penouta open pit according to particle size and grade classes.

Correction of the distribution of linear grades is important to the prediction of mineral liberation. The linear grade distribution that is obtained, when a binary ore is comminuted can be predicted, and the application of the stereological correction extends the prediction to the full distribution of particle volume grade (King, 1979). To describe the populations of particles with different mineral content a distribution function will used. This distribution function is based on the beta distribution that is used in mathematical calculations. Three groups of particle populations can be distinguished: liberated particles of gangue, liberated particles of ore, and the

particles that are all composed of mixtures of the two minerals. The distribution of mineral grades over the third group is called the interior grade distribution, and the beta distribution function is used as a model.

Table 4.9. Liberation of cassiterite and CGM from the Penouta open pit leucogranite. Grade is reported in volume %, and minerals content in wt.%.

	Casssiterite				**Columbite-group minerals**			
	HPGR+BM		**BM**		**HPGR+BM**		**BM**	
Grade	**–250**	**+250**	**–250**	**+250**	**–250**	**+250**	**–250**	**+250**
<10	0.08	0.14	0.10	0.16	1.20	17.51	1.79	15.37
10-20	0.00	0.79	0.00	0.00	1.39	16.64	0.18	10.56
20-30	0.44	1.79	0.55	4.14	1.07	15.66	2.79	18.68
30-40	0.00	3.96	0.88	1.86	2.25	11.83	2.06	22.01
40-50	0.11	4.84	1.96	2.46	1.43	9.24	2.30	0.00
50-60	0.34	4.38	0.63	0.56	1.77	10.58	3.10	13.48
60-70	3.53	16.02	5.42	8.40	8.85	1.57	8.37	0.10
70-80	7.35	16.76	2.71	4.23	10.32	2.70	6.49	0.00
80-90	4.21	22.74	17.98	40.83	19.82	5.51	21.88	2.97
>90	83.95	28.59	69.76	37.36	51.90	8.76	51.04	16.83

The modelling results are shown in Figure 4.23, where it is a comparison between the cumulate mass from the experimental data and the simulated data of the results.

The simulated data have been obtained with back calculation with experimental data and using the beta distribution. King (2012) and Schneider (1995) proposed beta distribution as an alternative in order to understand the behavior the mineral liberation. The results show a better agreement in some interval sizes than in others. The complete results from these back calculations are in the Table reported in Appendix B. The n, g, g^M, L_0 and L_1 are experimental data and they represent the number of particles, average grade, average grade without L_1, mass fraction when the grade is 0% and 100% respectively. α^M and β^M are the beta function parameters. The variance of the distribution $(\sigma^2)^M$ and the γ parameter (calculated by α^M and β^M) are also shown in these tables. The below equations show how γ and $(\sigma^2)^M$ have been calculated according the beta distribution features.

The parameters α^M and β^M are related to the mean and the variance through the expressions:

$$\alpha^M = g^M \gamma \qquad (4\text{-}2)$$

$$\beta^M = (1 - g^M)\gamma \qquad (4\text{-}3)$$

$$\gamma = \frac{\bar{g}^M - (\bar{g}^M)^2 - (\sigma^2)^M}{(\sigma^2)^M} \qquad (4\text{-}4)$$

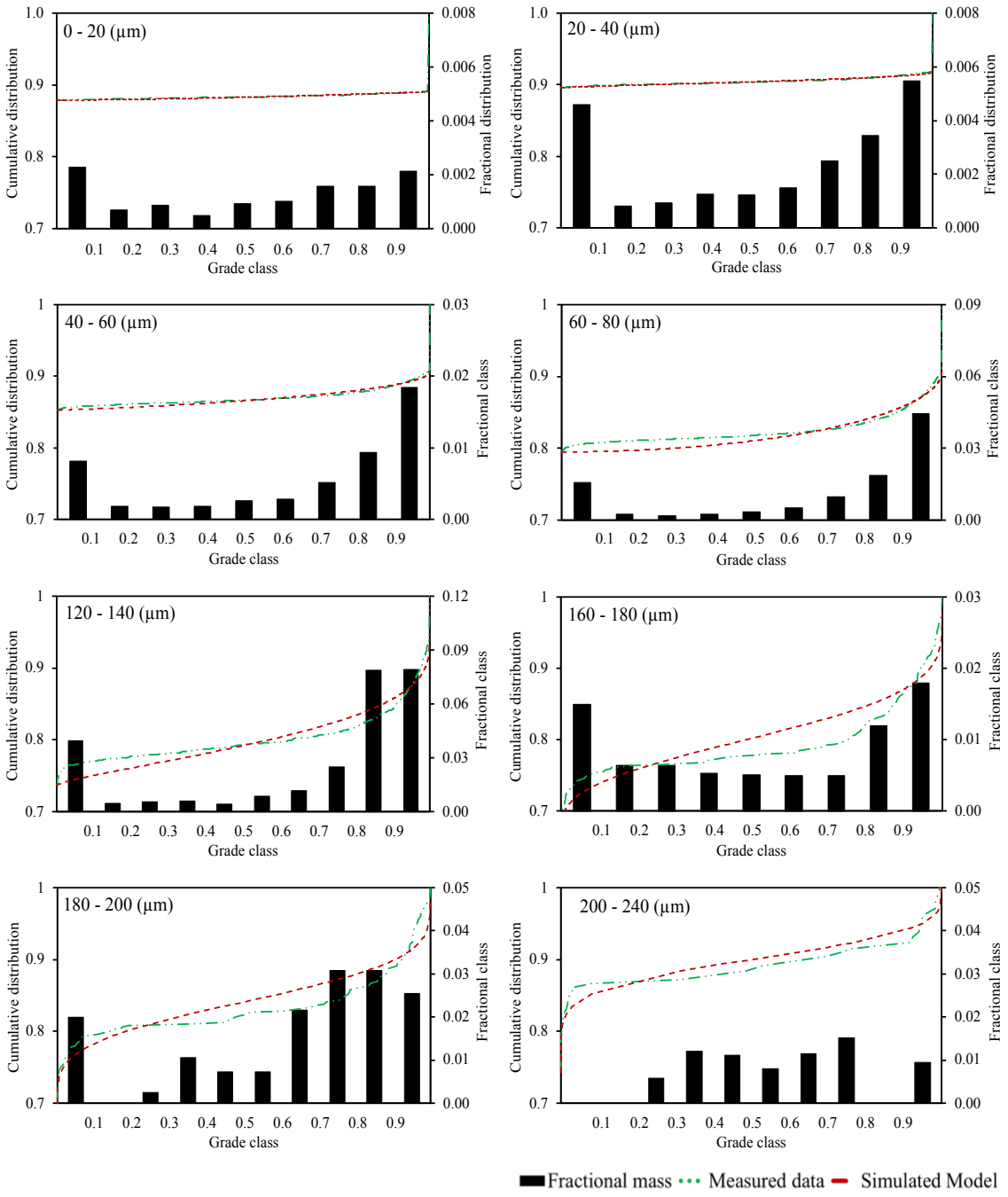

Figure 4.23. Cumulative distribution function for a description of mineral liberation in the Penouta ore (open pit) for different sizes.

With these dates, the density (ρ(g)) and cumulative mass (P(g)) modelling equation can be written. Below there is the general formulation of these equations.

$$\rho(g) = \begin{cases} g = 0 & L_0 \\ 0 < g < 1 & (1 - L_0 - L_1)\ \frac{g^{\alpha^M - 1}(1-g)^{\beta^M - 1}}{\int_0^1 x^{\alpha^M - 1}(1-x)^{\beta^M - 1} dx} \\ g = 1 & L_1 \end{cases} \quad (4\text{-}5)$$

$$P(g) = \begin{cases} 0 \le g < 1 & L_0 + (1 - L_0 - L_1)\ \frac{1}{\int_0^1 g^{\alpha^M - 1}(1-g)^{\beta^M - 1} dg} \int_0^g x^{\alpha^M - 1}\,(1-x)^{\beta^M - 1} dx \\ g = 1 & 1 \end{cases} \quad (4\text{-}6)$$

The parameter α^M and β^M define the performance of the distribution, and they can transform the function from bell-shaped to U-shaped. For the Penouta ore (open pit) the distribution in the range of 0-180 μm is U-shaped and only in two last graphs (180-240 μm) from Figure 4.23 change to the bell shaped. This is good approximation and show that the fine particles have better distribution than the coarse particles. The sample are in the U-shaped, but the parameters α^M and β^M changes in the sample. They decrease when the particle size increase (Figure 4.24).

The variation of distribution function parameters with a constant liberation rate constant was investigated, and the results are shown in Figure 4.24. The values of α^M and β^M seem to satisfy a linear relationship while the liberation rate is constant, with correlation coefficients of 0.90 and 0.89, respectively. It follows that α^M and β^M values may be predicted from the liberation rate constant as follows:

$$\alpha^M = -0.11x + 1.30 \quad (4\text{-}7)$$

$$\beta^M = -0.07x + 0.99 \quad (4\text{-}8)$$

The relationship can be further interpreted to show that finer particles are expected for high α^M and β^M values. This agrees with what is displayed in Figure 4.24.

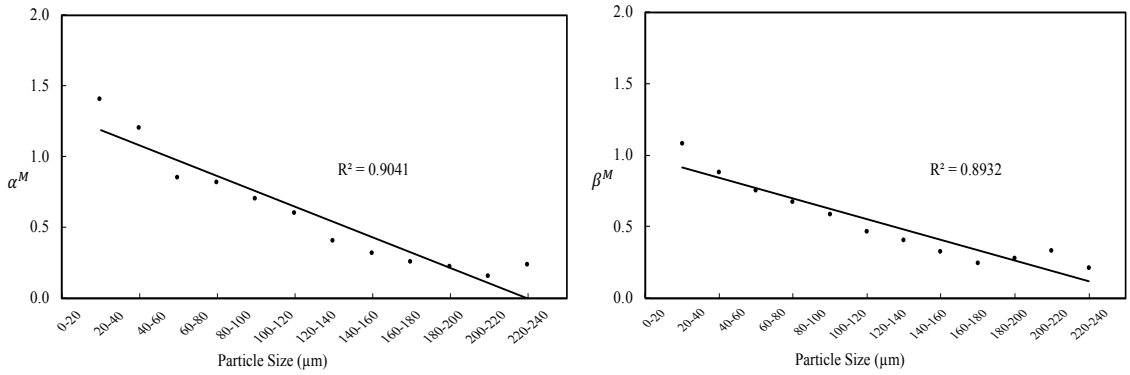

Figure 4.24. Beta distribution parameters of Penouta open pit sample for a description of mineral liberation. The potential tendency line is indicated.

4.1.7 Key findings

A comprehensive mineralogical assessment was undertaken using Level 2 characterization. The mineralogical characterization supported the use of a concentration process to recover and liberation modelling of tantalum through the production of a tantalum concentrate.

The key findings for Penouta ore (open pit) are summarized below:

1) Gangue mineralogy was represented mainly by kaolinite and quartz in this case study. The gangue mineralogy did not pose any significant issues with regard to the selection of concentrate as the separation process for liberation modelling.
2) Tantalum occurred mainly as solid solution in Sn-Ta (99% of the tantalum in the mill product from the mineralogical characterization). Therefore, the concentration process was developed to target the recovery of CGM.
3) From mineral liberation models, it was found that tantalum was well liberated in the mill product and a small proportion of the tantalite was present in the coarser size fractions which show poor liberation of tantalum, which resulted in the incorporation of mainstream inert grinding.
4) The grain size of the CGM minerals was relatively fine. Du to these minerals had represented a recovery target, the mill product size may have been a consideration in the development of the flow sheet because a much finer product sizing would have been needed.
5) The beta distribution resulted in an increase of fine fractions indicating that a proportion of the tantalum in the physical separation feed was fine.

This case study shows that cassiterite, which in almost all processing of base metal ores is considered as gangue, can be the most important mineral. It can carry the valuable element, which transforms this gangue mineral into the most important mineral to be recovered. Enhancing the recovery of cassiterite was supported by the mineral characterization for this ore, which was the most important stage for understanding the deportment of tantalum prior to concentration testing.

A combination of feed flow rate, shaking table tilt and angle, and stock rate of the table and the concentration procedure were used to improve the tantalum grade and recovery. As a result of these conditions, a tantalum recovery of 46.28% with a grade of 103 ppm was obtained from the ore, through batch rougher separation tests performed in one stage.

The liberation study by size indicated that cassiterite was mainly recovered in the liberated form, followed by binary composites and, to a lesser extent, as ternary composites. The main losses of this mineral were as binary composites in the 106 μm fraction (-180 μm+38 μm) and the size fraction below this one.

4.2 Penouta tailings

The Penouta tailings used methodology Level 1 to characterize this material that still is rich in ore minerals. The analytical procedures used were chemical analysis and mineralogy determined by XRD, optical microscopy and mineral liberation analyzer. In the following sections the output of these techniques is described.

4.2.1 Particle size distribution

The samples obtained from the tailings were sieved in 13 different sizes. The weight % retained fraction of two representative samples of the trench area is indicated in (Table 4.10).

Table 4.10. Particle size distribution of sample 7 and 8 from Balsa Grande.

Size (mm)	Sample 7 (wt%)	Sample 8 (Wt%)
>2	3.56	4.02
1.7-2.00	6.22	5.18
1.25-1.70	16.08	11.65
1.00-1.25	12.04	10.45
0.71-1.00	13.12	13.09
0.6-0.71	6.52	7.85
0.5-0.6	3.10	3.48
0.4-0.5	5.71	7.12
0.3-0.4	7.70	8.99
0.25-0.3	3.94	4.68
0.16-0.25	9.57	9.46
0.063-0.16	8.20	6.24
<0.063	4.24	1.10

4.2.2 Chemical composition

Ta content is highly variable in the different types of materials from Penouta. The greisens dump has 10-18 ppm of Ta, the Balsa Pequeña tailings has 79-215 ppm Ta. Results of samples obtained from different heights in the pit test of Balsa Grande, the richest area are in Table 4.11 (Pen-7 to Pen-10). The residue from the pilot plant that tested with raw materials from Balsa Grande also was analyzed and it has 20.3 ppm.

The composition of Penouta tailings, is similar to the Penouta open pit, and Size-by-size analysis of a bulk representative sample (Table 4.12) indicated that the – 160 μm size fraction had the highest tantalum analysis, while the coarse size fraction evaluated (+ 600 μm) had the lowest tantalum analysis. Ta content is varying from 40 - 226 ppm, Nb from 40 - 123 ppm and

Sn from 186 - 1110 ppm.

The composite sample used in this study has about 95 ppm of Ta. After laboratory concentration, the Ta content in the waste from the tailings sample was 20 ppm Ta. The Ta content varies with the grain size as demonstrated the analyses of the different size fractions. The Nb and Sn contents follow the same trend (Figure 4.25). The bulk analysis for U and Th showed a low content of these elements, while the fine size fractions are highly enriched, thus, they can be concentrated in the Ta concentrate.

Table 4.11. Chemical composition of Balsa Grande samples from Penouta tailings.

Oxides (Wt%)	Pen-7	Pen-8	Pen-9	Pen-10
SiO_2	80.65	59.26	76.59	74.45
Al_2O_3	9.30	10.35	9.01	11.56
TiO_2	0.05	0.05	0.10	0.03
FeO	0.68	0.82	1.13	0.73
MnO	0.08	0.10	0.26	0.12
CaO	0.06	0.07	0.06	0.06
MgO	0.12	0.12	0.18	0.08
K_2O	4.65	5.07	3.80	5.92
P_2O_5	0.02	0.02	0.02	0.03
Total	95.60	75.87	91.16	92.98
Traces (ppm)				
Nb	40	85.9	123.5	69.5
Ta	44	160	226	107
Sn	186	559	1110	312
W	417	321	292	228
U	2.2	3	3.2	3.3
Th	2.9	4	3.5	3.6
Pb	9.2	10.3	13.8	13.3
Rb	1200	1310	891	1470
Cs	49.7	56.3	43.3	59.6
Ba	192	235	267	98
Be	275	242	235	189

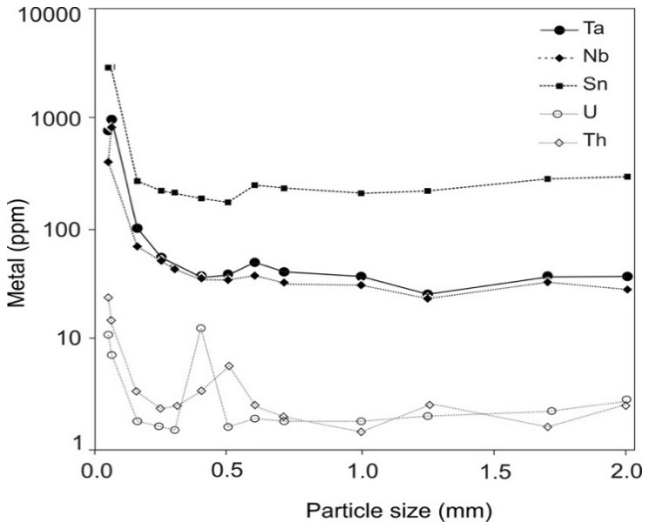

Figure 4.25. Variation of Ta, Nb and Sn with the particle size of the Penouta tailings.

Table 4.12. Chemical composition by fraction size (mm) of sample Pen-8 for Penouta tailings.

Size (mm) / Oxides (Wt%)	>2	1.70-2.00	1.25-1.70	1.00-1.25	0.71-1.00	0.60-0.70	0.50-0.60	0.40-0.50	0.30-0.40	0.25-0.30	0.16-0.25	0.06-0.16	<0.063
SiO_2	88.14	92.63	69.53	85.15	88.78	75.52	77.66	76.59	75.31	72.95	70.81	69.32	58.62
Al_2O_3	6.27	3.65	3.38	4.12	6.44	10.54	11.19	12.83	14.25	14.79	14.93	17.18	26.83
TiO_2	0.10	0.02	0.02	0.02	0.03	0.07	0.07	0.07	0.07	0.07	0.07	0.05	0.05
FeO	1.20	0.55	0.53	0.64	0.69	0.78	0.78	0.87	0.95	1.02	1.00	0.86	0.85
MnO	0.07	0.07	0.06	0.05	0.07	0.09	0.07	0.09	0.12	0.14	0.18	0.20	0.13
CaO	0.06	0.04	0.01	0.04	0.04	0.03	-	-	0.06	-	-	0.07	0.03
MgO	0.20	0.05	0.05	0.07	0.08	0.13	0.12	0.15	0.15	0.15	0.13	0.12	0.12
K2O	2.11	1.13	1.13	1.69	3.52	6.62	7.33	8.60	8.88	8.46	7.33	6.48	5.21
P_2O_5	0.03	-	-	-	0.02	0.02	0.02	0.03	0.03	0.03	0.03	0.04	0.05
Total	98.18	98.14	74.70	91.78	99.69	93.81	97.24	99.22	99.80	97.60	94.48	94.31	91.88
Traces (ppm)													
Nb	28.3	33	23.4	31	32.7	37.8	34.5	35.7	43.2	51.7	69.6	839	408
Ta	37.2	37.6	25.6	37.2	40.8	49.9	38.9	37.5	43.7	55.3	102	995	785
Sn	299	286	222	212	235	251	175	190	215	223	273	2980	2940
W	780	839	486	327	355	300	522	307	206	341	178	12.6	8.9
U	2.7	2.2	2	1.8	1.8	1.9	1.6	13.2	1.5	1.6	1.8	7.2	11
Th	2.6	1.6	2.5	1.5	2	2.5	5.6	3.4	2.4	2.4	3.3	14.2	23.9
Pb	40.3	-	21.2	19.1	10.6	23.4	16.2	20.7	25	21.7	23.3	35.8	18.8
Rb	532	289	268	378	754	1470	1430	1960	2190	2060	1890	1620	1310
Cs	47.6	34.6	21.2	22.6	34.9	60.4	58.1	80.7	91.3	94.1	88.4	76.7	67.4
Ba	116	73	38	49	70	112	85	110	120	116	120	111	84
Be	818	814	348	204	119	121	92	114	130	156	203	158	34

4.2.3 Mineralogical characterization

4.2.3.1 Bulk mineralogy

In the Penouta tailing the distribution of minerals is largely dependent of the particle size fractions. A semiquantitative determination by XRD using sieved samples from the tailing (Figure 4.26) shows that quartz is most abundant in the coarse particle size fraction, K-feldspar is more abundant in the medium size fractions, whereas albite and kaolinite are concentrated in the smallest fractions. The mineral distribution depends on the hardness of the minerals and the original texture. Quartz has the highest hardness of the major minerals and a significant amount occurs in grains of 1-2 mm. However, plagioclase is constituted of thinner crystals. Kaolinite is the product of alteration of feldspars and it is a clay mineral with a maximum grain size of few microns.

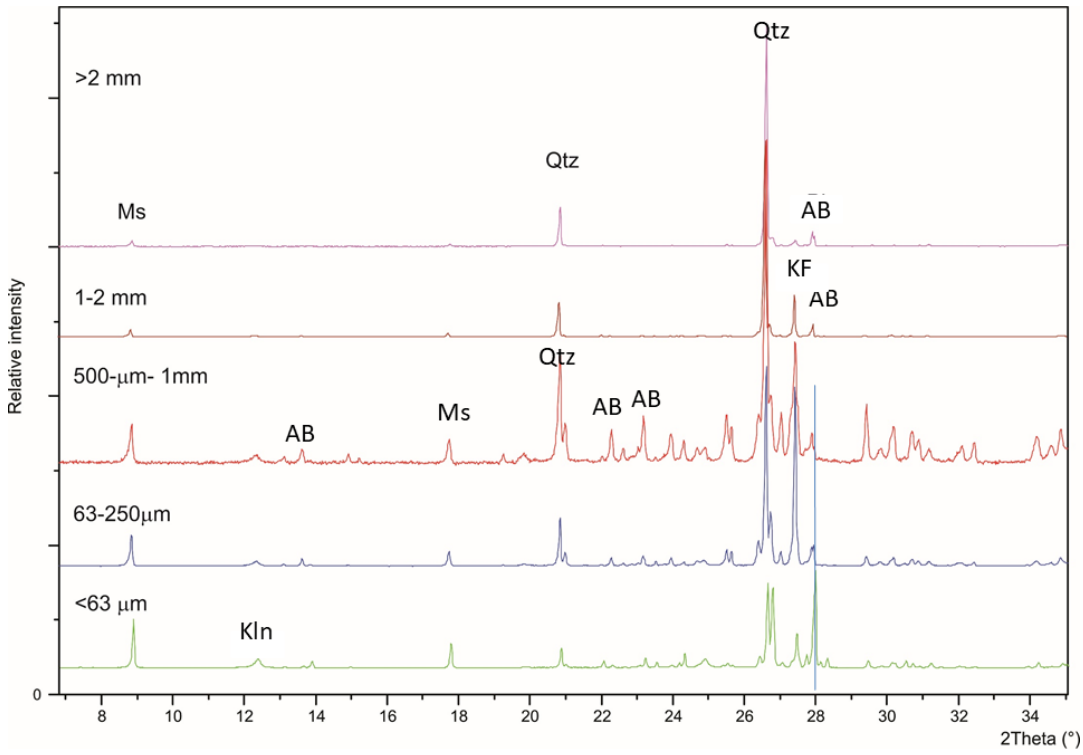

Figure 4.26. XRD diagrams that show the mineralogical composition of different particle size fractions in which the composite sample of the tailing was divided. Qtz, quartz; Ab, albite; FK, K-feldspar; Ms, muscovite; kln, kaolinite.

4.2.3.2 Tantalum-bearing oxide minerals

The ta-rich minerals are similar than those from the open pit. Most of oxides are mainly members of the CGM. CGM. Textures are similar than in the previous presented ores, with the most common textural pattern constituted by grains with a Ta-rich core and a Nb-rich rim (Figure 4.27). The EMPA results indicate that most CGM are classified as manganocolumbite and

manganotantalite. Columbite-tantalite crystals are usually zoned with a Nb-rich core and a Ta-rich rim; in other cases, crystals exhibit convoluted and patchy zonings (Figure 4.27), which is the result of the variation in the Ta/(Ta+Nb) ratio, being the Mn/(Mn+Fe) moderate, always with predominance of Mn.

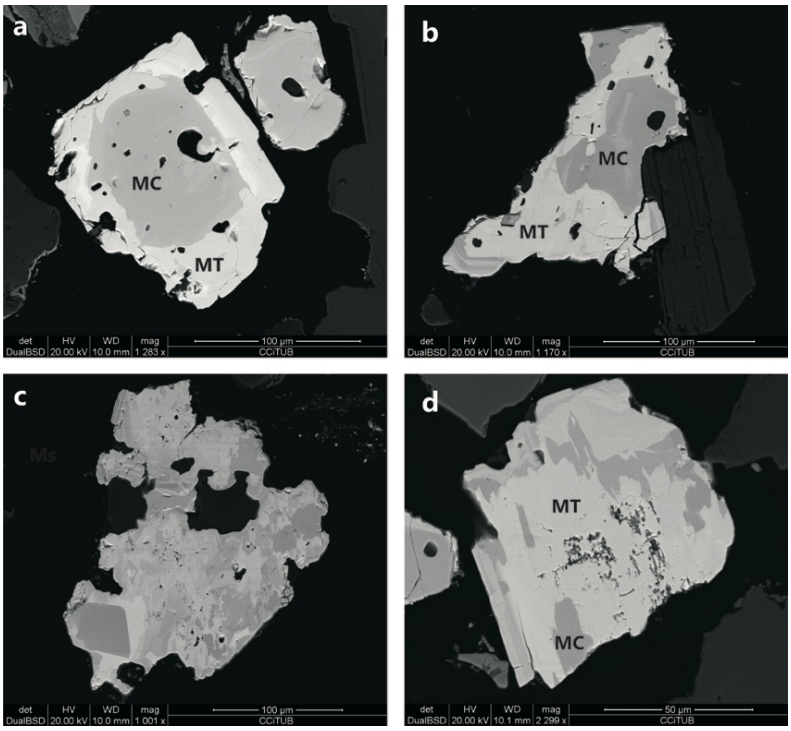

Figure 4.27. Columbite group minerals from the Penouta ore showing different textures: (a, b), concentric zoning; (c, d), patchy zoning. MC, manganocolumbite; MT, manganotantalite.

Microlite and wodginite, occur in minor amounts. Cassiterite is the most abundant ore mineral and occurs as homogeneous subhedral to anhedral crystals. Chemical composition shows a high Ta content, up to 9 wt.% of Ta_2O_5.

4.2.4 Characterization of the processed tantalum ores from tailings

As noted in the literature review, bulk concentration is used when there is a low concentration of base metal tantalum minerals in the ore. Accordingly, based on the mineralogical characterization, the concentration, was selected as the most appropriate concentration strategy to be used for recovering tantalum from these tailings.

Various concentration strategies were used to finally achieve the best processing flow sheet for this ore. The preliminary flow sheets and the operational conditions from the different batch tests were presented in Chapter 3. The first step was to perform the preconcentration test; various samples were tested to find the best concentration conditions for the tantalum minerals; then the incorporation of the ore minerals concentration was achieved, the shaking table setup

step was done; and finally, the amount of the appropriate flow rate to the flow sheet aimed to obtain a higher recovery and grade as a final product.

4.2.4.1 Quantitative automated mineralogy

To obtain the quantitative mineralogy, mineral liberation analysis (MLA) was used. This technique provided the characterization of 6481 grains and 21344 particles from a concentrate obtained from the tailings of the ancient exploitation of the Penouta mine. The results of EMPA were used to create the data base for the MLA mineral identification. Mineral distribution was mapped for visual appreciation and observation of shapes and texture (Figure 4.28). All size fractions were used to estimate the key mineralogical attributes, such as modal mineralogy, elemental classification, and texture for the ore.

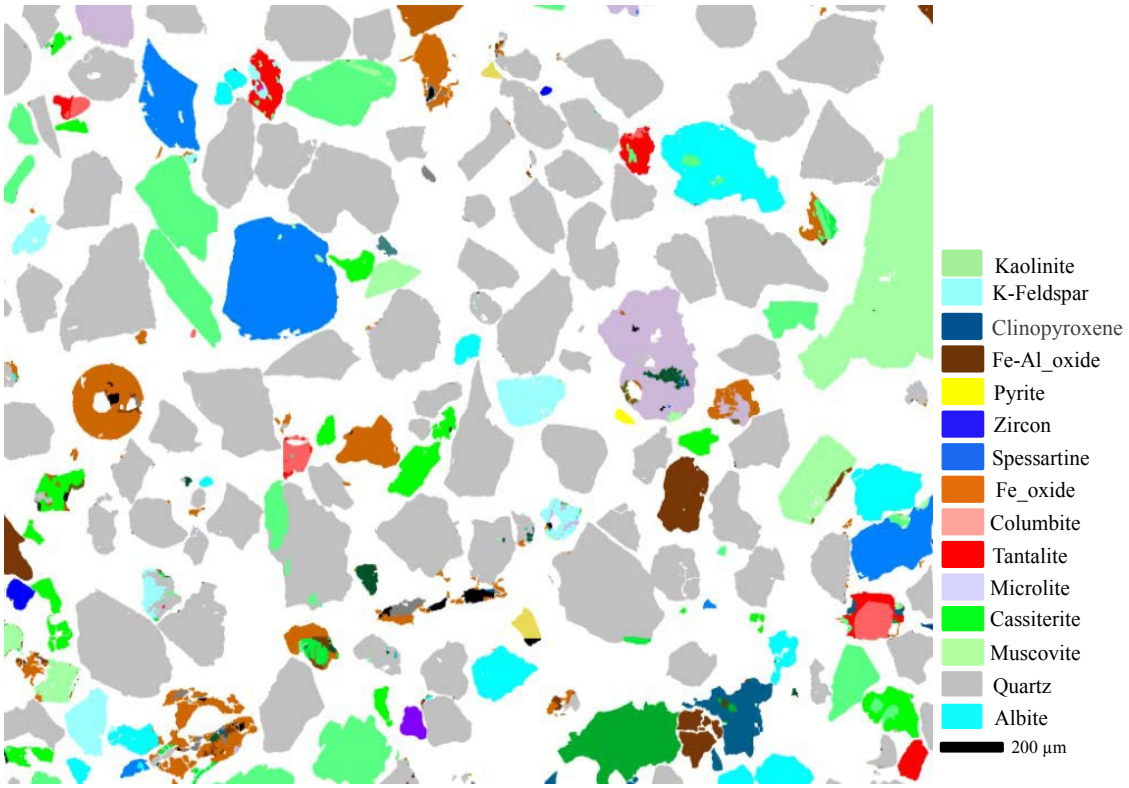

Figure 4.28. Representative pseudo-color particle maps from the Mineral Liberation Analysis of Penouta tailings.

4.2.4.2 Size distribution characteristics of the sample

❖ **particle size distributions (PSD)**

The particle size distributions (PSD) of the various stages of the sample are shown in Figure 4.29. For the laboratory test work, the particle size distribution for the sieved samples

resulted from the grinding stages as well as for the particle sized material with cumulative passing of the samples from sieving of the sample. The PSDs are broad with a shallow slope, although the ball mill PSD of tailing are steeper than those of the open pit. The size range for this work was selected to compare the two sample types in a size region where there is some overlap between the usages of the ball mill, with a relatively coarse feed size for ball mill. The particle size distribution in the concentrate varies according to the grade in CGM. In the sample, particles of liberated CGM have an average size <120 µm, whereas size from those with a CGM grade from 67 to 99 wt. % ranges from 150 to 250µm.

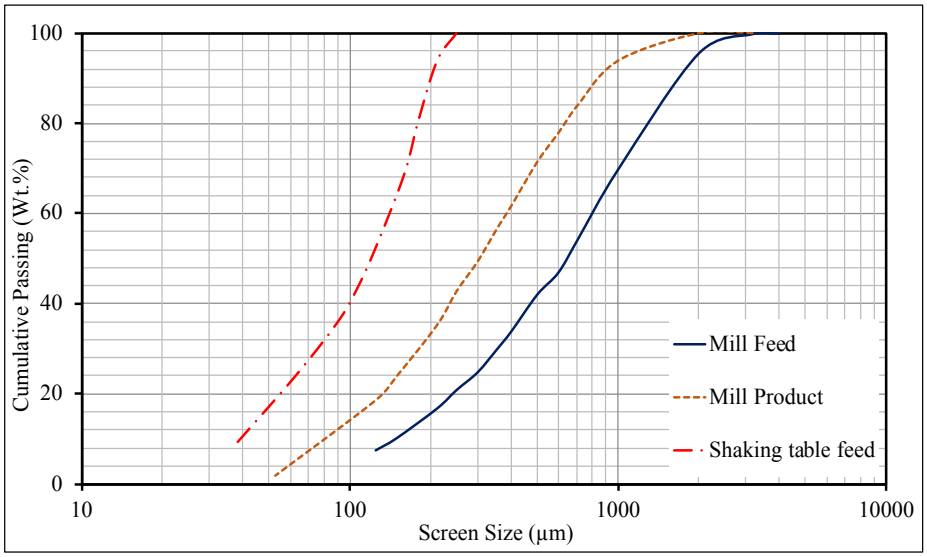

Figure 4.29. Particle size distributions of samples milled in the laboratory; tailings sample as determined by screening.

❖ Mineral grain size

The mineral grain size distributions of all columbite group minerals (CGM) minerals using MLA were grouped together to improve the number of observations and the confidence limits were evaluated. The graph in Figure 4.30 shows that most columbite and tantalite crystals are less than 150 µm, being those of tantalite slightly smaller than columbite. The tantalum minerals had a mineral grain size with a P80 of approximately 121 µm, this type of particle is expected as the size fraction measured was -250+100 µm. Pittard, 2010 also argue that when mineralogical analysis is performed in small or trace constituents, that is the case of this thesis i.e., tantalum; the key constituent is distributed on a small scale in the material to be sampled. Therefore, "liberated or not, the coarsest grains of such constituent must be measured and placed into the context of their average (Pitard, 2010).

Therefore, in this case fine grains are considered to be properly chosen. Indeed, this was confirmed with the concentration results and the stepped in the graph helped to choose the grain size (Appendix C).

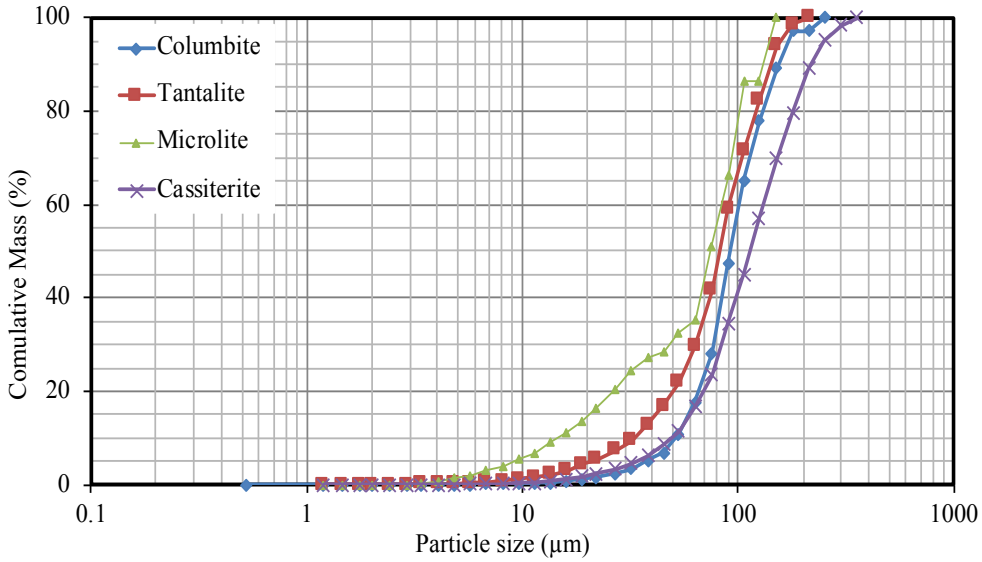

Figure 4.30. Grain size of ore minerals from the Penouta tailings determined by MLA.

❖ Mineral recovery by size

For analysis of mineral recovery-by-size for Penouta tailings, modal mineralogy from the MLA was used, because it provides a good reconciliation between the chemical analysis and the MLA's elemental analysis. Note that elemental analysis provides the total concentration of elements from various minerals in which they exist. In this ore, Ta analysis represented the total concentration from the contributions of CGM minerals. Figure 4.31 shows the mineral recovery-by-size graph for the combined tantalum minerals for this ore.

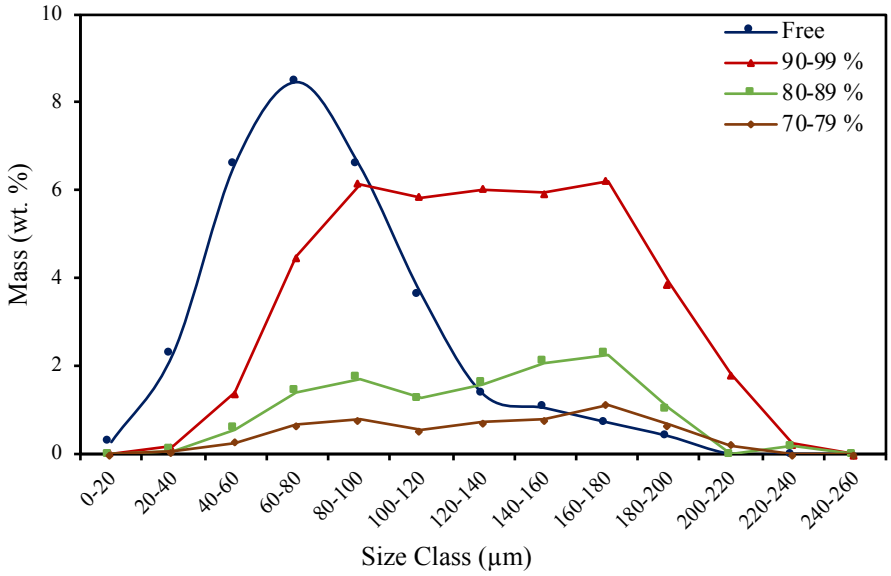

Figure 4.31. Size distribution of CGM-rich and liberated particles.

The tantalum minerals give a regular curve with the recovery-by-size data in comparison

to the well-known inverted U shape usually displayed in these types of analysis (Figure 4.31). Different zones can be identified in the graph as fine, intermediate and coarse zones. The finest zone (-100 µm) had the highest recovery for tantalum (free), the intermediate zone (-200+100 µm) illustrated a moderate decrease in the recovery (90-99%).

4.2.4.3 Modal Mineralogy

The MLA analysis of Penouta tailings identified the presence of approximately 55 different minerals (see Appendix D) with quartz, cassiterite, Fe_oxides and muscovite as the most abundant minerals. These results were consistent with XRD analysis. The most abundant ore mineral is cassiterite (10.15 wt. %), followed by tantalite (2.0 wt. %), columbite (1.35 wt. %) and microlite (0.11 wt. %). The columbite tantalite ratio is 0.7 for the tailing material (Figure 4.32). Although wodginite was determined by EMPA, it was not detected with MLA; it could be because this mineral is too similar to columbite-tantalite in terms of BSE contrast and energy dispersive spectrum. Several sulphides were determined; the most abundant was pyrite, with 0.7 wt. %. Other silicate minerals determined by MLA are garnets of spessartite type, with 4 wt. %, albite, with 2.3 wt.% and k-feldspar, with 2.41 wt.% and kaolinite, with 1.93 wt.%.

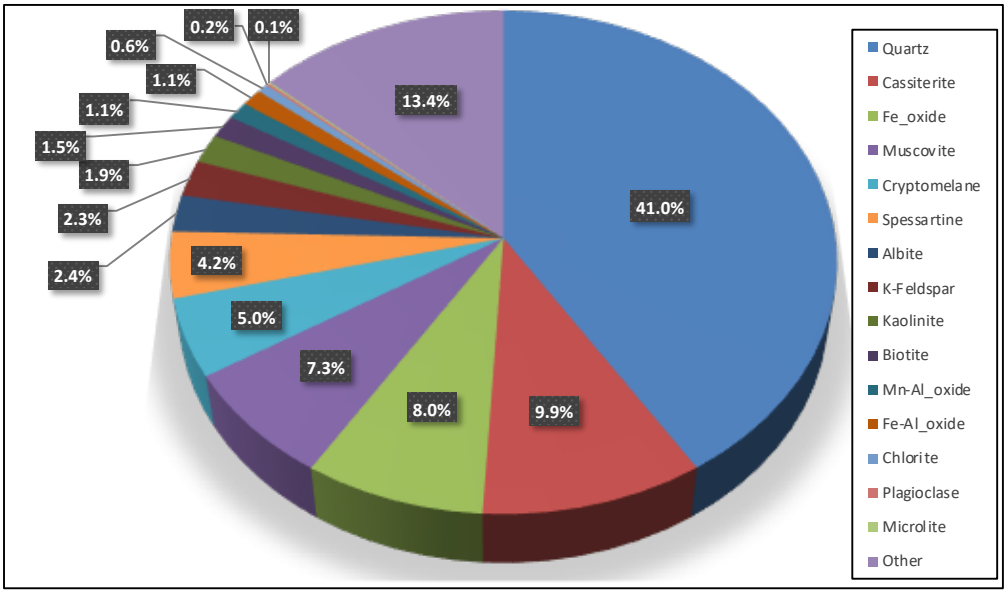

Figure 4.32. Modal mineralogy of Penouta tailings.

4.2.4.4 Mineral association

Analysis of the elemental deportment for Penouta tailings focused on Ta carriers due to the presence of large grains of columbite, cassiterite and other Ta-bearing minerals identified using both XRD and MLA. The MLA data indicates the ratio of columbite and tantalite that is

liberated or located in binary and ternary particles. As the CGM are a combination of columbite and tantalite, the CGM particles liberated are the sum those minerals when they are completely liberated and those binaries that contain only both minerals. The classification of these particles shows that 33.4 wt.% of tantalite completely liberated and about 51.00 wt.% there are in the binary particles (Table 4.13). The mineral association information was used to find if there were any Ta minerals that tended to associate with any minerals that may be considered problematic in a concentration context e.g. muscovite. It was also used to establish if any Ta minerals were associated with minerals which were recoverable by concentration, to assist with design of a processing strategy (Appendix E).

Mineral association with CGM depends on the particle grade of this mineral. When CGM are in a low grade, they usually are associated with cassiterite, whereas in the particles with more than 90 wt.% of CGM, they are mainly associated with muscovite, but also other minerals occur, as quartz, feldspar and kaolinite (Figure 4.33).

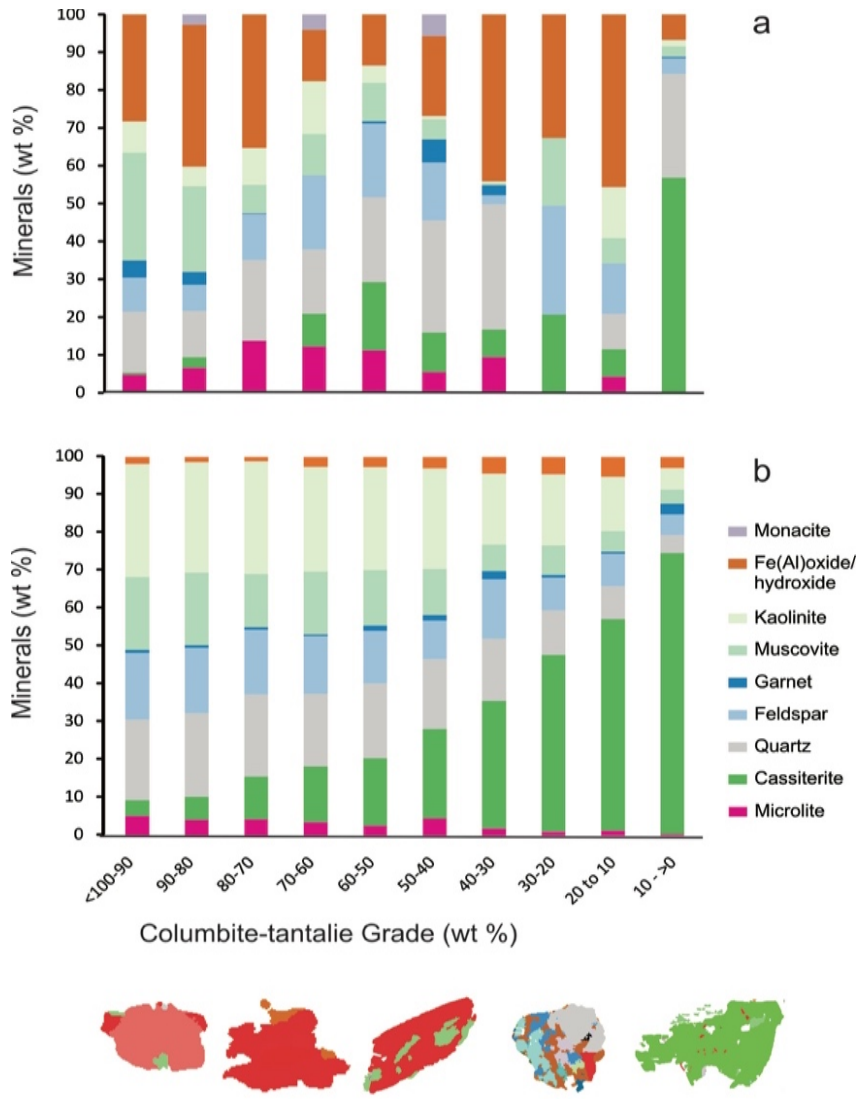

Figure 4.33. False color images showing the minerals association of CGM for the Penouta ore (a, open pit; b, tailings).

The mineral association of CGM is quite different in the tailing and in the open pit. In the tailing, cassiterite is most important; this is probably due to the former exploitation of cassiterite. Iron oxides, or hydroxides, are more abundant in the tailing, whereas kaolinite predominates in the open pit. Most of this iron oxides are not appeared as minerals and it could be the crashed particles from the mechanical machines which used during the previous processing of the ore.

Table 4.13. Classification of the ore, containing particles from Penouta tailings determined by Mineral Liberation Analysis.

Particles (wt.%)	Columbite	Tantalite
Liberated	16.6	33.4
Total Binary	63.62	51.0
Total Ternary	19.6	15.6
Total (Lib+Bin+Tern)	100	100
Liberated CGM	76.46	66.3

Tantalite is 2.2 to 2.7 times more liberated than columbite, probably due to the lower grain size of this mineral. The columbite-tantalite liberated particles are between 66 and 78 %. Most of the non-liberated columbite-tantalite particles are binary, where this mineral is mainly associated with muscovite or quartz, and less frequently with feldspar. A significant amount of tantalite from the open pit can occur associated with kaolinite. These results are significant for the optimization of the comminution and recovering process.

Table 4.14. Liberation and mineral locking of columbite group minerals (CGM) from Penouta tailings.

Weight % locked in...	Columbite	Tantalite
Liberated (%)	16.60	33.38
Columbite	-	32.94
Tantalite	59.86	-
Microlite	0.02	1.05
Cassiterite	0.11	1.15
Quartz	1.45	3.93
Albite	0.00	0.34
Plagioclase	0.00	0.00
K-Feldspar	0.35	1.27
Almandine	0.00	0.00
Spessartine	0.00	0.12
Biotite	0.00	1.46
Muscovite	0.20	4.24
Chlorite	0.00	0.01
Kaolinite	0.00	0.73
Mn,Fe,Al oxides	1.06	2.43
Zircon	0.53	0.00
Monazite	0.01	0.00
Xenotime	0.00	0.00
Crandallite	0.00	0.01
Pyrite	0.00	0.00
Other	19.79	16.94

Cassiterite is liberated in most of the particles (73-81 %). In other particles it is associated with muscovite (about 8 %) or quartz (4.4 %), Mn,Fe,Al oxides (4.2 %) and K-feldspar (2.1 %).

The results of a concentration feed characterization illustrate the status of the ore prior to a concentration test, allowing understanding of the final requirements for grinding in order to develop a flow sheet for processing this complex low-grade tantalum ore.

For Penouta tailings, the degree of liberation (Table 4.14) by mass of CGM minerals were analyzed at different size fraction of liberation and then was estimated using mineral liberation modelling and simulation methods.

Tantalite presented a higher degree of liberation when compared with columbite. For the Ta, the change in the degree of liberation for the Penouta tailings at different sizes was modeled. It was found that the finer size has a higher amount of Ta. This supports that coarse grinding (+ 600 μm) will allow reasonable Ta recoveries with the use of shaking table as the primary treatment for this ore.

Key findings of mineralogical characterization

The results from characterization of the ore resulted in the following key findings:

The valuable element of CGM was accounted for by tantalum, columbite and other minerals (shown in Table 4.13).

Tantalum in the -250 μm fraction of the ore is mainly associated with cassiterite, followed by muscovite, and in lesser extension also other minerals occur, as quartz, feldspar and kaolinite to Ta minerals, being these the tantalum carriers. Complex textures are present in the fine particulates (- 120 μm) analyzed and include features such as rimming minerals and intergrowth textures.

The mineral grain size for tantalum minerals (-150 μm size fraction) was fine in the ore characterization samples, due to the presence of large grains of tantalite (with a P80 of 121 μm) indicating fine grinding would be required to achieve sufficient levels of liberation for physical separation; this was supported by liberation analysis of the shaking table feed.

The information gained from the mineralogical characterization of this ore suggested that selective concentrate would be appropriate to recover the tantalum minerals. The selection of proper factor (flow rate, shaking table angle and stock rate) would selectively handle the tantalum minerals concentrate relative to the CGM present, noting that the ore contained base metal cassiterite.

4.2.5 Work index and energy consumption

Figure 4.34 show the relationships between the work index and the degree of tantalum

liberation in the processed material, the cumulative distribution of the liberated tantalum with the class mean size and the work index. The work index of the studied tailings ranges from 14.43 to 33.21 kWh/t, according to the particle size of the feed. From the figure, most of the liberated CGM has a size smaller than 200 µm, and about 80% of the liberated tantalum has a size smaller than 150 µm. The increase in the work index indicates a change in the consumed energy of the ore during the grinding. This has a negative impact on the milling energy costs. From a size smaller than 150 µm, with the progress of tantalum liberation production, the increase in the ore work index increases the energy consumption per ton of milled ore. This information helps determine the optimum operational conditions of mineral liberation in order to reduce energy consumption.

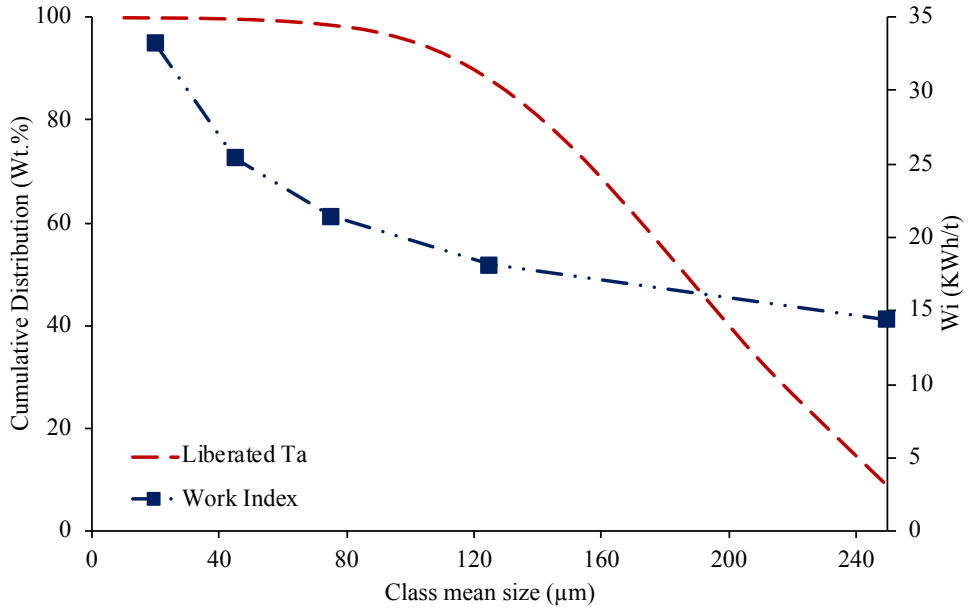

Figure 4.34. Dependence of work index on the cumulative distribution of Ta content in the material.

4.2.6 Simulation and Predication of Mineral Liberation for Penouta tailings

The main objective of the mineral liberation modelling was to investigate how the Penouta tailings ore would respond to concentration during a reprocessing, by using a combination of preconcentration and a factorial experimental design (to optimize grind size, concentration rate and minimize energy).

4.2.6.1 Mineral Liberation analysis (MLA)

A predictive liberation model was developed using a CGM ore and the gangue minerals. The calculation of distribution density and modelling of liberation is shown in Figure 4.35. Using

mineral liberation analyzer data, differential mass of all samples at different grade classes and size fractions were determined. From the figures the observed liberation size is -200 µm, due to this range represent the population of 80 % of the liberated particles. In the tailing, 99.2 wt.% of the particles do not contain CGM. Most of the particles-bearing CGM are or considerably rich (>90 wt% or poor (<10 wt% CMG). As Figure 4.35 shows, in most CGM particles with less than 10 wt.% CGM the predominant mineral is cassiterite. Textural observations indicate that these are cassiterite particles that contain small inclusions of CGM. Although this grade class represent 0.7 wt.% of the bulk leucogranite, it has about 0.03 wt.% of the total CGM (see Appendix A).

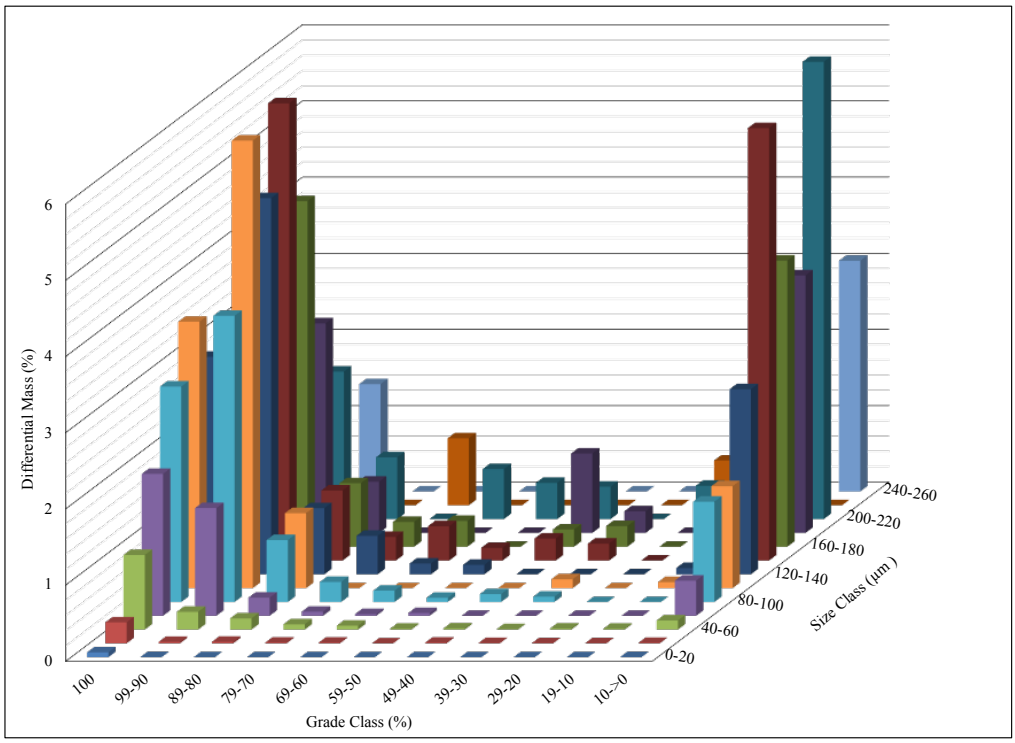

Figure 4.35. Distribution of the concentrate particles according their CGM grade classes, and particle size from Penouta tailings.

To complete the liberation distribution shown in Figure 4.35, Eq. (4-6) and the extent data were used to calculate the linear grade distribution of the CGM and liberated particles. The modeled values are compared with the measured distributions for eight size fractions (Figure 4.36).

The parameters α and β of the beta distribution function were calculated using the MATLAB, which are shown as cumulative distributions (Figure 4.36). Series of mineral liberation function equation were calculated based on this extracted data (Appendix B). These included beta distribution function of tantalum and relative density of each mineral within the sample.

The back calculated grade distributions must match the measured distributions, giving

the experiment data as shown in the Figure 4.36. When the particle size is distinctly smaller than the sizes of the mineral grains, the tendency for liberated and nearly liberated particles to appear is greatly enhanced and the beta distribution function reflects this tendency by exhibiting a strong U-shape (King, 2012). This is good approximation and it happened in the all fractions (0-200 µm). Otherwise, the distribution is bell-shape.

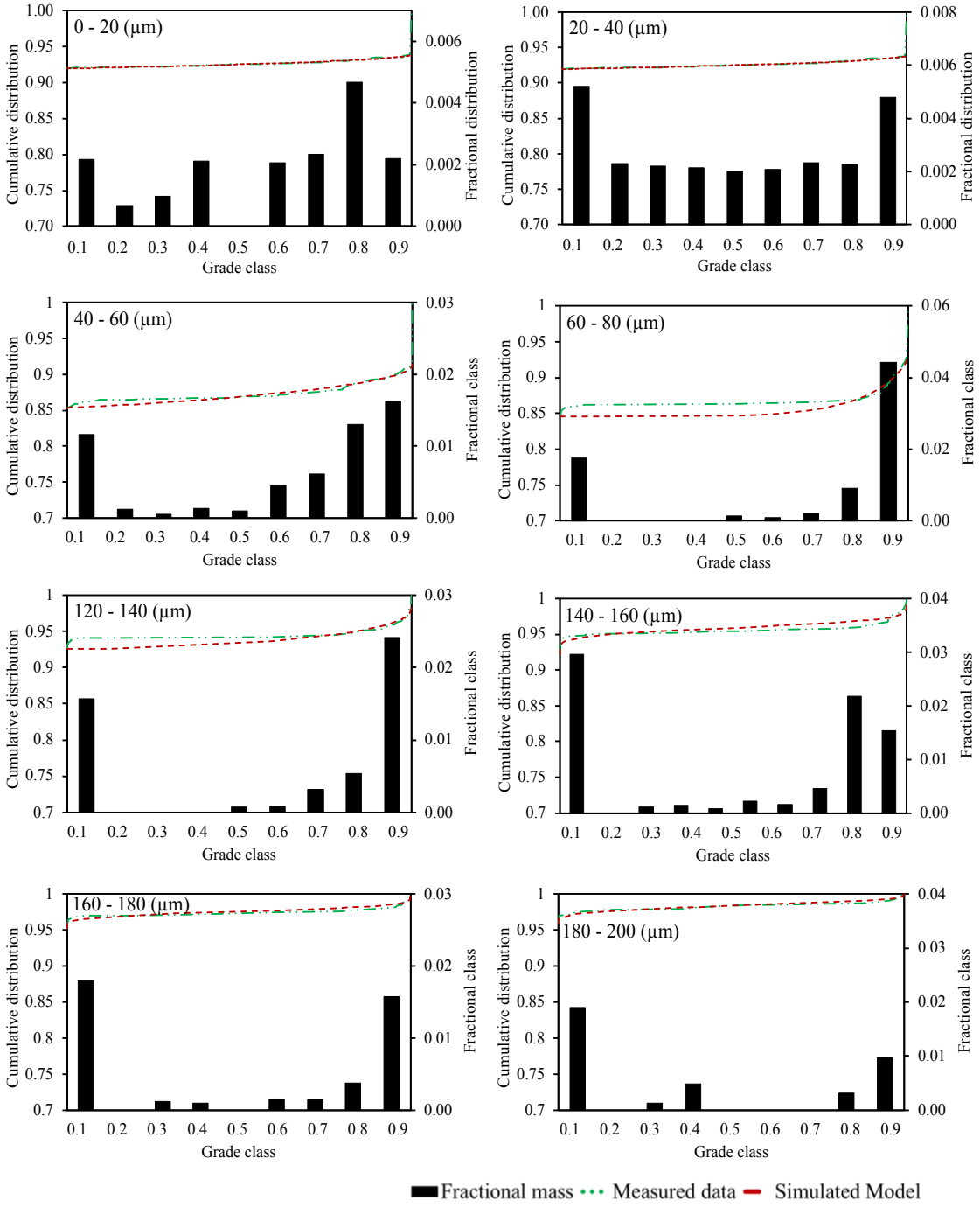

Figure 4.36. Cumulative distribution vs grade class of ore for eight cases in different particle sizes for Penouta tailings. The difference between the simulated and experimental data is shown.

To describe the mineral liberation distribution for different particle size the distribution

density of the sample shows that changing from bell-shaped to U-shaped occurred from lower graphs (180-200 μm) to upper graphs (20-60 μm) and It was not repeated for the size fraction of lower than 20 μm. Modelling results are shown in Figure 4.36 for the tantalum ore, where these is a comparison of the cumulative mass from the experimental data with the simulated data in different size class. The results show a reasonable fit to data in almost all interval sizes. In most cases the curves should superimpose upon each other, if α^M and β^M values are normalizable. Reasonable fitting is observed in almost all interval size, indicating that the calculated liberation could be a good approximation if the cumulative distribution is correct. Also, from Figure 4.36, it can be seen that the sample show a typical behavior as the distribution function do not depend on the particle size. The parameter g was from zero to one.

The variation of distribution function parameters with a constant liberation rate constant was investigated, and the results are shown in Figure 4.37. The values of α^M and β^M seem to satisfy a linear relationship while the liberation rate is constant, with correlation coefficients of 0.95 and 0.89, respectively. It follows that α^M and β^M values may be predicted from the liberation rate constant as shown in Eq. 4-9 and 4-10.

$$\alpha^M = -0.40x + 5.34 \quad (4\text{-}9)$$

$$\beta^M = -0.63x + 7.70 \quad (4\text{-}10)$$

The relationship can be further interpreted to show that finer particles are expected for high α^M and β^M values. This agrees with what is displayed in Figure 4.37.

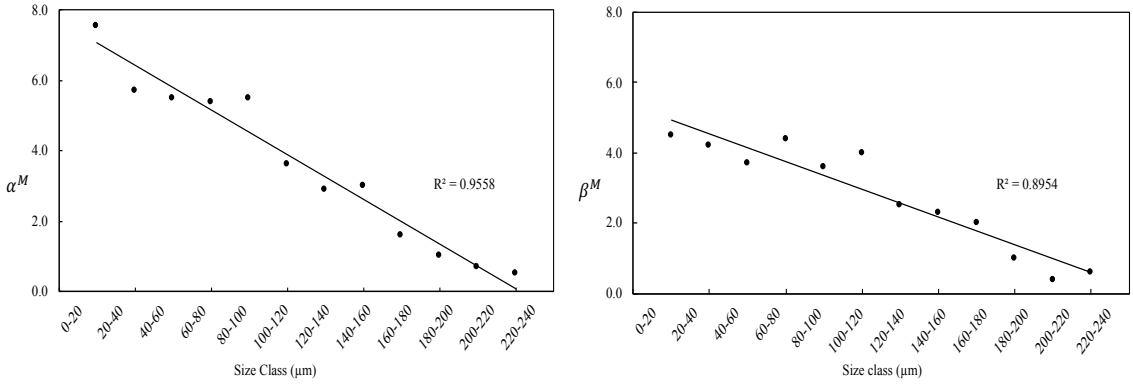

Figure 4.37. Beta distribution parameters of Penouta tailings sample for a description of mineral liberation. The potential tendency line is indicated.

Key findings

Modelling liberation of Penouta tailings was undertaken with the aim of developing a concentration flow sheet based on the key mineralogical characterization identified; these included:

1) Gangue mineralogy is represented by CGM, mainly cassiterite followed by quartz. The low

occurrences of minerals also indicated that this ore could be classified as a low-grade ore. No potentially problematic gangue minerals in the context of concentrate were identified.

2) Modelling liberation observed that the liberation size is -200 μm, due to this range represent the population of 80 % of the liberated particles. In the tailing, 99.2 wt.% of the particles do not contain CGM. Most of the particles-bearing CGM are or considerably rich (>90 wt% or poor (<10 wt% CMG). The grain sizes of the tantalum minerals are fine, indicating that it would be necessary to grind the shaking table feed to a fine size in order to achieve liberation.

3) The results show a reasonable fit to data in almost all interval sizes. In most cases the curves should superimpose upon each other, if α^M and β^M values are normalizable. Reasonable fitting is observed in almost all interval size, indicating that the calculated liberation could be a good approximation if the cumulative distribution is correct.

The use of selective concentrate for recovering a rich tantalum rougher concentrate was successfully undertaken for this complex low-grade tantalum ore from Penouta. The results obtained demonstrate that the use of the concentrate process for this type of ore is appropriate, using a combination of ball mill and shaking table feed particle size distribution (P80 of 191 μm) to obtain a tantalum concentrate with a grade of 103 ppm and a recovery between 66 and 78 %.

4.3 Mittersill ore

In the following section, the results of the Mittersill ore characterization are discussed with the emphasis on understanding the scheelite deportment and the liberation of the scheelite minerals that were the recovery targets in concentration.

The discussion begins with the most relevant results from chemical analysis and a description of the protocol that was developed to find the scheelite minerals that were initially identified from MLA analysis. This was then used to inform the standard modelling liberation of scheelite from Mittersill ore. This protocol, together with the other tools used in the characterization, provides an overall picture of the mineralogical characteristics and mineral liberation modelling for this ore.

4.3.1 Chemical composition

The chemical composition of the whole sample from the Mittersill processing plant is presented in Table 4.15. In the sample, the high content of MgO, FeO, and CaO is indicative that tungsten is associated with calc-silicate rocks. The W content is 2260 ppm, which indicates a medium-grade deposit. It also contains 7.17% CaO, 59.30% SiO_2, and 12.25% Al_2O_3. The W content for the concentrate and tailings material that resulted from physical separation is 3.52% and 0.13%, respectively.

Table 4.15. Chemical composition of the sample from the Mittersill processing plant.

Oxides	SiO_2	Al_2O_3	MnO	TiO_2	FeO	MgO	CaO	Na_2O	K_2O	MnO	P_2O_5	LOI	Total
(wt.%)	59.30	12.25	0.14	0.74	6.96	5.94	7.17	2.77	1.30	0.79	0.09	1.55	99.00

4.3.2 Size distribution characteristics of the sample

❖ **particle size distributions (PSD)**

The cumulative particle size distributions (PSDs) of the various streams of the flowsheet are shown in Figure 4.38. For the test work, the PSDs are broad with a shallow slope, although the shaking table feed, feed and mill product sample PSDs are steeper than the feed. About 53% of the mill material is smaller than 250 μm, and about 43% of the milled material in the shaking table feed is smaller than 106 μm. The measured particle size distribution shows that 80% of the concentrated material is approximately smaller than 106 μm. It was found that fine particles are strongly dominant in the shaking table feed data compared to analytical sieving.

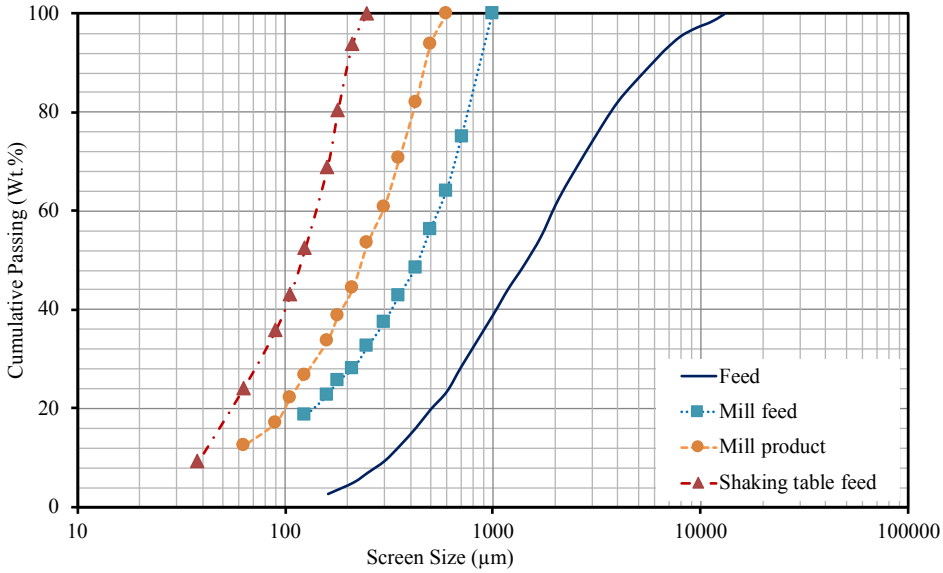

Figure 4.38. Particle size distribution of the feed, mill product, concentrate, and tailings of the ore sample obtained from gravity separation.

❖ Mineral grain size

The MLA data provide information on the size of all the measured particles. It is possible to determine the distribution of scheelite in the different particle size fractions and its liberation grade. Scheelite is significantly concentrated in the −250 + 106 µm size fractions. This is because scheelite grains occur naturally in these grain sizes of the ore deposit. The MLA-estimated scheelite grain size in the gravity concentrate is shown in Figure 4.39 (Appendix C).

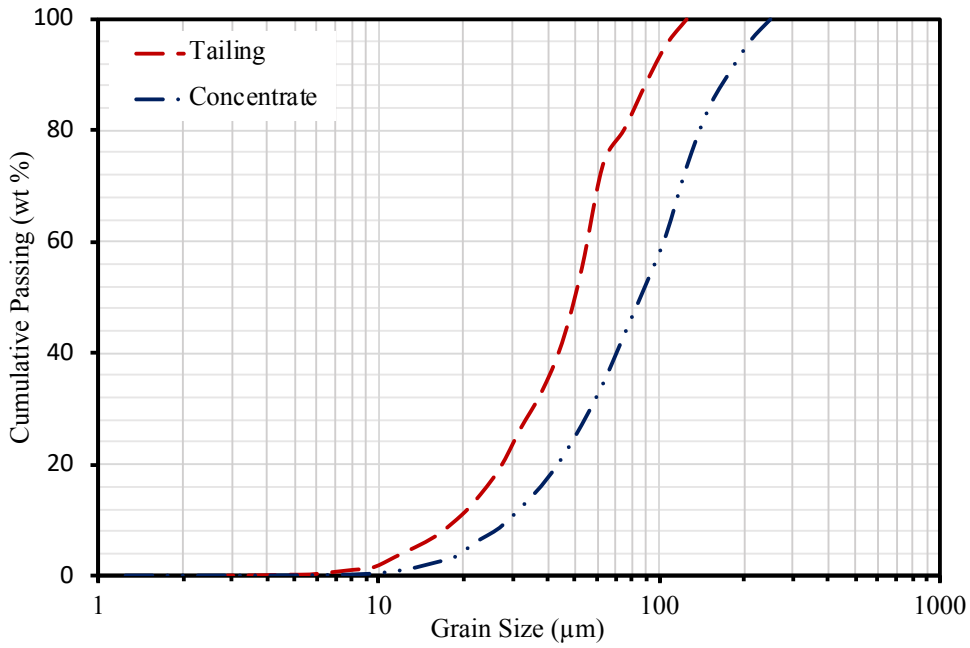

Figure 4.39. Mineral grain size distribution of scheelite from the sample determined by MLA.

The average grain size is 106 μm, and most grains are <250 μm. This information, coupled with the findings from the particle size distribution section, indicates that about 20% of scheelite grains are resistant to grinding and fractures in W-bearing. Figure 4.39 also shows the grain size distribution of the tailings. Almost all grains are <125 μm in the tailings and would require further grinding for sufficient liberation. This would significantly improve the liberation characteristics of scheelite and prove that coarser grinds can achieve sufficiently liberated scheelite. This suggests that coarse complex particles containing scheelite in the tailings are more difficult to grind, which may provide opportunities for concentrations at even coarser particle sizes.

4.3.3 Modal mineralogy

A combination of XRD and MLA analyses enabled a successful characterization of the mineralogy of the ore-bearing sample. Overall, 55 minerals were identified (Appendix D).

The averaged results of XRD and MLA measurements in the feed, concentrate, and tailings are presented in Table 4.16. The sample contained a similar content in hornblende and titanite in the concentrate and tailings. Actinolite and plagioclase content was highly variable. Expectedly, quartz concentrations above 17 wt.% were found in tailings, and about 7 wt.% concentrate minerals were found in the ore.

Table 4.16. Modal mineralogy of the whole sample, concentrate, and tailings determined by X-ray powder diffraction (XRD) and mineral liberation analysis (MLA).

Mineral (wt.%)	Density	XRD			MLA	
		Ore	Tailings	Concentrate	Tailings	Concentrate
Scheelite	6.01	0.35	0.20	17.01	0.85	17.82
Quartz	2.62	15.30	15.37	6.74	17.13	7.50
Plagioclase	2.68	22.30	22.42	7.90	28.27	8.39
K-feldspar	2.56	4.50	4.54	0.51	2.87	0.49
Hornblende	3.23	33.00	27.95	20.79	28.47	20.18
Actinolite	3.04	6.40	6.24	1.00	-	-
Pyroxene	3.40	1.00	8.02	3.20	9.08	2.91
Vesuvianite	3.40	-	0.98	0.27	-	0.22
Epidote	3.45	4.30	1.00	15.47	0.42	14.88
Biotite	3.09	7.70	5.90	2.92	6.22	1.80
Muscovite	2.82	-	2.15	0.30	1.76	0.28
Chlorite	2.65	4.90	-	0.29	-	0.41
Titanite	6.01	-	1.63	3.50	1.51	3.64
Fe oxide	2.62	-	0.02	0.31	0.04	0.17
Apatite	2.68	-	0.18	0.45	0.22	0.60
Calcite	2.56	-	1.50	0.63	1.45	0.70
Fluorite	3.23	-	0.02	0.04	0.02	0.04
Fe sulfide	3.04	-	1.10	17.35	1.06	18.20
Chalcopyrite	3.40	-	0.02	0.75	0.03	0.83
Arsenopyrite	3.40	-	-	0.11	-	0.13
Total		99.75	99.24	99.54	99.40	99.19

Scheelite is the only W-bearing mineral from the studied ore which was reported in MLA and XRD. The observation of the ore under UV light allowed the scheelite grains to be differentiated. All of them exhibit a bluish luminescence, which is typical when this mineral has a low content of molybdenum (Rozendaal, 2014). Other phyllosilicate minerals such as muscovite occur in minor amounts. Epidote, K-feldspar, and titanite are also present. The gangue mainly comprises quartz, plagioclase, hornblende, pyroxene, and biotite (Figure 4.40).

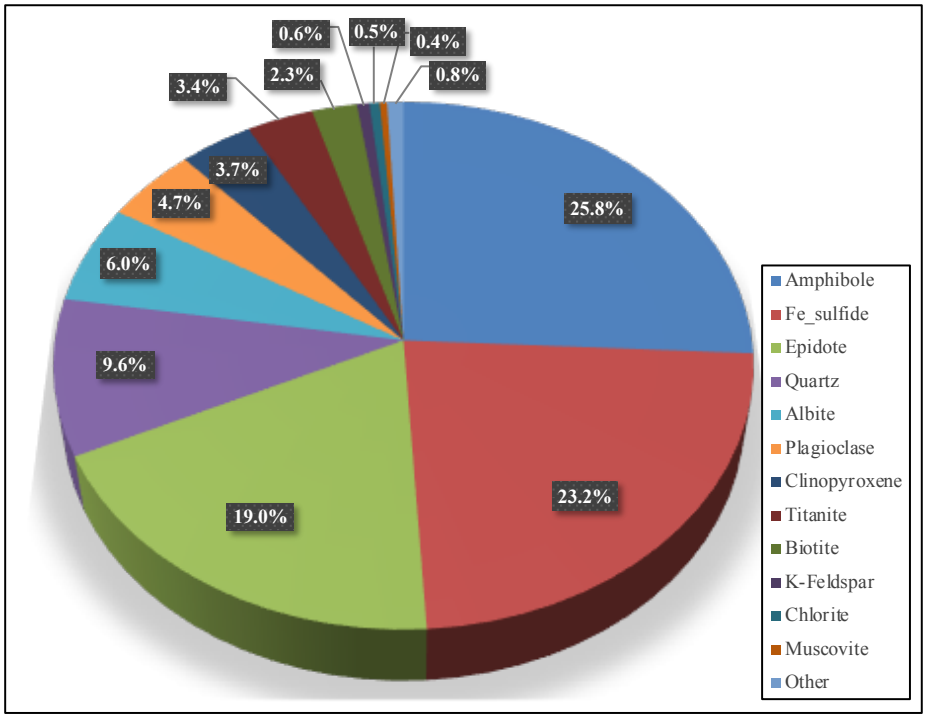

Figure 4.40. Modal mineralogy of the concentrate determined by MLA for Mittersill ore.

4.3.4 Mineral association

After this, the gravity concentration of the mineral association from the concentrate and tailings was determined using XRD and MLA. Predictably, low-density minerals are concentrated in the tailings, which are enriched in quartz, plagioclase, biotite, and muscovite. On the contrary, scheelite, sulphides minerals, and epidote are concentrated in the high-density fraction.

The distribution of the hornblende minerals varies. Hornblende is the predominant mineral in the concentrate and tailing in the ore. Titanite and epidote have a relatively high density (6.01 and 3.45 g/cm^3, respectively) and thus are concentrated in the heavy fraction, whereas the quartz and plagioclase (albite) content is variable in the tailings and remains in the light fraction. The comparison shows higher scheelite contents detected by MLA in the concentrate and tailings. A higher concentration of hornblende, epidote, and Fe-sulfide was primarily shown in the concentrate by XRD and MLA. Data acquired by XRD also show a lower content of hornblende compared to the MLA data. In the MLA, actinolite was not reported; it was probably identified

as a pyroxene phase, and thus its composition is similar to other pyroxenes, such as augite.

SEM images show that in the comminuted sample, a high number of scheelite grains are liberated. In other grains, it is associated with other minerals in binary, ternary, or multi-component particles (Figure 4.41).

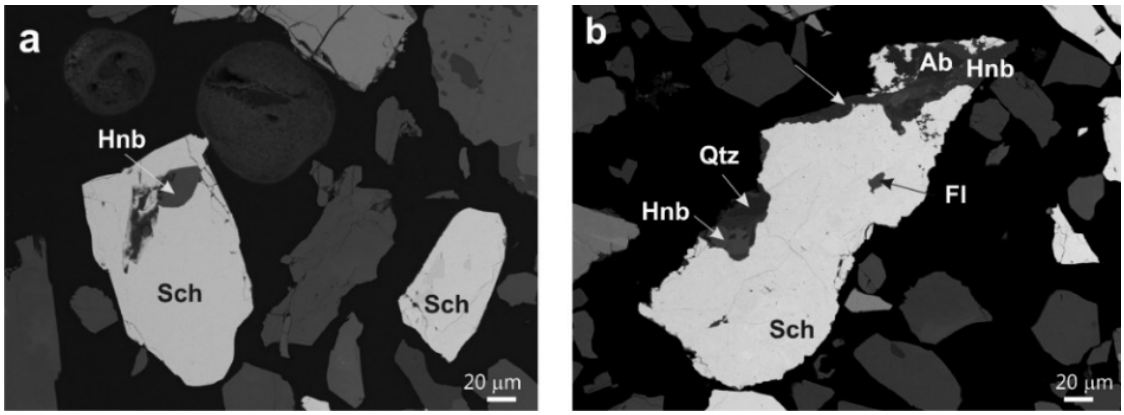

Figure 4.41. SEM-BSE images of the scheelite concentrate: (a) binary particle of scheelite and hornblende, and (b) multi-component particle. Sch, Scheelite; Hnb, hornblende; Qtz, quartz; Ab, albite; Fl, fluorite.

Figure 4.42 represents a color image of an area of the MLA of the concentrate sample. The image shows that the mineral association varies considerably according to the particle size fractions. Scheelite and pyrite are more concentrated in the fine fractions (Figure 4.42).

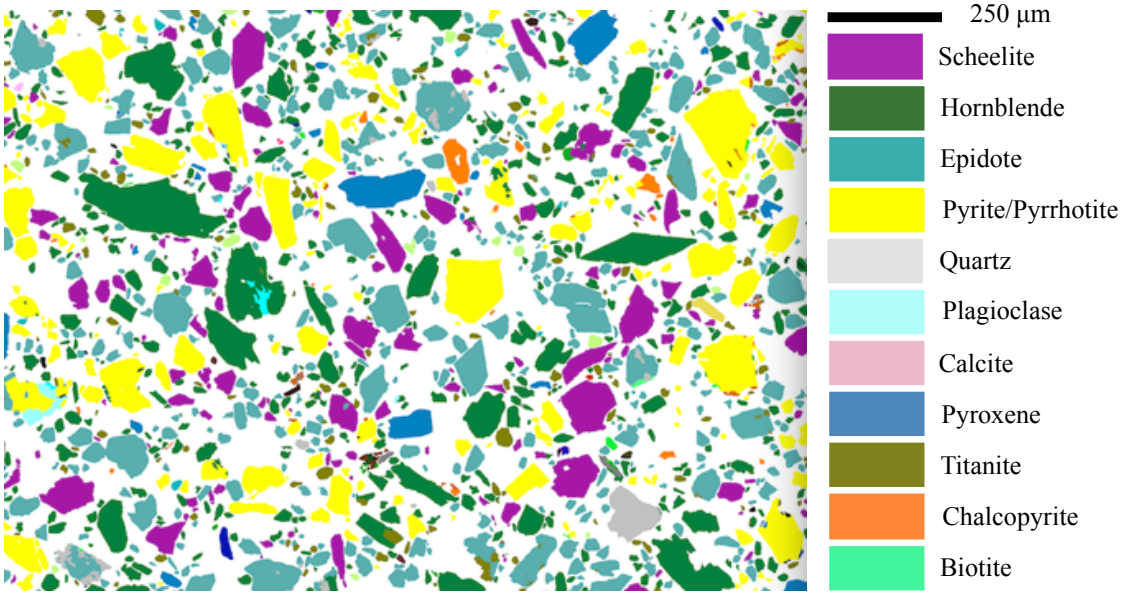

Figure 4.42. Mineral liberation analysis image showing the characteristics of minerals.

The number of characterized particles in the concentrated and tailing samples was 58,162 and 66,248, respectively. In the most basic liberation analysis method, mineral discrimination is only based on BSE grey level contrast, and the liberation data are generated through image analysis (European Commission, 2017). In the present case, scheelite shows a high contrast with

the other possible mineral phases, and it is possible to produce a basic method to calculate the scheelite minerals with a high rate of concentrated scheelite.

The liberation characteristics of scheelite in the concentrated sample are shown in Figure 4.43. More than 87 wt.% of scheelite is liberated, and about 11.2 wt.% occurs in binary particles (Appendix E). In most cases, scheelite constitutes particles associated with epidote, quartz, and hornblende (Figure 4.43).

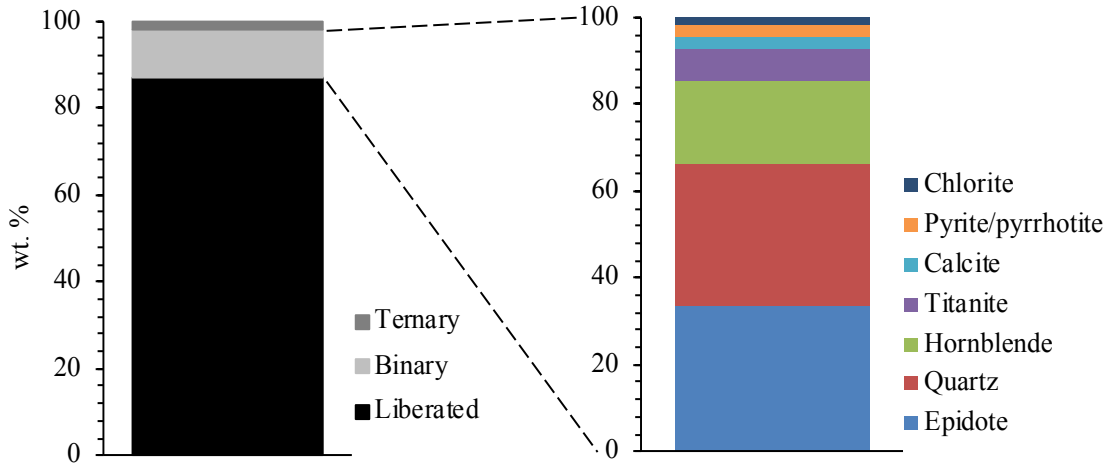

Figure 4.43. Mineral liberation of scheelite and association of non-liberated scheelite grains.

Key findings of mineralogical characterization

The mineralogical characterization of the Mittersill ore was complex because it required a high level in conjunction with the modelling results to finally understand the nature of the scheelite deportment. As a number of analytical and microscopic techniques were used for the ore, a protocol was developed to systematically identify W and even unknown W minerals not in the MLA library. In terms of W deportment, epidote, quartz and hornblende are the main scheelite carriers.

The gangue mineralogy indicated that quartz is the main non-sulphides gangue mineral present, followed by plagioclase (albite). It is possible that these could produce problems via inadequate dispersion and increased flow rate or shaking table angle for a given percentage of minerals. The textures present in the ore are complex, particularly with respect to the fine-grained nature of the scheelite minerals. As a consequence, the liberation level for the combined scheelite minerals in the rougher feed at a P80 of 250 μm was high (87%) indicating a finer separation feed size is needed to liberate the scheelite minerals adequately for physical separation to be effective.

Due to the nature of the scheelite minerals present selective physical separation was selected. As with the Mittersill ore, a combination of shaking table set up and feed rate is an important factor in enhancing the recovery of the scheelite minerals.

4.3.5 Work index and energy consumption

The work index of the studied ore ranges from 8.02 to 15.07 kWh/t, according to the particle size of the feed. The increase in the work index indicates a change in the consumed energy of the ore during the grinding. As was seen before, most of the liberated scheelite has a size smaller than 125 µm, and about 80% of the liberated scheelite has a size smaller than 110 µm. This has a negative impact on the milling energy costs. From a size smaller than 125 µm, with the progress of scheelite liberation production, the increase in the ore work index increases the energy consumption per ton of milled ore. This information helps determine the optimum operational conditions of mineral liberation in order to reduce energy consumption.

The relationships between the work index and the degree of scheelite liberation in the processed material, the cumulative distribution of the liberated scheelite with the class mean size and the work index have been plotted in Figure 4.44. These relationships can be explained by the fact that almost all liberated sheelite is in fine fractions, which causes the work index and energy consumption to increase. The material is a calk-silicate, so scheelite is associated with more than 60% quartz and epidote (Figure 4.43). They are the hardest minerals in the material. Therefore, the work index for the deposit ore may be predicted based on the quartz and epidote content of the material (Wikedzi et. al., 2018).

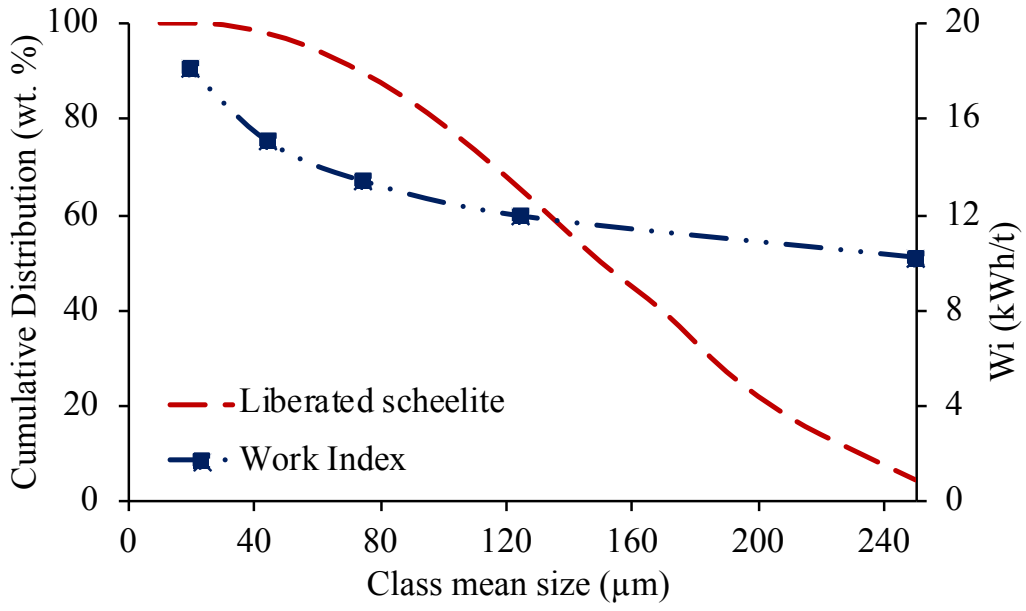

Figure 4.44. Dependence of work index on the cumulative distribution of scheelite content in the material.

4.3.6 Simulation and Predication of Mineral Liberation for Mittersill ore

4.3.6.1 Mineral liberation Analysis (MLA)

The concentrate of the gravity separation was selected for analysis of scheelite liberation. MLA reported data by size and liberation classes of scheelite mineral, which was finely ground and medium grade, used for the characterization in the flowsheet of this work. Using mineral liberation analysis data, the differential mass of the concentrated material with different grades of scheelite has been calculated. Mineralogical characterization was performed by the MLA technique and the stream samples was sized into 13 size classes from 0 to 260 μm using sieve analysis. The distribution of the concentrate mineral (scheelite) by particle size and liberation classes in terms of mass percentage, which was obtained from the data reported by MLA. Here, the highest mineral fractions belong to the medium size and highly liberated particles (5.65%) and less liberated particles (2.32%).

Figure 4.45 illustrates how scheelite treatment has resulted in a distribution of the ore from the low to high grade of liberation classes in the material. To calculate the distribution density, simulation, the range of 0 – 260 μm was divided into a particle size segments with intervals of 20 μm and liberation grade classes of >0–10, 10– 20 . . ., 90–<100 and 100 (Appendix A). In the concentrated sample the liberated scheelite is distributed along with the different size classes as shown in Figure 4.45. The categories presented here are based on the combined fractional area of scheelite, although all particles considered contain one or more scheelite grains.

Particles that contain scheelite show a bimodal distribution with a large amount of concentrate in the >0 to 10% of scheelite grade (Figure 4.45a). However, the amount of scheelite in these particles is small, thus a low quantity of ore would be obtained if they were liberated. The other accumulation of particles containing scheelite is formed by particles with a scheelite grade higher than 90%, where all of them can be considered as liberated.

The 3D diagram (Figure 4.45) indicates that liberated scheelite represents 15% of total mass of the concentrate and about 0.13% of the tailings. It is possible to recover the scheelite phases, with reasonable efficiency, by the use of gravity concentration.

In order to describe the particle populations with different mineral contents, a distribution function based on the beta distribution was carried out (King, 2012).

The equation (4-6) is used as the basis for the calculation of distribution grades when the distribution linear grades are known (King, 2012 and Zhang, 2012). By the use of equation (4-6) and back calculation technic in MATLAB, other parameters such as α^M and β^M have been calculated separately which is prepared in the table in (Appendix B). The n, $\bar{g}$, g^M, L_0 and L_1 are experimental data and they represent the number of particles, average grade, average grade without L_0 and L_1 on their edges, α^M and β^M are the beta function parameters.

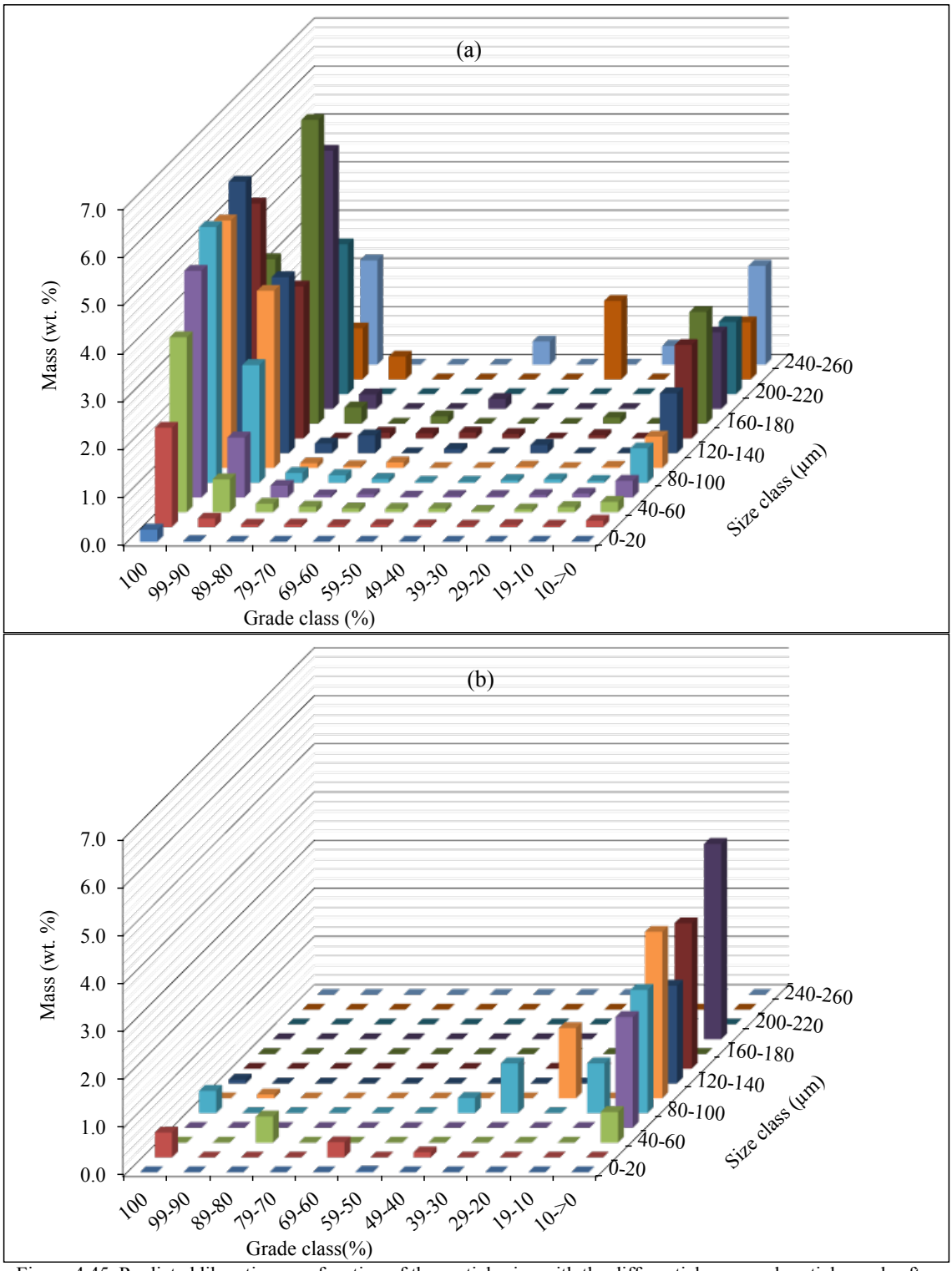

Figure 4.45. Predicted liberation as a function of the particle size with the differential mass and particle grade after comminution and gravity separation. (a) concentrate and (b) tailings resulted from this separation.

To complete the liberation distribution shown in Figure 4.45, Eq. (4-6) and the extent data were used to calculate the linear grade distribution of the scheelite and liberated particles. The modeled values are compared with the measured distributions in Figure 4.46 for eight size fractions.

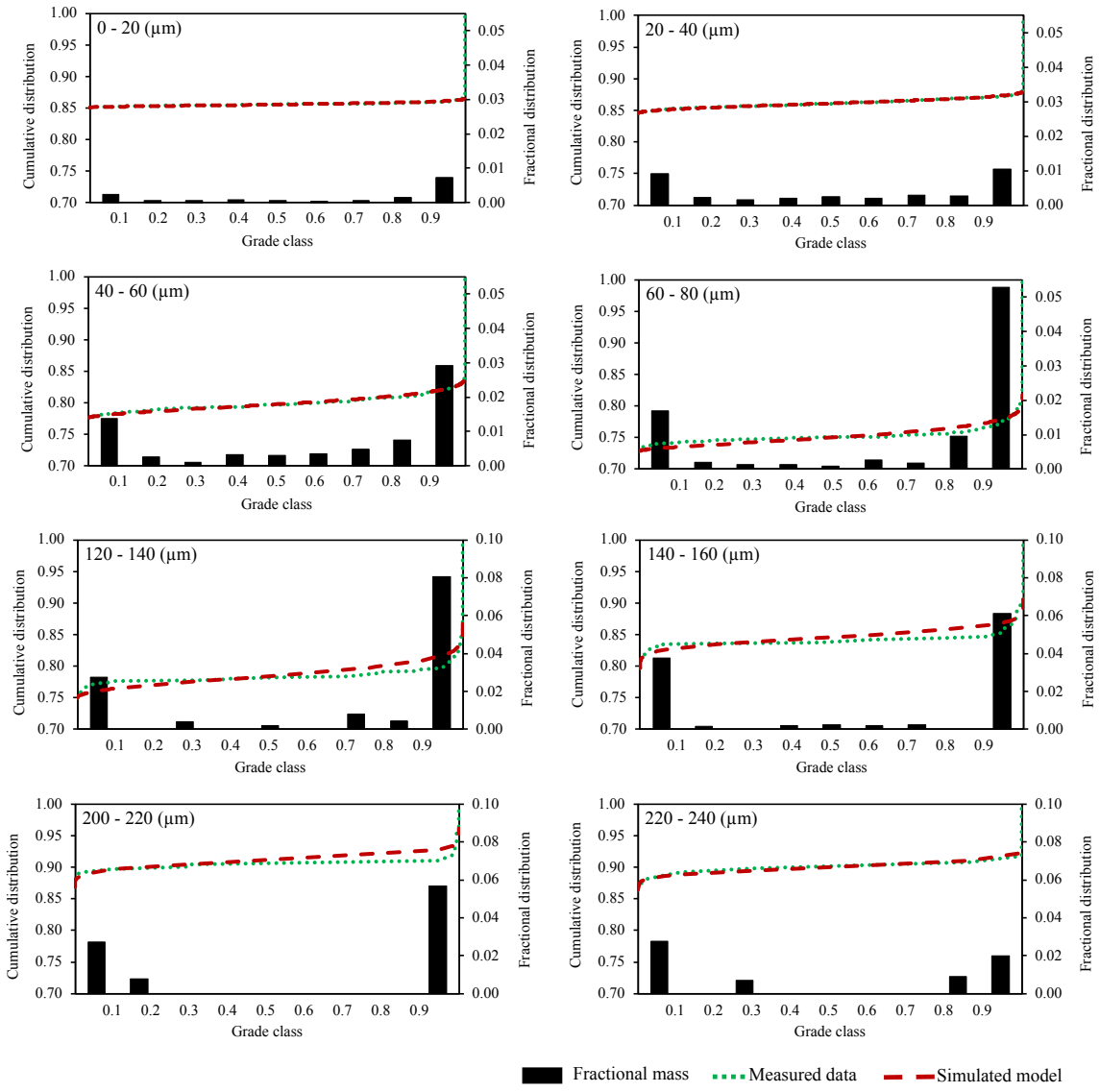

Figure 4.46. Cumulative distribution vs grade class of ore for eight cases in different particle sizes. The difference between the simulated and experimental data is shown.

The back calculated grade distributions must match the measured distributions, giving the experiment data as shown in the Figure 4.46. This is good approximation and it happened in the fine fractions (0-80 µm). Otherwise, the distribution is bell-shape. To describe the mineral liberation distribution for different particle size the distribution density of the sample shows that changing from bell-shaped to U-shaped occurred from lower graphs (200-240 µm) to upper graphs (0-80 µm).

Modelling results are shown in Figure 4.46 for the scheelite ore, where there is a comparison of the cumulative mass from the experimental data with the simulated data in different size class. The results show a better fit to data in some interval sizes than the others (e.g. the interval of 140-160 µm). In most cases the curves should superimpose upon each other, if α^M and

β^M values are normalizable. A reasonable agreement is observed in almost all interval size, indicating that the calculated liberation could be a good approximation of that of the cumulative distribution is correct. From Figure 4.46, it can be also seen that the sample shows a typical behavior as the distribution function do not depend on the particle size. The parameter g was from zero to one.

The sample is from bell-shape to U-shape, and the parameters α^M and β^M decrease when the particle size increase (Figure 4.47). This allows fitting of α^M and β^M values into Eq. (4-6) by back calculation technique and hence calculating the model parameters. In this case, the parameters n, g, g^M, L_0 and L_1 and g were determined by fitting Eq. (4-6) to α^M and β^M values for each fraction size using the back-calculation function in MATLAB. This is an optimization procedure which searches for the best combination of these parameters that minimizes the error between experimental and simulated α^M and β^M values.

The variation of distribution function parameters with a constant liberation rate constant was investigated (Appendix B), and the results are shown in Figure 4.47. The values of α^M and β^M seem to satisfy a linear relationship while the liberation rate is constant, with correlation coefficients of 0.90 and 0.92, respectively. It follows that α^M and β^M values may be predicted from the liberation rate constant as follows:

$$\alpha^M = -0.05x + 0.79 \quad (4\text{-}11)$$

$$\beta^M = -0.04x + 0.64 \quad (4\text{-}12)$$

The relationship can be further interpreted to show that finer particles are expected for high α^M and β^M values. This is in agreement with what is displayed in Figure 4.47.

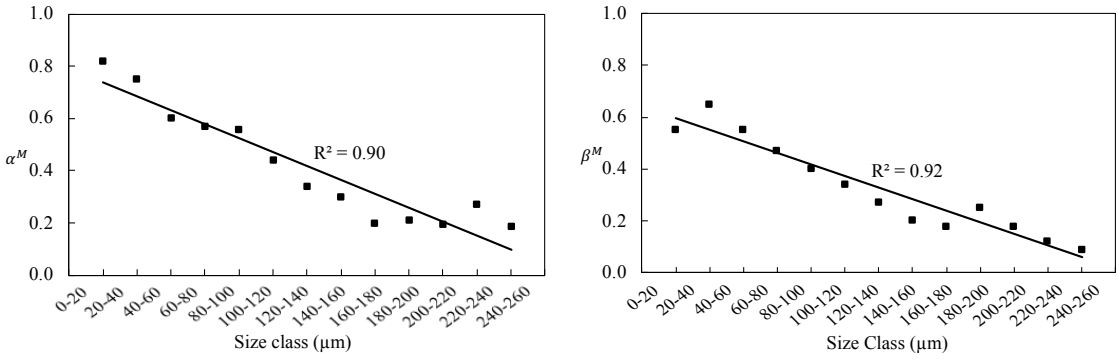

Figure 4.47. Beta distribution parameters of ore obtained for description of mineral liberation of scheelite.

4.3.7 Key findings

Penouta ore was characterized primarily by using step 3 mineral characterization. This is an extension of the step 2 mineral characterization, and also includes a protocol to identify the

deportment of those scheelite minerals that could not be identified in the previous steps of mineral characterization. The protocol for identifying the scheelite deportment was primarily devised to improve the understanding of scheelite deportment. During this process the associations was found between scheelite and other minerals. These were incorporated in the MLA mineral liberation modelling and used to reanalyze the data. By using the insights gained from mineralogical characterization in combination with the results that were being achieved in the modelling liberation, it was possible to quantify the scheelite deportment in this ore.

In terms of processing, the difficulty in quantifying the scheelite deportment and the after a long investigation of the mineralogical behavior of the ore, in terms of grain size and texture, it was possible to achieve a recovery of 87% of scheelite with a grade of 2260 ppm, after allowing increased liberation of scheelite minerals from a reduction in the size distribution of the ore from coarse grains to the fine grains.

At the conclusion of this case study, it can be demonstrated that a full understanding of the application of mineralogical analysis combined with modelling liberation can be used to obtain an acceptable separation using physical separation for this ore.

The size distribution and the liberation of scheelite allow a good estimation of the mineral distribution in the concentration feed. Suitable agreement between the experimental and simulated data was achieved by using a grain size distribution.

Using the beta distributions, the extent and the linear grade distribution of liberated particles have been calculated. The calculated values are compared with the measured distributions for eight size fractions.

Chapter V

Discussion

Chapter V
Discussion

This chapter discusses the key mineralogical characteristics for the three ores - two of them came from the same deposit and the other one came from different deposit - and their impact on the development of an effective physical separation strategy. Based on the knowledge gained through the mineralogical characterization and the liberation modeling, a new concept of processing for Ta and W ores is introduced.

5.1. Context

The main driver for this work was to identify the key mineralogical liberation characteristics for the ores from Penouta and Mittersill, so that an effective beneficiation process to recover tantalum ore and scheelite could be developed. Different questions were raised during the identification of these attributes, which became key to understanding the behavior of these ores during the gravimetric separation process. These questions are answered in this Chapter, which demonstrates how the characteristics of the different ores influence the development of an effective separation process.

5.2 Systematic approach developed to characterize tantalum and tungsten ores

As discussed in the literature review, there is currently no established methodology for carrying out systematic mineralogical characterization during processing tantalum and tungsten ores from low-grade deposits. Here a proposal of the systematic application of a series of characterization tools to identify the tantalum and scheelite deportment and other key mineralogical attributes in complex low-grade and intermediate ores is presented.

The most common microscopic techniques used for characterization of tantalum and tungsten ores are XRD, optical microscopy, SEM-based analyses and EMPA. Based on these techniques, the proposed framework to characterize systematically the minerals is presented in Figure 5.1. It consists of three steps of characterization. The first phase, Level 1 uses all the techniques that are routinely used to find the mineralogical characterization required to develop a process design. The behavior of the valuable minerals must be identified because it is the key factor that helps during the mineral processing to identify the issues that can cause the losses of

the tantalum and tungsten ores, which will go to the tailing fraction during the processing.

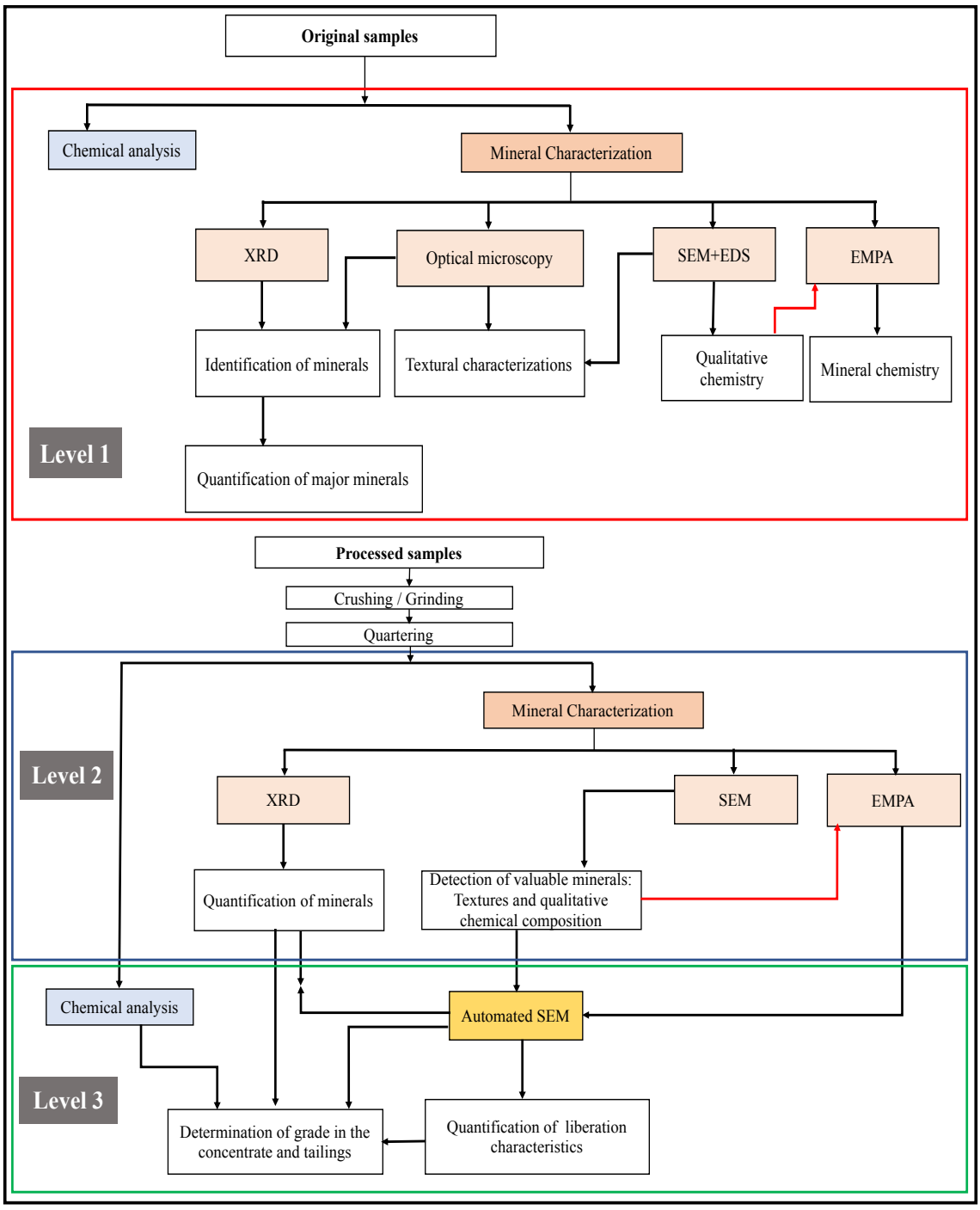

Figure 5.1. Systematic approach for identifying mineralogical characterizes.

Level 1 represents a complete physical and mineralogical characterization of the material that reaches the processing plant from the mine. If the tantalum ore and scheelite deportment is not in amount enough to be completely characterized by Level 1, then the characterization of these materials has to be complemented with their characterized from a concentration process using Level 2. At this level also the qualitative, or semiquantitative, characterization of the

material after different methods of processing is developed. Finally, the level 3 represents the quantification of the ores. This quantification allows to determine the characteristics of liberation and also the grade of concentrates and tailings.

5.3 Key mineralogical characteristics

As the key mineralogical characteristics were established i.e. modal mineralogy, elemental deportment, texture (mineral association and grain size) and liberation of the ores, it became possible to develop a flow sheet design for processing the ores. The way in which each of the characteristics impacted on the development of an effective physical separation strategy is discussed in the following sections.

Tantalum ore: In order to characterize the tantalum ore deportment, different characterization Level 1 was required for the ore. For the Penouta tailings Level 1 analysis show different in texture, from which it was determined that the predominant tantalum carriers for the ore were cassiterite and quartz which account for more than 60% of the tantalum in the ore. For the Penouta ore (open pit) all 3 Levels analysis were required due to the fine-grained nature of the ore and the more complex associations of CGM minerals.

In the development of a physical separation flowsheet for each ore, the Ta deportment was critical in determining the most appropriate separation suite to use for each ore. The Ta and W carriers were very different for the ores indicating that different physical separation strategies i.e. flow sheet design and shaking table schemes, were needed to recover tantalum and scheelite from the ores.

For Penouta deposit, complete characterization is important due to the presence of different valuable minerals which should recover as much as possible. In Penouta it was possible to recover Sn from cassiterite and Ta from CGM. The concept of ore and gangue minerals is variable during the years, whereas a gangue mineral can become an ore if, the mineral prices increase or the developing of the technology to recover the gangue minerals move to reach more efficient of it.

Whole-rock Ta distribution in the Penouta granite exhibits a progressive Ta enrichment upwards in the granite sheet. Evidence of the saturation of columbite-tantalite was not attained; if it had been, a depletion in Ta contents would have occurred once this mineral phase reached its saturation, as CGM contain Ta, an essential structural constituent (ESC) in these mineral phases (López Moro et al., 2017). There is petrographically evidence, however, of the occurrence of CGM from the bottom to the top of the Penouta granite body and an external origin (assimilated or residual minerals) can be ruled out (Figure 5.2).

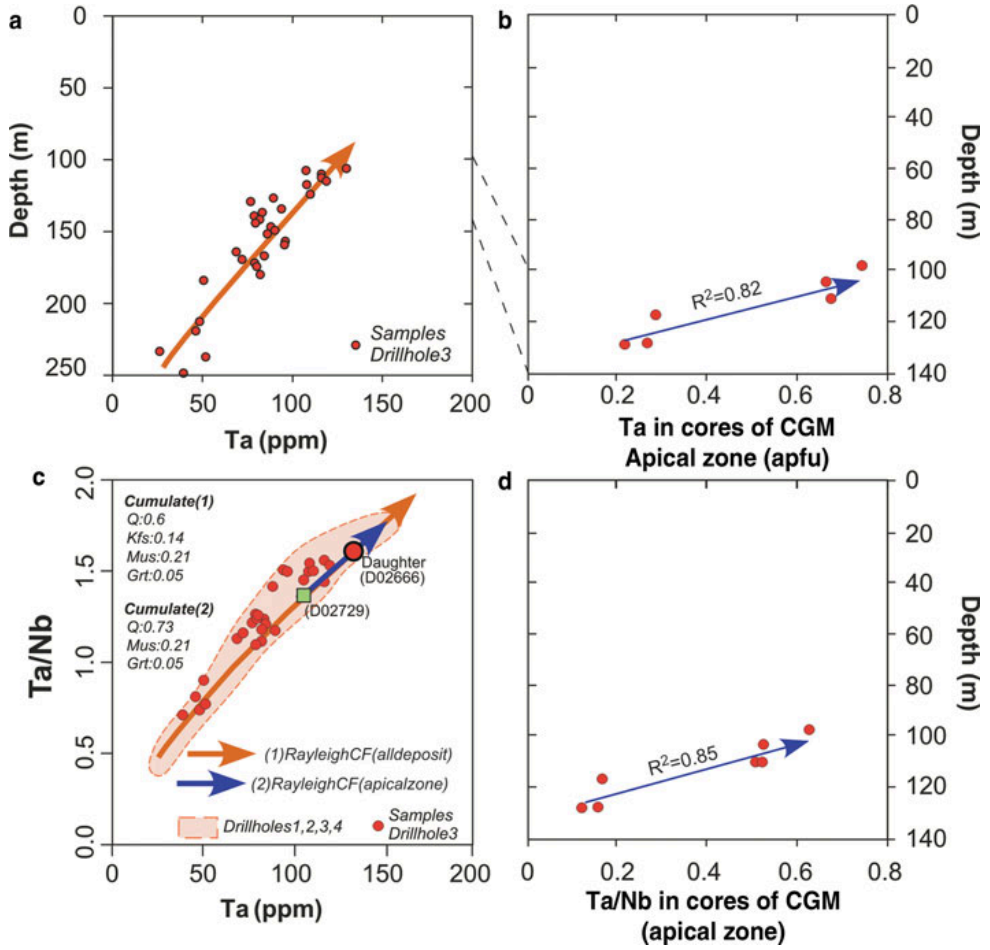

Figure 5.2 Variation with depth in the Penouta deposit: (a) Ta content in granite; (b) Ta content in cores of CGM; (c) Ta vs. Ta/Nb; and (d) Ta/Nb variation observed from bottom to top in the granite (Alfonso et al., 2018).

Tungsten ore: For the Mittersill ore also Level 1, Level 2 analysis was required as the majority of the scheelite was present at ppm levels in the ore.

The beneficiation process of scheelite and wolframite ores generally consists of pre-concentration after crushing and grinding, followed by roughing, cleaning and final purification stages to produce a concentrate with 65–75% WO_3, to meet the requirements of international trading (Krishna, 1996; Lassner and Schubert, 1998).

Rod milling of scheelite has a benefit compared to ball milling according a study by Li and Gao (2017), which concluded that the rod milled scheelite particles are deemed to be more hydrophobic and have a higher flotation recovery due to stronger interaction with the collector and easier attachment to air bubbles (Yang, 2018).

The mineralogical characterization of the Mittersill ore was required to develop the modeling results to finally understand the nature of the scheelite characteristics. A number of analytical and microscopic techniques were developed to identify W. In terms of W minerals, epidote, quartz and hornblende are the main scheelite carriers.

❖ **Mineral distribution**

The gangue is important to characterize so that any minerals can potentially interfere with physical separation. The gangue mineralogy indicated that quartz is the main gangue mineral present, followed by plagioclase (albite).

Tantalum ore: In the Penouta ore (open pit), cassiterite is the most abundant mineral in all fractions while in the Penouta tailings, quartz as a gangue being dominant from the concentrate material. A comparison of the modal mineralogy of the Penouta deposit is shown in Figure 5.3 and 5.4.

Due to the concentration process were followed in the open pit and in the tailings materials were different and this last was less accurate and still large amounts of quartz and other silicates remain in it, with eliminating of the low dense mineral from the material it was possible to describe the distribution of gangue and REE-rich minerals in the materials (Figure 5.4). The results show that the cassiterite still is most abundant in the materials and it shows a higher amount in Penouta open pit compared with the tailings. The amount of iron oxide is higher in the tailings, that it could be because of the old exploitation of cassiterite that during the process the iron cuttings of mechanical equipment remain in the tailings (Figure 4.28). An abundance of REE-rich and spessartine as a gangue mineral existed in those of the material which show higher amount in the tailings.

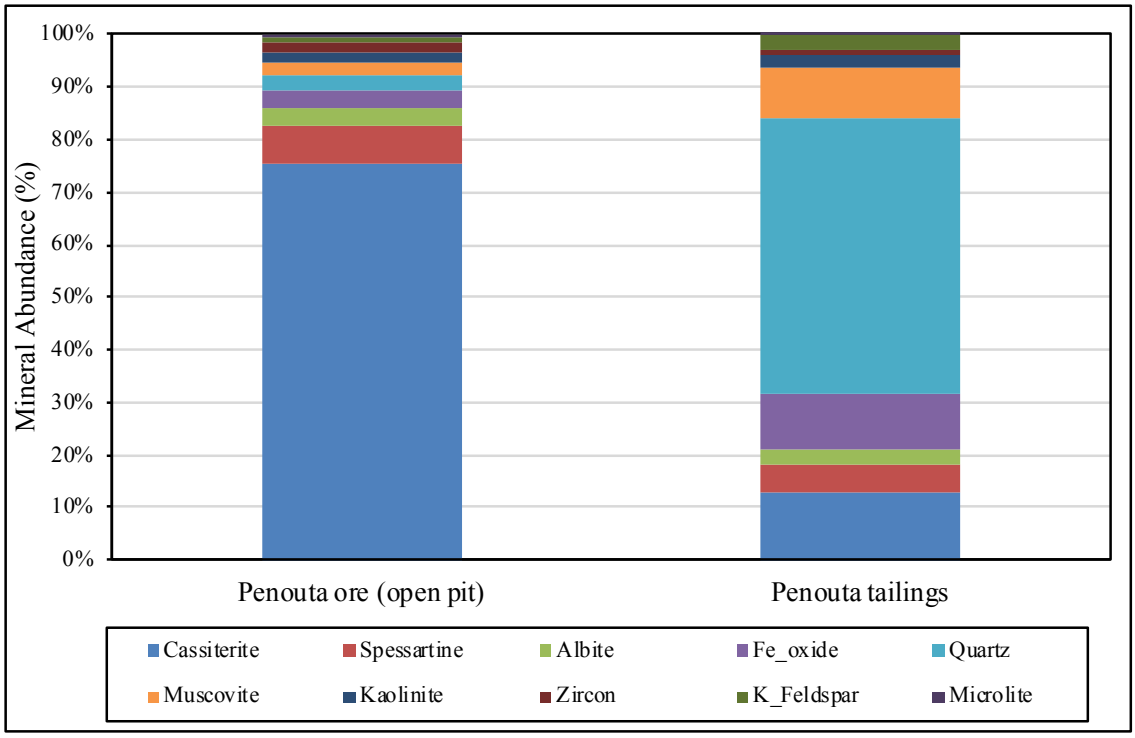

Figure 5.3. Modal mineralogy for Penouta open pit, Penouta tailings.

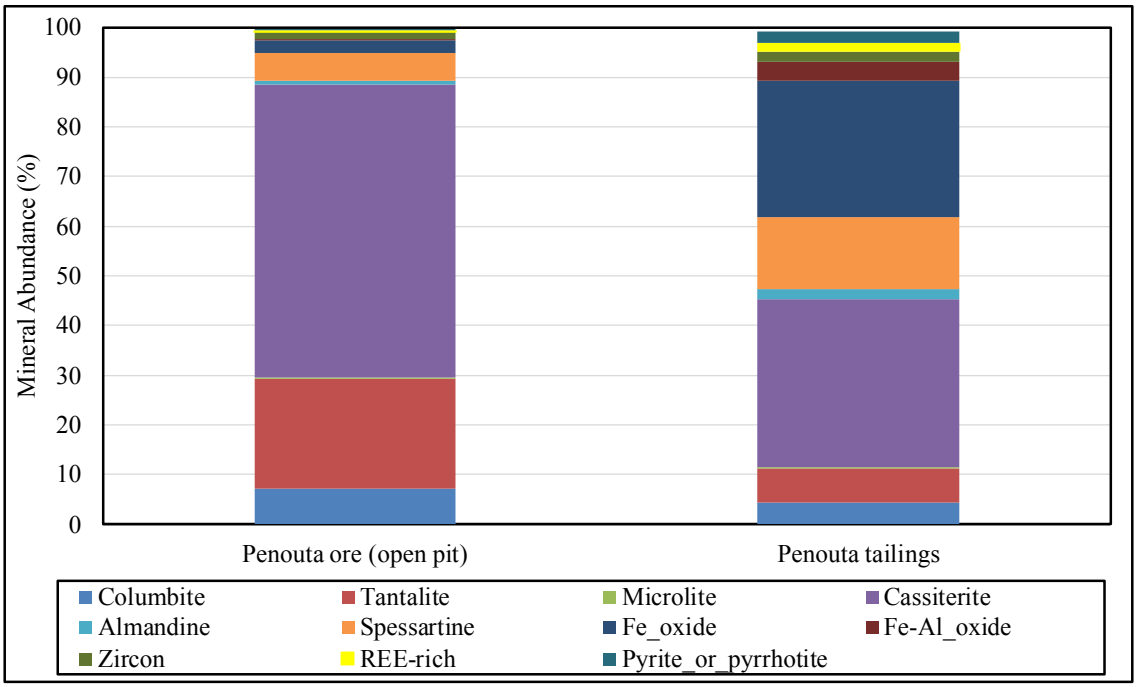

Figure 5.4. Modal mineralogy for Penouta open pit, Penouta tailings (include REE-rich minerals).

Tungsten ore: For the Mittersill ore, a large presence of amphibole with the same amount in the concentrate and tailings material have been reported. The amphibole mineral is most prevalent in the Mittersill ore. Quartz and albite show a higher amount in the tailings compared to the concentrate minerals in the Mittersill ore (Figure 5.5).

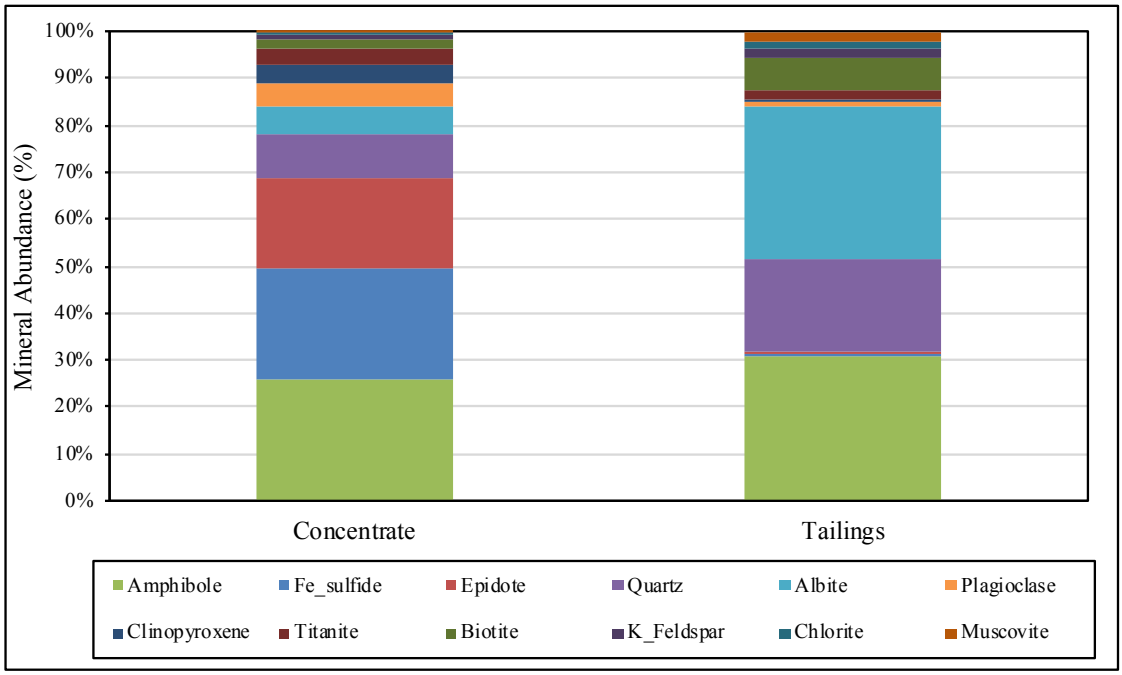

Figure 5.5. Modal mineralogy for proceed Mittersill ore (concentrate and tailings).

In the context of physical separation, the gangue matrix does not present any obvious minerals that could potentially be detrimental to physical separation. Due to the hardness of quartz, it is possible to produce problems via increasing consumed energy for a given percentage of scheelite minerals.

❖ **Texture of ores**

Hilden and Powell (2017) describe that the better models are needed to describe and simulate the process of mineral liberation: the extent to which minerals are released from their host rock upon breakage. The degree of liberation and the composition of the particle fragments is the product of both the breakage mechanisms and the texture of intact rocks. If the relationship between texture and liberation can be modeled successfully, this information can be used to optimize size-reduction and mineral extraction processes to maximize the value extracted from the ore. The term ore texture is used in this thesis to encompass a broad range of material characteristics including the mineralogical composition of the samples, grain size and size distribution, shape distribution, irregularity of the grain boundaries, spatial distribution of the grains, and associations between minerals (Jones, 1987). The complex nature of rock textures means that real ores are difficult to model or describe quantitatively (Barbery, 1991; Andrews and Mika, 1975). The wide range of grain morphologies present complicates even simple features such as grain size (Evans et al., 2012).

Tantalum ore: one of the most striking features of back-scattering images of CGM is the occurrence of a large number of micro holes, frequently grouped, and within areas with a marked Nb depletion and Ta enrichment relative to surrounding blackish areas of the crystal. These textures have been cited in many other occurrences (e.g. Galliski et al., 2008; Wise and Brown, 2010; Zhu et al., 2015), are known as ‘sponge-like’ textures and resemble textures related to overprinting processes in an environment enriched in fluids during their formation. However, the origin of this fluid is an open issue but could be linked to the evolution of the magma itself or processes unrelated to the magmatic process.

Ta-rich minerals, such as microlite, tapiolite and wodginite, are extremely scarce in the deposit and occur specifically in the apical zone of the leucogranite. Texturally, they seem to be late mineral phases, nucleated on previous CGM crystals and to resemble secondary minerals.

Tungsten ore: the texture of scheelite and symbiotic quartz (e.g., variable oscillating zonation revealed by cathodoluminescence; CL), can reveal the growth history of minerals and reflect fluid characteristics (Brugger et al., 2000). In situ major and trace element analysis of scheelite by electron microprobe (EPMS) and laser ablation inductively coupled plasma mass spectrometry (LA-ICP-MS) can reveal fluid features, evolutionary history and system dynamics (Bau et al.,

1991; Ghaderi et al., 1999; Brugger et al., 2002; Peng et al., 2005).

The textures present in the Mittersill ore are complex, particularly with respect to the fine-grained nature of the scheelite minerals. As a consequence, the liberation level for the combined scheelite minerals in the rougher feed at a P80 of 250 μm was high (87%) indicating a finer separation feed size is needed to liberate the scheelite minerals adequately for physical separation to be effective.

5.3.1 Mineralogical drivers for physical separation

The terms ”fines” and ”very fines” can be applied to particles less than 100 μm and 20 μm, respectively, according to the size classification proposed by Sivamohan and Forssberg (1985). In order to increase the recovery for low grade and finely disseminated mineral deposits, many separation operations need to improve the liberation of minerals by grinding them to very fine sizes (Miettinen et al., 2010).

This section explains how the mineralogical drivers, deportment and grain size, influenced the physical separation each of the ores. Deportment in this context relates to the deportment of valuable minerals based on their response to physical separation i.e. they are classified as concentrate valuable minerals (which include all of the tantalum and scheelite) and tantalum and scheelite occurring in solid solution. In this case Penouta ore (open pit) contains concentrate Ta-bearing minerals as carriers, however, the grain size of these minerals is relatively small and, from a metallurgical perspective, ultrafine grinding was required and was the motivation for decreasing the size of the shaking table feed to -250 μm. Penouta tailings also contains concentrate Ta-bearing minerals as carriers and, based on the fine grain size of these minerals the standard grind size for concentrate was adequate to recover Ta. Mittersill ore contained scheelite as the main W carrier; liberation studies indicate that the degree of scheelite liberation at a P_{80} of 600 μm was not enough to recover scheelite and in addition, the distribution of scheelite by size indicated that a large proportion of the scheelite was present in finer size fractions. Therefore, a modification of the grinding procedure was introduced, to reduce physical separation feed size to -250 microns.

Since the 1990s some experimental studies have been carried out on fine tungsten recovery by gravity separation methods (Traore et al., 1995; Wells, 1991). A multi-gravity separator (MGS) was evaluated through testing using a fine scheelite ore with a particle size of −100 μm (Traore et al., 1995). The design and optimization of fine gravity concentration circuits were described using some heavy minerals including scheelite and wolframite (Wells, 1991). However, most investigations on fine scheelite and wolframite beneficiation focused on flotation.

Due to the nature of the scheelite minerals present selective physical separation was selected. As with the Mittersill ore, a combination of shaking table set up and feed rate is an

important factor in enhancing the recovery of the scheelite minerals.

The mineralogical drivers provide insights into the likely behavior of the tantalum and tungsten-bearing minerals found in each of the ores during concentration and how this can be used to develop a framework for assessing the processing of each ore.

The information from mineralogical characterization resulted in the creation of different concentration flowsheets for each of the ores which were able to achieve the target recovery (over 80%).

5.4 Consequences for physical separation and mineral liberation

Figure 5.6 and 5.7 show graphs of the cumulative tantalum and tungsten recovery (x-axis) versus cumulative grade (y-axis) for each ore. For the Penouta ore it can be seen that Penouta ore (open pit) concentrate has a slightly lower grade than the concentration in Penouta tailings, in the higher grade than the cumulative grade decreases as expected in this type of graph. The final recovery of tantalum for Penouta tailings is 33% at a grade of 127 ppm. The grade recovery curve for the Penouta ore is also shown in Figure 5.5. The trend that is presented for tantalum illustrates that between concentrates of two ores, there is a gap which represents the effect of the shaking table concentrate used in this physical separation process that aims to maximize the Ta recovery through a CGM concentrate, which has an average grade of Ta approximately 103 ppm, representing the maximum tantalum grade that could be achieved theoretically.

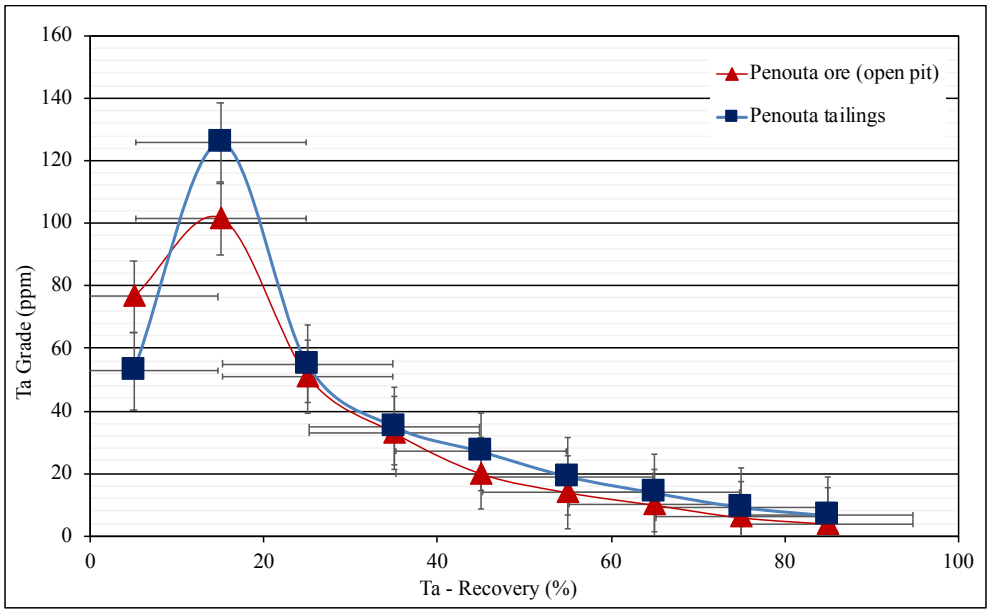

Figure 5.6. Grade – recovery curves of Ta for Penouta ore (open pit) and Penouta tailings.

Also, the appropriate setup of shaking table allows a significantly improved position of the Ta grade/recovery curve, by increasing the CGM minerals recovery. The fine particle size in

the shaking able feed contributes to the higher grade seen in this ore, in comparison to the Penouta tailings, due to the increased entrainment of gangue mineral resulting in a final Ta grade. Despite Penouta also containing cassiterite minerals the grade is higher as a consequence of the fine grinding required to achieve liberation, which as a consequence increased entrainment of CGM minerals and reduced rougher concentrate grade. The lowest final rougher concentrate was achieved with the Penouta ore (open pit) which was limited by Ta occurrence at ppm levels in CGM. The occurrence of the cassiterite in Penouta tailings also required the use of a physical separation stage to ensure adequate recovery of Ta.

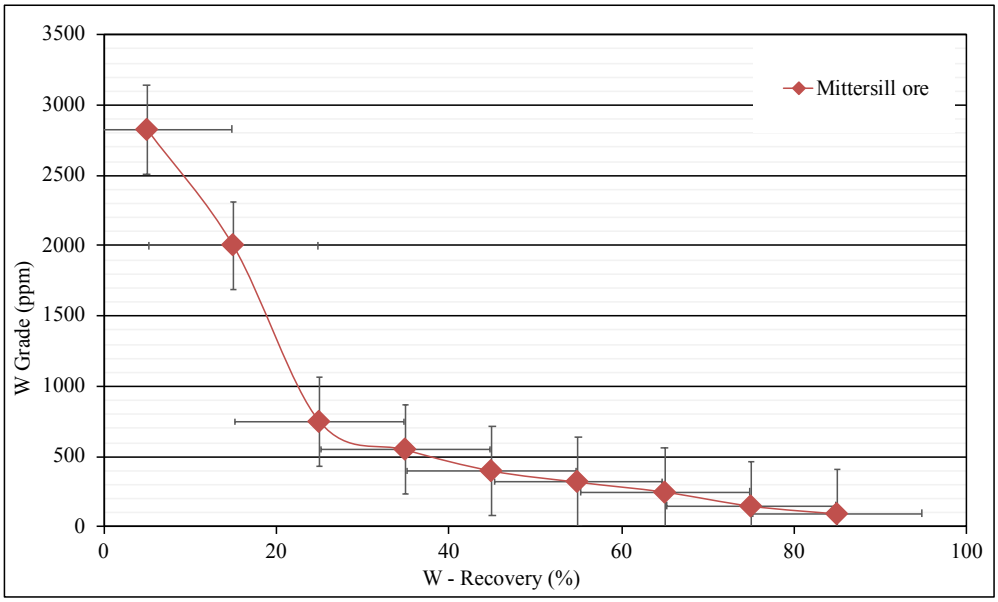

Figure 5.7. Grade – recovery curves of W for Mittersill ore.

The beneficiation recovery rate for the Mittersill ore has been estimated at 75–85% (Yong, 2018). The final recovery of scheelite for Mittersill ore is 87.2% at a grade of 2880 ppm. The relative positions of the grade recovery curves shown in Figure 5.7 reflect the scheelite mineralogy for the ore. The rougher concentrate produced from the shaking table of the Mittersill ore has the highest grade due to the presence of scheelite with a high scheelite composition.

❖ Size-by-size liberation

In the Penouta ore (open pit) CGM minerals were recovered as liberated particles in each of the size fractions studied. The main losses of Ta were in the coarse size fraction as binary composites. In Figure 5.8, the measured size/liberation spectrum of the Penouta ore (open pit) concentrate particles is shown. Approximately 50% of the particles are liberated, and almost all of these particles are in 40+180-micron particles. It is clear from the figure that the bulk of the particles, mainly in the coarser sizes, are unliberated. Below 40 microns, most particles are in the high-grade classes, but not many liberated particles of either phase are present. The transition

between this quasi liberation state and no liberation occurs between 40 and 180 microns. The presence of very few liberated or quasi liberated particles is due to that naturally mineral grains occur in these range size fraction. In the figure, the basic liberation characteristics of the Penouta ore can be observed, like the slow transition from unliberated to quasi liberated, and also the fast transition from quasi liberated to liberated at the end, giving rise to the liberation model modifications.

The measured size/differential mass in the Penouta tailings is shown in Figure 5.9. In Penouta tailings, CGM minerals were recovered in the liberated about (50% of the total) followed by binary composites with cassiterite.

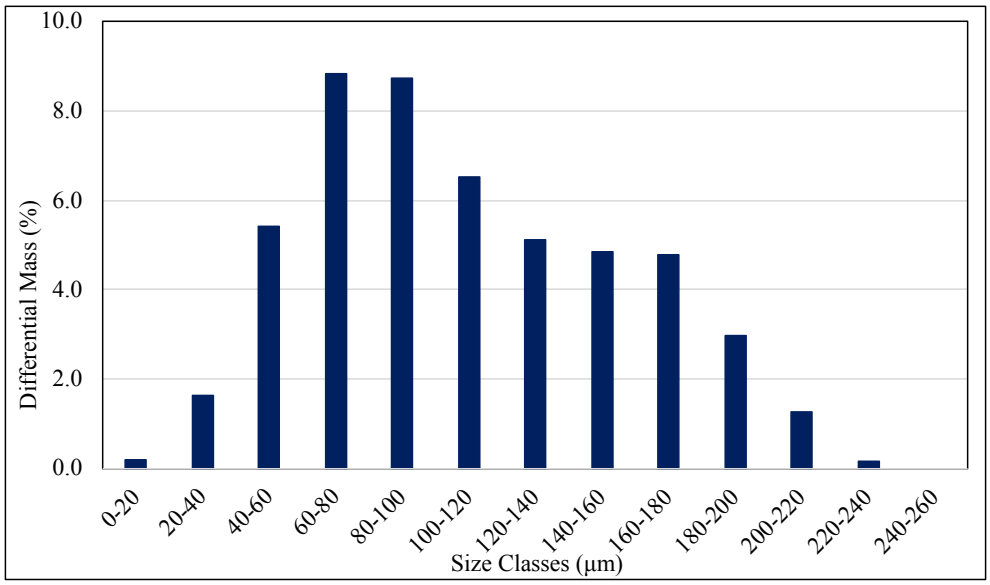

Figure 5.8. Liberation by size for Penouta ore (open pit).

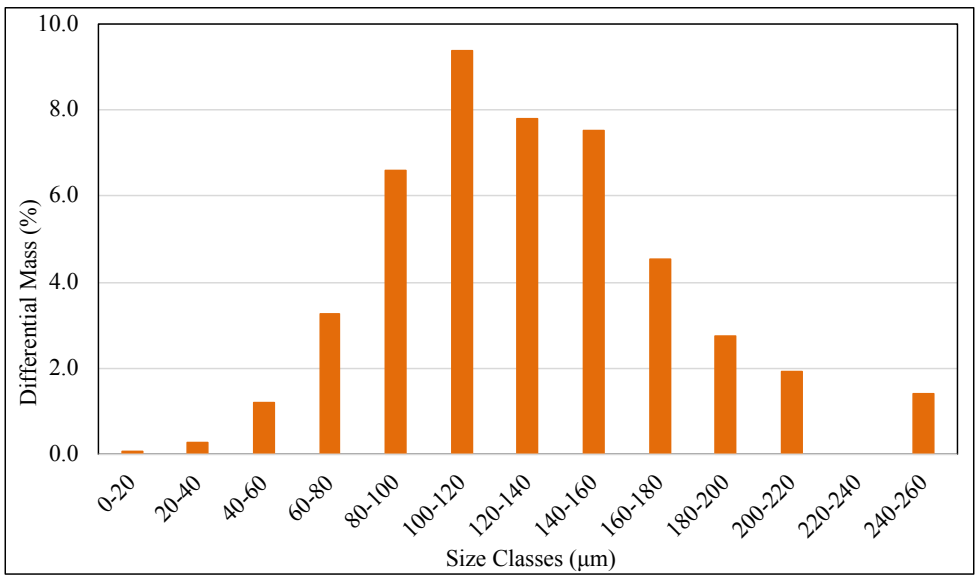

Figure 5.9. Liberation by size for Penouta tailings.

The main losses of Ta were in the liberated form in the coarsest size fraction, while the composites particles containing Ta caused losses in the – 250 + 220 µm size fractions.

In this ore the particles are comparatively finer, with approximately 35% of the particles smaller than 160 µm, due to the comminution. In the ore, a significant fraction of liberated particles is generated, and the bulk of these particles are found below 120 µm. This small "liberation size" characterizes the difficulty of processing the Penouta tailings.

For Mittersill ore, W minerals were mainly recovered as liberated particles. The main losses of scheelite were in the coarsest size fraction for liberated and in binary composite with quartz and epidote which is considered non-concentrate. Also, most of the liberated scheelite is in the size lower than 200 µm and about 80% of the liberated scheelite is in the size lower than 110 µm (Figure 5.10).

Most particles are high grade and liberated particles. Some contamination from larger, lower grade particles is observed, and this is probably due to ineffective concentrate in the shaking table.

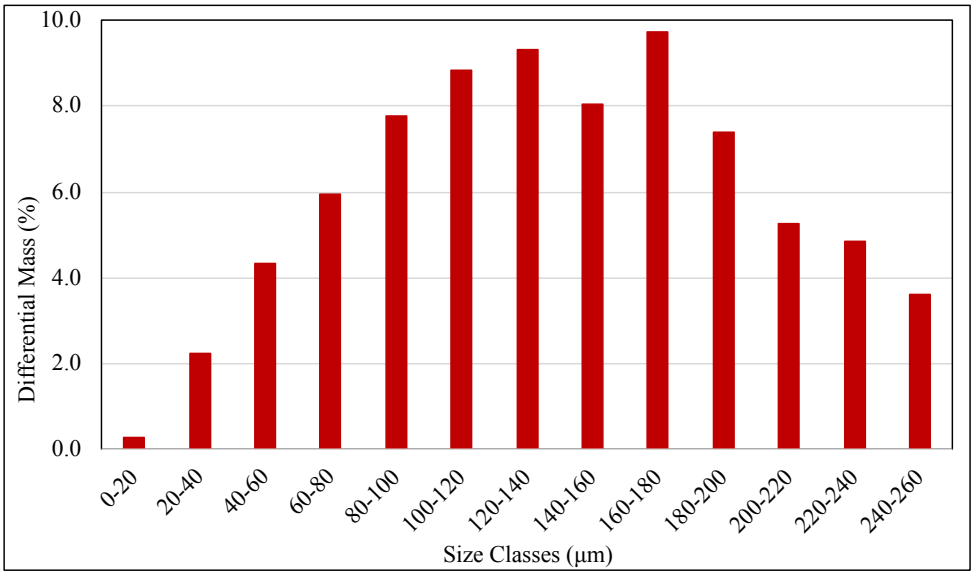

Figure 5.10. Liberation by size for Mittersill ore.

5.5 Simulation and modelling liberation of the ores

The essence of any useful liberation model is to relate the ores texture to its breakage characteristics, i.e., given a set of well-defined textural parameters that can be measured directly from the ore, it should be possible to calculate the grade distribution in the progeny produced by comminution (Schneider, 1995).

King (1975) developed a predictive liberation model by applying renewal theory to the alternating mineral and gangue intercepts encountered by randomly traversed straight lines on the polished sections of the parent rock. Davy (1984) and later Barbery and co-workers (Barbery,

1991; Barbery and Leroux, 1988) proposed a liberation model based on the texture of the parent rock. The ore texture, i.e. the distribution of valuable mineral and gangue within the parent rock was described by a covariance function.

King (2001) and Barbery (1991) describe the grade distribution of composite particles may be evaluated which is generally approximated by a beta distribution. Zhang and Subasinghe (2013) developed a model using the volumetric grade distribution of comminuted particles.

To complete the measurements through the streams involved in these separation processes with the new perspective that only this kind of detailed liberation analysis can provide, the measured size and grade distribution in all concentrates stream of the three ores is shown in Chapter 4. These information from concentrates complete, together with beta distribution functions, the liberation prediction, and mineral liberation modelling and simulation.

The objective of the simulation is primarily to reproduce, to the greatest accuracy, the measured size and grade distributions in the flow sheet of these thesis. There are six streams in the circuit for which measured and simulated results are available, namely the ball mill, the concentrate and the tailing, shaking table feed, and underflow and overflow streams, around the all flow sheet. The simulated size distributions in the streams above are compared to the adjusted size distributions, which represent measured data, in Figure 4.23, 4.36 and 4.46. There is excellent agreement between simulated and measured size distributions in every stream, with the exception of some coarser size, which could not be fully reproduced by simulation. The measured size distribution in the coarser size is considerably coarser than the corresponding simulated size distribution and loss of some interval grades. It is possible that the smallest particles were favored during sampling, either due to the random sampling point, located under the physical separators at a difficult point to reach from the flowsheet, or due to the relatively high-water flow rate in the stream and its low solids content in the feed stream.

However, it is very important to point out that if the stream had not been analyzed for its grade distribution, it would be possible to match the measured size distribution by simulation almost perfectly. This is because the grade distributions impose a tight constraint on the parameterization of the unit operations, and consequently, the simulation becomes considerably more realistic, and any sampling error more apparent.

5.6 Stereological correction of grade distributions for mineral liberation

The stereological correction is required because a linear probe through multiphase particulate material will report a significantly larger fraction of liberated intercepts than there are liberated particles. The entire linear distribution is considerably more dispersed than the volumetric distribution of grades that generates the linear distribution (Schneider, 1995).

As far as, multi-phase liberation data are still normally obtained from polished particle

sections using scanning electron microscopy systems such as MLA and QEMSCAN. 2D data from polished sections can be tessellated (Gay, 2004a; van der Wielen and Rollinson, 2016) or fragmented for example using finite element modeling (Wang, 2015) to calculate liberation statistics. Optical methods using polished sections of intact rock specimens and drill core can also be used to obtain 2D texture data (Lane et al., 2008; Klichowicz and Lieberwirth, 2016). Mineral identification and discrimination with 2D methods are reliable and accurate, however, the liberation estimates are subject to stereological bias (Spencer and Sutherland, 2000).

Liberation data which shown in chapter 4 as cumulative distribution per liberation size class, where liberation size classes are describe the distribution in two-dimensional (2D). Interestingly, and perhaps surprisingly, the difference that presence in the cumulative liberation trends of the measured which are shown as two-dimensional dataset and that of the three dimensional, "simulated" dataset is small for Penouta (open pit) and Mittersill ore of the valuable minerals investigated. These trends are illustrated in Figures 5-11, 5-12, and 5-13.

Figure 5-11, conceptually shows the liberation distribution, which is a cumulative fraction of the total mass of particles comprising a proportion x which created between two curves of the total mass of particles. The head and ends of the distribution correspond to the degrees of liberation of the ores, respectively. The figure shows that the two datasets are similar. Both the two-dimensional and three-dimensional datasets confirm the liberation state of tantalum in the Penouta ore (open pit).

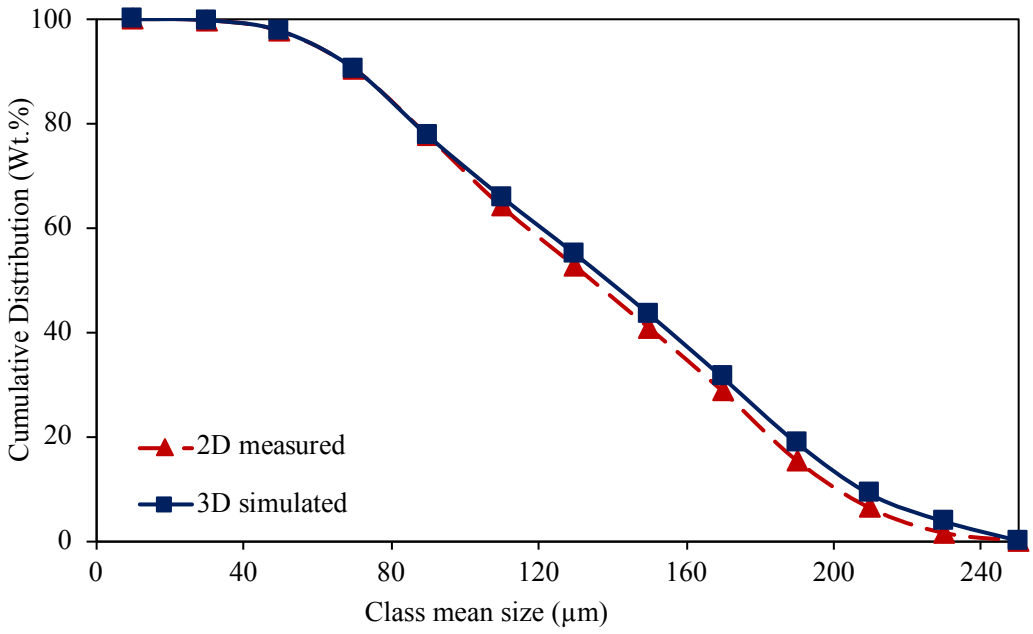

Figure 5.11. 2D liberation distributions based on liberation distribution and, on class mean size of particles, and 3D liberation distributions for Penouta ore (open pit).

X-ray computed tomography (CT) offers the potential for direct 3D measurement of the

internal structure of rocks (Miller and Lin, 2004). However, more than a hundred specimens may need to be scanned to representatively characterize an ore (Evans et al., 2012) which is costly and has rarely been performed. Moreover, current tomography techniques are limited in their ability to identify and discriminate between different mineral phases, noting however that CT techniques are constantly being improved (Hilden and Powell, 2017).

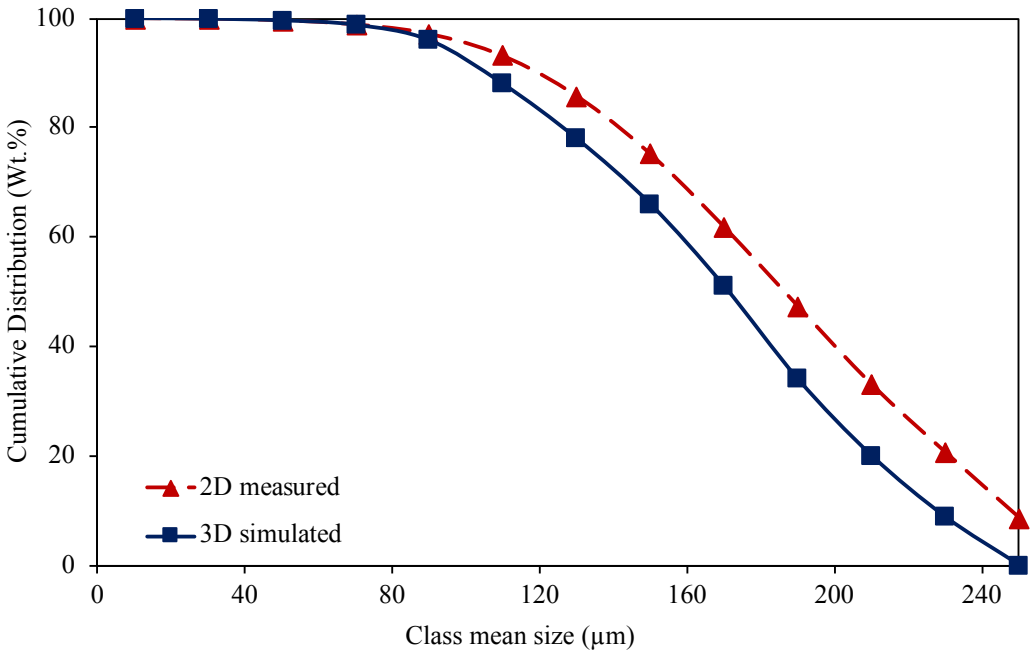

Figure 5.12. 2D liberation distributions based on liberation distribution and, on class mean size of particles, and 3D liberation distributions for Penouta tailings.

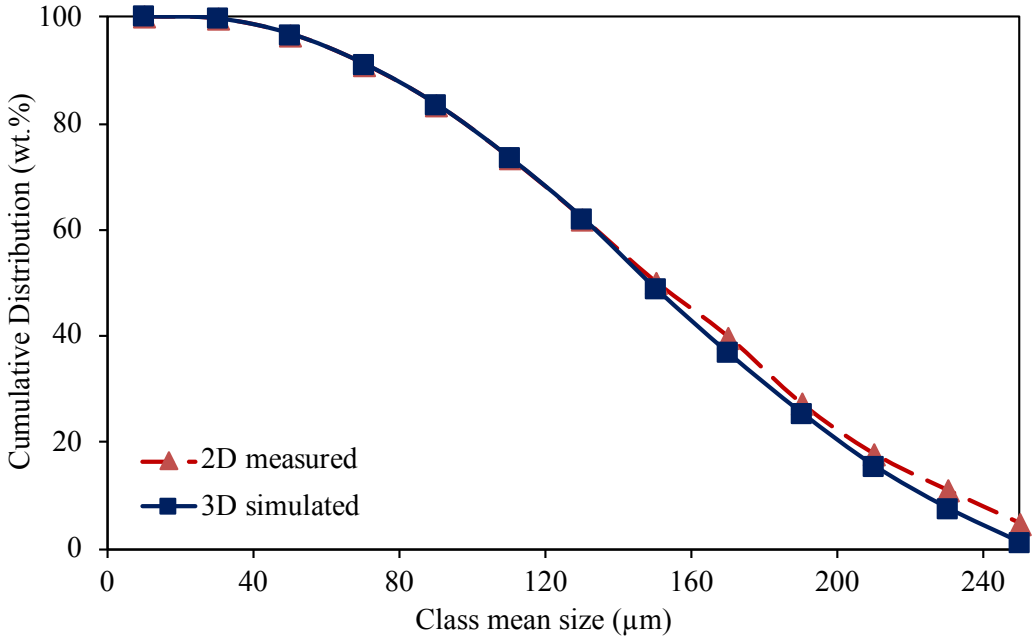

Figure 5.13. 2D liberation distributions based on liberation distribution and, on class mean size of particles, and 3D liberation distributions for Mittersill.

An equivalent dataset for tantalum is presented in Figure 5-12 and it was shown that the 2D measured and 3D simulated datasets are similar but there is an area between two curves that shows the higher error in the tailings sample.

Figure 5-13 shows the results for tungsten ore. The 2D measured and 3D simulated datasets are alike and these indices ranged between zero and one and vanished to zero for particle systems without any stereological bias in the Mittersill ore and a similar trend of Penouta ore (open pit) is again witnessed between the 2D measured and 3D constructed datasets.

The data presented in Figures 5-11, 5-12, and 5-13 suggest that, for the ores type and texture studied in this work, there is not a large difference between the 2D and 3D measurements and true liberation distributions. It needs to be noted that the textures displayed in these datasets are those of real ores. It may, therefore, be concluded that for of ore textures, the stereological bias may, in fact, be very small. In such cases, the use of an adjustment procedure will be extra and could even provide an incorrect result (Latti and Adair, 2001).

Chapter VI

Conclusions

Chapter VI
Conclusions

This thesis sought to address the following hypothesis:

Key mineralogical factors (mineral locking, liberation, and association) can be determined using a systematic application of mineralogical characterization tools, from which an effective gravity separation strategy for low-grade tantalum ores and intermediate scheelite ore can be developed and directed to the implementation of a procedure to solve the integral equation for mineral liberation modelling that relates to the linear grade distribution.

To assess the above hypothesis, a framework of analysis was developed and the conclusions drawn from these investigations are presented below. The objectives as described in Chapter 1 and how they were achieved are discussed in the following sections.

The ores studied in this work were all characterized using the standard procedures for chemical and mineralogical characterization. Chemical characterization was carried out on an unsized and size by-size basis for the ore feed, while the mineralogical characterization was based on standard mineralogical characterization techniques using different particle sizes for each technique. These included XRD, optical microscopy, SEM, EMPA, and automated quantitative mineralogy (MLA) to characterize the ore mineralogy from the ores. For the run of mine ore, Level 1 characterization was sufficient to fully identify the key mineralogical parameters and indicated that tantalum occurred mainly in the CGM minerals.

Results from the separation test work and mineral liberation modelling were used in combination from the insights gained from chemical and mineralogical characterization to understand fully the behavior of the ores. Most of the tantalum was present as CGM minerals, and, in minor amounts in cassiterite. However, a minor amount of tantalum occurs in muscovite, which is a low density mineral and is released with the gangue during gravity separation, rendering this component of the tantalum non-recoverable. The distribution of tantalum among minerals together with the extremely fine-grained nature of the remaining tantalum minerals made it challenging to develop the final flow sheet for Penouta ore.

The level 1 of characterization approach was developed specifically to identify minerals that were associated with the only W-bearing mineral, scheelite, in the Mittersill run of mine material and to create the MLA mineral reference library. This required detailed examination of

the samples using XRD, which in addition to hornblende, actinolite was identified and incorporated into the mineral reference library. In the MLA, actinolite was not reported; probably it was identified as a pyroxene phase, thus, its composition is similar than other pyroxenes, such as augite.

The results of combining and applying the different techniques of mineralogical characterization allowed for the development of a systematic methodology to identify unknown tantalum minerals that may have been missing from conventional ore microscopic routines used for ore mineralogy.

Once the ore characterization was done, the information regarding modal mineralogy, mineral association, mineral locking, textures, particle and grain size of the ores was established, it was possible to propose adequate strategies for ore treatment, through a gravity separation process at laboratory scale to obtain a rougher concentrate with the required characteristics. Typical separation strategies are in use to recover tantalum and scheelite. The selective separation that aims to selectively valuable minerals and to then concentrate intermediate and low-grade metals. This technique was successfully used, where suitable in this research to produce rougher concentrates. The challenges in the development of the gravity separation flow sheets were adequate preparation of the shaking table feed and selection of the appropriate flow rate scheme to produce a rougher concentrate that met the required characteristics. For the Penouta and Mittersill ores, the focus was on selective concentrate because of the occurrence of valuable minerals in the ores as discrete minerals and the absence of other sulphides minerals.

This work has shown that it is possible to use gravity separation as a separation technique for low-grade complex tantalum and scheelite ores, by selecting appropriate feed preparation and shaking table set up addition strategies which are based on understanding the key mineralogical attributes of the ore.

In the present work, the beta distribution function model and King's solution to the solve equation were tested. The test ores for the experimental validation has been done. The main conclusion was that the geometrical texture parameter cannot be measured in one absolute size class. A more detailed understanding of this textural parameter is required, and further studies must be carried out in this direction.

The Penouta ore is very favorable for liberation studies, with respect to composition and texture, to which the symmetric physical separation responded very well. The sampling strategy was successful and the results in general are excellent. The simulation opens up the possibility for significant improvement in the existing flowsheet with respect to physical separation recovery and grinding efficiency.

A reliable procedure was developed for mineral liberation data obtained by MLA and image analysis. This was an essential requirement to the main task because it would have been impossible to measure, by classical separation fractionation methods, the liberation of minerals

in the many samples that were necessary. The calculation procedure was confirmed by experimental liberation data that was generated in the laboratory and by data obtained from beta distribution function calculation.

It is suggested that the methodologies developed in this work can be applied to other complex tantalum and scheelite deposits to validate the usefulness of the approach. One of the areas of further work recommended for the methodology is the refinement of the MLA measurement settings to target finely grained tantalum and scheelite minerals. This would involve to prepare a complete data base with the list of minerals and their chemistry.

An investigation into the effects of the minerals associated with tantalum ores, such as muscovite, in low-grade tantalum ores, to determine the limits of the processing efficiency, is also recommended.

Other processing routes, such as magnetic separation, could be investigated for these ores in order to determine what the most suitable method for processing these ores is.

In terms of water in the physical separation, it is suggested that the ores should be treated by shaking table using the water from the recirculate in the plant.

The contribution of this liberation study to the understanding of the liberation problem, including measurement and prediction, is significant, when considering the state of the art when this study started. It could have a significant impact in mineral processing technology in the future.

In view of the importance of liberation effects in the efficient concentration of the ores, it is recommended that future effort be directed towards the measurement of specific MLA analysis in different stages of processing in the flowsheet for these ore types.

References

References

Abdalla, H.M., Helba, H., & Matsueda, H. (2009). Chemistry of zircon in rare metal granitoids and associated rocks, Eastern Desert, Egypt. Resource geology, 59(1), 51–68.

Abdalla, H.M., Helba, H.A. & Mohamed, F.H. (1998). Chemistry of columbite-tantalite minerals in rare metal granitoids, Eastern Desert, Egypt. Mineralogical Magazine, 62, 82–836.

Ahmad Hamid, S., Alfonso, P., Oliva, J., Anticoi, H., Guasch, E., Hoffmann Sampaio, C., Garcia-Valles, M., & Escobet, T. (2019). Modeling the Liberation of Comminuted Scheelite Using Mineralogical Properties. Minerals, 9(9), 536.

Alfonso, P., Anticoi, H., Yubero, T., Bascompta, M., Henao, L., Garcia–Valles, M., Palacios, S., & Yáñez, J. (2019). The Importance of Mineralogical Knowledge in the Sustainability of Artisanal Gold Mining: A Mid-South Peru Case. Minerals, 9(6), 345.

Alfonso, P., Corbella, M. & Melgarejo, J.C. (1995). Nb–Ta–minerals from the Cap de Creus pegmatite field, eastern Pyrenees: distribution and geochemical trends. Mineralogy and Petrology, 55, 53–69.

Alfonso, P., Hamid, S. A., García-Vallès, M., Llorens, T., Moro, F. L., Tomasa, O., Calvo D., Guasch E., Anticoi H., Oliva J., & Parcerisa, D. (2018). Textural and mineral-chemistry constraints on columbite-group minerals in the Penouta deposit: evidence from magmatic and fluid-related processes. Mineralogical magazine, 82(S1), S199–S222.

Altringer, P.B. (1985). Recovery of Tungsten from Searles Lake Brines by an Ion-exchange Process. Bull. US Dept of the Interior, Bureau of Mines, 682, pp. 47.

Allain, E., Kanari, N., Diot, F., & Yvon, J. (2019). Development of a process for the concentration of the strategic tantalum and niobium oxides from tin slags. Minerals Engineering, 134, 97–103.

Anderson, M.O., Lentz, D.R., McFarlane, C.R., & Falck, H. (2013). A geological, geochemical and textural study of an LCT pegmatite: implications for the magmatic versus metasomatic origin of Nb-Ta mineralization in the Moose II pegmatite, Northwest Territories, Canada. Journal of Geosciences, 58(4), 299–320.

Anderson, S.T. (2011). Mineral Industry of Bolivia. 2009 Minerals Yearbook, United States Geological Survey, pp. 17.

Andrews, J.R.G., & Mika, T.S. (1975). Comminution of a heterogeneous material: development of a model for liberation phenomena. In: Proceedings of XI International Mineral Processing Congress, Cagliari, pp. 59–79.

Anticoi, H., Guasch, E., Hamid, S.A., Oliva, J., Alfonso, P., Garcia-Valles, M., Bascompta, M., Sanmiquel, L., Escobet, T., & Argelaguet, R. (2018). Breakage Function for HPGR: Mineral and Mechanical Characterization of Tantalum and Tungsten Ores. Minerals, 8, 170.

Arias, D., Farias, P. & Marcos, A. (2002). Estratigrafía y estructura del Antiforme del Ollo de Sapo en el área de Viana do Bolo-A Gudiña (Provincia de Orense, NO de España): nuevos datos sobre la posición estratigráfica de la Formación porfiroide Ollo de Sapo. Trabajos de Geología, 23, 9–19.

Arribas, A. & Mangas, J. (1991) Fluid inclusion study of tin-mineralized greisens and quartz veins in the Penouta apogranite (Orense, Spain). Mineralogical Magazine, 55, 211–223.

Atencio, D., Andrade, M.B., Christy, A.G., Gieré, R., & Kartashov, P. M. (2010). The pyrochlore supergroup of minerals: nomenclature. The Canadian Mineralogist, 48(3), 673-698.

Australia, G. (2015). Digital elevation model (DEM) of Australia derived from LiDAR 5 Metre grid. Commonwealth of Australia and Geoscience Australia: Canberra.

Ayeni, F.A., Madugu, I.A., Sukop, P., Ibitoye, S.A., Adeleke, A.A., & Abdulwahab, M. (2012). Secondary Recovery of Columbite from tailing dump in Nigerian Jos mines field. Journal of Minerals and Materials Characterization and Engineering, 11(06), 587.

Bacon, C.R. (1989). Crystallization of accessory phases in magmas by local saturation adjacent to phenocrysts. Geochimica et Cosmochimica Acta, 53, 1055–1066.

Bafilemba, F., Mueller, T., & Lezhnev, S. (2014). The impact of Dodd-Frank and conflict minerals reforms on Eastern Congo's conflict. The Enough Project.

Bale, M.D., & May, A.V. (1989). Processing of ores to produce tantalum and lithium. Minerals engineering, 2(3), 299-320.

Barbery, G. (1991). Mineral Liberation-Measurement, Simulation and Practical Use in Mineral Processing; Quebec Éditions: Montreal, QC, Canada.

Barbery, G., Leroux, D. (1988). Prediction of particle composition distribution after fragmentation of heterogeneous materials. Int. J. Miner. Process. 1988, 22, 9–24.

Barton, W.R. (1962). Columbium and tantalum, a materials survey: U.S. Bureau of Mines Information Circular 8120, 110 p.

Basto, M., Figuerido, M.O., Legrand, F., Chevallier, P., Melo, Z., and Ramos, M.T. (1995). Gold assessment in micas by XRF using synchrotron radiation. Chemical Geology 124, pp. 1–2 and pp. 83–90.

Bau, M. (1991). Rare-earth element mobility during hydrothermal and metamorphic fluid-rock interaction and the significance of the oxidation state of europium. Chemical Geology, 93(3–4), 219–230.

Baum, W., Lotter, N.O., & Whittaker, P.J. (2004). Process mineralogy - A new generation for ore characterisation and plant optimisation, 2003 SME Annual Meeting (Feb.), Denver, Preprint 04-12.

Becker, M., Brough, C., Smith, D., & Bradshaw, D. (2008). Geometallurgical characterisation of the Merensky Reef and Northam platinum mine; comparison of normal, pothole and transitional reef types. International Congress for Applied Mineralogy, Brisbane, Queensland, Conference Proceedings, pp. 391-399.

Belkasmi, M., Cuney, M., Pollard, P. J., & Bastoul, A. (2000). Chemistry of the Ta-Nb-Sn-W oxide minerals from the Yichun rare metal granite (SE China): genetic implications and comparison with Moroccan and French Hercynian examples. Mineralogical Magazine, 64(3), 507-523.

Belzile, E. (2009). NI 43–101 technical report for Niobec Mine, Quebec, Canada, prepared for IAMGOLD Corp. [Filing date March 9, 2009]: Toronto, Ontario, Canada, Belzile Solutions Inc., 104 p.

Bernhart, W. (2015). Processing of tungsten bearing ores - mineral processing and metallurgy. METSO, Austria, DOI: 10.26649/musci.2015.020.

British Geological Survey (BGS), (2014). World Mineral Production 2007–2011, British Geological Survey, Keyworth, Nottingham.

British Geological Survey (BGS), (2018). World Mineral Production 2012–2017, British Geological Survey, Keyworth, Nottingham.

Bleischwitz, R., Dittrich, M., & Pierdicca, C. (2012). Coltan from Central Africa, international trade and implications for any certification. Resources Policy, 37(1), 19-29.

Bleiwas, D. I., Papp, J. F., & Yager, T. R. (2015). Shift in global tantalum mine production, 2000–2014 (No. 2015-3079). US Geological Survey.

Bojcevski, D. (2004). Metallurgical characterisation of George Fisher meso-textures and micro-textures. Masters Thesis, School of Engineering, The University of Queensland. 376pp.

Borodin, L.S. & Nazarenko, I.I. (1957). Chemical composition of pyrochlore and diadochic substitution in the A2B2X7 molecule. Geokhimiya 4, 386-400 (in Russian; transl. Geochemistry International 4, 330-349, 1957.

Bose, M.K. (2008). Proterozoic dykes from Singhbhum granite pluton; In: *Indian dykes* (eds) Srivastava R K, Sivaji Ch and Rao C (New Delhi: Narosa Publ.), pp. 413–445.

Bonnici, N.K. (2012). The mineralogical and textural characteristics of copper - gold deposits linked to mineral processing attributes. PhD thesis, University of Tasmania. 249pp.

Burt, R.O. (1985). Gravity Concentration Technology, Elsevier, Amsterdam.

Butcher, A. (2010). Chapter 4 A practical Guide to Some Aspects of Mineralogy that Affect Flotation. Spectrum Series 16, Flotation plant Optimisation, pp. 83-93.

Bradley, D., & McCauley, A., (2013). A preliminary deposit model for lithium-cesium-tantalum (LCT) pegma- tites: U.S. Geological Survey Open-File Report 2013–1008, 7 p.

Brand, A.A. (2008). Mineralogy, geochemistry and geochro- nology of the Northern Dancer tungsten-molybdenum deposit, Yukon and British Columbia. MSc thesis, University of British Columbia.

Browning, P.N., Patankar, S., Kulkarni, A.K., Matson, L., & Singh, J. (2015). Microstructure and mechanical properties of W-Ta and W-Ta-TiC alloys sintered by field assisted sintering technique. Advances in Powder Metallurgy and Particulate Materials - Proceedings of the 2015 International Conference on Powder Metallurgy and Particulate Materials, PowderMet 2015. Metal Powder Industries Federation.

Brugger, J., Gieré, R., Graeser, S. & Meisser, N. (1997). The crystal chemistry of roméite. Contributions to Mineralogy and Petrology 127, 136-146.

Brugger, J., Lahaye, Y., Costa, S., Lambert, D., Bateman, R. (2000). In homogeneous distribution of REE in scheelite and dynamics of Archean hydrothermal systems (Mt. Charlotte and Drysdale gold deposits, Western Australia). Contrib Mineral Petrol, 139, 251–264.

Brugger, J., Mass, R., Lahaye, Y., Mcrae, C., Ghaderi, M., Costa, S., Lambert, D., Bateman, R., & Prince, K. (2002). Origins of Nd–Sr–Pb isotopic variations in single scheelite grains from Archaean gold deposits, Western Australia. Chemical Geology, 182(2–4), 203–225.

Cameron, E.N., Jahns, R.H., McNair, A.H., & Page, L.R. (1949). Internal structure of granitic pegmatites: Urbana, Ill., Economic Geology Publishing Co., Monograph 2, 155 p., folded maps.

Černý, P.. Blevin, P.L.. Cuney, M.. & London, D. (2005). Granite-related ore deposits. In Economic Geology 100th Anniversary Volume; Hedenquist, J.W., Thompson, J.F.H., Goldfarb, R.J., Richards, J.P., Eds.; Society of Economic Geologists: Littleton, CO, USA, pp. 337–370.

Černý, Petr, (1991a). Rare-element granitic pegmatites, part I— Regional to global environments and petrogenesis: Geoscience Canada, v. 18, no. 2, p. 49–67.

Černý, Petr, (1991b). Rare-element granitic pegmatites, part II—Regional to global environments and petrogenesis: Geoscience Canada, v. 18, no. 2, p. 68–81.

Černý, P. & Ercit, T.S. (1989). Mineralogy of niobium and tantalum: crystal chemical relationships, paragenetic aspects and their economic implications. Pp. 27–79 in: Lanthanides, Tantalum and Niobium (P. Moller, P. Černý and F. Saupe, editors). Springer-Verlag, New York.

Černý, P., Roberts, W.L., Ercit, T.S., & Chapman, R. (1985). Zirconium and hafnium in minerals of the columbite and wodginite groups from granitic pegmatites. The Canadian Mineralogist, 45, 185–202.

Černý, P., Chapman, R., Ferreira, K., & Smeds S.A. (2004). Geochemistry of oxide minerals of Nb, Ta, Sn, and Sb in the Varuträsk granitic pegmatite, Sweden: The case of an "anomalous" columbite-tantalite trend. American Mineralogist, 89, 505–518.

Černý, P. (2005). The Tanco rare-element pegmatite deposit, Manitoba—Regional context, internal anatomy, and global comparisons, in Linnen, R.L., Samson, I.M., and Martin, R.F., eds., Rare-element geochemistry and mineral deposits: St. Johns, Newfoundland and Labrador, Canada, Geological Association of Canada, Short Course Notes, v. 17, p. 127–158.

Černý, P., & Ercit, T.S. (2005). The classification of granitic pegmatites revisited: Canadian Mineralogist, v. 43, no. 6, p. 2005–2026.

Černý, P., Ercit, T.S., Smeds, S.A., Groat, L.A. & Chapman, R. (2007). Wodginite and associated oxide minerals from the Peerless pegmatite, Pennington County, South Dakota. American Mineralogist, 70, 1044–1049.

Chakhmouradian, A.R., Smith, M.P., & Kynicky, J. (2015). From "strategic" tungsten to "green" neodymium: A century of critical metals at a glance. Ore Geol. Rev. 64, 455–458.

Chang, Z. (2005). World Skarn Deposits - China. Appendix 2 of Mernert et al. (2005). World Skarn Deposits. In: Hedenquist, J.W., Thompson, J.F.H., Goldfarb R.J. and Richards J.R. (eds.) Society of Economic Geologists One hundredth Anniversary Volume (1905–2005).

Chasan, E. (2015). "Conflict minerals" prove hard to trace. The Wall Street Journal. 4 August (p. B4).

Chicharro, E., Martín-Crespo, T., Gómez-Ortiz, D., López-García, J.A., Oyarzun, R. & Villaseca, C. (2015). Geology and gravity modeling of the Logrosán Sn–(W) ore deposits (Central Iberian Zone, Spain). Ore Geology Reviews, 65, 294–307.

Christie, T and Brathwaite, B. (1996). Mineral commodity report 12 - Tungsten. Ministry of Economic Development, New Zealand. http://www.nzpam. govt.nz/cms/pdf-library/minerals/publications/Commodity%20Reports.

Chung, C.K. (1975). Tungsten and molybdenum deposits in South Korea. Korean Institute of Mineral and Mining Engineers Journal 12, 192–199.

Clauer, N., Fallick, A.E., Galán, E., Aparicio, P., Miras, A., Fernández-Caliani, J.C. & Aubert, A. (2015). Stable isotope constraints on the origin of kaolin deposits from Variscan granitoids of Galicia (NW Spain). Chemical Geology, 417, 90–101.

Cordeiro, P.F.O., Brod, J.A., Palmieri, Matheus, Oliveira, C.G., Barbosa, E.S.R., Santos, R.V., Gaspar, J.C., & Assis, L.C. (2011). The Catalão I niobium deposit, central Brazil—Resources, geology, and pyrochlore chemistry: Ore Geology Reviews, v. 41, no. 1, p. 112–121.

Cox, D.P., & Bagby, W.C. (1986). Descriptive model of W veins. In: Cox, D.P. and Singer, D.A. (eds.) Mineral deposit models: U.S. Geological Survey Bulletin 1693, p. 64.

Craig, J.R., (2001). Ore-mineral textures and the tales they tell. The Canadian Mineralogist. Vol.39, pp. 937-956.

Daigle, Paul, (2012). Elk Creek Nb Project, Nebraska, US resource estimate update, NI 43–101 report prepared for Quantum Rare Earth Developments Corp.: Toronto, Ontario, Canada, Tetra Tech Wardrop, 143 p., accessed October 15, at http://www.quantumrareearth.com/projects.html.

De Roo, J.A. (1988). Structural controls on the emplacement of the vein-type tungsten-tin ore at Mount Carbine, Queensland, Australia. Economic Geology 83, 1170–1180.

Dick, L.A. & Hodgson, C.J. (1982). The Mactung tungsten- copper-zinc contact metasomatic and related deposits of the northeastern Canadian cordillera. Economic Geology 77, 845–867.

Díez, A., Martínez Catalán, J.R. & Bellido Mulas, F. (2010). Role of the Ollo de Sapo massive felsic volcanism of NW Iberia in the Early Ordovician dynamics of northern Gondwana. Gondwana Research, 17, 363–376.

Díez Montes, A. (2006). La Geología del Dominio "Ollo de Sapo" en las comarcas de Sanabria y Terra do Bolo. (Geology of the "Ollo de Sapo" domain in the Sanabria and Terra do Bolo regions). PhD thesis, University of Salamanca-IGME, Spain.

Dill, H.G., Dohrmann, R., Kaufhold, S. & Balaban, S.I. (2015). Kaolinization – a tool to unravel the formation and unroofing of the Pleystein pegmatite–aplite system (SE Germany). Ore Geology Reviews, 69, 33–56.

Eichhorn, R., Höll, R., Loth, G. & Kennedy, A. (1999). Implications of U-Pb SHRIMP zircon data on the age and evolution of the Ferbertal tungsten deposit (Tauern Window, Austria). Geologische Rundschau 88, 496–512.

Einaudi, M.T., Meinert, L.D. & Newberry, R.J. (1981). Skarn deposits. Economic Geology 75th Anniversary Volume, 317–391.

Elliott, J.E. (1992). Tungsten - geology and resources of deposits in southeastern China. In: DeYoung Jr, J.J. and Hammarstrom J.M. (eds.) Contributions to commodity geology research. U.S. Geological Survey Bulletin 1877, I1–I10.

Elliott, J.E., Kamilli, R.J., Miller, W.R. & Livo, K.E. (1995). Vein and greisen Sn and W deposits. In: Du Bray, E.A. (ed.) Preliminary compilation of descrip- tive geoenvironmental mineral deposit models. U.S. Geological Survey Open-File Report 95-831, 62–69.

Ercit, T.S., Hawthorne, F.C. & Černý, P. (1992a). The wodginite group. I. Structural crystallography. The Canadian Mineralogist, 30, 597–611.

Ercit, T.S., Černý, P., Hawthorne, F.C. & McGammon, C.A. (1992b). The wodginite group. II. Crystal chemistry. The Canadian Mineralogist, 30, 613–631.

Ercit, T.S., Hawthorne, F.C. & Černý, P. (1994). The structural chemistry of kalipyrochlore, a "hydropyrochlore". Canadian Mineralogist 32, 415-420.

Ercit, T.S. & Robinson, G.W. (1994). A refinement of the structure of ferritungstite from Kalzas Mountain, Yukon, and observation tungsten pyrochlores. Canadian Mineralogist 32, 74.

Erdmann, L., & Graedel, T. E. (2011). Criticality of non-fuel minerals: a review of major approaches and analyses. Environmental science & technology, 45(18), 7620-7630.

European Commission, (2017). Study on the Review of the List of Critical Raw Materials. Available online: https://publications.europa.eu/en/publication-detail/ /publication/08fdab5f-9766 11e7- b92d-01aa75ed71a1/language-en (accessed on 9 February 2018).

Evans, C.L. (2010). Development of a methodology to estimate flotation separability from ore microtexture, PhD Thesis, JKMRC, The University of Queensland.

Evans, C.L., Wightman, E.M., & Yuan, X. (2012). Characterising ore micro-texture using Xray micro-tomography. In: 44th Annual Canadian Mineral Processors Operator Conference, Ottawa, Ontario.

Fandrich, R., Gu, Y., Burrows, D., & Moeller, K. (2007). Modern SEM-based mineral liberation analysis. Int. J. Miner. Process. 84, 310–320.

Ferragne, A. (1972). Le Précambrien et le paleozoïque de la province d'Orense (nord-ouest de l'Espagne). Stratigraphie-tectonique-métamorphisme. PhD thesis, University of Bordeaux, France, 249 pp.

Fetherston, J.M. (2004). Tantalum in Western Australia: Geological Survey of Western Australia, Mineral Resource Bulletin 22, 162 p., 1 folded map in pocket, accessed April 9, 2014, at http://www.commerceresources.com/i/pdf/10-Complete.pdf.

Filippova, I.V., Filippov, L.O., Duverger, A., & Severov, V.V. (2014). Synergetic effect of a mixture of anionic and nonionic reagents: Ca mineral contrast separation by flotation at neutral pH. Miner. Eng. 2014, 66–68, 135–144.

Filippov, L. O., Foucaud, Y., Filippova, I. V., & Badawi, M. (2018). New reagent formulations for selective flotation of scheelite from a skarn ore with complex calcium minerals gangue. Minerals Engineering, 123, 85-94.

Finch, J. (1979). Laboratory simulation of a closed-circuit grind for a heterogeneous ore. Canadian Mining and Metallurgical Bulletin, 72(803), 198-200.

Gasparrini, C. (1983). The mineralogy of gold and its significance in metal extraction, CIM Bulletin, Vol. 76, 851, pp. 144-153.

Gasparrini, C. (1984A). The mineralogy of silver and its significance in metal extraction, CIM Bulletin, June, pp. 99-110.

Gaudin, A.M. (1939). Principles of Mineral Dressing (New York: McGraw-Hill).

Gay, S.L. (2004a). Simple texture based liberation modelling of ores. Miner. Eng. 17, 1209–1216. http://dx.doi.org/10.1016/j.mineng.2004.06.032.

Ghaderi, M., Palin, J.M., Campbell, I.H., & Sylvester P.J. (1999). Rare earth element systematics in scheelite from hydrothermal gold deposits in the Kalgoorlie Norseman region, Western Australia. Economic Geology, 94(3), 423–438.

Ghorbani, Y., Fitzpatrick, R., Kinchington, M., Rollinson, G. & Hegarty, P. (2017). A Process Mineralogy Approach to Gravity Concentration of Tantalum Bearing Minerals. Minerals, 7, 194.

Goodall, W.R., Scales, P.J., & Butcher, A.R. (2015). The use QEMSCAN and diagnostic leaching in the characterisation of visible gold in complex ores. Miner. Eng., 18, 877–886.

Goodall,W.R., & Scales, P.J. (2007). An overview of the advantages and disadvantages of the determination of gold mineralogy by automated mineralogy. Minerals Engineering 20 Vol. 5, pp. 506-517.

Goossens, P.J. (1978). The metallogenic provinces of Burma—their definitions, geologic relationships, and extension into China, India, and Thailand. In: Nutalaya, P. (ed.) Proceedings of the Third Regional Conference on Geology and Mineral Resources of Southeast Asia, Bangkok, Thailand, 14–18 November 1978, 431–492.

Gottlieb, P., Wilkie, G., Sutherland, D., Ho-Tun, E., Suthers, S., Perera, K., Jenkins, B., Spencer, S., Butcher, A., & Rayner, J. (2000). Using Quantitative Electron Microscopy for Process Mineral Applications. Journal of Metals, Vol. 52, pp. 24-25.

Grice, J.D., Černý, Petr, & Ferguson, R.B. (1972). The Tanco pegmatite at Bernic Lake, Manitoba Wodginite, tantalite, pseudo-ixiolite and related minerals: Canadian Mineralogist, v. 11, p. 609–642.

Guasch, E., Anticoi, H., Hamid, S.A., Oliva, J., Alfonso, P., Escobet, T., Sanmiquel L., & Bascompta, M. (2018). New approach to ball mill modelling as a piston flow process. Minerals engineering, 116, 82-87.

Gu, J Y. (1982). Morphological zoning of the vein-type tungsten deposits in southern China. In: Hepworth, J.V. and Zhang, Y.H. (eds.) Proceedings of Symposium on Tungsten Ore deposits, Geological Publishing House, Beijing, 269–278.

Gu, Y. (2003). Automated Scanning Electron Microscope Based Mineral Liberation analysis. Journal of Minerals and Materials Characterisation and Engineering, Vol. 2, pp. 33-41.

Guerenko, A., & Schmincke, H.U. (2002). Tungsten in Searles Lake. Mining Engineering 11, 301–303.

Guerney, P.J., Laplante, A.R., & O'Leary, S. (2003). Gravity recoverable gold and the Mineral Liberation Analyser, Proc. 35th Annual Meeting of the Canadian Mineral Processors, CMP, CIMMP, Ontario (Jan.), 401-416.

Guiliani, G., Li, Y.D. & Sheng, T.F. (1988). Fluid inclusion study of Zihuashan tungsten deposit in southern Jiangxi province, China. Mineralium Deposita 23, 24–33.

Gupta, A., & Yan, D. S. (2016). Mineral processing design and operations: an introduction. Elsevier.

Gupta, A., & D. S. Yan. (2006). Introduction to mineral processing design and operation. Perth, Australia (2006): 564-570.

Gutiérrez-Alonso, G., Collins, A.S., Fernández-Suárez, J., Pastor-Galán, D., González-Clavijo, E., Jourdan, F., Weil, A.B. & Johnston, S.T. (2015). Dating of lithospheric buckling: 40Ar/39Ar ages of syn-orocline strike–slip shear zones in northwestern Iberia. Tectonophysics, 643, 44–54.

Hagni, R. D. (1982). Process Mineralogy II: Applications in Metallurgy, Ceramics and Geology. Dallas, Tex, 14-18 Feb. 1982, 1982.

Hagni, R. (1986, January). Process Mineralogy VI. In Vortragsband des Symposiums" Process Mineralogy" der Metallurgical Society (pp. 431-456).

Hamid, S.A., Alfonso, P., Anticoi, H., Guasch, E., Oliva, J., Dosbaba, M., Garcia-Valles N., & Chugunova, M. (2018). Quantitative mineralogical comparison between HPGR and ball mill products of a Sn-Ta ore. Minerals, 8(4), 151.

Harris, D.D. The Mineralogy of gold and its relevance to gold recoveries. Miner. Deposita 1990, 25, S3–S7.

Han, Y.X., Liu, L., Yuan, Z.T., Wang, Z.H., & Zhang, P. (2012). Comparison of low-grade hematite product characteristics in a high-pressure grinding roller and jaw crusher. Miner. Metall. Process. 29, 75–80.

Hatert, F. & Burke, E.A.J. (2008). The IMA–CNMNC dominant-constituent rule revisited and extended. Canadian Mineralogist 46, 717-728.

Hausen, D.M. (1991). The role of mineralogy in mineral beneficiation, in Evaluation and Optimization of Metallurgical Performance, ed. D. Malhotra et al., SME Inc., Chapter 17.

Henley, K. J. (1983). Ore-dressing mineralogy-a review of techniques, applications and recent developments. In ICAM 81.

Herbst, J. A., Rajamani, K., Lin, C. L., & Miller, J. D. (1988). Development of a multicomponent-multisize liberation model. Minerals engineering, 1(2), 97-111.

Hilden, M. M., & Powell, M. S. (2017). A geometrical texture model for multi-mineral liberation prediction. Minerals Engineering, 111, 25-35.

Hill, R.J., Tsambourakis, G., & Madsen, I.C. (1993). Improved petrological modal analyses from X-ray powder diffraction data by use of the rietveld method I. selected igneous, volcanic, and metamorphic rocks. J. Petrol., 34, 867–900.

Hinde, C. (ed.). (2008). Tungsten. Mining Journal Special Publication. p16 http://www.miningjournal.com/_data/assets/supplement_file_attachment/0014/123314/tungsten-scr.pdf

Hogarth, D.D. (1977). Classification and nomenclature of the pyrochlore group. American Mineralogist 62, 403-410.

Höll, R. & Eichhorn, R. (2000). Tungsten mineralization and metamorphic remobilisation in the Ferbertal scheelite deposit (Central Alps, Austria). In: Spry, P.G., Longstaff, F.J. and Vokes F.M. (eds.) Metamorphosed and metamorphogenic Ore Deposits: Rev. Economic Geology 11, 233–264.

Höll, R., Maucher, A., & Westenberger, H. (1972). Synsedimentary diagenetic ore fabrics in the strata- and time-bound scheelite deposits of Kleinarltal and Felbertal in the Eastern Alps. Mineralium Deposita, 7, 217–226.

Honaker, R., Hower, J., Eble, C., Weisenfluh, J., Groppo, J., Rezaee, M., Bhagavatula, A., Luttrell, G.H., Bratton, R.C., & Yoon, R. H. (2014). Laboratory and bench-scale testing for rare earth elements. Cell, 724, 554-3652.

Hrstka, T., Gottlieb, P., Skala, R., Breiter, K., & Motl, D. (2018). Automated mineralogy and petrology-applications of TESCAN Integrated Mineral Analyzer (TIMA). Journal of Geosciences, 63(1), 47-63.

Huang, C. & Xiao, Z. (1986). A general review of the tungsten deposits in China. In Beus, A.A. (ed.) 1986 Geology of Tungsten. International Geological Correlation Programme Project 26 'MAWAM' (Mineralisation Associated with Acid Magmatism). United Nations Educational, Scientific and Cultural Organisation, Paris, France.

Hu, Y., Gao, Z., Sun,W., & Liu, X. (2012). Anisotropic surface energies and adsorption behaviors of scheelite crystal. Colloid. Surface A, 415, 439–448.

Iglesias, M. & Choukroune, P. (1980). Shear zones in the Iberian Arc. Journal of Structural Geology, 114, 63–68.

Ilhan, S., Kalpakli, A.O., Kahruman, C., Yusufoglu, I. (2013). The investigation of dissolution behavior of gangue materials during the dissolution of scheelite concentrate in oxalic acid solution. Hydrometallurgy, 136, 15–26.

Jarchovsky, T. (2006). The nature and genesis of greisens stocks at Krásno, Slavkovský les area – western Bohemia, Czech Republic. Journal of the Czech Geological Society 51, 201–215.

Johnson, N. W., & Munro, P. D. (2002). Overview of Flotation Technology and Plant Practice for Complex Sulphide Ores. In: Mineral Processing Plant Design Practice and Control, Vol. 1, SME, USA, pp. 1097-1123.

Jones, M.P. (1977). Automatic Image Analysis in Physical Methods in Determinative Mineralogy (J. Zussman editor, 2nd Edition, Academic Press).

Jones, M.P. (1987). Applied Mineralogy: A Quantitative Approach, Graham and Trotman, London.

Jones, M.P., & Gavrilovic, J. (1970). Automatic quantitative mineralogy in minerals technology. Rudy, Vol. 5, pp. 189-197.

Kazerani Nejad, R., & Sam, A. (2017). Limitation of HPGR application. Miner. Process. Ext. Met., 126, 224–230.

Keats, W. (1981). Alteration and replacement of wolframite in the Hemerdon tungsten deposit, Devon. PhD thesis, Open University.

Kelemen, P.B., Hanghøj, K., & Greene, A.R. (2003). One view of the geochemistry of subduction-related magmatic arcs, with an emphasis on primitive andesite and lower crust, in Rudnick, R.L., ed., The crust, v. 3 of Holland, H.D., and Turekian, K.K., eds., Treatise on geochemistry: Oxford, United Kingdom, Elsevier-Pergamon, v. 3, p. 593– 659.

Kelly, W.C. & Rye, R.O. (1979). Geologic, fluid inclusion, and stable isotope studies of the tin-tungsten deposits of Panasqueira, Portugal. Economic Geology 74, 1721–1822.

Keppler, H. (1993). Influence of fluorine on the enrichment of high field strength trace elements in granitic rocks. Contributions to Mineralogy and Petrology, 114, 479–488.

Kerr, P.F. (1940). Tungsten-bearing manganese deposits at Galconda, Nevada. Geological Society of America Bulletin 51, 1359–1389.

King, R. P., & Schneider, C. L. (1998). Stereological correction of linear grade distributions for mineral liberation. Powder Technology, 98(1), 21-37.

King, R.P. (1975). Simulation of flotation plants. Transactions of the AIME, 258:286–293.

King, R.P. (1979). A Model for the Quantitative Estimation of Mineral Liberation from Mineralogical Texture, Int. J. Miner. Process., 6, p. 207.

King, R.P. (1982). The Prediction of Mineral Liberation from Mineralogical Texture," XIV Int. Proc. 8th Int. Mineral Processing Congress, Toronto, p. 11.

King, R.P. (2012). Modelling and Simulation of Mineral Processing Systems, Society for Mining, Metallurgy, and Exploration, Inc. (SME): Englewood, CO, USA, pp. 55–96.

Klichowicz, M., & Lieberwirth, H. (2016). Modeling of realistic microstructures as basis for comminution simulations. In: Proceedings XXVIII International Mineral Processing Congress, Quebec City, Canada. September 11–15 2016.

Knights, J., & Patterson, D. (1988). Process mineralogy of silver in lead-zinc-silver ores at Mount Isa, Australia, In Proceedings Silver – Exploration, Mining and Treatment, IMM, Mexico City, pp. 101-110.

Kravchenko, S.M., & Pokrovsky, B.G. (1995). The Tomtor alkaline ultrabasic massif and related REE-Nb depos its, northern Siberia: Economic Geology, v. 90, p. 676–689.

Kogarko, L.N., Lahaye, Y., & Brey, G.P. (2010). Plume- related mantle source of super-large rare metal deposits from the Lovozero and Khibina massifs on the Kola Peninsula, eastern part of the Baltic Shield—Sr, Nd, and Hf isotope systematics: Mineralogy and Petrology, v. 98, nos. 1– 4, p. 197–208.

Kogarko, L.N., Williams, C.T., & Woolley, A.R. (2002). Chemical evolution and petrogenetic implications of loparite in layered, agpaitic Lovozero complex, Kola Peninsula, Rus ia: Mineralogy and Petrology, v. 74, no. 1, p. 1–24.

Kooiman, G.J.A., McLeod, M.J. & Sinclair, W.D. (1986). Porphyry tungsten-molybdenum orebodies, polymetallic veins and replacement bodies and tin-bearing greisens zones in the Five Tower zone, Mount Pleasant, New Brunswick. Economic Geology 81, 1356–1373.

Küster, D., (2009). Granitoid-hosted Ta mineralization in the Arabian-Nubian Shield—Ore deposit types, tectono-metallogenetic setting and petrogenetic framework: Ore Geology Reviews, v. 35, no. 1, p. 68–86.

Krishna, R. (1996). Beneficiation of tungsten ores in India: a review. Bull. Mater. Sci. 19,201–265.

Kwak, T.A.P. (1987). W-Sn skarn deposits and related metamorphic skarns and granitoids. Developments in Economic Geology, 24, Elsevier Publ. Co., pp. 451.

Kwak, T.A.P., & Tan, T.H. (1981). The geochemistry of zoning in the skarn minerals at King Island (Dolphin) mine. Economic Geology 76, 468–497.

Lassner, E., & Schubert, W. (1999). Tungsten: Properties, Chemistry, Technology of the Element, Alloys, and Chemical Compounds; Springer: New York, NY, USA.

Lagache, M., and Quéméneur, J. (1997). The Volta Grande pegmatites, Minas Gerais, Brazil—An example of rare-element granitic pegmatites exceptionally enriched in lithium and rubidium: Canadian Mineralogist, v. 35, no. 1, p. 153–165.

Lamberg, P. (2011). Particles – The bridge between geology and metallurgy: Proceedings Conference in Mineral Engineering, Luleå, Sweden, pp. 1-16.

Landis, Gary P. & Rye, R.O. (1974). Geologic fluid inclusion and stable isotope studies of the Pasto Bueno tungsten-base metal ore deposit, northern Peru. Economic Geology 69, 1025–1059.

Lastra R. (2007). Seven practical application cases of liberation analysis. International Journal of Mineral Processing, Vol., 84, pp. 337-347.

Lahti, S. I. (1987). Zoning in columbite-tantalite crystals from the granitic pegmatites of the Eräjärvi area, southern Finland. Geochimica et Cosmochimica Acta, 51(3), 509-517.

Lane, G.R., Martin, C., & Pirard, E. (2008). Techniques and applications for predictive metallurgy and ore characterisation using optical image analysis. Miner. Eng. 21, 568–577.

Lätti, D., & Adair, B. J. I. (2001). An assessment of stereological adjustment procedures. Minerals engineering, 14(12), 1579-1587.

Levine, R.M. (2011). The Mineral Industry of Russia. 2009 Minerals Yearbook. United States Geological Survey, pp. 26.

Li, C., & Gao, Z. (2017). Effect of grinding media on the surface property and flotation behavior of scheelite particles. Powder Technol. 322, 386–392.

Li, G.L., Hua, R.M., Zhang, W.L., Hu, D., Wei, X., Huang, X., Xie, L., Yao, J., & Wang, X. (2011). He-Ar isotope composition of pyrite and wolframite in the Tieshanlong tungsten deposit, Jiangxi, China: Implications for fluid evolution. Resource Geology 61, 356–366.

Li, S.R., Wang, D.H., Liang, T., Qu, W.J. & Ying, L.J. (2008). Metallogenic epochs of the Damingshan tungsten deposit in Guangxi and its prospecting potential. Acta Geologica Sinica 82 873–879 (in Chinese with English abstract).

Li, X.H., Liu, D., Sun, M., Li, W.X., Liang, X.R. & Liu Y. (2004). Precise Sm-Nd and U-Pb isotopic dating of the supergiant Shizhuyuan polymetallic deposit and its host granite, SE China. Geological Magazine 141 (2), 225–231.

Lin, C.L., Miller, J.D. & Herbst, J.A. (1987). "Solutions to the Transformation Equation for Volumetric Grade Distribution from Linear and/or Areal Grade Distributions," Powder Technology, 50, p. 55.

Linnen, R.L. (1998). The solubility of Nb–Ta–Zr–Hf–Win granitic melts with Li and Li + F: constraints for mineralization in rare metal granites and pegmatites. Economic Geology, 93, 1013–1025.

Linnen, R.L., & Cuney, M. (2005). Granite-related rare-element deposits and experimental constraints on Ta-Nb-W-Sn-Zr-Hf mineralization, in Linnen, R.L., Samson, I.M., and Martin, R.F., eds., Rare-element geochemistry and mineral deposits: St. John's, Newfoundland and Labrador, Canada, Geological Association of Canada, Short Course Notes, v. 17, p. 45–68.

Linnen, R.L. & Keppler, H. (1997). Columbite solubility in granitic melts: consequences for the enrichment and fractionation of Nb and Ta in the Earth's crust. Contributions to Mineralogy and Petrology, 128, 213–227.

Liu, W. (1980). Geological Features of Mineralisation of the Xingluokeng Tungsten (Molybdenum) Deposit, Fujian Province. In: Hepworth, J.V. and Lu, H.Z. (eds.) Tungsten Geology, China, ESCAP/RMRDC, Bandung, Indonesia, 338–348.

Liu, Y.J & Ma, D.S. (1993). Vein-type tungsten deposits of China and adjoining regions. Ore Geology Reviews 8, 233–246.

Llorens González, T., García Polonio, F., López Moro, F. J., Fernández-Fernández, A., Sans Contreras, J.L. & Moro Benito, M.C. (2017). Tin-tantalum-niobium mineralization in the Penouta deposit (NW Spain): Textural features and mineral chemistry to unravel the genesis and evolution of cassiterite and columbite group minerals in a peraluminous system. Ore Geology Reviews, 81, 79–95.

López Moro, F.J., García Polonio, F., Llorens González, T., Sanz Contreras, J.L., Fernández-Fernández, A. & Moro Benito, M.C. (2017). Ta and Sn concentration by muscovite fractionation and degassing in a lens-like granite body: The case study of the Penouta rare-metal albite granite (NW Spain). Ore Geology Reviews, 82, 10–30.

Lu, H.Z., Liu, Y., Wang, C., Xu, Y. & Li, H. (2003). Mineralisation and fluid inclusion study of the Shizhuyuan W-Sn-Bi-Mo-F skarn deposit, Hunan Province, China. Economic Geology 98, 955–974.

Lumpkin, G.R. & ewing, R.C. (1992). Geochemical alteration of pyrochlore group minerals: microlite subgroup. American Mineralogist 77, 179-188.

Lumpkin, G.R. & Ewing, R.C. (1995). Geochemical alteration of pyrochlore group minerals: pyrochlore subgroup. American Mineralogist 80, 732-743.

Ma, L. (1982). The geological characteristics of Damingshan sedimentary-magmatic-hydrothermal wolframite deposit, Guangxi Zhuang Autonomous Region, China. In: Hepworth, J.V., & Yu, H.Z., (eds.) Symposium on Tungsten Geology [Jiangxi, China, October 1981]: Bandung [Indonesia], ESCAP/RMRDC and Beijing, Geological Publishing House, 374–384.

Martins, J.P. (1996). Kinetics of soda ash leaching of low-grade scheelite concentrates. Hydrometallurgy, 42(2), 221-236.

Mackay, D.A.R., & Simandl, G.J. (2014). Geology, market and supply chain of niobium and tantalum—A review. Miner. Deposita 2014, 49, 1025–1047.

Mangas, J. & Arribas, A. (1991). Fluid inclusion study of tin-mineralized greisens and quartz veins in the Penouta apogranite (Orense, Spain). Mineralogical Magazine, 55, 211–223.

Mariano, A.N. (1989). Nature of economic mineralization in carbonatites and related rocks, in Bell, Keith, ed., Carbonatites—Genesis and evolution: Boston, Mass., Unwin Hyman, p. 149–176.

Marsh, S.P. & Erickson, R.L. (1975). Integrated geologic and geochemical studies, Edna Mountain, Nevada. In: Elliot, I.L. and Fletcher, W.K. (eds.) Geochemical Exploration 1974. Elsevier Publ. Co., Amsterdam, Netherlands, 237–250.

Martin, R. F., & Wülser, P. A. (2014). Niobium and tantalum in minerals: siderophile, chalcophile or lithophile, and polyvalent. Journal of Geochemical Exploration, 147, 16-25.

Martins, T., Lima, A., Simmons, W.B., Falster, U. & Noronha, F. (2011). Geochemical fractionation of Nb–Ta oxides in Li-bearing pegmatites from the Barroso– Alvão pegmatite field, Northern Portugal. The Canadian Mineralogist, 49, 777–791.

Masau, M., Černý, P. & Chapman, R. (2000). Exsolution of zirconian-hafnian wodginite from manganoantantalian cassiterite, Annie claim #3 granitic pegmatite, Southeastern Manitoba, Canada. The Canadian Mineralogist, 38, 685–694.

McArthur, G.J. (1996). Textural evolution of the Hellyer massive sulfide deposit. Unpublished PhD thesis, University of Tasmania, Hobart, Australia. 272pp.

Meinert, L. (2014). Personal communication. Program Coordinator, Mineral Resources Program, US Geological Survey, Reston, VA.

Meinert, L.D., Dipple, G.M. & Nicolescu, S. (2005). World Skarn Deposits. In: Hedenquist, J.W., Thompson, J.F.H., Goldfarb, R.J. and Richards, J.R. (eds.) Society of Economic Geologists One hundredth Anniversary Volume (1905–2005), 299–336.

Meloy, T.P., U. Preti & G. Ferrara, (1987). Liberation - Volume and Mass Lockedness Profiles Derived - Theoretical and Practical Conclusions, Int. J. Miner. Process., (1987), 20, p. 17.

Miettinen, T., Ralston, J., & Fornasiero, D. (2010). The limits of fine particle flotation. Miner. Eng. 23 (5), 420–437.

Miller, J.D., & Lin, C.L. (2004). Three dimensional analysis of particulates in mineral processing systems by cone beam X-ray microtomography. Miner. Metall. Process. 21, 113–124.

Mining Magazine (1979). Hemerdon – Britain's largest tungsten deposit. Mining Magazine, 342–351.

Mitchell, R.H. (2005). Mineralogical and experimental constraints on the origins of niobium mineralization in carbonatites, in Linnen, R.L., Samson, I.M., and Martin, R.F., eds., Rare-element geochemistry and mineral deposits: St. Johns, Newfoundland and Labrador, Canada, Geological Association of Canada, Short Course Notes, v. 17, p. 201–215.

Mohammadnejad, S., Noaparast, M., Hosseini, S., Aghazadeh, S., Mousavinezhad, S., & Hosseini, F. (2018). Physical methods and flotation practice in the beneficiation of a low grade tungsten-bearing scheelite ore. Russ. J. Non-Ferr. Met., 59, 6–15.

Molavi, M., Hollett, G., Board, W.S., Bolu, M., Smith, P., Lemieux, J., Netherton, D.E., Nyland, E. & Weston, S. (2011). Preliminary Economic Assessment for the Northern Dancer Project, Yukon, Canada. Prepared by AMC for Largo Resources Ltd. Filed on www.sedar.com on 7 April 2011.

Moore, D.M., & Reynolds, R.C. (1989). X-ray Diffraction and the Identification and Analysis of Clay Minerals; Oxford University Press: New York, NY, USA.

Mudd, G. M. (2010). The Environmental Sustainability of Mining in Australia: Key Mega Trends and Looming Constraints. Resources Policy, 35 Vol. 2, pp. 98-115.

Narciso, H., Iakovlev, I., & de Ruijter, M.A. (2009). Amended Technical Report on the Mactung Property, prepared by Wardrop et al. for North American Tungsten Corp. Ltd. www.sedar.com on 18 May 2010.

Nasraoui, M. & Waerenborgh, J.C. (2001). Fe speciation in weathered pyrochlore-group minerals from the Lueshe and Araxá (Barreiro) carbonatites by 57Fe Mössbauer spectroscopy. Canadian Mineralogist 39, 1073-1080.

National Bureau of Statistics of China (NBSC). (2012). Statistical Yearbook of China 2011. http://www.stats.gov.cn/english/statisticaldata/yearlydata/.

National Research Council (US). Committee on Nutrient Requirements of Small Ruminants, Board on Agriculture, Division on Earth, & Life Studies. (2007). Nutrient requirements of small ruminants: sheep, goats, cervids, and new world camelids.

Neinavale, H., Thalmann, F., Ataii, B. & Beran, A. (1989). Wolframite and scheelite-bearing carbonate rocks of the Nock Mountains, Austria: A new type of tungsten mineralisation in the Eastern Alps. Mineralium Deposita 24, 14–18.

Neiva, A. M., Gomes, M. E., Ramos, J. M., & Silva, P. B. (2008). Geochemistry of granitic aplite-pegmatite sills and their minerals from Arcozelo da Serra area (Gouveia, central Portugal). European Journal of Mineralogy, 20(4), 465-485.

Newbury, D. E., Joy, D. C., Echlin, P., Fiori, C. E., & Goldstein, J. I. (1986). Advanced Scanning Electron Microscopy and X-ray Microanalvsis. Plenum Press, New York. 454 pp.

Newberry, R.J. & Einaudi, M.T. (1981). Tectonic and geochemical setting of tungsten skarn mineralization in the Cordillera. Arizona Geological Society Digest 14, 99–111.

Niu, Y., & O'Hara, M.J. (2003). Origin of ocean island basalts—A new perspective from petrology, geochemistry, and mineral physics considerations: Journal of Geophysical Research, v. 108, no. B4, p. 2209.

Noble, S.R., Spooner, E.T.C. and Harris, F.R. (1984). The Logtung large tonnage, low-grade W (scheelite)-Mo porphyry deposit, south-central Yukon Territory. Economic Geology 79, 848–868.

Papp, J.F. (2013a). Niobium and tantalum, in Metals and minerals:U.S. Geological Survey Minerals Yearbook 2011, v. I, p. 52.1–52.14. [Also available at http://minerals.usgs.gov/minerals/pubs/commodity/niobium/.]

Parker, R.L., & Adams, J.W. (1973). Niobium (columbium) and tantalum, in Brobst, D.A., and Pratt, W.P., eds., United States mineral resources: U.S. Geological Survey Professional Paper 820, p. 443– 454.

Parker, R.L., & Fleischer, Michael (1968). Geochemistry of niobium and tantalum: U.S. Geological Survey Professional Paper 612, 43 p. [Also available at http://pubs.er.usgs.gov/publication/pp612.].

Partington, G.A., McNaughton, N.J., & Williams, I.S. (1995). A review of the geology, mineralization, and geochro- nology of the Greenbushes pegmatite, Western Australia: Economic Geology, v. 90, p. 616 – 635.

Peng J.T., Hu R.Z., Zhao J.H., Fu Y.Z., & Yuan S.D. (2005). Rare earth element (REE) geochemistry for scheelite from the Woxi Au–Sb–W deposit, western Hunan, Geochimica, 34(2), 115–122.

Petruk, W. (2000). Applied mineralogy in the mining industry, Elsevier Science, Amsterdam. 268.

Pitard, F.F., 2010. Theoretical, practical, and economic difficulties in sampling for trace constituents. The Journal of The Southern African Institute of Mining and Metallurgy, Vol. 110, pp. 313-321.

Pitfield, P.E.J. Brown, T.J., & Idoine, N.E. (2010). Mineral Information and Statistics for the BRIC countries 1999–2008. British Geological Survey. http://www.bgs.uk/mineralsuk.

Plimer, I. (1975). Wolfram Camp wolframite-molybdenitebismuth quartz pipes, North Queensland. In: Knight, C.L. (ed.) Economic Geology of Australasia and Papua New Guinea v.1. Metals. Australasian Institute of Mining and Metallurgy Monograph Series 5, 760–762.

Pollard, P.J. (1995). A special issue devoted to the geology of rare metal deposits—Geology of rare metal deposits—An introduction and overview: Economic Geology, v. 90, p. 489– 494.

Polinares. (2013). Coltan, Congo & Conflict - Polinares Case Study. The Hague Centre for Strategic Studies.

Rahfeld, A., Kleeberg, R., Möckel, R., & Gutzmer, J. (2018). Quantitative mineralogical analysis of European Kupferschiefer ore. Miner. Eng., 115, 21–32.

Raimbault, L., & Burnol, L. (1998). The Richemont rhyolite dyke (French Massif Central): a subvolcanic equivalent of rare-metal granites. The Canadian Mineralogist, 36, 265–282.

Raith, J.G., & Schmidt, S. (2010). Tungsten Deposit Felbertal, Salzburg, Austria: IMA2010 Field Trip Guide AT3 Department of Mineralogy, Geochemistry and Petrology, University of Szeged.

Raith, J.G., & Stein, H.J. (2006). Variscan ore formation and metamorphism at the Felbertal scheelite deposit (Austria): constraining tungsten mineralisation from Re–Os dating of molybdenite Contributions to Mineralogy and Petrology, 152(4), 505-521.

Rao, C., Wang, R.C., Hu, H. & Zhang, W.L. (2009). Complex internal textures in oxide minerals from the Nanping no. 31 dyke of granitic pegmatite, Fujian province, Southeastern China. The Canadian Mineralogist, 47, 1195–1212.

Ray, G.E. (1995). Tungsten Skarns, in Selected British Columbia Mineral Deposit Profiles, Volume 1 - Metallics and Coal, Lefebure, D.V. and Ray, G.E., Editors, British Columbia Ministry of Employment and Investment, 20, 71–74.

Reed, S.J.B. (2005). Electron Microprobe Analysis and Scanning Electron Microscopy in Geology. Second Edition, Cambridge University Press.

Research in China (2011). China Tungsten Industry Report 2010-11, Abstract. http://www.researchinchina.com/Htmls/Report/2011/6076.html

Reichl, C., Schatz, M., & Zsak, G. (2018). World mining data. Minerals Production International Organizing Committee for the World Mining Congresses.

Rieck, G.D. (1967). Tungsten and Its Compounds; Pergamon Press: Norwich, UK.

Riquelme, J. (2014). Improved process development for complex silver ore through systematic, advanced mineral characterisation (Doctoral dissertation, Queensland University, Mineral Institute, Australia).

Roskill Information Services Ltd. (2012). Tantalum—Marketoutlook to 2016 (11th ed.): London, United Kingdom, Roskill Information Services Ltd., 164 p.

Rouse, R.C., Dunn, P.J., Peacor, D.R. & Wang, L. (1998). Structural studies of the natural antimonian pyrochlores. I. Mixed valency, cation site splitting, and symmetry reduction in lewisite. Journal of Solid State Chemistry 141, 562-569.

Rozendaal, A., le Roux, S.G., & du Plessis, A. (2018). Application of microCT scanning in the recovery of endo-skarn associated scheelite from the Riviera Deposit, South Africa. Miner. Eng., 116, 163–178.

Rubinstein, J.P. & Barsky, L.A. (2002). Mineral Deposit and Resources of the Former Soviet Union, Vol 1: Non-Ferrous Metal Ores: Deposits, Minerals and Plants. Taylor and Francis, pp. 411.

Rudnick, R.L., & Gao, S. (2003). Composition of the continental crust, in Rudnick, R.L., ed., The crust, v. 3 of Holland, H.D., and Turekian, K.K., eds., Treatise on geochemistry, v. 3: Oxford, United Kingdom, Elsevier-Pergamon, p. 1–64. [Also available at http://dx.doi.org/10.1016/B0-08-043751-6/03016-4.]

Salvi, S., & Williams-Jones, A.E. (2005). Alkaline granite-syenite deposits, in Linnen, R.L., Samson, I.M., Martin, R.F., eds., Rare-element geochemistry and mineral deposits: St. Johns, Newfoundland and Labrador, Canada, Geological Association of Canada, Short Course Notes, v. 17, p. 315–341.

Sandmann D. (2015). Method Development in Automated Mineralogy, TU Bergakademie, Freiberg.

Schaap,W. (1979). Illustrated liberation-flotation recovery model for a disseminated mineral in low-grade ore. Trans. Inst. Min. Metall. Section C-Miner. Process. Extr. Metall., 88, C220–C228.

Schmidt, S. (2012). From deposit to concentrate: The basics of tungsten mining. Part 1: Project generation and project development. International Tungsten Industry Association newsletter.

Schneider, C.L. (1995). The Measurement and Calculation of Liberation in Continuous Grinding Circuits. Ph.D. thesis, University of Utah.

Schneider, C.L. Lin, C.L., King, R.P., & Miller, J.D. (1991). An Improved Transformation Technique for the Prediction of Liberation by a Random Fracture Model, Powder Technology, 67, p. 103.

Schwela, U. (2007). Tantalum. Mining Journal Supplement.

Schwela, U. (2010). Mining Journal special publication—Tantalum (A supplement to Mining Journal), with a section on the state of tantalum mining: London, United Kingdom, Aspermont, September, 11 p., accessed December 15, 2012, at http://www.mining-journal.com/__data/assets/supplement_file_attachment/0011/237287/Tantalum2010_scr.pdf.

Selway, J.B., Breaks, F.W., & Tindle, A.G. (2005). A review of rare-element (Li-Cs-Ta) pegmatite exploration tech- niques for the Superior Province, Canada, and large worldwide tantalum deposits: Exploration and Mining Geology, v. 14, nos. 1– 4, p. 1–30.

Semenov, E. (1997). Minerals and ores of the Khibiny-Lovozero alkaline massif, Kola: Moscow, Russian Academy of Sciences, Fersman Mineralogical Museum, 70 p.

Shedd, K B. (2012a). Tungsten. Mineral Commodity Summaries, United States Geological Survey. http://minerals.usgs.gov/minerals/pubs/commodity/tungsten/680400.pdf

Shedd, K.B. (2012b). Tungsten. 2010 Minerals Yearbook. United States Geological Survey. http://minerals.usgs.gov/minerals/pubs/commodity/tungsten/myb1-2010-tungs.pdf

Shepeta, E.D., Samatova, L.A., & Kondrat'ev, S.A. (2012). Kinetics of calcium minerals flotation fromscheelite–carbonate ores. J. Min. Sci., 48, 746–753.

Shore, M. & Fowler, A.D. (1996). Oscillatory zoning in minerals; a common phenomenon. The Canadian Mineralogist, 34, 1111–1126.

Simmons, S.F. & Sawkins, F.J. (1983). Mineralogic and fluid inclusion studies of the Washington Cu-Mo-W bearing breccia pipe, Sonora, Mexico. Economic Geology 78, 521–526.

Sivamohan, R., & Forssberg, E. (1985). Recovery of heavy minerals from slimes. Int. J. Miner. Process. 15, 297–314.

Snow, R.J. & Coker, W.B. (1986). Overburden geochemistry related to W-Cu-Mo mineralisation at Sisson Brook, New Brunswick, Canada: an example of short- and long-distance glacial dispersal. Journal of Geochemical Exploration, 28, 353–368.

Soloviev, S.G. & Krivoschchekov, N.N. (2011). Vostok-2 gold-base-metal-tungsten skarn deposit, Central Sikhote-Alin, Russia. Geology of Ore Deposits 53, 478–500.

Sørensen, H. (2001). Brief introduction to the geology of the Ilímaussaq alkaline complex, South Greenland, and its exploration history, in Sørensen, Henning, ed., The Ilímaussaq Alkaline Complex, South Greenland—Status of mineralogical research with new results (Anniversary volume): Copenhagen, Denmark, Geological Survey of Denmark and Greenland, v. 190, p. 7–24.

Sørensen, H., ed. (1974). The alkaline rocks: New York, N.Y., Wiley Interscience, 622 p.

Spencer, S., & Shutherland, D. (2000). Stereological correction of mineral liberation grade distributions estimated by single sectioning of particles. Image Anal. Stereol., 19, 175–182.

Spilde, N. & Shearer, C.K. (1992). A comparison of tantalum-niobium oxide assemblages in two mineralogically distinct rare-element granitic pegmatites, Black Hills, South Dakota. The Canadian Mineralogist, 30, 719–737.

Steenfelt, A. (1991). High technology metals in alkaline and carbonatitic rocks in Greenland—Recognition and exploration: Journal of Geochemical Exploration, v. 40, nos. 1–3, p. 263–279.

Stepanov, A., Mavrogenes, J.A., Meffre, S. & Davidson, P. (2014). The key role of mica during igneous concentration of tantalum. Contributions to Mineralogy and Petrology, 167, 1–8.

Subasinghe, G.K.N. (2008). The prediction of flotation characteristics of a disseminated ore using ore texture data. In Proceedings of the XXIV International Mineral Processing Congress, Beijing, China, 24–28 September (2008) Wang, D.Z., Sun, C.Y., Wang, F.L., Zhang, L.C., Han, L., Eds.; Science Press: Beijing, China, 2008; pp. 2339–2349.

Sweetapple, M.T., & Collins, P.L.F. (2002). Genetic frame- work for the classification and distribution of Archean rare metal pegmatites in the north Pilbara Craton, Western Australia: Economic Geology, v. 97, p. 873–895.

Sykora, S., Cooke, D.R., Meffre, S., Stephanov, A.S., Gardner, K., Scott, R., Selley, D., & Harris, A.C. (2018). Evolution of pyrite trace element compositions from porphyry-style and epithermal conditions at the Lihir gold deposit: Implications for ore genesis and mineral processing. Econ. Geol., 113, 193–208.

Taylor, W. J., Seifried, L. M., Wolf, W. D., Ries, A. J., & Kast, J. E. (2011). U.S. Patent No. 7,966,070. Washington, DC: U.S. Patent and Trademark Office.

Thalhammer, O.A.R, Stumpfl, E.F., & Jahoda, R. (1989). The Mittersill scheelite deposit, Austria Economic Geology, 84(5), 1153-1171.

Tindle, A.G. & Breaks, F.W. (2000). Columbite-tantalite mineral chemistry from rare element granitic pegmatites: Separation Lake area, NW Ontario, Canada. Mineralogy and Petrology, 70, 165–198.

Todd, R.G. (1989). Evaporites and strata-bound tungsten mineralisation. Geology 17, 139–143.

Tornos, F., Galindo, C., Crespo, J. L., & Spiro, B. F. (2007). Geochemistry and origin of calcic tungsten-bearing skarns, Los Santos, Central Iberian Zone, Spain. Canadian Mineralogist 46, 87–109.

Traore, A., Conil, P., Houot, R., & Save, M. (1995). An evaluation of the Mozley MGS for fine particle gravity separation. Minerals Engineering, 8(7), 767-778.

Ueda, T., Oki, T., & Koyaanaka, S. (2017). Comparison of Seven Texture Analysis Indices for Their Applicability to Stereological Correction of Mineral Liberation Assessment in Binary Particle Systems. Minerals, 7, 222.

Ueda, T., Oki, T., & Koyanaka, S. (2017). Stereological correction method based on sectional texture analysis for the liberation distribution of binary particle systems. Advanced Powder Technology, 28(5), 1391-1398.

Uher, P., Žitňan, P. & Ozdín, D. (2007). Pegmatitic Nb-Ta oxide minerals in alluvial placers from Limbach, Bratislava Massif, Western Carpathians, Slovakia: Compositional variations and evolutionary trend. Journal of Geosciences, 52, 133–141.

U.S. Department of State. (2015). About the great lakes region. http://www.state.gov/s/greatlakes_drc/191417.htm.

U.S. Geological Survey (2019). Mineral Commodity Summaries, U.S. Geological Survey: Reston, VA, USA.

U.S. Geological Survey (2017). Mineral Commodity Summaries; U.S. Geological Survey: Reston, VA, USA.

U.S. Geological Survey (2014). Mineral Commodity Summaries; U.S. Geological Survey: Reston, VA, USA.

U.S., Securities & Exchange Commission. (2012). The laws that govern the securities industry. U.S Securities and Exchange Commission (accessed January 31, 2015). http://www. sec. gov/about/laws. shtml# sox2002.

Upton, B.G.J., Emeleus, C.H., Heaman, L.M., Goodenough, K.M., & Finch, A.A. (2003). Magmatism of the mid-Proterozoic Gardar Province, South Greenland—Chronology, petrogenesis and geological setting: Lithos, v. 68, nos. 1–2, p. 43– 65.

Van der Wielen, K.P., & Rollinson, G. (2016). Texture based analysis of liberation behaviour using Voroni tessellations. Miner. Eng. 89, 93–107 10.1016.j.mineng.2015.09.008.

Van Wambeke, L., (1970). The alteration processes of the comuences. Neues hrbuch für Mineralogie, Abhandlungen 112, 117-149.

Vegas, N., Aranguren, A., Cuevas, J. & Tubía, J.M. (2001). Variaciones en losmecanismos de emplazamiento de los granitos del eje Sanabria-Viana doBolo (Macizo Ibérico, España). Boletín Geológico y Minero, 112, 79–88.

Videla, A.R., Lin, C.L., & Miller, J.D. (2007). 3D characterization of individual multiphase particles in packed particle beds by X-ray microtomography (XMT). International Journal of Mineral Processing, 84(1-4), 321-326.

Vizcarra, T.G., Wightman, E.M., Johnson, N.W., & Manlapig, E.V. (2010). The effect of breakage mechanism on the mineral liberation properties of sulphide ores. Miner. Eng., 23, 374–382.

Wang, F.Y., Li, C.Y., Ling, M.X., Zhang, H., Sun, Y.L. & Sun, W. (2011). Geochronology of the Xihuashan tungsten deposit in southeastern China: constraints from RE-Os and U-Pb dating. Resource Geology 61, 414–423.

Wang, Y., McClung, C., Lin, C. L., & Miller, J. D. (2018). Stereological correction of perimeter based estimates of exposed grain surface area. Minerals Engineering, 126, 64-73.

Wiegel, R.L. & Li, K. (1967). A Random Model for Mineral Liberation by Size Reduction. Trans. SME-AIME, 238, p. 179.

Wells, A. (1991). Some experiences in the design and optimisation of fine gravity concentration circuits, Minerals Engng., 4(3/4), 383.

Welsby, S.D.D., Vianna, S.M.S.M., & Franzidis, J.P. (2010). Assigning physical significance to floatability components. International Journal of Mineral Processing, 97(1-4), 59-67.

Werner, A.B.T., Sinclair, W.D. & Amey, E.B. (1998). International Strategic Mineral Issues Summary Report – Tungsten. U.S. Geological Survey Circular 930-0. http://pubs.usgs.gov/pdf/circular/c930-0.html

Wikedzi, A., Arinanda, M.A., Leißner, T., Peuker, U.A., & Mütze, T. (2018). Breakage and liberation characteristics of low grade sulphide gold ore blends. Miner. Eng., 115, 33–40.

Wills, B. A., & Finch, J. (2015). Wills' mineral processing technology: an introduction to the practical aspects of ore treatment and mineral recovery. Butterworth-Heinemann.

Wills, B. A., & Napier-Munn, T. J. (2006). An introduction to the practical aspects of ore treatment and mineral recovery. Wills' Mineral Processing Technology, 267-352.

Wise, M.A. & Brown, C.D. (2010). Mineral chemistry, petrology and geochemistry of the Sebago granite– pegmatite system, southern Maine, USA. Journal of Geosciences, 55, 3–26.

Wise, M.A., Černý, P., & Falster, A.U. (1998). Scandium substitution in columbite-group minerals and ixiolite. The Canadian Mineralogist, 36, 673–680.

Wood, S.A. (2005). The aqueous geochemistry of zirconium, hafnium, niobium, and tantalum, in Linnen, R.L., Samson, I.M., and Martin, R.F., eds., Rare-element geochemistry and mineral deposits: St. Johns, Newfoundland and Labrador, Canada, Geological Association of Canada, Short Course Notes, v. 17, p. 217–268.

Woolley, A.R., & Kjarsgaard, B.A. (2008). Carbonatite occurrences of the world—Map and database: Geological Survey of Canada Open File 5796, 28 p., 1 CD-ROM plus 1 map, scale approx. 1:19,000,000.

Yager, T. R. (2014). The mineral industry of Rwanda. ― Reston (Virginia, U.S.), U.S. Geological Survey, 2012 Minerals Yearbook – Rwanda, pp. 35.1-35.3.

Yang, X. (2018). Beneficiation studies of tungsten ores–A review. Minerals Engineering, 125, 111-119.

Yin, L., Pollard, P.J., Shouxi, Hu, & Taylor, R.G.,(1995). Geologic and geochemical characteristics of the Yichun Ta-Nb-Li deposit, Jiangxi Province, south China: Economic Geology, v. 90, p. 577–585.

Zaraisky, G.I., & Dubinina, E.O. (2001). On duration of the magmatic and hydrothermal processes at Akchatau greisen W-Mo deposit in central Kazakhstan. In: Piestrzynski et al. (eds.) Mineral Deposits at the Beginning of the 21st Century, Swets and Zeitlinger B.V., Lisse, Netherlands, 505–510.

Zhang, J., Chen, Z., Wang, D., Chen, Z., Liu, S., & Wang, C. (2008). Geological characteristics and metallogenic epoch of the Xungluokeng tungsten deposit, Fujian Province. Geotectonica et Metallogenia 32, 92–97.

Zhang, J. (2012). Prediction and Influence of Mineral Liberation on Froth Flotation Performance. Ph.D. Thesis, Curtin University, Perth, Australia, p. 222.

Zhang, J., & Subasinghe, N. (2016). Development of a flotation model incorporating liberation characteristics. Miner. Eng., 98, 1–8.

Zhang, J., & Subasinghe, N. (2013). Prediction of mineral liberation characteristics of comminuted particles of high grade ores. Minerals Engineering, 49, 68-76.

Zhang, R., Lu, J., Zhu, J., Wang, R., Chen, J. & Gao, J. (2011). Re-Os and U-Pb geochronology of large Xintianling skarn-type scheelite deposit, Nanling Range, China. 11th Biennial Meeting SGA 2011. https://sga2011conference services.net/ resources/

Zhang, Z., Mao, J., Yang, J., Wang, Z. & Zhang, Z. (2003). Geology and genesis of the Ta'ergou skarn-quartz vein tungsten deposit in north Qilian Caledonian orogenic belt, northwest China. Resource Geology 53, 101–114.

Zhao, Y., Wenwei, L., Chengsi, B., Daxin, L., & Chongjun, J. (1990). Skarn Ore Deposits in China. Beijing, Geological Press, pp. 354.

Zhaolin, L. & Zhongfang, Y. (1996). Rock forming and ore-forming temperatures of Lianhuashan tungsten deposit, Guangdong Province. Chinese Journal of Geochemistry 15, 239–248.

Zhou, J. (2010). Process mineralogy of silver ores and applications in flowsheet design and plant optimization, 42nd Annual Meeting Canadian Mineral Processors, Ottawa. pp.143-161.

Zhu, T., Yang, Y., Yu, R. C., Ambaye, H., Lauter, V., & Xiao, J. Q. (2012). The study of perpendicular magnetic anisotropy in CoFeB sandwiched by MgO and tantalum layers using polarized neutron reflectometry. Applied Physics Letters, 100(20), 202406.

Appendix A: Grade distribution by particle size and liberation (differential mass).

Table A.1. Grade distribution by particle size and liberation (differential mass) for Penouta ore (open pit).

Mass (wt.%)	Grade class (%)										
Size Class (µm)	100	99-90	89-80	79-70	69-60	59-50	49-40	39-30	29-20	19-10	10->0
< 20	0.1793	0.00395	0.0026	0.0026	0.001569	0.00154	0.000854	0.001449	0.001194	0.00166	0.002843
20-40	1.51568	0.11027	0.06429	0.0452	0.026847	0.02338	0.023612	0.019143	0.017269	0.03222	0.08121
40-60	4.36475	0.96633	0.43142	0.237	0.132162	0.12032	0.09315	0.090356	0.108815	0.13873	0.403129
60-80	5.58289	3.08389	1.09023	0.5726	0.312958	0.20372	0.149959	0.108298	0.177636	0.21797	1.089973
80-100	4.33882	4.22444	1.31766	0.6871	0.348184	0.21747	0.162986	0.172883	0.191746	0.21496	1.461715
100-120	2.40129	4.00552	0.97565	0.4648	0.356059	0.14939	0.240401	0.244365	0.212118	0.35988	1.886739
120-140	0.89916	4.12663	1.22521	0.6198	0.377292	0.3619	0.127567	0.234835	0.358329	0.42707	2.835737
140-160	0.69008	4.0741	1.59544	0.6926	0.224957	0.19705	0.206885	0.347559	0.505892	0.27565	3.126782
160-180	0.47592	4.23216	1.72874	0.9592	0.382025	0.13769	0.22657	0.187831	0.030576	0.48431	4.1941
180-200	0.26591	2.65744	0.78191	0.5716	0.198712	0.16141	0.293965	0.083812	0	0.44943	3.577796
200-220	0	1.24492	0	0.1767	0.114114	0.15293	0.133941	0.115532	0	0	2.743742
220-240	0	0.15553	0.13038	0	0	0	0	0.078343	0	0.15331	0.908928
240-260	0	0	0	0	0	0	0	0	0	0	0

Table A.2. Grade distribution by particle size and liberation (differential mass) for Penouta tailings.

Mass (wt.%)	Grade class (%)										
Size Class (µm)	100	99-90	89-80	79-70	69-60	59-50	49-40	39-30	29-20	19-10	10->0
< 20	0.06405	0.00257	0.00075	0.00111	0.00106	0.00039	0.00100	0.00124	0.00047	0.00083	0.00257
20-40	0.27614	0.02023	0.02119	0.01062	0.00941	0.00000	0.00966	0.00448	0.00307	0.00251	0.00735
40-60	0.98004	0.23365	0.14734	0.06970	0.05182	0.01145	0.01563	0.00580	0.01393	0.01130	0.12042
60-80	1.86253	1.41327	0.23805	0.05364	0.02175	0.03637	0.00000	0.00000	0.00000	0.00000	0.46140
80-100	2.82729	3.75560	0.81347	0.26337	0.14861	0.05485	0.10414	0.06938	0.00000	0.00000	1.31651
100-120	3.49702	5.87398	0.98476	0.00000	0.00000	0.00000	0.00000	0.11794	0.00000	0.07986	1.33886
120-140	2.85529	4.93637	0.86847	0.50514	0.14299	0.12442	0.00000	0.00000	0.00000	0.08337	2.42956
140-160	0.95518	6.55419	0.91914	0.30964	0.45036	0.16708	0.28942	0.22223	0.00000	0.31420	5.67467
160-180	0.00000	4.53500	0.83327	0.32551	0.33849	0.00000	0.22634	0.27129	0.00000	0.19784	3.75474
180-200	0.00000	2.75018	0.67210	0.00000	0.00000	0.00000	1.04192	0.28386	0.00000	0.73192	3.37991
200-220	0.00000	1.93551	0.81136	0.00000	0.65761	0.47590	0.42550	0.00000	0.43811	0.00000	6.35983
220-240	0.00000	0.00000	0.00000	0.87913	0.00000	0.00000	0.00000	0.00000	0.58774	0.00000	0.00000
240-260	0.00000	1.40859	0.00000	0.00000	0.00000	0.00000	0.00000	0.00000	0.00000	0.00000	3.02776

Appendix A: Grade distribution by particle size and liberation (differential mass).

Table A.3. Grade distribution by particle size and liberation (differential mass) for Mittersill ore.

Mass (wt.%)	Grade class (%)										
Size Class (µm)	100	99-90	89-80	79-70	69-60	59-50	49-40	39-30	29-20	19-10	10->0
< 20	0.25230	0.01324	0.00291	0.00129	0.00078	0.00110	0.00164	0.00119	0.00131	0.00178	0.00283
20-40	2.06631	0.17606	0.04780	0.05102	0.03572	0.04312	0.03425	0.02623	0.03974	0.02824	0.13116
40-60	3.64043	0.68406	0.17836	0.11645	0.08060	0.07228	0.07814	0.02509	0.06097	0.10948	0.21648
60-80	4.71506	1.24819	0.24502	0.04658	0.06721	0.02004	0.03267	0.03317	0.05204	0.08078	0.34765
80-100	5.31945	2.44746	0.20515	0.15824	0.08022	0.02072	0.01942	0.05358	0.07081	0.03895	0.71463
100-120	5.15052	3.68636	0.09848	0.03688	0.11597	0.00000	0.00000	0.02899	0.00000	0.02519	0.65307
120-140	5.64925	3.66308	0.20256	0.37134	0.00000	0.08786	0.00000	0.17213	0.00000	0.00000	1.24475
140-160	4.89057	3.16260	0.00000	0.12141	0.10757	0.12630	0.09006	0.00000	0.07081	0.00000	1.94500
160-180	3.42261	6.31990	0.33896	0.00000	0.15302	0.00000	0.00000	0.00000	0.12889	0.00000	2.32433
180-200	2.01419	5.37223	0.30136	0.00000	0.00000	0.20797	0.00000	0.00000	0.00000	0.14270	1.59444
200-220	2.13394	3.11985	0.00000	0.00000	0.00000	0.00000	0.00000	0.00000	0.00000	0.00000	1.50337
220-240	3.80202	1.05969	0.47473	0.00000	0.00000	0.00000	0.00000	1.63392	0.00000	0.26549	1.18753
240-260	1.45549	2.17102	0.00000	0.00000	0.00000	0.48482	0.00000	0.00000	0.39127	0.00000	2.05611

Appendix B: Beta Distribution function parameters for the ore.

Table B.1. Beta distribution function parameters for Penouta ore (open pit).

Size Class (μm) / Parameter	**0-20**	**20-40**	**40-60**	**60-80**	**80-100**	**100-120**	**120-140**	**140-160**	**160-180**	**180-200**	**200-220**	**220-240**
n	591	1355	1880	1788	1102	604	426	299	228	113	48	13
$\mathbf{L_0}$	0.893	0.907	0.868	0.816	0.778	0.756	0.737	0.726	0.689	0.711	0.731	0.828
$\mathbf{L_1}$	0.096	0.071	0.081	0.081	0.071	0.051	0.020	0.016	0.011	0.008	0.000	0.000
g	0.102	0.083	0.113	0.151	0.175	0.171	0.160	0.162	0.173	0.139	0.088	0.038
$\mathbf{g^M}$	0.563	0.556	0.632	0.680	0.687	0.624	0.577	0.568	0.540	0.466	0.326	0.219
α^M	1.400	1.200	0.850	0.810	0.700	0.600	0.400	0.312	0.253	0.217	0.149	0.232
β^M	1.076	0.880	0.750	0.670	0.580	0.460	0.400	0.320	0.242	0.272	0.332	0.210

Table B.2. Beta distribution function parameters for Penouta tailings.

Size Class (μm) / Parameter	**0-20**	**20-40**	**40-60**	**60-80**	**80-100**	**100-120**	**120-140**	**140-160**	**160-180**	**180-200**	**200-220**	**220-240**
n	48	42	65	67	97	73	53	58	30	20	19	4
$\mathbf{L_0}$	0.934	0.920	0.854	0.845	0.846	0.893	0.926	0.922	0.952	0.959	0.941	0.992
$\mathbf{L_1}$	0.056	0.061	0.086	0.071	0.047	0.031	0.018	0.005	0.000	0.000	0.000	0.000
g	0.061	0.074	0.127	0.133	0.124	0.091	0.056	0.045	0.027	0.019	0.019	0.004
$\mathbf{g^M}$	0.516	0.676	0.675	0.741	0.724	0.787	0.670	0.543	0.563	0.453	0.315	0.542
α^M	7.546	5.700	5.500	5.375	5.500	3.600	2.900	3.000	1.600	1.000	0.700	0.500
β^M	4.500	4.200	3.700	4.400	3.600	4.000	2.500	2.300	2.000	1.000	0.400	0.600

Table B.3. Beta distribution function parameters for Mittersill ore.

Size Class (μm) / Parameter	**0-20**	**20-40**	**40-60**	**60-80**	**80-100**	**100-120**	**120-140**	**140-160**	**160-180**	**180-200**	**200-220**	**220-240**
n	217	605	356	180	137	94	67	51	50	32	18	10
$\mathbf{L_0}$	0.938	0.942	0.936	0.930	0.914	0.915	0.915	0.928	0.910	0.911	0.918	0.894
$\mathbf{L_1}$	0.056	0.044	0.045	0.048	0.051	0.046	0.046	0.035	0.029	0.024	0.029	0.065
g	0.060	0.052	0.057	0.064	0.076	0.076	0.073	0.056	0.072	0.070	0.061	0.081
$\mathbf{g^M}$	0.686	0.564	0.648	0.717	0.707	0.775	0.688	0.568	0.694	0.700	0.612	0.388
α^M	0.82	0.75	0.60	0.57	0.56	0.44	0.34	0.30	0.20	0.21	0.19	0.27
β^M	0.55	0.65	0.55	0.47	0.40	0.34	0.27	0.20	0.18	0.25	0.18	0.12

Table C.1. Mineral grain size distribution of columbite from Penouta ore (open pit).

Sieve Size	P1-P2 - Retained Wt%	P1-P2 - Cum. Retained Wt%	P1-P2 - Cum. Passing Wt%
300	0.00	0.00	100.00
250	0.60	0.60	99.40
212	0.37	0.96	99.04
180	1.13	2.09	97.91
150	3.85	5.94	94.06
125	6.79	12.74	87.26
106	11.35	24.09	75.91
90	12.27	36.36	63.64
75	16.33	52.69	47.31
63	14.81	67.49	32.51
53	11.78	79.27	20.73
45	7.49	86.76	13.24
38	5.04	91.79	8.21
32	3.25	95.05	4.95
27	1.90	96.95	3.05
22	1.24	98.19	1.81
19	0.58	98.76	1.24
16	0.46	99.22	0.78
13.5	0.31	99.53	0.47
11.4	0.20	99.73	0.27
9.6	0.13	99.86	0.14
8.1	0.07	99.93	0.07
6.8	0.03	99.96	0.04
5.7	0.02	99.98	0.02
4.8	0.01	99.99	0.01
4.1	0.01	99.99	0.01
3.4	0.00	99.99	0.01
2.9	0.00	100.00	0.00
2.4	0.00	100.00	0.00
2	0.00	100.00	0.00
1.75	0.00	100.00	0.00
1.45	0.00	100.00	0.00
1.2	0.00	100.00	0.00
0.52	0.00	0.00	0.00
0	0.00	0.00	0.00

Table C.2. Mineral grain size distribution of tantalite from Penouta ore (open pit).

Sieve Size	P1-P2 - Retained Wt%	P1-P2 - Cum. Retained Wt%	P1-P2 - Cum. Passing Wt%
212	0.00	0.00	100.00
180	0.36	0.36	99.64
150	3.17	3.52	96.48
125	5.64	9.17	90.83
106	7.49	16.66	83.34
90	8.25	24.92	75.08
75	14.16	39.08	60.92
63	13.59	52.67	47.33
53	13.06	65.73	34.27
45	9.33	75.06	24.94
38	7.62	82.68	17.32
32	5.24	87.92	12.08
27	3.65	91.57	8.43
22	2.89	94.46	5.54
19	1.46	95.92	4.08
16	1.28	97.20	2.80
13.5	0.97	98.17	1.83
11.4	0.71	98.88	1.12
9.6	0.36	99.24	0.76
8.1	0.26	99.50	0.50
6.8	0.16	99.66	0.34
5.7	0.13	99.79	0.21
4.8	0.07	99.86	0.14
4.1	0.08	99.94	0.06
3.4	0.03	99.97	0.03
2.9	0.03	100.00	0.00
2.4	0.00	100.00	0.00
2	0.00	100.00	0.00
1.75	0.00	100.00	0.00
1.45	0.00	100.00	0.00
1.2	0.00	100.00	0.00

Table C.3. Mineral grain size distribution of microlite from Penouta ore (open pit).

Sieve Size	P1-P2 - Retained Wt%	P1-P2 - Cum. Retained Wt%	P1-P2 - Cum. Passing Wt%
180	0.00	0.00	100.00
150	6.54	6.54	93.46
125	0.00	6.54	93.46
106	2.93	9.47	90.53
90	0.00	9.47	90.53
75	4.73	14.19	85.81
63	6.62	20.81	79.19
53	7.09	27.90	72.10
45	6.18	34.07	65.93
38	4.92	38.99	61.01
32	8.74	47.74	52.26
27	7.21	54.94	45.06
22	7.43	62.37	37.63
19	5.22	67.59	32.41
16	6.26	73.86	26.14
13.5	5.79	79.65	20.35
11.4	4.11	83.76	16.24
9.6	2.74	86.49	13.51
8.1	3.32	89.82	10.18
6.8	2.78	92.59	7.41
5.7	1.96	94.56	5.44
4.8	1.67	96.23	3.77
4.1	2.01	98.24	1.76
3.4	0.77	99.01	0.99
2.9	0.97	99.98	0.02
2.4	0.00	99.98	0.02
2	0.02	99.99	0.01
1.75	0.00	99.99	0.01
1.45	0.01	100.00	0.00
1.2	0.00	100.00	0.00

Table C.4 Mineral grain size distribution of cassiterite from Penouta ore (open pit).

Sieve Size	P1-P2 - Retained Wt%	P1-P2 - Cum. Retained Wt%	P1-P2 - Cum. Passing Wt%
355	0.00	0.00	100.00
300	0.13	0.13	99.87
250	0.26	0.38	99.62
212	2.40	2.79	97.21
180	6.93	9.72	90.28
150	11.50	21.21	78.79
125	10.22	31.44	68.56
106	8.07	39.51	60.49
90	8.20	47.70	52.30
75	10.55	58.25	41.75
63	10.03	68.28	31.72
53	8.47	76.76	23.24
45	6.65	83.40	16.60
38	5.19	88.59	11.41
32	3.90	92.49	7.51
27	2.59	95.08	4.92
22	2.02	97.10	2.90
19	0.89	97.99	2.01
16	0.75	98.74	1.26
13.5	0.54	99.28	0.72
11.4	0.36	99.64	0.36
9.6	0.15	99.79	0.21
8.1	0.09	99.88	0.12
6.8	0.05	99.93	0.07
5.7	0.03	99.96	0.04
4.8	0.02	99.98	0.02
4.1	0.01	99.99	0.01
3.4	0.00	99.99	0.01
2.9	0.00	100.00	0.00
2.4	0.00	100.00	0.00
2	0.00	100.00	0.00
1.75	0.00	100.00	0.00
1.45	0.00	100.00	0.00
1.2	0.00	100.00	0.00

Table C.5. Mineral grain size distribution of columbite from Penouta tailings.

Sieve Size	P3 - Retained Wt%	P3 - Cum. Retained Wt%	P3 - Cum. Passing Wt%
300	0.00	0.00	0.00
250	0.00	0.00	100.00
212	2.93	2.93	97.07
180	0.00	2.93	97.07
150	8.02	10.94	89.06
125	11.19	22.14	77.86
106	12.66	34.80	65.20
90	17.83	52.63	47.37
75	19.34	71.97	28.03
63	10.42	82.39	17.61
53	6.81	89.20	10.80
45	4.08	93.29	6.71
38	1.49	94.78	5.22
32	1.78	96.56	3.44
27	1.01	97.56	2.44
22	0.87	98.43	1.57
19	0.40	98.83	1.17
16	0.44	99.27	0.73
13.5	0.30	99.57	0.43
11.4	0.16	99.74	0.26
9.6	0.11	99.85	0.15
8.1	0.06	99.91	0.09
6.8	0.04	99.95	0.05
5.7	0.03	99.98	0.02
4.8	0.01	99.99	0.01
4.1	0.01	100.00	0.00
3.4	0.00	100.00	0.00
2.9	0.00	100.00	0.00
2.4	0.00	100.00	0.00
2	0.00	100.00	0.00
1.75	0.00	100.00	0.00
1.45	0.00	100.00	0.00
1.2	0.00	100.00	0.00
0.52	0.00	0.00	0.00
0	0.00	0.00	0.00

Table C.6. Mineral grain size distribution of tantalite from Penouta tailings.

Sieve Size	P3 - Retained Wt%	P3 - Cum. Retained Wt%	P3 - Cum. Passing Wt%
212	0.00	0.00	100.00
180	1.45	1.45	98.55
150	4.61	6.06	93.94
125	11.66	17.72	82.28
106	10.81	28.53	71.47
90	12.29	40.82	59.18
75	17.59	58.41	41.59
63	12.00	70.41	29.59
53	7.64	78.05	21.95
45	5.14	83.19	16.81
38	4.05	87.24	12.76
32	3.36	90.60	9.40
27	1.99	92.59	7.41
22	1.97	94.56	5.44
19	1.09	95.66	4.34
16	1.30	96.95	3.05
13.5	0.95	97.90	2.10
11.4	0.59	98.49	1.51
9.6	0.42	98.91	1.09
8.1	0.33	99.24	0.76
6.8	0.20	99.44	0.56
5.7	0.20	99.64	0.36
4.8	0.11	99.76	0.24
4.1	0.13	99.89	0.11
3.4	0.05	99.94	0.06
2.9	0.06	100.00	0.00
2.4	0.00	100.00	0.00
2	0.00	100.00	0.00
1.75	0.00	100.00	0.00
1.45	0.00	100.00	0.00
1.2	0.00	100.00	0.00

Table C.7. Mineral grain size distribution of microlite from Penouta tailings.

Sieve Size	P3 - Retained Wt%	P3 - Cum. Retained Wt%	P3 - Cum. Passing Wt%
180	0.00	0.00	0.00
150	0.00	0.00	100.00
125	13.79	13.79	86.21
106	0.00	13.79	86.21
90	20.08	33.87	66.13
75	15.05	48.92	51.08
63	15.82	64.74	35.26
53	2.80	67.53	32.47
45	3.90	71.44	28.56
38	1.16	72.60	27.40
32	3.10	75.70	24.30
27	3.78	79.48	20.52
22	4.36	83.85	16.15
19	2.71	86.56	13.44
16	2.17	88.73	11.27
13.5	2.20	90.93	9.07
11.4	2.48	93.41	6.59
9.6	1.06	94.47	5.53
8.1	1.53	96.00	4.00
6.8	1.00	97.00	3.00
5.7	1.07	98.07	1.93
4.8	0.43	98.50	1.50
4.1	0.79	99.29	0.71
3.4	0.37	99.65	0.35
2.9	0.34	100.00	0.00
2.4	0.00	100.00	0.00
2	0.00	100.00	0.00
1.75	0.00	100.00	0.00
1.45	0.00	0.00	0.00
1.2	0.00	0.00	0.00

Table C.8. Mineral grain size distribution of cassiterite from Penouta tailings.

Sieve Size	P3 - Retained Wt%	P3 - Cum. Retained Wt%	P3 - Cum. Passing Wt%
355	0.00	0.00	100.00
300	1.67	1.67	98.33
250	3.10	4.77	95.23
212	6.06	10.83	89.17
180	9.44	20.27	79.73
150	9.95	30.23	69.77
125	12.71	42.94	57.06
106	11.95	54.89	45.11
90	10.59	65.48	34.52
75	11.00	76.47	23.53
63	6.81	83.28	16.72
53	5.33	88.62	11.38
45	2.86	91.48	8.52
38	2.25	93.73	6.27
32	1.76	95.48	4.52
27	1.14	96.62	3.38
22	1.05	97.67	2.33
19	0.64	98.31	1.69
16	0.52	98.83	1.17
13.5	0.46	99.28	0.72
11.4	0.31	99.59	0.41
9.6	0.15	99.74	0.26
8.1	0.10	99.84	0.16
6.8	0.05	99.89	0.11
5.7	0.05	99.94	0.06
4.8	0.03	99.97	0.03
4.1	0.02	99.98	0.02
3.4	0.01	99.99	0.01
2.9	0.01	100.00	0.00
2.4	0.00	100.00	0.00
2	0.00	100.00	0.00
1.75	0.00	100.00	0.00
1.45	0.00	100.00	0.00
1.2	0.00	100.00	0.00

Table C.9. Mineral grain size distribution of scheelite from Mittersill ore (concentrate).

Sieve Size	M1-M2 - Retained Wt%	M1-M2 - Cum. Retained Wt%	M1-M2 - Cum. Passing Wt%
850	0.00	0.00	100.00
710	8.85	8.85	91.15
600	2.04	10.90	89.10
500	4.06	14.96	85.04
425	2.90	17.86	82.14
355	2.82	20.68	79.32
300	1.41	22.09	77.91
250	2.99	25.08	74.92
212	4.24	29.32	70.68
180	5.36	34.67	65.33
150	8.31	42.98	57.02
125	9.32	52.30	47.70
106	6.85	59.15	40.85
90	7.20	66.35	33.65
75	6.86	73.21	26.79
63	5.68	78.89	21.11
53	4.68	83.57	16.43
45	3.89	87.46	12.54
38	3.09	90.56	9.44
32	2.74	93.30	6.70
27	2.10	95.40	4.60
22	1.87	97.27	2.73
19	0.88	98.15	1.85
16	0.73	98.89	1.11
13.5	0.53	99.42	0.58
11.4	0.31	99.72	0.28
9.6	0.12	99.84	0.16
8.1	0.07	99.91	0.09
6.8	0.03	99.94	0.06
5.7	0.03	99.97	0.03
4.8	0.01	99.98	0.02
4.1	0.01	99.99	0.01
3.4	0.00	99.99	0.01
2.9	0.00	100.00	0.00
2.4	0.00	100.00	0.00
2	0.00	100.00	0.00
1.75	0.00	100.00	0.00
1.45	0.00	100.00	0.00
1.2	0.00	100.00	0.00

Table C.10. Mineral grain size distribution of scheelite from Mittersill ore (tailings).

Sieve Size	W1-W2- Retained Wt%	W1-W2 -Cum. Retained Wt%	W1-W2-Cum. Passing Wt%
1000	0.00	0.00	100.00
850	51.21	51.21	48.79
710	0.00	51.21	48.79
600	29.55	80.76	19.24
500	0.00	80.76	19.24
425	0.00	80.76	19.24
355	0.00	80.76	19.24
300	0.00	80.76	19.24
250	9.31	90.07	9.93
212	0.00	90.07	9.93
180	2.82	92.89	7.11
150	2.23	95.12	4.88
125	3.95	99.07	0.93
106	0.00	99.07	0.93
90	0.59	99.66	0.34
75	0.00	99.66	0.34
63	0.00	99.66	0.34
53	0.00	99.66	0.34
45	0.00	99.66	0.34
38	0.14	99.80	0.20
32	0.00	99.80	0.20
27	0.00	99.80	0.20
22	0.05	99.84	0.16
19	0.00	99.84	0.16
16	0.04	99.89	0.11
13.5	0.04	99.93	0.07
11.4	0.01	99.94	0.06
9.6	0.03	99.97	0.03
8.1	0.01	99.98	0.02
6.8	0.01	99.99	0.01
5.7	0.01	99.99	0.01
4.8	0.00	100.00	0.00
4.1	0.00	100.00	0.00
3.4	0.00	100.00	0.00

Table D.1. Modal mineralogy of minerals from Penouta ore (open pit).

Mineral	P1-P2 - Wt%	P1-P2 - Area%	P1-P2 - Area (µm)	P1-P2 - Particle Count	P1-P2 - Grain Count
Unknown	0.00	0.97	1505065.05	3981	4774
Columbite	6.53	6.43	9971280.11	3972	4441
Tantalite	20.09	19.76	30654437.08	19729	28804
Microlite	0.25	0.21	328237.98	1485	2501
Cassiterite	53.61	41.27	64027634.38	30444	32534
Scheelite	0.08	0.07	105852.88	41	45
Quartz	1.98	4.01	6221986.32	5426	6597
Albite	2.56	5.18	8036720.33	6733	7810
Plagioclase	0.05	0.09	138804.24	412	454
K-Feldspar	0.87	1.81	2816021.49	2355	2846
Clinopyroxene	0.00	0.00	1199.09	5	5
Almandine	0.50	0.63	976590.27	840	1059
Spessartine	5.13	6.52	10116091.05	3831	4607
Vesuvianite	0.00	0.00	7347.52	32	33
Rhodonite	0.01	0.01	20128.07	4	4
Epidote	0.01	0.01	22672.48	8	17
Zoisite	0.02	0.03	44575.56	51	54
Hornblende	0.03	0.05	78561.77	51	52
Staurolite	0.15	0.22	334759.86	1118	1306
Biotite	0.05	0.09	132428.59	425	494
Muscovite	1.66	3.12	4836162.11	5339	7977
Chlorite	0.03	0.05	72341.35	466	641
Kaolinite	1.52	3.10	4805417.71	9101	12533
Titanite	0.00	0.00	4940.34	7	10
Rutile	0.01	0.01	16618.53	22	23
Fe_oxide_or_hydroxide	2.40	2.48	3845167.01	3331	5184
Ilmenite	0.02	0.03	40897.30	15	15
Mn-Al_oxide_or_hydroxide	0.01	0.02	25441.86	52	84
Mn-Fe_oxide_or_hydroxide	0.02	0.02	31621.78	60	83
Fe-Al_oxide_or_hydroxide	0.17	0.23	362784.37	1293	2489
Fe-Zn_oxide_or_hydroxide	0.00	0.00	2209.21	23	25
Apatite	0.02	0.03	41614.95	20	20
Cryptomelane	0.04	0.04	67704.72	56	72
Zircon	1.30	1.48	2299899.82	1366	1473
Monazite_LREE-rich	0.05	0.05	74001.63	56	59
Monazite_MREE-rich	0.16	0.16	256000.11	282	325
Xenotime	0.12	0.14	212124.21	275	324
Crandallite-Sr	0.05	0.07	101137.51	312	340
Rhabdophane-Th	0.01	0.02	30350.70	66	96
Pyrite_or_pyrrhotite	0.24	0.25	394482.65	308	324
Chalcopyrite	0.01	0.01	11563.46	27	28
Arsenopyrite	0.01	0.01	19329.42	12	13
Sphalerite with mediumFe	0.01	0.01	11109.02	16	16
Native Bi	0.01	0.04	61439.31	39	39
Iron	0.03	0.17	264031.54	205	439
Total	100.00	100.00	155154448.67	70194	136042

Table D.2. Modal mineralogy of minerals from Penouta tailings.

Mineral	P3 - Wt%	P3 - Area%	P3 - Area (μm)	P3 - Particle Count	P3 - Grain Count
Unknown	0.00	0.60	1117443.99	2468	3853
Columbite	1.35	0.81	1517575.64	404	522
Tantalite	2.01	1.21	2259155.50	1055	2159
Microlite	0.11	0.06	107618.90	199	345
Cassiterite	10.15	4.76	8911491.43	2943	3463
Scheelite	0.80	0.43	806670.43	155	202
Quartz	42.12	51.93	97181179.96	7628	8458
Albite	2.43	3.00	5611365.99	1322	1548
Plagioclase	0.17	0.20	380876.46	163	177
K-Feldspar	2.41	3.05	5698409.14	940	1279
Almandine	0.66	0.51	946891.99	1160	1792
Spessartine	4.35	3.37	6302710.05	804	1683
Vesuvianite	0.10	0.10	182470.92	19	22
Rhodonite	0.09	0.08	153065.09	63	173
Epidote	0.04	0.03	61488.80	38	79
Zoisite	0.03	0.03	48953.47	56	83
Hornblende	0.01	0.01	16758.02	128	154
Staurolite	0.66	0.57	1069689.61	788	1084
Biotite	1.51	1.57	2947064.27	1031	2030
Muscovite	7.45	8.53	15970845.34	1851	3024
Chlorite	0.59	0.65	1213089.99	750	1504
Kaolinite	1.93	2.40	4484853.46	1196	2026
Titanite	0.02	0.01	28056.01	8	9
Rutile	0.29	0.22	406977.48	158	244
Fe_oxide_or_hydroxide	8.23	5.18	9684945.04	7790	13575
Ilmenite	0.46	0.31	584058.12	159	245
Mn-Al_oxide_or_hydroxide	1.17	0.95	1774003.19	237	733
Mn-Fe_oxide_or_hydroxide	0.63	0.41	772504.24	368	1180
Fe-Al_oxide_or_hydroxide	1.13	0.93	1736995.63	1927	3575
Fe-Zn_oxide_or_hydroxide	0.15	0.09	177355.10	123	209
Apatite	0.26	0.26	487114.04	56	68
Cryptomelane	5.14	3.78	7069036.62	561	1657
Dolomite	0.01	0.01	17666.89	6	6
Fluorite	0.03	0.03	64514.65	4	5
Barite	0.01	0.00	9014.55	16	26
Zn_sulphate	0.16	0.12	228094.83	20	80
Zircon	0.64	0.45	835795.05	295	312
Monazite_LREE-rich	0.25	0.16	291849.08	118	149
Monazite_MREE-rich	0.13	0.08	151094.35	116	192
Xenotime	0.15	0.10	192713.80	71	97
Crandallite-Sr	0.06	0.05	84494.23	96	137
Rhabdophane-Th	0.00	0.00	110.24	4	5
Pyrite_or_pyrrhotite	0.66	0.42	794105.86	144	183
Chalcopyrite	0.02	0.01	24949.17	63	231
Arsenopyrite	0.71	0.38	711271.90	103	136
Sphalerite with mediumFe	0.10	0.08	158480.12	21	43
Bismuthinite	0.03	0.01	24701.71	15	18
Iron	0.41	1.32	2463509.25	852	1253
Total	100.00	100.00	187129340.43	21696	62547

Table D.3. Modal mineralogy of minerals from Mittersill ore (concentrate).

Mineral	M1-M2 - Wt%	M1-M2 - Area%	M1-M2 - Area (µm)	M1-M2 - Particle Count	M1-M2 - Grain Count
Unknown	0.00	0.25	430961.53	1122	1544
Columbite	0.00	0.00	0.00	0	0
Tantalite	0.00	0.00	4843.60	29	32
Microlite	0.00	0.00	616.42	10	12
Cassiterite	0.00	0.00	1658.03	11	11
Scheelite	17.82	10.20	17294737.55	6644	6921
Quartz	7.50	9.82	16651584.32	1661	2922
Albite	4.72	6.20	10511275.61	766	1093
Plagioclase	3.67	4.69	7961429.62	1229	2056
K-Feldspar	0.49	0.65	1108575.68	422	1253
Clinopyroxene	2.91	2.94	4984835.79	864	910
Almandine	0.05	0.04	64024.21	110	129
Spessartine	0.00	0.00	6062.94	3	3
Vesuvianite	0.22	0.22	379695.37	443	530
Rhodonite	0.00	0.00	0.00	0	0
Epidote	0.04	0.04	64595.64	112	146
Zoisite	14.84	15.46	26217065.79	16677	19190
Hornblende	20.18	23.93	40588387.92	18932	22178
Staurolite	0.07	0.07	112170.04	380	523
Biotite	1.80	1.99	3379317.13	819	1333
Muscovite	0.28	0.34	584809.52	219	339
Chlorite	0.41	0.48	810899.87	552	945
Kaolinite	0.00	0.01	9232.77	54	57
Titanite	2.64	2.61	4424424.27	7619	10950
Rutile	0.06	0.05	82161.29	88	100
Fe_oxide_or_hydroxide	0.17	0.11	191584.45	636	814
Ilmenite	0.04	0.03	51119.93	61	66
Gahnite	0.00	0.00	233.97	3	3
Mn-Al_oxide_or_hydroxide	0.00	0.00	89.99	1	1
Mn-Fe_oxide_or_hydroxide	0.00	0.00	461.19	5	5
Fe-Al_oxide_or_hydroxide	0.02	0.01	23410.38	99	118
Fe-Zn_oxide_or_hydroxide	0.01	0.00	6859.34	37	42
Apatite	0.60	0.64	1090839.04	1046	1153
Cryptomelane	0.00	0.00	0.00	0	0
Calcite	0.65	0.82	1393653.16	216	274
Dolomite	0.07	0.09	147573.57	25	25
Fluorite	0.04	0.04	70487.60	54	220
Zircon	0.02	0.01	21180.93	257	295
Pyrite_or_pyrrhotite	18.20	12.49	21180507.15	9555	10235
Chalcopyrite	0.63	0.52	880377.35	1271	1447
Arsenopyrite	0.13	0.07	125090.07	56	58
Sphalerite with mediumFe	0.01	0.01	18332.81	20	20
Cobaltite-Ni	0.06	0.03	57124.38	33	33
Pentlandite-Co	0.01	0.01	16130.35	43	53
Molybdenite	0.06	0.04	64444.91	132	164
Bismuthinite	0.28	0.12	202164.79	156	179
Native Bi	0.01	0.04	72289.61	102	120
Iron	0.01	0.05	85873.30	112	143
Total	100.00	100.00	169582193.28	60267	91826

Table D.4. Modal mineralogy of minerals from Mittersill ore (tailings).

Mineral	Wt%	Area%	Area (µm)	Particle Count	Grain Count
Albite	18.58	20.11	28067032.00	10642	11890
Ankerite	0.26	0.24	340600.00	149	168
Anorthite	5.60	5.80	8097356.00	7605	10125
Apatite	0.23	0.21	289052.00	367	384
Arsenopyrite	0.00	0.00	204.00	2	2
Arsenopyrite (Co, Ni enriched)	0.00	0.00	164.00	1	1
Augite	9.24	7.71	10761116.00	8827	10929
Betafite	0.06	0.04	56160.00	700	718
Biotite	5.09	4.65	6494876.00	4143	4833
Bismuthinite	0.00	0.00	664.00	10	12
Calcite	1.59	1.66	2322108.00	1047	1140
Chalcopyrite	0.03	0.02	31896.00	65	70
Cummingtonite (aph)	0.25	0.21	299900.00	400	551
Epidote	0.40	0.33	455760.00	1526	1888
Fluorite	0.03	0.03	40332.00	43	51
Gypsum	0.00	0.00	164.00	2	2
Hematite	0.05	0.03	37880.00	113	150
Hornblende	33.87	33.13	46221988.00	36149	41105
Ilmenite	0.00	0.00	4144.00	8	8
Manganite	0.00	0.00	0.00	0	0
Molybdenite	0.01	0.01	7172.00	16	19
Muscovite	2.13	2.14	2988080.00	2145	3050
Orthoclase	2.15	2.39	3331740.00	1685	2522
Orthoclase_altered	0.08	0.09	131372.00	628	951
Pentlandite	0.01	0.00	5440.00	65	70
Pyrite	0.10	0.05	75840.00	79	83
Pyrrhotite	0.77	0.47	659548.00	807	840
Quartz	16.62	17.96	25058764.00	8191	9340
Rutile	0.01	0.00	6060.00	23	30
Scheelite	0.13	0.06	87516.00	90	94
Serpentine	1.15	1.36	1897368.00	2245	3008
Sphalerite with hiFe	0.00	0.00	488.00	4	4
Titanite	1.51	1.23	1719980.00	4087	5615
Zircon	0.01	0.00	6152.00	97	103
Aluminum	0.00	0.00	1512.00	6	6
Cement	0.01	0.01	18720.00	114	140
Steel	0.01	0.00	4400.00	21	22
Unknown	0.00	0.00	0.00	0	0
Total	100.00	100.00	139533628.00	66248	109989

Table E.1. Mineral association of columbite from Penouta ore (open pit).

Columbite Weight% locked in...	P1-P2 - Binary Particle (%)	P1-P2 - Ternary+ Particle (%)
Unknown	0.00	0.00
Low_Counts	0.00	0.00
No_XRay	0.00	0.00
Tantalite	59.31	12.34
Microlite	0.00	0.13
Cassiterite	0.72	0.41
Scheelite	0.00	0.00
Quartz	0.49	0.98
Albite	0.28	1.44
Plagioclase	0.07	0.00
K-Feldspar	0.07	0.33
Clinopyroxene	0.00	0.00
Almandine	0.02	0.02
Spessartine	0.10	0.03
Vesuvianite	0.00	0.00
Rhodonite	0.00	0.00
Epidote	0.00	0.00
Zoisite	0.00	0.00
Hornblende	0.00	0.00
Staurolite	0.10	0.11
Biotite	0.01	0.05
Muscovite	0.40	1.29
Chlorite	0.00	0.01
Kaolinite	0.27	0.65
Titanite	0.00	0.00
Rutile	0.00	0.00
Fe_oxide_or_hydroxide	0.12	0.24
Ilmenite	0.00	0.00
Gahnite	0.00	0.00
Mn-Al_oxide_or_hydroxide	0.00	0.00
Mn-Fe_oxide_or_hydroxide	0.00	0.00
Fe-Al_oxide_or_hydroxide	0.00	0.07
Fe-Zn_oxide_or_hydroxide	0.00	0.01
Apatite	0.00	0.00
Cryptomelane	0.00	0.00
Zn_sulphate	0.00	0.00
Zircon	0.19	0.40
Monazite_LREE-rich	0.00	0.00
Monazite_MREE-rich	0.04	0.07
Xenotime	0.00	0.00
Crandallite-Sr	0.07	0.03
Rhabdophane-Th	0.00	0.01
Pyrite_or_pyrrhotite	0.09	0.04

Table E.2. Mineral association of tantalite from Penouta ore (open pit).

Tantalite Weight% locked in...	P1-P2 - Binary Particle (%)	P1-P2 - Ternary+ Particle (%)
Unknown	0.00	0.00
Low_Counts	0.00	0.00
No_XRay	0.00	0.00
Columbite	16.49	4.44
Microlite	1.15	0.56
Cassiterite	2.81	1.44
Scheelite	0.00	0.00
Quartz	4.81	1.68
Albite	2.57	1.17
Plagioclase	0.05	0.05
K-Feldspar	1.32	0.73
Clinopyroxene	0.00	0.00
Almandine	0.03	0.03
Spessartine	0.03	0.02
Vesuvianite	0.00	0.00
Rhodonite	0.00	0.00
Epidote	0.00	0.00
Zoisite	0.00	0.00
Hornblende	0.00	0.00
Staurolite	0.33	0.10
Biotite	0.07	0.02
Muscovite	3.75	1.21
Chlorite	0.02	0.00
Kaolinite	5.34	1.67
Titanite	0.00	0.00
Rutile	0.00	0.00
Fe_oxide_or_hydroxide	0.18	0.31
Ilmenite	0.00	0.00
Gahnite	0.00	0.00
Mn-Al_oxide_or_hydroxide	0.00	0.00
Mn-Fe_oxide_or_hydroxide	0.02	0.00
Fe-Al_oxide_or_hydroxide	0.05	0.03
Fe-Zn_oxide_or_hydroxide	0.00	0.00
Apatite	0.00	0.00
Cryptomelane	0.00	0.00
Calcite	0.00	0.00
Dolomite	0.00	0.00
Fluorite	0.00	0.00
Barite	0.00	0.00
Zn_sulphate	0.00	0.00
Zircon	0.43	0.20
Monazite_LREE-rich	0.00	0.01
Monazite_MREE-rich	0.01	0.01
Xenotime	0.13	0.03
Crandallite-Sr	0.12	0.05
Rhabdophane-Th	0.00	0.00
Pyrite_or_pyrrhotite	0.01	0.00
Chalcopyrite	0.00	0.00
Covellite	0.00	0.00
Arsenopyrite	0.00	0.00

Table E.3. Mineral association of microlite from Penouta ore (open pit).

Microlite Weight% locked in...	P1-P2 - Binary Particle (%)	P1-P2 - Ternary+ Particle (%)
Unknown	0.00	0.00
Low_Counts	0.00	0.00
No_XRay	0.00	0.00
Columbite	0.00	4.11
Tantalite	35.07	20.34
Cassiterite	16.20	5.38
Scheelite	0.00	0.00
Quartz	0.33	1.78
Albite	0.16	0.70
Plagioclase	0.00	0.04
K-Feldspar	0.18	0.47
Clinopyroxene	0.00	0.00
Almandine	0.00	0.07
Spessartine	0.00	0.02
Vesuvianite	0.01	0.00
Rhodonite	0.00	0.00
Epidote	0.00	0.00
Zoisite	0.00	0.00
Hornblende	0.00	0.00
Staurolite	0.03	0.02
Biotite	0.04	0.01
Muscovite	0.01	0.65
Chlorite	0.00	0.00
Kaolinite	0.36	0.98
Titanite	0.00	0.00
Rutile	0.00	0.00
Fe_oxide_or_hydroxide	0.01	0.09
Ilmenite	0.00	0.00
Gahnite	0.00	0.00
Mn-Al_oxide_or_hydroxide	0.00	0.00
Mn-Fe_oxide_or_hydroxide	0.00	0.00
Fe-Al_oxide_or_hydroxide	0.00	0.01
Fe-Zn_oxide_or_hydroxide	0.00	0.00
Apatite	0.00	0.00
Cryptomelane	0.00	0.00
Calcite	0.00	0.00
Dolomite	0.00	0.00
Fluorite	0.00	0.00
Barite	0.00	0.00
Zn_sulphate	0.00	0.00
Zircon	0.00	0.52
Monazite_LREE-rich	0.00	0.00
Monazite_MREE-rich	0.01	0.00
Xenotime	0.00	0.00
Crandallite-Sr	0.00	0.00
Rhabdophane-Th	0.00	0.00
Pyrite_or_pyrrhotite	0.00	0.00
Chalcopyrite	0.00	0.00

Table E.4. Mineral association of cassiterite from Penouta ore (open pit).

Cassiterite Weight% locked in...	P1-P2 - Binary Particle (%)	P1-P2 - Ternary+ Particle (%)
Unknown	0.00	0.00
Low_Counts	0.00	0.00
No_XRay	0.00	0.00
Columbite	0.17	0.06
Tantalite	2.98	0.71
Microlite	0.28	0.04
Scheelite	0.00	0.00
Quartz	2.52	0.38
Albite	1.88	0.25
Plagioclase	0.03	0.00
K-Feldspar	1.66	0.27
Clinopyroxene	0.00	0.00
Almandine	0.08	0.01
Spessartine	0.08	0.02
Vesuvianite	0.01	0.00
Rhodonite	0.00	0.00
Epidote	0.00	0.00
Zoisite	0.00	0.00
Hornblende	0.00	0.00
Staurolite	0.09	0.03
Biotite	0.04	0.00
Muscovite	4.52	0.49
Chlorite	0.04	0.00
Kaolinite	0.75	0.25
Titanite	0.00	0.00
Rutile	0.00	0.00
Fe_oxide_or_hydroxide	0.39	0.29
Ilmenite	0.00	0.00
Gahnite	0.00	0.00
Mn-Al_oxide_or_hydroxide	0.03	0.00
Mn-Fe_oxide_or_hydroxide	0.00	0.00
Fe-Al_oxide_or_hydroxide	0.04	0.04
Fe-Zn_oxide_or_hydroxide	0.00	0.00
Apatite	0.00	0.00
Cryptomelane	0.00	0.00
Calcite	0.00	0.00
Dolomite	0.00	0.00
Fluorite	0.00	0.00
Barite	0.00	0.00
Zn_sulphate	0.00	0.00
Zircon	0.11	0.03
Monazite_LREE-rich	0.00	0.00
Monazite_MREE-rich	0.01	0.00
Xenotime	0.03	0.00
Crandallite-Sr	0.02	0.00
Rhabdophane-Th	0.00	0.00
Pyrite_or_pyrrhotite	0.01	0.00
Chalcopyrite	0.00	0.00
Covellite	0.00	0.00
Arsenopyrite	0.00	0.00
Sphalerite with mediumFe	0.02	0.00

Table E.5. Mineral association of columbite from Penouta tailings.

Columbite Weight% locked in...	P3 - Binary Particle (%)	P3 - Ternary+ Particle (%)
Unknown	0.00	0.00
Low_Counts	0.00	0.00
No_XRay	0.00	0.00
Tantalite	59.86	12.99
Microlite	0.02	0.05
Cassiterite	0.11	0.31
Scheelite	0.00	0.05
Quartz	1.45	1.67
Albite	0.00	0.14
Plagioclase	0.00	0.00
K-Feldspar	0.35	1.19
Clinopyroxene	0.00	0.00
Almandine	0.00	0.08
Spessartine	0.00	0.23
Vesuvianite	0.00	0.00
Rhodonite	0.00	0.00
Epidote	0.00	0.07
Zoisite	0.00	0.00
Hornblende	0.00	0.00
Staurolite	0.00	0.07
Biotite	0.00	0.05
Muscovite	0.20	1.07
Chlorite	0.00	0.00
Kaolinite	0.00	0.28
Titanite	0.00	0.00
Rutile	0.00	0.00
Fe_oxide_or_hydroxide	0.85	0.78
Ilmenite	0.00	0.00
Gahnite	0.00	0.00
Mn-Al_oxide_or_hydroxide	0.00	0.00
Mn-Fe_oxide_or_hydroxide	0.00	0.00
Fe-Al_oxide_or_hydroxide	0.21	0.10
Fe-Zn_oxide_or_hydroxide	0.00	0.00
Apatite	0.00	0.00
Cryptomelane	0.00	0.00
Calcite	0.00	0.00
Dolomite	0.00	0.00
Fluorite	0.00	0.00
Barite	0.00	0.00
Zn_sulphate	0.00	0.00
Zircon	0.53	0.37
Monazite_LREE-rich	0.01	0.14
Monazite_MREE-rich	0.00	0.00
Xenotime	0.00	0.00
Crandallite-Sr	0.00	0.06
Rhabdophane-Th	0.00	0.00
Pyrite_or_pyrrhotite	0.00	0.00
Chalcopyrite	0.00	0.00
Covellite	0.00	0.00

Table E.6. Mineral association of tantalite from Penouta tailings.

Tantalite Weight% locked in...	P3 - Binary Particle (%)	P3 - Ternary+ Particle (%)
Unknown	0.00	0.00
Low_Counts	0.00	0.00
No_XRay	0.00	0.00
Columbite	32.94	8.05
Microlite	1.05	0.54
Cassiterite	1.15	0.27
Scheelite	0.00	0.10
Quartz	3.93	2.19
Albite	0.34	0.27
Plagioclase	0.00	0.00
K-Feldspar	1.27	1.17
Clinopyroxene	0.00	0.00
Almandine	0.00	0.06
Spessartine	0.12	0.05
Vesuvianite	0.00	0.00
Rhodonite	0.00	0.00
Epidote	0.00	0.01
Zoisite	0.00	0.00
Hornblende	0.00	0.00
Staurolite	0.87	0.06
Biotite	1.46	0.02
Muscovite	4.24	1.54
Chlorite	0.01	0.00
Kaolinite	0.73	0.20
Titanite	0.00	0.00
Rutile	0.00	0.00
Fe_oxide_or_hydroxide	1.62	0.92
Ilmenite	0.00	0.00
Gahnite	0.00	0.00
Mn-Al_oxide_or_hydroxide	0.04	0.01
Mn-Fe_oxide_or_hydroxide	0.00	0.02
Fe-Al_oxide_or_hydroxide	0.77	0.02
Fe-Zn_oxide_or_hydroxide	0.00	0.00
Apatite	0.00	0.00
Cryptomelane	0.00	0.00
Calcite	0.00	0.00
Dolomite	0.00	0.00
Fluorite	0.00	0.00
Barite	0.00	0.00
Zn_sulphate	0.00	0.00
Zircon	0.00	0.07
Monazite_LREE-rich	0.00	0.01
Monazite_MREE-rich	0.00	0.00
Xenotime	0.00	0.00
Crandallite-Sr	0.01	0.00
Rhabdophane-Th	0.00	0.00
Pyrite_or_pyrrhotite	0.00	0.00
Chalcopyrite	0.00	0.00

Table E.6. Mineral association of microlite from Penouta tailings.

Microlite Weight% locked in...	P3 - Binary Particle (%)	P3 - Ternary+ Particle (%)
Unknown	0.00	0.00
Low_Counts	0.00	0.00
No_XRay	0.00	0.00
Columbite	0.20	1.05
Tantalite	4.84	10.72
Cassiterite	7.83	3.28
Scheelite	0.00	0.00
Quartz	3.62	2.15
Albite	0.00	0.14
Plagioclase	0.00	0.00
K-Feldspar	0.00	0.13
Clinopyroxene	0.00	0.00
Almandine	0.00	0.11
Spessartine	0.06	0.14
Vesuvianite	0.00	0.00
Rhodonite	0.00	0.00
Epidote	0.00	0.00
Zoisite	0.00	0.00
Hornblende	0.00	0.00
Staurolite	0.00	0.00
Biotite	0.14	0.00
Muscovite	0.00	0.01
Chlorite	0.00	0.00
Kaolinite	0.01	0.01
Titanite	0.00	0.00
Rutile	0.00	0.00
Fe_oxide_or_hydroxide	0.01	1.04
Ilmenite	0.00	0.00
Gahnite	0.00	0.00
Mn-Al_oxide_or_hydroxide	0.00	0.01
Mn-Fe_oxide_or_hydroxide	0.00	0.00
Fe-Al_oxide_or_hydroxide	0.00	0.00
Fe-Zn_oxide_or_hydroxide	0.00	0.00
Apatite	0.03	0.00
Cryptomelane	0.00	0.00
Calcite	0.00	0.00
Dolomite	0.00	0.00
Fluorite	0.00	0.00
Barite	0.00	0.00
Zn_sulphate	0.00	0.00
Zircon	0.06	1.50
Monazite_LREE-rich	0.00	0.00
Monazite_MREE-rich	0.00	0.00
Xenotime	0.00	0.00
Crandallite-Sr	0.00	0.00
Rhabdophane-Th	0.00	0.00
Pyrite_or_pyrrhotite	0.00	0.00
Chalcopyrite	0.00	0.00

Table E.8. Mineral association of cassiterite from Penouta tailings.

Cassiterite Weight% locked in...	P3 - Binary Particle (%)	P3 - Ternary+ Particle (%)
Unknown	0.00	0.00
Low_Counts	0.00	0.00
No_XRay	0.00	0.00
Columbite	0.19	0.06
Tantalite	0.78	0.07
Microlite	0.52	0.03
Scheelite	0.00	0.00
Quartz	4.42	0.59
Albite	1.00	0.02
Plagioclase	0.00	0.01
K-Feldspar	2.09	0.12
Clinopyroxene	0.00	0.00
Almandine	0.05	0.02
Spessartine	0.07	0.03
Vesuvianite	0.00	0.00
Rhodonite	0.00	0.00
Epidote	0.00	0.00
Zoisite	0.00	0.00
Hornblende	0.00	0.00
Staurolite	0.73	0.05
Biotite	0.08	0.00
Muscovite	8.36	0.56
Chlorite	0.05	0.00
Kaolinite	0.58	0.16
Titanite	0.00	0.00
Rutile	0.00	0.00
Fe_oxide_or_hydroxide	2.37	0.22
Ilmenite	0.00	0.00
Gahnite	0.00	0.01
Mn-Al_oxide_or_hydroxide	0.69	0.32
Mn-Fe_oxide_or_hydroxide	0.00	0.16
Fe-Al_oxide_or_hydroxide	1.19	0.12
Fe-Zn_oxide_or_hydroxide	0.00	0.00
Apatite	0.00	0.00
Cryptomelane	0.07	0.14
Calcite	0.00	0.00
Dolomite	0.00	0.00
Fluorite	0.00	0.00
Barite	0.00	0.00
Zn_sulphate	0.00	0.00
Zircon	0.00	0.01
Monazite_LREE-rich	0.00	0.00
Monazite_MREE-rich	0.00	0.00
Xenotime	0.00	0.00
Crandallite-Sr	0.00	0.00
Rhabdophane-Th	0.00	0.00
Pyrite_or_pyrrhotite	0.00	0.00
Chalcopyrite	0.00	0.00
Covellite	0.00	0.00

Table E.9. Mineral association of scheelite from Mittersill (concentrate).

Scheelite Weight% locked in...	M1-M2 - Binary Particle (%)	M1-M2 - Ternary+ Particle (%)
Unknown	0.00	0.00
Low_Counts	0.00	0.00
No_XRay	0.00	0.00
Columbite	0.00	0.00
Tantalite	0.00	0.00
Microlite	0.00	0.00
Cassiterite	0.00	0.00
Quartz	3.26	0.49
Albite	0.01	0.22
Plagioclase	0.02	0.06
K-Feldspar	0.03	0.01
Clinopyroxene	0.14	0.05
Almandine	0.00	0.01
Spessartine	0.00	0.00
Vesuvianite	0.01	0.00
Rhodonite	0.00	0.00
Epidote	0.01	0.05
Zoisite	3.35	0.35
Hornblende	1.92	0.19
Staurolite	0.27	0.00
Biotite	0.01	0.05
Muscovite	0.13	0.04
Chlorite	0.18	0.09
Kaolinite	0.00	0.00
Titanite	0.73	0.03
Rutile	0.00	0.00
Fe_oxide_or_hydroxide	0.06	0.01
Ilmenite	0.00	0.00
Gahnite	0.00	0.00
Mn-Al_oxide_or_hydroxide	0.00	0.00
Mn-Fe_oxide_or_hydroxide	0.00	0.00
Fe-Al_oxide_or_hydroxide	0.00	0.00
Fe-Zn_oxide_or_hydroxide	0.00	0.00
Apatite	0.16	0.00
Cryptomelane	0.00	0.00
Calcite	0.29	0.04
Dolomite	0.00	0.00
Fluorite	0.05	0.00
Barite	0.00	0.00
Zn_sulphate	0.00	0.00
Zircon	0.00	0.00
Monazite_LREE-rich	0.00	0.00
Monazite_MREE-rich	0.00	0.00
Xenotime	0.00	0.00
Pyrite_or_pyrrhotite	0.25	0.09
Chalcopyrite	0.13	0.00
Molybdenite	0.04	0.00

Table E.10. Mineral association of scheelite from Mittersill (tailings).

Scheelite Weight% locked in...	W1-W2 - Binary Particle (%)	W1-W2 - Ternary+ Particle (%)
Unknown	0.40	0.00
Albite	0.24	0.00
Ankerite	0.50	0.00
Anorthite	0.22	0.00
Apatite	0.00	0.00
Arsenopyrite	0.00	0.00
Arsenopyrite (Co, Ni enriched)	0.60	0.00
Augite	0.05	0.49
Betafite	3.34	0.22
Biotite	0.00	0.06
Bismuthinite	0.44	0.01
Calcite	3.32	0.05
Chalcopyrite	8.04	0.01
Cummingtonite (aph)	1.01	0.00
Epidote	1.01	0.00
Fluorite	0.00	0.00
Gypsum	2.06	0.05
Hematite	0.66	0.35
Hornblende	1.74	0.19
Ilmenite	0.00	0.00
Manganite	5.44	0.05
Molybdenite	0.82	0.04
Muscovite	1.58	0.09
Orthoclase	2.91	0.00
Orthoclase_altered	0.84	0.03
Pentlandite	0.98	0.00
Pyrite	0.29	0.01
Pyrrhotite	0.49	0.00
Quartz	9.88	0.00
Rutile	0.00	0.00
Scheelite	0.42	0.00
Serpentine	13.94	0.00
Sphalerite with hiFe	0.99	0.00
Titanite	1.27	0.00
Zircon	0.00	0.00
Aluminum	1.12	0.04
Albite	6.06	0.00
Ankerite	0.00	0.00
Anorthite	0.00	0.00
Apatite	0.00	0.00
Arsenopyrite	0.40	0.00
Arsenopyrite (Co, Ni enriched)	0.24	0.09
Augite	0.50	0.00
Betafite	0.22	0.00